Mechanistic Evaluation of Geosynthetic Interlayer Performance in Asphalt Overlays: Effects of Temperature, Loading Rate, and Placement Depth

by

Van-Thang HO

MANUSCRIPT-BASED THESIS PRESENTED TO ÉCOLE DE TECHNOLOGIE SUPÉRIEURE IN PARTIAL FULFILLMENT FOR THE DEGREE OF DOCTOR OF PHILOSOPHY
Ph.D.

MONTREAL, SEPTEMBER 4, 2026

ÉCOLE DE TECHNOLOGIE SUPÉRIEURE
UNIVERSITÉ DU QUÉBEC

BOARD OF EXAMINERS

THIS THESIS HAS BEEN EVALUATED

BY THE FOLLOWING BOARD OF EXAMINERS

Dr. Alan Carter, Thesis Supervisor
Department of Construction Engineering, École de technologie supérieure

Dr. Michel Vaillancourt, Thesis Co-supervisor
Department of Construction Engineering, École de technologie supérieure

Dr. Eshan Dave, Thesis Co-supervisor
Department of Civil and Environmental Engineering, University of New Hampshire

Dr. Andy Shih, President of the Board of Examiners
Department of Electrical Engineering, École de technologie supérieure

Dr. Diego Ramirez Cardona, Member of the jury
Department of Construction Engineering, École de technologie supérieure

Dr. Christiane Raab, External Evaluator
Swiss Federal Laboratories for Materials Science and Technology

THIS THESIS WAS PRESENTED AND DEFENDED

IN THE PRESENCE OF A BOARD OF EXAMINERS AND PUBLIC

ON JULY 09, 2026

AT ÉCOLE DE TECHNOLOGIE SUPÉRIEURE

ACKNOWLEDGEMENTS

I would like to express my deepest gratitude to my thesis supervisor, Professor Alan Carter, for his invaluable guidance, continuous support, and patience throughout my doctoral studies at École de technologie supérieure. His expertise in pavement engineering and his dedication to research excellence have been instrumental in shaping this work. Professor Carter's mentorship extended beyond academic guidance; his encouragement during challenging times and his commitment to fostering independent thinking have profoundly influenced my development as a researcher.

I am equally grateful to my co-supervisors, Professor Michel Vaillancourt and Professor Eshan Dave, for their insightful comments, constructive feedback, and encouragement. Professor Vaillancourt's expertise in materials characterization and his meticulous attention to experimental details have significantly enriched this research. Professor Dave's knowledge of fracture mechanics and his valuable perspectives on the broader implications of this work have been essential in positioning this thesis within the international research context.

I would like to thank the Natural Sciences and Engineering Research Council (NSERC) and TEXEL Corporation for their financial support, which made this research possible. Their investment in fundamental research on pavement materials demonstrates a commitment to advancing infrastructure sustainability.

Special thanks go to my colleagues at the Laboratoire de Chaussées et Matériaux Bitumineux (LCMB) for their assistance during experimental work and for creating a stimulating research environment. I am particularly grateful to Dr. Ehsan Solatiyan, whose pioneering work on the crack widening device provided the foundation for this thesis. Our collaborative discussions and shared experimental challenges have been both professionally enriching and personally rewarding.

I would also like to acknowledge the technical staff at ÉTS who assisted with specimen preparation, testing equipment maintenance, and laboratory facilities management. Their expertise and dedication to maintaining high-quality experimental conditions were essential for the success of this research.

Finally, I express my heartfelt gratitude to my family for their unconditional love, support, and sacrifices throughout this journey. Their encouragement during difficult moments and their unwavering belief in my abilities have been my greatest source of strength. This achievement would not have been possible without their patience and understanding during the many long hours dedicated to this research.

Évaluation mécanistique de la performance des intercouches géosynthétiques dans les rechargements en enrobé bitumineux : Effets de la température, du taux de chargement et de la profondeur de placement

Van-Thang HO

RÉSUMÉ

La fissuration réflective demeure un défi majeur pour la réhabilitation des chaussées bitumineuses. Cette forme de dégradation se produit lorsque les fissures existantes dans la chaussée sous-jacente se propagent vers le haut à travers le rechargement d'asphalte, compromettant ainsi la durabilité de la réhabilitation et nécessitant des interventions d'entretien répétées. Les intercouches géosynthétiques offrent une solution prometteuse pour atténuer ce problème, mais leur efficacité dépend de multiples facteurs qui n'ont que rarement été étudiés de manière systématique.

Cette thèse présente une évaluation mécanistique complète de trois types d'intercouches géosynthétiques - un géotextile (tissu de pavage, PF), une géogrille verre-carbone (Carbophalt GB) et un géocomposite en fibre de verre (Glasphalt GV) - en utilisant un dispositif d'élargissement de fissure développé à l'ÉTS. Ce dispositif permet une évaluation rapide et reproductible de la résistance à la fissuration des systèmes bitumineux renforcés en utilisant des éprouvettes compactes (80 mm × 80 mm × 80 mm).

Le programme expérimental examine systématiquement les effets de la température (-20 °C, 25 °C et 40 °C), du taux de chargement (2 et 5 mm/min) et de la profondeur de placement (un tiers, mi-hauteur et deux tiers depuis le bas de l'éprouvette), le plan factoriel complet taux-profondeur étant réalisé à 25 °C et 40 °C. Les paramètres de performance comprennent les indices de rigidité ($K_{0\text{-}4mm}$ et $\bar{K}_{10\text{-}30\%}$), l'énergie de dissipation, le facteur d'amélioration de la ténacité (TIF), l'énergie de fracture (G_{IC}) et l'intégrale J interfaciale.

Les résultats révèlent des différences significatives de comportement entre les matériaux. Le tissu de pavage offre une performance stable avec une faible sensibilité au taux de chargement (TIF de 1,36-1,54 à 2 mm/min et 1,08-1,21 à 5 mm/min), attribuable à l'activation progressive des fibres qui permet une absorption d'énergie efficace aux deux taux de chargement. Le Glasphalt GV présente une forte sensibilité au taux de chargement : une performance médiocre à 2 mm/min (TIF de 0,54-0,57) s'inverse vers une excellente performance à 5 mm/min (TIF de 1,12-1,29), indiquant que son réseau de fibres de verre nécessite un chargement dynamique pour une activation efficace. Le Carbophalt GB démontre une performance modérée et stable (TIF ≈ 1,0).

Le placement à un tiers de profondeur surpasse systématiquement les autres positions pour tous les matériaux et conditions, permettant une interception précoce des fissures et une redistribution efficace des contraintes. Les éprouvettes non renforcées atteignent une rigidité

plus élevée mais présentent une rupture fragile, tandis que les systèmes renforcés échangent la rigidité contre la ductilité - précisément la fonction prévue des intercouches géosynthétiques.

Ces résultats fournissent des recommandations pratiques pour la sélection et le positionnement des intercouches: le tissu de pavage pour les applications générales avec des conditions de trafic variables, le Glasphalt GV uniquement pour les environnements de chargement dynamique à haute vitesse, et le placement à un tiers de profondeur pour tous les types de géosynthétiques.

Une étude complémentaire d'arrachement a montré que le montage boulonné provoquait une rupture en traction du géotextile plutôt qu'un décollement d'interface, ce qui fournit des enseignements méthodologiques pour les futurs protocoles d'essai d'adhérence. Un modèle par éléments finis calibré sur la réponse mesurée a reproduit la force au pic, le déplacement au pic et le travail dissipé à moins de 3 pour cent. Un cadre de corrélation exploratoire entre les paramètres de chargement monotone et de fatigue cyclique a été développé par régression log-linéaire sur trois ensembles de données cohérents, offrant un outil de diagnostic pour anticiper le classement en fatigue à partir d'essais monotones plus rapides.

Mots-clés : dispositif d'élargissement de fissure, dissipation d'énergie, fissuration réflective, facteur d'amélioration de la ténacité, interface bitumineuse, énergie de fracture, géosynthétiques, rechargement d'asphalte

Mechanistic Evaluation of Geosynthetic Interlayer Performance in Asphalt Overlays: Effects of Temperature, Loading Rate, and Placement Depth

Van-Thang HO

ABSTRACT

Reflective cracking remains a critical challenge in bituminous pavement rehabilitation. This distress occurs when existing cracks in the underlying pavement propagate upward through the asphalt overlay, compromising rehabilitation durability and necessitating repeated maintenance interventions. Geosynthetic interlayers offer a promising solution for mitigating this problem, but their effectiveness depends on multiple factors that have rarely been studied systematically.

This thesis presents a mechanistic evaluation of three geosynthetic interlayer types - a paving fabric (PF), a carbon-glass fiber geogrid (Carbophalt GB), and a fiberglass geocomposite (Glasphalt GV) - using a crack widening device developed at ÉTS. This device enables rapid, reproducible assessment of crack resistance in reinforced bituminous systems using compact specimens (80 mm × 80 mm × 80 mm).

The experimental program systematically examines the effects of temperature (-20 °C, 25 °C, and 40 °C), loading rate (2 and 5 mm/min), and placement depth (one-third, one-half, and two-thirds from the specimen bottom), with the full rate-depth factorial conducted at 25 °C and 40 °C. Performance parameters include stiffness indices ($K_{0\text{-}4mm}$ and $\bar{K}_{10\text{-}30\%}$), energy dissipation, Toughness Improvement Factor (TIF), fracture energy (G_{IC}), and interfacial J-integral.

The results show clear behavioral differences among materials. Paving fabric delivers stable performance with low rate-sensitivity (TIF of 1.36-1.54 at 2 mm/min and 1.08-1.21 at 5 mm/min), attributable to progressive fiber activation that enables effective energy absorption across both displacement rates. Glasphalt GV shows strong rate sensitivity: poor performance at 2 mm/min (TIF of 0.54 - 0.57) reverses to excellent performance at 5 mm/min (TIF of 1.12-1.29), indicating its glass fiber network requires dynamic loading for effective activation. Carbophalt GB shows moderate, stable performance (TIF ≈ 1.0).

One-third depth placement consistently outperforms other positions across all materials and conditions, enabling early crack interception and effective stress redistribution before significant damage accumulates in the upper asphalt layer. Unreinforced specimens achieve higher stiffness but exhibit brittle failure, whereas reinforced systems trade stiffness for ductility - precisely the intended function of geosynthetic interlayers.

At elevated temperature (40 °C), reduced asphalt viscosity limits force development despite increased deformation capacity. The interfacial J-integral analysis confirms that paving fabric at one-third depth requires the highest energy for crack propagation, validating its superior crack resistance.

A supplementary pull-out investigation revealed that the bolt-clamped configuration induced tensile-tearing failure of the geotextile rather than interface debonding, providing lessons for future bond-strength testing protocols. A finite element model calibrated against the measured response reproduced the peak force, the peak displacement, and the dissipated work within 3 percent. An exploratory correlation framework between monotonic and cyclic fatigue loading parameters was developed using log-linear regression on three consistent material datasets, providing a diagnostic tool for anticipating fatigue ranking from faster monotonic tests.

This research provides practical recommendations for interlayer selection and placement: paving fabric for general applications across variable traffic conditions, Glasphalt GV only for high-speed dynamic loading environments, and one-third depth placement for all geosynthetic types. The findings also show that laboratory testing protocols should incorporate multiple loading rates, as single-rate testing may misrepresent field performance.

Keywords: crack widening device, energy dissipation, reflective cracking, toughness improvement factor, bituminous interface, fracture energy, geosynthetics, asphalt overlay.

TABLE OF CONTENTS

Page

INTRODUCTION 1
0.1 Background and Context..1
0.2 The Reflective Cracking Problem...1
0.3 Current Rehabilitation Strategies and Their Limitations 2
0.4 Geosynthetic Interlayers as a Promising Solution 2
0.5 Research Gaps and Motivation 2
0.6 Research Objectives 3
0.7 Research Scope and Limitations...4
0.8 Thesis Organization 5

CHAPTER 1 BIBLIOGRAPHIC REVIEW 7
1.1 Introduction...7
1.2 Reflective Cracking Mechanisms 8
1.2.1 Phenomenological Description 8
1.2.2 Traffic-Induced Mechanisms 10
1.2.3 Thermal Mechanisms...12
1.2.4 Environmental and Material Factors..13
1.3 Fracture Mechanics Principles...16
1.3.1 Linear Elastic Fracture Mechanics...16
1.3.2 Viscoelastic Fracture Mechanics 17
1.3.3 Fatigue Crack Growth..19
1.3.4 Mixed-Mode Fracture 19
1.4 Interlayer Systems for Crack Mitigation..23
1.4.1 Overview of Interlayer Systems...23
1.4.2 Geosynthetic Interlayers 24
1.4.3 Performance Mechanisms 27
1.4.4 Interface Bonding and Placement Considerations 29
1.5 Laboratory Testing Methods...30
1.6 Field Performance Evaluation...38
1.7 Design Considerations and Best Practices 41
1.8 Identified Research Gaps 41
1.9 Summary 43

CHAPTER 2 METHODOLOGY 45
2.1 Introduction..45
2.2 Experimental Program Overview 45
2.3 Materials 46

2.3.1 Asphalt Mixture 46
2.3.2 Geosynthetic Interlayer Materials 47
2.3.3 Tack Coat and Bonding Agents 48
2.4 Specimen Fabrication 48
2.4.1 Slab Compaction 48
2.4.2 Interlayer Installation 49
2.4.3 Specimen Cutting and Surface Preparation 50
2.5 Crack Widening Device (CWD) 51
2.5.1 Device Configuration and Mechanical Principles 51
2.5.2 Test Procedure 53
2.5.3 Geometric Relationship: Vertical to Horizontal Displacement 53
2.5.4 Force Analysis and Load Cell Interpretation 54
2.5.5 Spring Mechanism Management 54
2.5.6 Validated Test Parameters 55
2.6 Experimental Program 56
2.6.1 Test Variables and Conditions 56
2.6.2 Test Matrix 56
2.7 Data Analysis Framework 57
2.7.1 Force-Displacement Response 57
2.7.2 Stiffness Indices 58
2.7.3 Energy Dissipation and Crack Propagation Energy 58
2.7.4 Toughness Improvement Factor (TIF) 59
2.7.5 Fracture Toughness (G_{IC}) 59
2.7.6 Interfacial J-integral 59
2.8 Summary 59

CHAPTER 3 EVALUATION OF CRACK DEVELOPMENT THROUGH A BITUMINOUS INTERFACE REINFORCED WITH GEOSYNTHETIC MATERIALS BY USING A NOVEL APPROACH 61
Abstract 61
3.1 Introduction 62
3.2 Research Background 63
3.3 Method 65
3.3.1 Material 66
3.3.2 Test Setup 70
3.3.3 Crack Widening Device 71
3.4 Results and Discussion 73
3.4.1 Result and Discussion for Energy Dissipation 73
3.4.2 Result and Discussion for Crack Stiffness Evolution 75
3.5 Conclusions 78

CHAPTER 4 STUDY THE CRACK DEVELOPMENT OF GEOSYNTHETICS INTERLAYERS IN BITUMINOUS STRUCTURES UNDER DIFFERENT TEMPERATURES 81
Abstract 81
4.1 Introduction 82
4.2 Research Background 83
4.3 Methodology 85
4.3.1 Materials 85
4.3.2 Test Setup 90
4.4 Results and Discussion 91
4.4.1 Performance of Reinforcement at Different Positions 92
4.4.2 The Effectiveness of Temperature on Performance of Geosynthetics 95
4.4.3 Energy Dissipation 97
4.4.4 Relation between Force and Time 98
4.5 Conclusion 101
4.5.1 Optimal Reinforcement Position 102
4.5.2 Temperature-Dependent Performance 103
4.5.3 Geotextile Superiority Over Geogrids 103
4.5.4 Unreinforced Samples and Emulsion Limitations 103
4.5.5 Implications for Pavement Engineering 103

CHAPTER 5 FRACTURE-ENERGY-BASED ASSESSMENT OF GEOSYNTHETIC INTERLAYERS IN ASPHALT OVERLAYS UNDER VARIABLE TEMPERATURE, DISPLACEMENT RATE, AND PLACEMENT DEPTH 105
Abstract 105
5.1 Introduction 106
5.2 Research Background 107
5.3 Problem Statement 109
5.4 Methodology 110
5.4.1 Materials 111
5.4.2 Specimen Preparation 112
5.4.3 Test Setup 114
5.4.4 Data Analysis 115
5.5 Results and Discussion 116
5.5.1 Stiffness Analysis Framework 117
5.5.1.1 Effect of Temperature on Stiffness Response 118
5.5.1.2 Effect of Displacement Rate on Stiffness Response 120
5.5.1.3 Effect of Placement Depth 122
5.5.1.4 Summary of Stiffness Analysis 123
5.5.2 Effect of Displacement Rate on Force-Displacement Response 124
5.5.3 Optimum Placement Depth for Reinforcement in Asphalt Systems 126
5.5.4 Energy Dissipation 128

5.5.5 Crack-Interlayer Interaction Analysis ... 131
5.5.6 Influence of Reinforcement Type and Placement on Toughness Improvement Factor ... 134
5.5.7 Fracture Toughness G_{IC} ... 136
5.5.8 Effect of Reinforcement/Emulsion Position on J-Integral ... 138
5.6 Conclusion ... 140

CHAPTER 6 SUPPLEMENTARY INVESTIGATION: PULL-OUT RESISTANCE OF GEOTEXTILE INTERLAYER IN ASPHALT SPECIMENS ... 143
6.1 Introduction ... 143
6.2 Test Setup and Procedure ... 143
6.2.1 Specimen Configuration ... 143
6.2.2 Pull-out Test Apparatus ... 144
6.2.3 Testing Protocol ... 146
6.2.4 Finite Element Visualization of the Pull-out Configuration ... 146
6.3 Test Results and Failure Mode Identification ... 148
6.3.1 Load-Displacement Response ... 148
6.3.2 Identification of Failure Mode ... 150
6.4 Expected Interface Debonding Behavior ... 152
6.5 Comparative Analysis ... 157
6.6 Calibration of the Finite Element Model Against the Measured Response ... 160
6.7 Mechanistic Interpretation of the Failure Mode ... 164
6.7.1 Fundamental Differences: Soil vs. Asphalt Pull-out ... 164
6.7.2 The Role of Clamping Configuration ... 165
6.8 Discussion and Recommendations ... 167
6.9 Summary ... 169

CHAPTER 7 CORRELATION BETWEEN MONOTONIC AND CYCLIC FATIGUE LOADING BEHAVIOR OF GEOSYNTHETIC-REINFORCED ASPHALT INTERLAYERS ... 171
7.1 Introduction ... 171
7.2 Cyclic Test Protocol ... 171
7.3 Monotonic Loading Test Results ... 173
7.3.1 Force-Displacement Response at 5 mm/min ... 173
7.3.2 Force-Displacement Response at 2 mm/min ... 174
7.3.3 Summary of Monotonic Test Parameters ... 175
7.4 Loading Rate Sensitivity Analysis ... 177
7.5 Cyclic Fatigue Loading Test Results ... 178
7.5.1 S-N Curves and Basquin Regression ... 178
7.5.2 Fatigue Improvement Factor ... 180
7.5.3 Basquin Slope Analysis ... 181
7.6 Monotonic-Fatigue Correlation Model ... 182
7.6.1 Methodology ... 182

7.6.2 Correlation Results....184
7.6.3 Per-Load Level Predictions....187
7.7 Predicted S-N Curves for PF Geotextile....188
7.8 Dissipated Energy Analysis....189
7.9 Discussion....191
7.9.1 Mechanistic Interpretation of PF Geotextile Behavior....191
7.9.2 Possible Sources of Experimental Error....192
7.9.3 Limitations of the Correlation Model....193
7.10 Summary....194

CONCLUSION....195

LIST OF BIBLIOGRAPHIC REFERENCES....201

LIST OF TABLES

Page

Table 1.1 Summary of reflective cracking mechanisms in asphalt overlays 14

Table 1.1 Summary of reflective cracking mechanisms in asphalt overlays (continued) 15

Table 1.2 Summary of fracture mechanics parameters for asphalt pavement analysis 20

Table 1.2 Summary of fracture mechanics parameters for asphalt pavement analysis (continued) 21

Table 1.2 Summary of fracture mechanics parameters for asphalt pavement analysis (continued) 22

Table 1.3 Comparative properties of geosynthetic interlayer types for pavement rehabilitation 28

Table 1.3 Comparative properties of geosynthetic interlayer types for pavement rehabilitation (continued) 29

Table 1.4 Comparison of laboratory test methods for reflective cracking evaluation 31

Table 1.4 Comparison of laboratory test methods for reflective cracking evaluation (continued) 32

Table 1.4 Comparison of laboratory test methods for reflective cracking evaluation (continued) 33

Table 1.5	Summary of key research studies on geosynthetic interlayer performance	39
Table 1.5	Summary of key research studies on geosynthetic interlayer performance (continued)	40
Table 2.1	Experimental matrix across the three studies	57
Table 3.1	The specifications of Hot Mix Asphalt	67
Table 3.2	Technical properties of grids (provided by the geogrid supplier)	68
Table 3.3	Principal mechanical specification of paving fabric (PF) (supplied by the company)	68
Table 4.1	The specification of hot mix asphalt	86
Table 4.2	The mechanical properties of paving fabric (PF)	86
Table 4.3	The mechanical properties of geosynthetics	87
Table 5.1	The specifications of Hot Mix Asphalt	111
Table 5.2	The mechanical properties of paving fabric (PF) (supplied by the company)	112
Table 5.3	The mechanical properties of geosynthetics	112
Table 6.1	Discretization of the pull-out finite element model	147
Table 6.2	Quantitative comparison of actual versus expected pull-out test response	159
Table 6.3	Calibrated model versus measured pull-out response	163

Table 7.1	Monotonic test parameters at one-half placement (percentage values at 2 mm/min relative to Control)	177
Table 7.2	Correlation model parameters and PF predictions (mean N_f at 1 Hz)	186
Table 7.3	Per-load PF predictions at 1 Hz (time-based model)	188
Table 7.4	Monotonic dissipated energy and displacement parameters	191

LIST OF FIGURES

Page

Figure 1.1 Mechanisms of reflective cracking: (a) thermal, (b) traffic induced, (c) surface initiated, and (d) position of wheel load showing bending and shearing stress distributions at the crack tip After Hu et al.,2010 10

Figure 1.2 Three fundamental modes of crack loading in fracture mechanics: Mode I (opening), Mode II (in-plane shearing), and Mode III (out-of-plane tearing) After Anderson, 2005......17

Figure 1.3 Example of a high-strength fiber geotextile used as an asphalt interlayer Taken from Albayati et al., 2023 24

Figure 1.4 Types of geosynthetic interlayers used in asphalt pavement rehabilitation: (a) Geocomposite with nonwoven backing (Glasphalt GV), and (b) Carbon-glass fiber geogrid (Carbophalt GB)......26

Figure 1.5 Conceptual illustration of stress redistribution for unreinforced versus geogrid-reinforced overlays After Ragni et al., 2020a......27

Figure 1.6 Example specimen preparation and overlay testing configuration used to evaluate cracking performance under controlled temperature conditions Taken from Albayati et al., 2023 30

Figure 1.7 Example full-scale trial section and cross-sectional configuration for evaluating geogrid-reinforced asphalt interlayers. Taken from Ragni et al., 2020a......33

Figure 1.8 Semi-circular bending (SCB) specimen and loading configuration commonly used for fracture characterization of asphalt mixtures Taken from Pszczola and Szydlowski, 2018 34

Figure 1.9 Overlay Test (OT) apparatus used to apply cyclic direct-tension displacement to asphalt mixture specimens for evaluating cracking potential. Taken from FHWA-HIF-21-017; U.S. Government work/public domain 34

Figure 1.10 Example four-point bending (4PB) fatigue loading configuration for asphalt beam specimens. Taken from Thives et al., 2022 35

Figure 1.11 Schematic illustration of reflective cracking device concept and associated measurement approach. After Thives et al., 2022 35

Figure 1.12 Illustration of interface shear forces and representative failure modes associated with insufficient tack coat/bonding between asphalt layers. After Kim and Mun, 2021...36

Figure 1.13 Typical experimental setup and specimen configuration for interface shear strength testing (ISST). Taken from Kim and Mun, 2021 36

Figure 1.14 Example analysis of interface shear response and strength interpretation from ISST results. After Kim and Mun, 2021...37

Figure 1.15 Example large-scale slab specimen fabrication and geogrid placement for laboratory evaluation of reinforced asphalt overlays. Taken from Rueda et al., 2023..40

Figure 2.1 Specimen fabrication process using the French roller compactor: (a) compacted bottom asphalt layer in the steel mold, (b) paving fabric interlayer installed over the cured bottom layer, and (c)

	French roller compactor applying compaction to the top asphalt overlay	50
Figure 2.2	Schematic diagram of the crack widening device (CWD) showing the principal components: (1) double-layer bituminous sample, (2) sliding parts, (3) triangular-shape base, (4) screw, (5) spring, (6) loading arm, (7) supporting arm, (8) notch, and (9) protruding edge After Solatiyan et al., 2023	52
Figure 3.1	Criteria employed to differentiate among different types of geosynthetics	66
Figure 3.2	Gradation curves for each type of hot mixture. Note: ESG-10 = surface course mix (10 mm); ESG-14 = binder course mix (14 mm); GB-20 = base course mix (20 mm)	67
Figure 3.3	The shape, size, and dimensions of specimens	70
Figure 3.4	The crack widening device (CWD)	72
Figure 3.5	A typical force-displacement curve obtained from the crack performance tester device on two samples including the reinforcement grid made of carbon at the interface surrounded by a surface course mix with a nominal maximum aggregate size of 10 mm and a binder course mix with a nominal maximum aggregate size of 14 mm	73
Figure 3.6	Changes in energy dissipation during the bottom-up crack propagation stage in two different double-layer structures. Note: GR = carbon grid; GB = glass-carbon grid; GV = geocomposite; PF = paving fabric; UN = unreinforced	74
Figure 3.7	Crack stiffness evolution in double-layer structures composed of ESG-10 over ESG-14 reinforced with different types of interlayers and the unreinforced structure	75
Figure 3.8	Crack stiffness evolution in double-layer structures composed of ESG-14 over GB-20 reinforced with different types of interlayers and the unreinforced structure	76

Figure 3.9 Changes in maximum force and displacement and initial crack stiffness in different interface types 78

Figure 4.1 Schematic of shape, size, and dimensions of specimens 89

Figure 4.2 A view of crack widening device and how it works 91

Figure 4.3 Force-displacement relationship for all samples with reinforcement and emulsion placed at one-third from the bottom of specimens underwent different temperatures: (A) high temperature (40°C), (B) room temperature (25°C), and (C) low temperature (−20°C) 93

Figure 4.4 Force-displacement relationship for all samples with reinforcement and emulsion placed at two-thirds from the bottom of the specimens underwent different temperatures: (A) high temperature (40°C), (B) room temperature (25°C), and (C) low temperature (−20°C) 94

Figure 4.5 The influence of temperature on performance of reinforced and unreinforced samples: (A) at one-third, (B) at two-thirds, (C) at one-third, (D) at two-thirds, (E) at one-third, (F) at two-thirds, (G) at one-third, and (H) at two-thirds 96

Figure 4.6 Energy dissipation under different temperatures and positions of reinforcement for reinforced and unreinforced samples: (A) high temperature (40°C), (B) room temperature (25°C), and (C) low temperature (-20°C) 98

Figure 4.7 Relationship between maximum force and time for reinforced and unreinforced samples: (A) high temperature (40°C), (B) room temperature (25°C), and (C) low temperature (-20°C) 99

Figure 4.8 Maximum force and time between peak load and failure: (A) high temperature (40°C), (B) room temperature (25°C), and (C) low temperature (−20°C) 101

Figure 5.1 Schematic of shape, size, and dimensions of specimens 113

Figure 5.2 Sketch of the crack widening apparatus with detail components 114

Figure 5.3 Placement depth of reinforcement/emulsion within the specimens......115

Figure 5.4 Initial and working-range stiffness parameters at 40 °C for one-third and two-thirds placement depths under displacement rates of 5 and 2 mm/min 119

Figure 5.5 Initial and working-range stiffness parameters at 25 °C for one-third and two-thirds placement depths under displacement rates of 5 and 2 mm/min 121

Figure 5.6 Effect of displacement rate on the force-displacement response of Geotextile PF, Control test, Glasphalt GV and Carbophalt GB at one-third and two-thirds embedment depths under 25 °C and 40 °C. ...126

Figure 5.7 Force-displacement response of Geotextile PF, Control, Glassphalt GV, and Carbophalt GB at one-third, one-half, and two-thirds placement depths at 25°C under displacement rates of 5 and 2 mm/min. 128

Figure 5.8 Calculation for energy dissipation 128

Figure 5.9 Dissipated energy at 25 °C for different placement depths and displacement rates. 130

Figure 5.10 Time to interlayer and force at interlayer for different placement depths. 133

Figure 5.12 Fracture Toughness Comparison 138

Figure 5.13 The J-integral at the interface according to displacement rate and placement of reinforcement/emulsion..........139

Figure 6.1 Specimen preparation sequence showing geotextile insertion between asphalt layers, positioning of the interlayer, and assembled specimen in the steel mold..........145

Figure 6.2 Pull-out test setup: laboratory photographs showing specimen with geotextile extending from mold, clamping assembly, and top view (top); schematic illustration showing the excessive clamping issue at the interface (bottom) ... 145

Figure 6.3 Construction of the pull-out finite element model: (a) exploded view of the asphalt lifts and the geotextile interlayer shell; (b) geotextile mesh (10 mm grid) with the loaded edge ... 147

Figure 6.4 Finite element visualization of the pull-out configuration (illustrative, uncalibrated model): (a) displacement magnitude contours showing the prescribed 5 mm pull-out of the geotextile relative to the fixed asphalt block; (b) von Mises stress on the geotextile shell, increasing toward the loaded end ... 148

Figure 6.5 Load-displacement curve from the pull-out test on paving fabric (nonwoven geotextile) in ESG-10 asphalt, showing four phases of tensile deformation leading to tearing failure ... 149

Figure 6.6 Evidence of tensile failure mode: geotextile being pulled from mold showing stretching (a), post-test specimen showing severe necking (b) ... 151

Figure 6.7 Schematic illustration of (a) the observed tensile-tearing failure, in which the geotextile elongates and ruptures while remaining bonded to the asphalt, and (b) the intended interface debonding failure, in which the geotextile slides as an intact body relative to the asphalt ... 151

Figure 6.8 Expected load-displacement response for true interface debonding behavior of geotextile from ESG-10 asphalt layers ... 156

Figure 6.9 Comparison of actual pull-out response (geotextile tearing) and expected response (interface debonding): (a) full scale; (b) zoomed view showing initial stiffness contrast ... 158

Figure 6.10 Measured pull-out response compared with the calibrated finite element model: the model reproduces the peak force (-1.4%), the displacement at peak (+1.4%), and the dissipated work (-2.2%), and tears at the mold exit; the rising-branch shape and the post-peak rate are outside the scope of the elastic-plastic material law (see text). 164

Figure 6.11 Effect of confinement system on the failure mode: (a) field-like overlay self-weight (~1-1.5 kPa) allows interface dilation and natural debonding; (b) bolt-tightened laboratory clamping imposes normal stresses well above field levels and suppresses debonding, forcing tensile failure of the geotextile 166

Figure 7.1 Loading history of a representative cyclic test (GV geocomposite, 1 Hz, 3 kN target load, one-half placement): (a) applied sinusoidal loading waveform over cycles 50 to 54; (b) per-cycle envelope of the maximum and minimum applied force, showing a constant load amplitude over the full test; (c) per-cycle envelope of the axial displacement, showing progressive accumulation up to failure at N_f = 244 cycles. 173

Figure 7.2 Monotonic force-displacement curves at 5 mm/min loading rate (one-half placement) 174

Figure 7.3 Monotonic force-displacement curves at 2 mm/min loading rate (one-half placement) 175

Figure 7.4 Effect of displacement rate on the monotonic response of the four interlayer configurations at the one-half placement, comparing 5 mm/min and 2 mm/min: (a) time to failure; (b) peak axial force; (c) displacement at failure. Error bars represent ±1 SD estimated from the coefficient of variation observed across placement positions within the same testing campaign (~8% for time and displacement; ~4% for peak force). 176

Figure 7.5 Loading rate sensitivity index (time ratio 2 mm/min to 5 mm/min) 177

Figure 7.8 Fatigue Improvement Factor (FIF) relative to control at (a) 1 Hz and (b) 2 Hz 181

Figure 7.9 Basquin slope magnitude |B| comparison 182

Figure 7.10 Monotonic-fatigue correlation models: (a) energy, (b) time, (c) rate sensitivity, (d) peak force 186

Figure 7.11 PF predicted (navy) versus measured (blue) fatigue life at each applied load level: (a) 1 Hz and (b) 2 Hz loading frequency 187

Figure 7.12 S-N curves at (a) 1 Hz and (b) 2 Hz with PF predicted Basquin regression (dashed navy). Faded points show PF measured data 189

Figure 7.13 Dissipated energy at the one-half placement: (a) monotonic dissipated energy at 5 mm/min and 2 mm/min for the four configurations, (b) the energy-retention ratio E_{2mm}/E_{5mm} (1.0 = full retention), and (c) the monotonic dissipated energy at 2 mm/min plotted against 5 mm/min with the 1:1 line 190

LIST OF ABBREVIATIONS AND ACRONYMS

2PB	Two-point bending
4PB	Four-point bending
AASHTO	American Association of State Highway and Transportation Officials
AC	Asphalt concrete
APT	Accelerated pavement testing
ASTM	American Society for Testing and Materials
BMD	Balanced mix design
C3D8R	Eight-node linear brick element with reduced integration (Abaqus)
CFE	Critical fracture energy (overlay tester parameter)
CGSB	Canadian General Standards Board
CIB	Coefficient of interface bonding
COD	Crack opening displacement
COV	Coefficient of variation
CPR	Crack progression rate (overlay tester parameter)
CSS-1H	Slow-setting cationic asphalt emulsion

CTE	Coefficient of thermal expansion
CT_{index}	Cracking tolerance index
CTOD	Crack tip opening displacement
CWD	Crack widening device
DCB	Double cantilever beam
DER	Dissipated energy ratio
DIC	Digital image correlation
EME-14	High-modulus asphalt mixture (14 mm NMAS)
EN	European standard (Norme européenne)
ESG-10	Surface course hot mix asphalt (10 mm NMAS)
ESG-14	Binder course hot mix asphalt (14 mm NMAS)
ÉTS	École de technologie supérieure
FE	Finite element
FEM	Finite element method
FHWA	Federal Highway Administration
FI	Flexibility index
FIF	Fatigue improvement factor

FWD	Falling weight deflectometer
GB	Geogrid (Carbophalt GB)
GB-20	Base course hot mix asphalt (20 mm NMAS)
GR	Geogrid (glass and carbon fibers)
GV	Geocomposite (Glasphalt GV 120/120)
HMA	Hot mix asphalt
I-FIT	Illinois Flexibility Index Test
IDEAL-CT	Indirect Tensile Asphalt Cracking Test
ISST	Interface shear strength testing
LC	Laboratoire des chaussées (MTQ test method designation)
LCMB	Laboratoire de Chaussées et Matériaux Bitumineux
LEFM	Linear elastic fracture mechanics
LPDS	Layer-parallel direct shear (test)
LTPP	Long-Term Pavement Performance
LVDT	Linear variable differential transformer
MEPDG	Mechanistic-Empirical Pavement Design Guide
MLS10	Mobile Load Simulator (full-scale)

MMLS3	Model Mobile Load Simulator (third-scale)
MTD	Mean texture depth
MTQ	Ministère des Transports du Québec
MTS	Material testing system
NMAS	Nominal maximum aggregate size
NSERC	Natural Sciences and Engineering Research Council of Canada
OT	Overlay tester
PF	Paving fabric (needle-punched nonwoven geotextile)
PG	Performance grade
QC/QA	Quality control / quality assurance
RAP	Reclaimed asphalt pavement
RAS	Recycled asphalt shingles
RDEC	Ratio of dissipated energy change
S4R	Four-node shell element with reduced integration (Abaqus)
SAMI	Stress-absorbing membrane interlayer
SCB	Semi-circular bending
SD	Standard deviation

TC	Tension-compression (test)
TIF	Toughness improvement factor
TxDOT	Texas Department of Transportation
UGR-FACT	University of Granada Fatigue Asphalt Cracking Test
UN	Unreinforced (control)
WLF	Williams-Landel-Ferry
WRC	Wheel reflective cracking

LIST OF SYMBOLS AND UNITS OF MEASUREMENT

a	Crack length	mm
a_0	Initial notch length	mm
A	Basquin intercept / Paris coefficient / Bonded area	- / - / m^2
A_{lig}	Ligament area	mm^2
b	Specimen thickness	mm
B	Basquin regression slope	-
da/dN	Fatigue crack growth rate (Paris law)	mm/cycle
$d\tau/d\delta$	Interface shear stiffness	kPa/mm
D_i	Force-derivative indicator at data point i	N
E	Young's modulus	MPa
E_{2mm}, E_{5mm}	Energy dissipated at 2 and 5 mm/min	J
F	Applied force	N or kN
F_i	Applied force at data point i	N
$F_{interlayer}$	Force at the moment of interlayer engagement	N
$\tilde{F}_i$	Smoothed force at data point i	N

F_{peak}	Peak force	N or kN
F_{res}	Residual pull-out force	kN
F_s	Spring restoring force in CWD	N
FIF	Fatigue improvement factor	-
G	Energy release rate	J/m^2
G_c	Cohesive fracture energy (cohesive zone model)	J/m^2
G_f	Fracture energy from load-displacement curve	J/m^2
G_I, G_{II}	Mode I and mode II energy release rates	J/m^2
G_{IC}	Mode I critical energy release rate (fracture toughness)	kJ/m^2
J	J-integral	N/mm
J_c	Critical J-integral	N/mm
J_{inter}	Interfacial J-integral	N/mm
K	Stress intensity factor	$MPa \cdot m^{1/2}$
$K_{0\text{-}4mm}$	Initial crack stiffness (0-4 mm displacement range)	N/mm
K_1, K_2	Strain-based fatigue power-law coefficients	-
K_{10}, K_{20}, K_{30}	Secant stiffness at 10, 20 and 30% of peak force	N/mm
$\bar{K}_{10\text{-}30\%}$	Working-range stiffness (averaged 10-30% of peak load)	N/mm

K_{exp}	Expected initial pull-out stiffness	kN/mm
K_I, K_{II}, K_{III}	Mode I, II and III stress intensity factors	$MPa \cdot m^{1/2}$
K_{IC}	Mode I critical stress intensity factor (fracture toughness)	$MPa \cdot m^{1/2}$
K_X	Secant stiffness at X% of peak force	N/mm
ℓ_{lig}	Ligament length	mm
L, w	Length and width of the bonded (embedded) area	mm
n	Paris law exponent	-
N	Normal contact force on CWD wedge face	N
N_f	Number of cycles to failure	cycles
P_i, δ_i	Sampled force and displacement values (trapezoidal integration)	N, mm
R	Specimen resistance force	N
R^2	Coefficient of determination	-
s	Sliding distance along inclined wedge face	mm
t	Time	s
t*	Time-to-interlayer marker	s
t_0, t_{peak}	Time at loading start and at peak force	s
T	Temperature / Friction force	°C / N

$T_{interlayer}$	Time to interlayer engagement	s
TIF	Toughness improvement factor	-
u_i	Actuator displacement at data point i	mm
u_X	Displacement at X% of peak force	mm
v	Displacement rate	mm/min
V	Load cell reading (vertical force)	N
W	Specimen width	mm
W_{int}	Mechanical work absorbed up to interlayer engagement	N·mm
W_{total}	Total energy dissipated during crack propagation	J
y_i	Force value at data point i (trapezoidal integration)	N
y_{int}	Interface depth	mm
ΔE	Incremental energy (trapezoidal integration)	J
ΔK	Stress intensity factor range (Paris law)	$MPa \cdot m^{1/2}$
Δx	Horizontal displacement of sliding block	mm
Δz	Vertical actuator displacement	mm
Σ	Summation operator	-
δ	Displacement	mm

δ_c	Critical separation displacement (cohesive zone model)	mm
$\delta_{interlayer}$	Displacement at interlayer engagement	mm
σ_a	Stress amplitude	MPa
σ_c	Cohesive strength (cohesive zone model)	MPa
σ_f	Fatigue strength coefficient	MPa
τ	Interface shear stress	kPa
τ_{peak}	Peak interface shear strength	kPa
τ_{res}	Residual interface shear stress	kPa
ε	Strain	microstrain
$\mu\varepsilon$	Microstrain	10^{-6} strain
θ	Inclination angle of CWD wedge faces	degrees
μ	Coefficient of friction	-
ν	Poisson's ratio	-

INTRODUCTION

0.1 Background and Context

Road pavements underpin economic activity and social connectivity by enabling reliable movement of people and goods. Because flexible (bituminous) pavements dominate many road networks, agencies routinely rely on asphalt overlays to restore ride quality and structural capacity without full reconstruction. Despite their practical advantages, overlays remain highly vulnerable to crack-related deterioration, especially in climates with large thermal gradients that intensify seasonal contraction-expansion cycles and freeze-thaw damage.

Cracking is particularly damaging because it compromises the surface's waterproofing function. Once cracks reach to the surface, they accelerate moisture infiltration and aging, weakening asphalt and unbound layers and reducing the effectiveness of subsequent maintenance.

0.2 The Reflective Cracking Problem

A persistent limitation of conventional overlays is reflective cracking: pre-existing discontinuities concentrate stresses that drive crack propagation through the new overlay (Lytton, 1989). Reflective cracking is commonly governed by (i) traffic-induced differential vertical deflection across a discontinuity (mixed Mode I/Mode II), (ii) thermally driven horizontal movements that open cracks (Mode I), and (iii) combined traffic-thermal actions that often represent the most severe in-service condition (Jayawickrama and Lytton, 1987; Lytton, 1989).

When reflective cracks reach the overlay surface, they create direct pathways for water ingress and rapidly reduce the functional service life of the rehabilitation treatment. As a result, transportation agencies face repeated maintenance cycles and increased life-cycle costs in networks where cracking activity is high. In many networks, reflective cracking can reduce overlay service life by approximately 30 - 60% (Lytton, 1989; Jayawickrama and Lytton, 1987), leading to markedly higher rehabilitation frequencies and costs.

0.3 Current Rehabilitation Strategies and Their Limitations

Common approaches to delay reflective cracking include crack sealing and patching of the existing pavement, milling and replacing the distressed surface, increasing overlay thickness, and using crack-relief mixtures or stress-absorbing membrane interlayers (SAMIs). Thickness increases can delay crack breakthrough, but the required thickness is often costly and may create geometric constraints at curbs, drainage structures, and bridge approaches. Mixture and interlayer solutions can be effective in specific contexts, yet performance varies strongly with climate, traffic, pavement condition, and construction quality.

0.4 Geosynthetic Interlayers as a Promising Solution

Geosynthetic interlayers - installed between the existing cracked pavement and the overlay - have emerged as a widely adopted method for reflective cracking mitigation. Depending on product type and installation, geosynthetics can provide (i) stress absorption and waterproofing (typically paving fabrics), (ii) structural reinforcement through tensile resistance and stress redistribution (typically geogrids), or (iii) combined functions (geo-composites) (Koerner, 2012).

While many laboratory and field studies report improved overlay performance with properly installed geosynthetics, outcomes remain inconsistent across projects. Geosynthetic interlayers are now used extensively across North America, Europe, and Australia as part of standard overlay practice; however, their performance remains inconsistent without guidance that accounts for climate, traffic, and placement-specific conditions. This motivates a more mechanistic basis for selection and design.

0.5 Research Gaps and Motivation

A critical review of the literature shows several persistent gaps that limit reliable design and selection of geosynthetic interlayers for reflective cracking control. First, temperature effects are rarely mapped systematically across the range encountered in service, despite the strong temperature dependence of asphalt viscoelasticity and interface behavior. Second, loading-rate sensitivity has received limited attention even though field displacement rates vary widely with traffic speed and operational conditions (e.g., slow-moving traffic at intersections versus highway speeds). Third, placement depth is known to influence performance, but comparative studies across multiple depths under consistent conditions remain scarce.

Progress on these questions is further constrained by the limitations of available laboratory methods. Many reflective-cracking tests require large specimens, complex apparatus, or long test durations, which restrict broad parametric evaluation. To address this limitation, recent work introduced a compact Crack Widening Device (CWD) for geosynthetic-reinforced systems (Solatiyan et al., 2023), and subsequent research extended the method to quantify temperature-dependent performance trends (Ho et al., 2025). Building on this foundation, this thesis delivers the first integrated, controlled evaluation of temperature, displacement rate, and placement depth using the CWD, enabling a systematic assessment of their individual and interactive effects under conditions relevant to overlay service.

0.6 Research Objectives

The overarching objective of this research is to develop a mechanistic and practical understanding of how geosynthetic interlayer performance depends on temperature, displacement rate, and placement depth in geosynthetic-reinforced asphalt overlays. This objective is pursued through the following specific goals:

- Evaluate crack resistance of three representative interlayer types (paving fabric, carbon-glass fiber geogrid, and fiberglass geocomposite) using the crack widening device methodology;
- Quantify temperature effects from winter to warm-season service conditions (-20 °C, 25 °C, and 40 °C);
- Assess loading-rate sensitivity by comparing quasi-static and faster displacement rates (2 mm/min and 5 mm/min) representing different traffic-speed conditions;

- Determine placement-depth effects by testing interlayers at one-third, one-half, and two-thirds of the overlay thickness measured from the specimen bottom;

- Synthesize interactions among material type, placement depth, temperature, and displacement rate to propose practical guidance for interlayer selection and placement.

By clarifying how temperature, displacement rate, and placement depth interact to influence interlayer performance, the findings support more reliable design guidance and selection criteria. They aim to reduce premature cracking and extend overlay service life, improving the cost-effectiveness of pavement rehabilitation.

0.7 Research Scope and Limitations

The scope of this research is a laboratory-based experimental program designed to control and systematically vary key parameters governing reflective cracking. It uses bi-layer asphalt specimens incorporating commercially available geosynthetic products representative of the main interlayer categories. A homogeneous hot-mix asphalt configuration is adopted to isolate the influence of the interlayer on crack propagation behavior. The CWD approach uses compact specimens with a pre-cut notch to focus on crack propagation from an existing discontinuity, a key mechanism in reflective cracking.

As with any laboratory study, limitations should be recognized. The controlled specimen geometry and loading conditions cannot replicate the full complexity of field pavements (e.g., multi-axle traffic wander, aging gradients, moisture damage, and construction variability). The findings are, therefore, intended to complement field evidence and support improved mechanistic interpretation and rational design decisions.

The experimental strategy is built around the Crack Widening Device (CWD) to provide controlled, repeatable crack-opening conditions while systematically varying interlayer type, temperature, displacement rate, and placement depth. This approach isolates reflective-cracking mechanisms that are difficult to capture in accelerated pavement testing or field sections, enabling efficient parametric evaluation and clearer interpretation of interactions among variables.

0.8 Thesis Organization

This paper-based thesis is organized into seven chapters in addition to this introduction. It progresses from background and methodology through experimental investigation to conclusions and recommendations.

Chapter 1 reviews the literature on reflective cracking mechanisms, fracture mechanics principles, geosynthetic interlayer types and functions, laboratory testing methods, and factors affecting interlayer performance.

Chapter 2 describes the experimental methodology, including materials characterization, specimen preparation procedures, the crack widening device test configuration, and the testing program design for evaluating geosynthetic interlayer performance.

Chapter 3 presents the first published paper on development and validation of the crack widening device for evaluating geosynthetic-reinforced bituminous interfaces.

Chapter 4 presents the second published paper investigating temperature effects on geosynthetic interlayer performance at multiple placement depths.

Chapter 5 presents the third paper that covers a parametric study of the combined effects of temperature, displacement rate, and placement depth on three interlayer types.

Chapter 6 presents a supplementary investigation of the pull-out resistance of the paving fabric geotextile interlayer in asphalt specimens, documenting the test setup, identifying the tensile failure mode that occurred instead of the intended interface debonding, comparing actual versus expected pull-out behavior, and calibrating a finite element model against the measured response.

Chapter 7 presents a correlation analysis between monotonic and cyclic fatigue loading behavior for all four interlayer configurations. Using log-linear regression models calibrated on three consistent datasets, this chapter applies the four resulting predictors to the PF geotextile as an independent check, identifies two specimen-preparation factors as candidate contributors to the deviation observed under the time-based reading, and proposes an exploratory diagnostic framework for relating fatigue life to monotonic test parameters.

The thesis concludes with a synthesis of all experimental findings and provides recommendations for engineering practice, specimen preparation protocols, and future research directions.

CHAPTER 1

BIBLIOGRAPHIC REVIEW

1.1 Introduction

Asphalt overlays represent one of the most widely employed rehabilitation techniques for distressed pavements, offering the ability to restore ride quality and structural capacity with relatively limited traffic disruption and at lower cost compared to full reconstruction. However, a recurring and persistent challenge in overlay performance is reflective cracking, wherein existing cracks or joints in the underlying pavement layers propagate upward through the new overlay and reappear at the surface. This phenomenon significantly reduces overlay serviceability, accelerates moisture ingress into the pavement structure, and often triggers premature maintenance requirements, making reflective cracking one of the most performance-limiting distresses in asphalt overlays worldwide (Lytton, 1989; Button and Lytton, 2007).

The reflective cracking problem is governed by complex interactions among pavement structure, traffic loading, environmental conditions, and material properties. Under traffic loading, tensile and shear stresses concentrate near existing discontinuities in the underlying pavement, promoting crack initiation and incremental growth through the overlay material. Under thermal cycling, restrained contraction and expansion of the pavement structure can drive crack opening and closing movements that further contribute to damage accumulation. The combination of traffic and thermal actions, which often represent the most severe field condition, creates a coupled thermomechanical loading scenario that challenges even well-designed overlay systems (Molenaar, 1983; Cleveland et al., 2002).

To address the reflective cracking challenge, various mitigation strategies have been developed and implemented over the past several decades. Among these strategies, geosynthetic interlayers have attracted considerable interest because they can provide multiple beneficial functions: stress absorption, reinforcement, crack arrest, and moisture control. However, despite extensive research and numerous field applications, the performance of geosynthetic interlayers remains variable across projects, suggesting that effectiveness depends on factors beyond simple product selection-including temperature conditions, loading characteristics, placement depth, and interface bonding quality (Button and Lytton, 2007; Nithin et al., 2015; AASHTO, 2008).

This chapter reviews the current state of knowledge regarding reflective cracking mechanisms, fracture mechanics principles applicable to asphalt materials, geosynthetic interlayer systems and their performance mechanisms, laboratory testing methods for crack resistance evaluation, field performance evidence, and design considerations. The review synthesizes findings from peer-reviewed journal articles, conference papers, technical reports, and design guidance documents to establish the scientific foundation for the experimental investigations presented in subsequent chapters and to identify specific research gaps that motivate this thesis.

1.2 Reflective Cracking Mechanisms

1.2.1 Phenomenological Description

Reflective cracking manifests as a progressive deterioration process that typically initiates within the first few years after overlay construction and continues throughout the pavement's service life if left unmitigated. The process begins at discontinuities in the underlying pavement-existing cracks in asphalt layers or joints in concrete pavements-where stress concentrations develop under the combined effects of traffic loading and thermal movements. These stress concentrations cause microscopic damage to accumulate in the overlay material located directly above the discontinuity, with repeated loading cycles causing damage to grow incrementally until microcracks coalesce into macroscopic cracks (Lytton, 1989; Molenaar, 1983).

Once initiated, cracks propagate upward through the overlay thickness following paths influenced by material properties, loading conditions, and interface characteristics. In relatively thin overlays (less than 75 mm), cracks tend to propagate quickly and follow nearly vertical paths from the underlying discontinuity to the pavement surface. In thicker overlays (greater than 150 mm), crack propagation is slower and may follow more tortuous paths, potentially branching or deviating from the vertical direction as cracks interact with aggregate particles and material heterogeneities. The crack propagation rate typically follows a power-law relationship with the number of load applications, exhibiting behavior similar to fatigue crack growth in metals and other engineering materials (Cleveland et al., 2002; Button and Lytton, 2007).

Field monitoring studies have documented characteristic temporal patterns in reflective cracking development. Initially, few or no cracks are visible at the pavement surface, although damage may be accumulating internally within the overlay structure. After a certain initiation period-which depends on overlay thickness, traffic intensity, climate severity, and other factors-cracks begin appearing at the surface, typically first at locations with the most severe underlying distress or highest stress concentrations. The percentage of underlying cracks that have reflected to the surface then increases over time, often following a sigmoidal progression curve. Eventually, most or all underlying cracks reflect to the surface, and existing cracks widen and deteriorate further with continued service (Button and Lytton, 2007; Cleveland et al., 2002).

The appearance and morphology of reflective cracks at the pavement surface vary depending on the characteristics of the underlying distress. Cracks reflecting from transverse cracks in asphalt pavements or transverse joints in concrete pavements appear as relatively straight transverse cracks across the overlay surface. Longitudinal cracks and joints similarly reflect as longitudinal surface cracks. In some cases, a single underlying crack may manifest as multiple parallel surface cracks, indicating crack branching within the overlay structure. Crack widths at the surface typically range from hairline (less than 1 mm) to wide openings (greater than 10 mm), with width depending on crack age, underlying joint movement magnitude, traffic loading, and environmental exposure (Molenaar, 1983; Nithin et al., 2015). Figure 1.1 illustrates the principal mechanisms of reflective cracking following Hu et al. (2010): (a) thermal cracking due to substrate joint movement under temperature variation; (b) traffic-induced cracking from bending and shearing actions at the existing crack; (c) surface-initiated cracking from thermal gradients producing greater contraction at the surface; and (d) bending and shearing stress distributions at the crack tip under wheel loading.

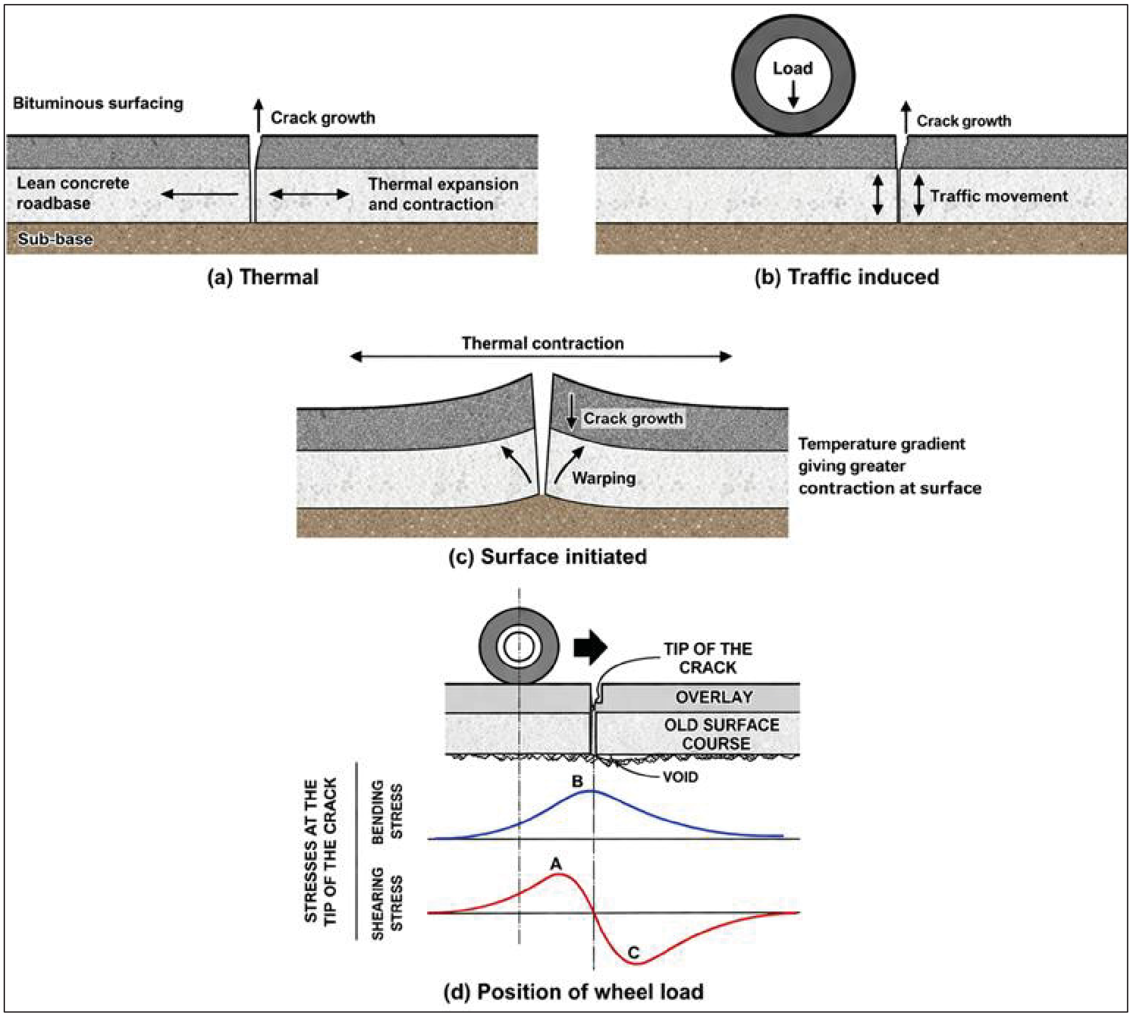

Figure 1.1 Mechanisms of reflective cracking: (a) thermal, (b) traffic induced, (c) surface initiated, and (d) position of wheel load showing bending and shearing stress distributions at the crack tip
After Hu et al.,2010

1.2.2 Traffic-Induced Mechanisms

Traffic loading represents the primary driving force for reflective crack propagation in most pavement structures. Each passage of a vehicle wheel load creates a complex three-dimensional stress state within the pavement structure, with stress concentrations occurring at crack tips and other discontinuities. The magnitude and distribution of these traffic-induced stresses depend on numerous factors including wheel load magnitude, tire contact pressure and geometry, vehicle speed, pavement temperature (which affects layer stiffness), and the thickness and stiffness of individual pavement layers. Heavy truck traffic, particularly when combined with overloaded vehicles or high tire pressures, generates the most severe stress concentrations and causes the most rapid crack propagation (Lytton, 1989; Cleveland et al., 2002).

The stress concentration mechanism at crack tips involves both opening (Mode I) and shearing (Mode II) components. As a wheel load approaches a crack location in the underlying pavement, differential deflection occurs across the crack faces: one side of the crack deflects more than the other due to the loss of load transfer across the discontinuity. This differential deflection creates both vertical separation (Mode I) and horizontal sliding (Mode II) between the crack faces, which transmits to the overlay material as concentrated tensile and shear stresses. The relative proportions of Mode I and Mode II loading depend on the wheel position relative to the crack, the interface bonding condition between overlay and substrate, and the stiffness contrast between layers (Molenaar, 1983; Cleveland et al., 2002).

The fatigue damage accumulation process in asphalt concrete follows principles analogous to those observed in metals and other structural materials, but with important complications arising from the material's viscoelastic and temperature-dependent behavior. Each load application causes some incremental damage, quantified by parameters such as dissipated pseudo-strain energy, accumulated inelastic strain, or crack extension. Damage accumulates with repeated load cycles according to damage evolution laws that may be linear (Miner's rule) or nonlinear depending on stress levels and material characteristics. When accumulated damage reaches a critical value, macroscopic crack initiation or propagation occurs (Button and Lytton, 2007; Dave and Buttlar, 2010).

Vehicle speed influences crack propagation through its effect on loading duration and material response. At higher speeds, loading duration is shorter, giving the asphalt material less time to relax stresses through viscous flow mechanisms. This results in higher effective stiffness and correspondingly higher stress concentrations, but also less total deformation per load cycle and potentially less damage per cycle. At lower speeds, the material has more time to relax, reducing peak stresses but allowing greater total deformation and potentially increasing damage through viscous mechanisms. The net effect of speed on crack propagation depends on temperature and material properties, with some studies indicating faster crack growth at low speeds and others indicating faster growth at high speeds (Molenaar, 1983; Dave and Buttlar, 2010).

1.2.3 Thermal Mechanisms

Thermal stresses in asphalt overlays arise from temperature variations that cause expansion and contraction of the pavement structure. Daily temperature cycles (diurnal variations) and seasonal temperature changes subject the overlay to repeated thermal straining, with strain magnitude depending on the coefficient of thermal expansion of the materials, the temperature range experienced, and the degree of restraint imposed by bonding to underlying layers and friction with adjacent structures. Asphalt concrete typically exhibits a coefficient of thermal expansion (CTE) in the range of 20 to 30 × 10^{-6} /°C. This means that for every degree Celsius of temperature change, the material expands or contracts by 20 to 30 millionths of its original length. As a result, a 30°C temperature variation can generate thermal strains of 600 to 900 microstrain (με) in a restrained overlay (Lytton, 1989; Molenaar, 1983).

Low-temperature cracking occurs when thermal stresses exceed the tensile strength of the asphalt mixture during extreme cold weather events or rapid cooling. This mechanism is distinct from traffic-induced reflective cracking but interacts with it significantly. Thermal cracks typically initiate at the pavement surface, where cooling is most rapid and thermal stresses are highest, and propagate downward through the overlay thickness. However, when thermal cracks encounter existing discontinuities in the underlying pavement, they tend to follow these discontinuities, effectively accelerating the reflective cracking process. The susceptibility to low-temperature cracking depends strongly on asphalt binder properties, particularly the low-temperature grade in the Performance Grade (PG) specification system (Button and Lytton, 2007; Nithin et al., 2015).

Thermal movements at joints in underlying concrete pavements are a major driver of reflective cracking in composite pavement systems. Concrete pavements experience significant thermal expansion and contraction, with combined thermal and shrinkage-induced joint movements typically ranging from 2 to 7 mm for typical joint spacings (4.5-6 meters) and temperature ranges encountered in continental climates. These movements are transferred to the overlay through interface friction and bonding, creating concentrated tensile stresses in the overlay material directly above joints. The overlay must accommodate these movements either through elastic and viscoelastic deformation or through cracking; in most cases, the movement magnitude exceeds the overlay's deformation capacity, making reflective cracking inevitable without mitigation measures (Cleveland et al., 2002; Molenaar, 1983).

Temperature gradients through the overlay thickness create additional stresses through differential thermal strains. During daytime heating, the pavement surface becomes warmer than the bottom of the overlay, causing the surface to expand more and inducing compressive stresses at the surface and tensile stresses at the bottom. During nighttime cooling, the pattern reverses, with tensile stresses developing at the surface. These thermally induced bending stresses are superimposed on stresses from traffic loading and can significantly influence crack propagation behavior. The magnitude of temperature gradients depends on solar radiation intensity, air temperature, wind speed, pavement surface characteristics, and thermal properties of the pavement materials (Baek and Al-Qadi, 2006; Baek and Al-Qadi, 2008).

1.2.4 Environmental and Material Factors

Moisture damage significantly accelerates reflective crack propagation by weakening the asphalt-aggregate bond and reducing mixture cohesive strength. Water infiltration through surface cracks reaches the crack tip region, where it can cause stripping-the loss of adhesion between asphalt binder and aggregate surfaces. The stripping process is exacerbated by repeated traffic loading, which creates pumping action that forces water into and out of cracks, generating hydraulic pressures that drive water into the asphalt-aggregate interface. Once stripping occurs, the material's resistance to crack propagation decreases substantially, accelerating the reflective cracking process. Moisture susceptibility depends on aggregate mineralogy, asphalt binder chemistry, presence of anti-stripping additives, and air void characteristics of the mixture (Lytton, 1989; Cleveland et al., 2002).

Freeze-thaw cycling in cold climates creates additional damage mechanisms that compound the reflective cracking problem. Water trapped in cracks, voids, and the asphalt-aggregate interface expands approximately 9% by volume upon freezing, generating internal pressures that can exceed the tensile strength of the surrounding material. Repeated freeze-thaw cycles progressively widen existing cracks and create new microcracking in the vicinity of crack tips. The severity of freeze-thaw damage depends on the degree of water saturation, the number and rate of freeze-thaw cycles, and the tensile strength of the material. Pavements in regions with frequent temperature oscillations around 0°C experience more severe freeze-thaw damage than pavements in consistently cold or consistently warm climates (Molenaar, 1983; Nithin et al., 2015).

Aging of asphalt binder leads to progressive stiffening and embrittlement that reduces the mixture's ability to accommodate deformation without cracking. Aging occurs primarily through oxidation, which increases the proportion of high-molecular-weight asphaltene compounds relative to lower-molecular-weight maltene compounds, making the binder harder and more brittle over time. The aging rate depends on temperature exposure, air void content (which controls oxygen diffusion into the mixture), binder composition, and asphalt film thickness around aggregate particles. Aged asphalt mixtures exhibit higher stiffness but lower tensile strain capacity, making them increasingly susceptible to cracking as they age. The effect of aging on reflective cracking is particularly important for long-term overlay performance, as overlays may perform adequately when new but become increasingly crack-susceptible as aging progresses (Button and Lytton, 2007; Dave and Buttlar, 2010).

Table 1.1 summarizes the primary mechanisms driving reflective cracking in asphalt overlays, identifying the dominant fracture mode and controlling factors for each mechanism type.

Table 1.1 Summary of reflective cracking mechanisms in asphalt overlays

Mechanism	**Driving Force**	**Crack Mode**	**Key Controlling Factors**	**Field Manifestation**

Table 1.1 Summary of reflective cracking mechanisms in asphalt overlays (continued)

Thermal contraction (cold-snap event)	Severe temperature drop generating tensile stress concentration at existing crack tip	Mode I (opening)	Low-temperature binder grade (PG); cooling rate; restraint; joint spacing	Sudden transverse cracks aligned with underlying joints/cracks
Cyclic thermal fatigue	Repeated diurnal/seasonal temperature cycling causing progressive crack opening	Mode I (cyclic, fatigue)	Diurnal temperature range; binder aging and oxidation; overlay stiffness	Progressive widening and lengthening of reflected cracks over service life
Traffic-induced bending	Wheel load directly above crack producing tensile stress at overlay base	Mode I (opening)	Load magnitude; overlay thickness; base/subgrade support stiffness	Longitudinal cracks above pre-existing distress in wheel paths
Traffic-induced shearing	Differential vertical deflection across crack faces during near-crack wheel passage	Mode II (in-plane shear)	Load offset from crack; subgrade stiffness; crack width; interface bonding	Transverse cracks with progressive vertical faulting
Surface-initiated thermal	Temperature gradient causing greater contraction at surface than at depth, inducing warping	Mode I (opening, top-down)	Surface-to-base temperature differential; binder aging; overlay viscoelasticity	Top-down surface cracks not necessarily aligned with underlying joints
Combined thermo-mechanical	Synergistic action of traffic loading on thermally pre-stressed pavement	Mixed Mode I/II	Climate severity; traffic intensity; viscoelastic interaction; pavement age	Complex crack networks with accelerated propagation rate

1.3 Fracture Mechanics Principles

1.3.1 Linear Elastic Fracture Mechanics

Linear elastic fracture mechanics (LEFM) provides the fundamental theoretical framework for analyzing crack propagation in materials that behave predominantly elastically. The central concept of LEFM is that the stress field in the vicinity of a crack tip can be characterized by a single parameter called the stress intensity factor (K), which quantifies the intensity of the stress singularity at the crack tip. The stress intensity factor depends on the applied loading, crack geometry, and specimen or structure geometry, but is independent of material properties. When the stress intensity factor reaches a critical value-the fracture toughness (Kc)-unstable crack propagation occurs (Anderson, 2005).

Three fundamental modes of crack loading are recognized in fracture mechanics. Mode I (opening mode) involves crack face separation perpendicular to the crack plane, with tensile stresses acting normal to the crack faces. Mode II (sliding mode or in-plane shear) involves crack face sliding in the crack plane and perpendicular to the crack front, with shear stresses acting parallel to the crack plane. Mode III (tearing mode or out-of-plane shear) involves crack face sliding parallel to the crack front. For reflective cracking in pavements, Mode I and Mode II are most relevant, as traffic and thermal loading create combinations of opening and sliding displacements at underlying cracks. Mixed-mode conditions, involving simultaneous Mode I and Mode II loading, are characteristic of most pavement cracking scenarios (Molenaar, 1983; Anderson, 2005).

The energy release rate (G) provides an alternative but mathematically equivalent approach to LEFM based on energy rather than stress considerations. The energy release rate is defined as the rate of change of potential energy with respect to crack area, representing the mechanical energy available to drive crack propagation. For linear elastic materials, the energy release rate is related to the stress intensity factor through the relationship $G = K^2/E'$ (for Mode I), where E' equals Young's modulus E for plane stress conditions or $E/(1-\nu^2)$ for plane strain conditions, with ν being Poisson's ratio. The critical energy release rate (Gc), corresponding to the fracture toughness, represents the energy required to create new crack surfaces (Anderson, 2005; Molenaar, 1983). Figure 1.2 depicts the three fundamental modes of crack loading as defined in classical fracture mechanics, which form the basis for characterizing crack propagation in pavement structures.

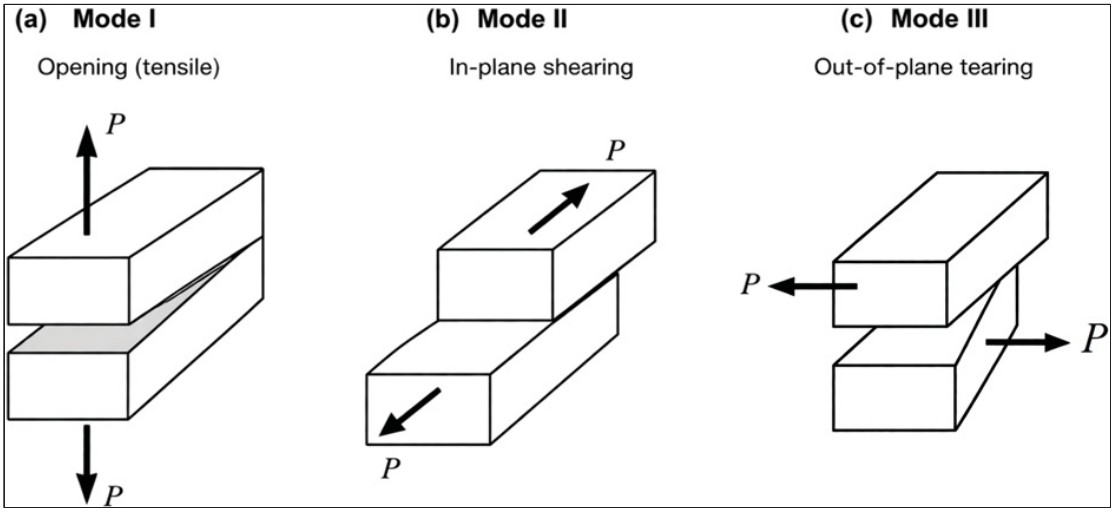

Figure 1.2 Three fundamental modes of crack loading in fracture mechanics: Mode I (opening), Mode II (in-plane shearing), and Mode III (out-of-plane tearing)
After Anderson, 2005

The application of LEFM to asphalt concrete is limited by the material's viscoelastic behavior and by the size of the fracture process zone relative to specimen dimensions. LEFM assumes purely elastic material response, which is not valid for asphalt at moderate to high temperatures or under slow loading where viscous effects are significant. LEFM also assumes that inelastic deformation is confined to a small zone immediately around the crack tip (small-scale yielding condition); for asphalt concrete, the fracture process zone can extend several millimeters to centimeters from the crack tip, violating this assumption. Despite these limitations, LEFM provides useful insights and reasonable predictions for crack propagation in asphalt under cold conditions or fast loading where elastic behavior dominates (Dave and Buttlar, 2010).

1.3.2 Viscoelastic Fracture Mechanics

Viscoelastic fracture mechanics extends classical fracture mechanics principles to materials exhibiting time-dependent behavior, as is characteristic of asphalt concrete across most service temperatures. Unlike purely elastic materials where stress and strain are instantaneously related, viscoelastic materials exhibit stress relaxation under constant strain and creep under constant stress. These time-dependent behaviors significantly affect crack propagation, as the stress field at a crack tip evolves with time even under nominally constant applied loading. Consequently, crack propagation rates in viscoelastic materials depend not only on stress magnitude but also on displacement rate and loading history (Schapery, 1984).

The correspondence principle provides a mathematical framework for extending elastic solutions to viscoelastic problems using Laplace transform techniques. For a viscoelastic material with known relaxation modulus E(t), the stress intensity factor can be calculated by replacing the elastic modulus in corresponding elastic solutions with the transformed relaxation modulus in the Laplace domain. This approach enables the extensive library of elastic fracture mechanics solutions to be adapted for viscoelastic materials. However, the correspondence principle is strictly valid only for linear viscoelastic materials and becomes approximate when significant nonlinearity or damage accumulation occurs. For asphalt concrete, the correspondence principle provides reasonable predictions at small strain levels but may be less accurate at high strains where material nonlinearity becomes important (Schapery, 1984).

The J-integral, originally developed by Rice (1968) for elastic-plastic materials, provides a path-independent characterization of the energy release rate that can be extended to viscoelastic materials. For viscoelastic materials, the J-integral can be expressed in terms of pseudo-strain energy density, which accounts for time-dependent material response through the concept of pseudo-strain. The critical value of the J-integral (J_c) represents the material's fracture resistance under the specific loading and environmental conditions of the test. The J-integral approach is particularly valuable for analyzing crack propagation under conditions where the small-scale yielding assumption of LEFM is violated (Schapery, 1984). For asphalt concrete specifically, this limitation has motivated the development of energy-based fracture characterization methods that measure fracture energy (G_f) rather than the stress intensity factor, as exemplified by the disk-shaped compact tension test (Wagoner et al., 2005).

Time-temperature superposition is a fundamental principle that relates material behavior at different temperatures and displacement rates. This principle states that the effect of temperature on viscoelastic response is mathematically equivalent to a shift in the time or frequency scale, allowing behavior at high temperature and slow loading to be related to behavior at low temperature and fast loading. The shift factor, which quantifies this temperature-time equivalence, typically follows the Williams-Landel-Ferry (WLF) equation for temperatures above the glass transition, or an Arrhenius relationship for lower temperatures. Time-temperature superposition enables the construction of master curves that describe material behavior over ranges of temperature and displacement rate, far exceeding those practically achievable in laboratory testing (Anderson, 2005; Molenaar, 1983).

1.3.3 Fatigue Crack Growth

Fatigue crack growth under repeated loading is the dominant mechanism of crack propagation in most pavement applications. Unlike monotonic fracture where a single load application causes failure, fatigue involves progressive crack extension under numerous repeated load cycles, each causing subcritical damage. The fatigue crack growth process can be conceptually divided into three stages: crack initiation (nucleation of cracks from material flaws or stress concentrations), stable crack propagation (steady crack extension at rates depending on stress intensity), and unstable propagation leading to failure. For reflective cracking, the initiation stage is often bypassed since cracks nucleate from existing discontinuities in the underlying pavement; the stable propagation stage typically dominates overlay service life (Paris and Erdogan, 1963; Molenaar, 1983).

The Paris law provides a widely-used empirical relationship for fatigue crack growth rates as a function of the stress intensity factor range. The law states that $da/dN = A(\Delta K)^n$, where da/dN is the crack growth increment per load cycle, ΔK is the stress intensity factor range (difference between maximum and minimum values during a load cycle), and A and n are material constants determined from laboratory testing. The exponent n typically ranges from 2 to 4 for asphalt concrete, with higher values indicating greater sensitivity to stress level. The Paris law has been successfully applied to predict crack propagation in asphalt pavements, though modifications are sometimes needed to account for temperature effects, displacement rate effects, and the influence of mean stress level (Jacobs et al., 1996; Molenaar, 1983).

1.3.4 Mixed-Mode Fracture

Mixed-mode fracture, involving simultaneous Mode I and Mode II loading, is characteristic of reflective cracking in real pavements. Traffic loading on pavements with underlying cracks creates both vertical displacement discontinuities (Mode I) and horizontal displacement discontinuities (Mode II) across cracks, with the relative proportions depending on wheel position, interface conditions, and layer properties. Several failure criteria have been proposed for predicting crack propagation under mixed-mode conditions, including the maximum tangential stress criterion, the strain energy density criterion, and the maximum energy release rate criterion. These criteria generally predict that cracks propagate in directions that deviate from the original crack plane under mixed-mode loading, with kink angles depending on the mode-mixity ratio K_{II}/K_I (Anderson, 2005).

Table 1.2 summarizes the principal fracture mechanics parameters used in characterizing crack propagation in asphalt pavements, their definitions, applications, and inherent limitations when applied to viscoelastic bituminous materials.

Table 1.2 Summary of fracture mechanics parameters for asphalt pavement analysis

Parameter	**Symbol**	**Definition**	**Application**	**Limitations**
Stress intensity factor	K (K_I, K_{II}, K_{III})	Magnitude of stress field singularity at crack tip; function of applied loading, geometry, and crack length	Linear elastic fracture mechanics (LEFM); crack propagation prediction in brittle and quasi-brittle materials	Requires linear elastic behavior and small-scale yielding; not directly applicable to highly viscoelastic asphalt response at intermediate temperatures
Energy release rate	G (G_I, G_{II})	Rate of change of potential energy with respect to crack area; mechanical energy available to drive crack growth	Critical energy criterion ($G \geq G_c$) for crack initiation; equivalent to K through $G = K^2/E'$ for linear elastic materials	Assumes elastic behavior; path-dependent in mixed-mode loading; limited for inhomogeneous viscoelastic media

Table 1.2 Summary of fracture mechanics parameters for asphalt pavement analysis (continued)

J-integral	J	Path-independent contour integral around crack tip representing energy flux into the fracture process zone	Elastic-plastic and viscoelastic crack analysis; widely used for asphalt mixtures and reinforced interfaces	Requires monotonic, proportional loading for path independence; computational complexity for 3D geometries
Crack tip opening displacement	CTOD (δ)	Physical opening displacement of crack faces measured at the crack tip	Ductile materials and large-scale yielding regimes	Difficult to measure accurately in asphalt mixtures; no standardized HMA test method
Paris law coefficients	A, n	Empirical coefficients in $da/dN = A(\Delta K)^n$ relating crack growth rate to stress intensity factor range	Cyclic fatigue crack propagation; pavement fatigue life prediction	Empirical; strongly material-, temperature-, and frequency-dependent; requires LEFM validity
C* integral	C*	Time-dependent equivalent of J-integral for steady-state creep crack growth in viscoelastic materials	Creep crack growth analysis at high service temperatures	Requires steady-state creep conditions; complex experimental determination
Fracture energy	G_f	Total energy dissipated per unit area of crack surface; area under load-displacement curve normalized by ligament area	Semi-circular bending test (SCB; AASHTO TP 105); intermediate-temperature crack resistance ranking	Sensitive to specimen geometry, notch length, and displacement rate; does not capture post-peak ductility behavior
Flexibility Index	FI	$FI = (G_f / \|m\|) \times A$, where m is post-peak slope at inflection and A is a unit conversion constant (Ozer et al., 2016)	Illinois Flexibility Index Test (I-FIT; AASHTO T 393); cracking screening for Balanced Mix Design (BMD); sensitive to RAP/RAS content and aging	Test variability; threshold values are mix- and climate-specific; relatively new metric (post-2016) under continued refinement

Table 1.2 Summary of fracture mechanics parameters for asphalt pavement analysis (continued)

Cracking Tolerance Index	CT_{index}	$CT_{index} = (t/62) \times (l_{75}/D) \times (G_f / \lvert m_{75} \rvert) \times 10^6$, combining fracture energy, post-peak slope at 75% peak, and post-peak displacement (Zhou et al., 2017)	Indirect Tensile Asphalt Cracking Test (IDEAL-CT; ASTM D8225); BMD framework; QC/QA cracking acceptance	Inter-laboratory variability (COV ≈15-20%); requires correction for air voids and specimen thickness; threshold values still being calibrated
Overlay Tester parameters	N_f, CFE, CPR	Number of cycles to 93% load reduction (N_f); critical fracture energy from first cycle (CFE); crack progression rate from power-law fit to load-cycle curve (CPR)	Texas Overlay Tester (Tex-248-F); reflective cracking and fatigue resistance evaluation	High variability (COV >30% for dense-graded mixes); sensitive to specimen preparation, gluing, and trimming procedures
Cohesive Zone Model parameters	σ_c, δ_c, G_c	Cohesive strength (σ_c), critical separation displacement (δ_c), and cohesive fracture energy (G_c) defining the traction-separation law in the fracture process zone	Finite element modeling of crack initiation and propagation in viscoelastic asphalt mixtures and reinforced interfaces	Parameters difficult to measure independently; calibration-dependent; computationally intensive
Toughness Improvement Factor	TIF	$TIF = U_{reinforced} / U_{control}$; ratio of total energy absorbed (area under force-displacement curve) by geosynthetic-reinforced specimen to that absorbed by unreinforced control under identical test conditions	Quantification of interlayer effectiveness in Crack Widening Device (CWD) and equivalent tests for reinforced bituminous systems (Solatiyan et al., 2023; Ho et al., 2025)	Specific to interlayer-reinforced systems; depends on test geometry, loading mode, and reference control selection

1.4 Interlayer Systems for Crack Mitigation

1.4.1 Overview of Interlayer Systems

Interlayer systems represent one of the most actively researched and widely implemented strategies for mitigating reflective cracking in asphalt overlays. These systems are installed between the existing cracked pavement and the new overlay to intercept crack propagation, dissipate stress concentrations, or provide stress relief through controlled mechanisms. Interlayers can be broadly classified into three main categories: stress-absorbing membrane interlayers (SAMIs), geosynthetic reinforcement systems, and thick asphalt interlayers with modified properties. Each category operates through different primary mechanisms and is suited to different pavement conditions, performance requirements, and construction constraints (Button and Lytton, 2007; Nithin et al., 2015).

Stress-absorbing membrane interlayers (SAMIs) typically consist of asphalt-rubber, polymer-modified asphalt, or other compliant materials that can deform to accommodate stress concentrations without transmitting them to the overlay. The primary mechanism is stress absorption through plastic or viscoelastic deformation of the membrane material. SAMIs are particularly effective for pavements with thermal cracking or joint movements, where the interlayer can stretch to accommodate opening displacements. However, SAMIs may reduce interface shear strength between layers, potentially causing slippage or delamination under heavy traffic loading if not properly designed (Cleveland et al., 2002; Button and Lytton, 2007). Figure 1.3 shows an example of a high-strength fiber geotextile commonly used as a stress-absorbing interlayer in asphalt overlay applications.

Figure 1.3 Example of a high-strength fiber geotextile used as an asphalt interlayer
Taken from Albayati et al., 2023

1.4.2 Geosynthetic Interlayers

Geosynthetic interlayers used in pavement applications fall into three main categories: geogrids, geotextiles (including paving fabrics), and geocomposites. Each type has distinct structural characteristics that determine its function in crack mitigation.

- Geogrids consist of polymer ribs arranged in a grid pattern with apertures (openings) typically ranging from 10 to 40 mm. These apertures serve a critical function: they allow aggregate particles from the asphalt mixture to penetrate and interlock with the grid structure, creating mechanical anchorage between the interlayer and the surrounding asphalt layers. The reinforcement mechanism operates primarily through tensile resistance - as the crack attempts to open, the geogrid stretches and mobilizes tensile stress across the crack faces, effectively bridging the discontinuity and redistributing the concentrated stress over a wider area.
- The polymer composition varies among products. Fiberglass geogrids offer high tensile strength (typically 50-70 kN/m) but limited elongation capacity (2-4%). Carbon fiber variants provide even higher stiffness. Polymer geogrids made from polypropylene or polyester exhibit lower strength but greater elongation at break (10-15%), allowing more deformation before failure. This trade-off between stiffness and ductility has practical implications: high-strength, low-elongation grids activate at small crack openings but may debond or rupture under large movements, while lower-strength, high-elongation grids

accommodate greater movement but may not engage effectively until cracks have already propagated significantly (Koerner, 2012; Zornberg and Thompson, 2012).

- Geotextiles are continuous fabric sheets manufactured through weaving, knitting, or needle-punching processes. Unlike geogrids, geotextiles have no apertures - they form a continuous membrane when saturated with asphalt binder. For pavement interlayer applications, nonwoven needle-punched fabrics dominate the market because their fibrous structure readily absorbs and retains asphalt during installation.

  Paving fabrics represent the most common geotextile type used for reflective cracking mitigation. These products typically have mass per unit area of 130-200 g/m² and asphalt retention capacity of 0.9-1.4 L/m². During installation, hot tack coat (typically applied at 1.0-1.4 L/m²) saturates the fabric, filling the void spaces between fibers. This saturation process accomplishes two functions: it bonds the fabric to the underlying pavement and creates a waterproof membrane that prevents moisture infiltration even if cracks eventually propagate through the overlay.

  The stress relief mechanism of paving fabrics differs fundamentally from geogrid reinforcement. Rather than resisting crack opening through tensile stiffness, the asphalt-saturated fabric creates a flexible interlayer that absorbs localized deformation. When the underlying crack moves, the fabric stretches locally while the thick asphalt film within the fabric accommodates shear deformation. This mechanism works most effectively for thermal movements and slow crack opening; under rapid loading, the asphalt within the fabric behaves more stiffly and provides less stress absorption (Button and Lytton, 2007; Nithin et al., 2015).

- Geocomposites combine grid and fabric elements into a single product, attempting to provide both reinforcement and stress relief functions. A typical geocomposite consists of a fiberglass or polymer grid laminated to a lightweight nonwoven backing. The grid component provides tensile reinforcement while the fabric component facilitates handling, improves asphalt bonding, and may contribute some stress absorption capacity.

However, the performance of geocomposites is not simply the sum of their components. The lamination process and the interaction between grid and fabric elements create a system with distinct behavior. Some geocomposites perform well under dynamic loading conditions where the grid component can engage effectively, but show limited benefit under slow monotonic loading where neither the reinforcement nor stress relief mechanisms activate fully. This rate-dependent behavior has important implications for laboratory testing protocols and field performance prediction. The geosynthetic products investigated in this thesis - paving fabric (PF), the carbon-glass fiber geogrid (Carbophalt GB), the all-carbon geogrid (Carbophalt GR, used in Study 1 only), and the fiberglass geocomposite (Glasphalt GV) - exemplify the contrasting structural concepts described above. Figure 1.4 shows close-up views of both materials, showing the open-aperture grid architecture of the geogrid that enables aggregate interlock, and the laminated grid-fabric construction of the geocomposite that combines reinforcement with stress-absorbing capacity.

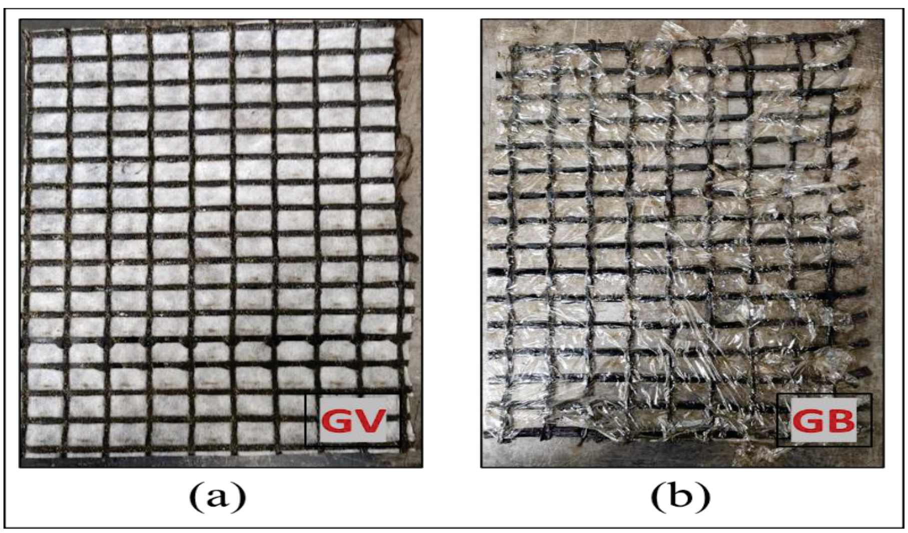

Figure 1.4 Types of geosynthetic interlayers used in asphalt pavement rehabilitation: (a) Geocomposite with nonwoven backing (Glasphalt GV), and (b) Carbon-glass fiber geogrid (Carbophalt GB)

Beyond their physical configuration, the practical benefit of geosynthetic interlayers lies in how they alter the stress field within an asphalt overlay under traffic loading. Figure 1.5 contrasts the stress distribution between an unreinforced overlay and a geosynthetic-reinforced overlay: in the unreinforced case, the wheel-load stress concentrates sharply above the crack tip, whereas in the reinforced case the interlayer mobilizes tensile resistance and redistributes the stress over a wider zone, lowering its peak intensity at the critical crack-tip region.

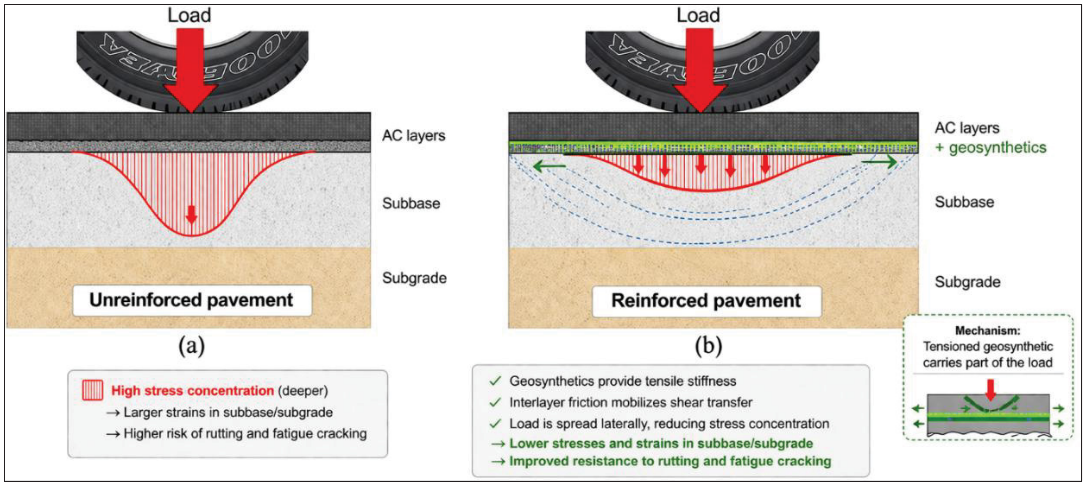

Figure 1.5 Conceptual illustration of stress redistribution for unreinforced versus geogrid-reinforced overlays
After Ragni et al., 2020a

1.4.3 Performance Mechanisms

Geosynthetic interlayers affect reflective cracking through multiple mechanisms whose relative importance depends on product characteristics, installation conditions, and service environment. Stress redistribution occurs when the interlayer spreads concentrated stresses at crack tips over larger areas, reducing peak stress intensity. This mechanism is most effective for stiff interlayers (geogrids) that can distribute loads efficiently. Crack arrest or deflection occurs when the interlayer provides a physical barrier that intercepts propagating cracks and diverts them horizontally along the interlayer plane rather than vertically through the overlay. This mechanism dissipates crack energy through horizontal propagation and interface debonding (Button and Lytton, 2007; Lytton et al., 2010).

Tensile reinforcement occurs when properly bonded interlayers transfer tensile stresses through the reinforcing elements, effectively increasing the tensile capacity of the composite system. This mechanism requires good interface bonding to develop tensile stress in the interlayer and sufficient interlayer strength and stiffness to resist the developed stresses. Waterproofing occurs when saturated fabrics or coated products prevent moisture infiltration through the interlayer plane, protecting the underlying pavement from moisture damage even if cracks eventually propagate through the overlay (Button and Lytton, 2007; Nithin et al., 2015).

Table 1.3 summarizes the key physical and mechanical properties of the three main categories of geosynthetic interlayers used in pavement rehabilitation, along with their primary crack mitigation mechanisms and practical considerations.

Table 1.3 Comparative properties of geosynthetic interlayer types for pavement rehabilitation

Property	**Paving Fabric (Geotextile)**	**Geogrid**	**Geocomposite**
Material	Needle-punched nonwoven polyester or polypropylene	Glass, carbon, or glass-carbon fiber grid	Glass/carbon grid laminated to nonwoven backing
Primary mechanism	Stress absorption; moisture barrier; bituminous membrane	Tensile reinforcement; load redistribution	Combined reinforcement and stress absorption
Tensile strength	Low to moderate (0.4-1.5 kN/m)	High (50-200 kN/m)	High (50-200 kN/m, from grid component)
Elongation at break	High (40-80%)	Low (2-5%)	Moderate (depends on grid component)
Bitumen retention	High (0.9-1.4 L/m²)	None (coating dependent)	Moderate (from nonwoven backing)
Moisture barrier	Yes (when properly saturated)	No	Partial (from nonwoven component)
Interface bond	Strong adhesion but reduces interface shear strength (creates bitumen-rich weak plane)	Slight reduction in shear strength; depends on aperture size and tack coat	Variable; depends on coating, grid coverage, and tack coat application
Shear bond effect	Significantly reduces interface shear strength; functions as stress-relief plane	Minor to moderate reduction; aggregate interlock through apertures partly compensates	Moderate reduction; lamination and surface treatment influence shear transfer

Table 1.3 Comparative properties of geosynthetic interlayer types for pavement rehabilitation (continued)

Crack bridging	By membrane action and stress absorption	By tensile reinforcement and stress redistribution	By both mechanisms simultaneously
Installation	Requires bitumen saturation in field	Direct placement on tack coat	Direct placement on tack coat
Typical applications	Thin overlays; crack sealing; moisture protection	Thick overlays; heavy traffic; structural reinforcement	General rehabilitation; combined performance needs
Cost (relative)	Low	Moderate to high	Moderate to high

1.4.4 Interface Bonding and Placement Considerations

Interface bonding between geosynthetic interlayers and adjacent asphalt layers is critical for achieving intended performance. Poor bonding can lead to slippage under traffic loading, premature delamination, and reduction or elimination of reinforcement effectiveness. Interface bonding depends on tack coat application rate, tack coat material properties, surface preparation, compaction conditions, and asphalt mixture temperature during placement. Research has shown that optimal tack coat application rates for geosynthetic interlayers differ from those for conventional asphalt-to-asphalt bonding, with higher rates generally required to achieve adequate saturation and adhesion (Correia et al., 2024).

Placement depth within the overlay structure affects interlayer effectiveness through its influence on crack interception timing and stress distribution. Interlayers placed near the bottom of the overlay (closer to the crack source) can intercept propagating cracks earlier, before significant damage accumulates in the material above. However, placement near the overlay bottom may increase interface shear stresses under traffic loading. Interlayers placed at mid-depth or higher allow more crack propagation before interception but may experience lower shear stresses. Research by Ho et al. (2025) demonstrated that one-third placement from the specimen bottom provides superior crack resistance compared to two-thirds placement, with the trend observed at all three tested temperatures (-20 °C, 25 °C, and 40 °C), suggesting that early crack interception provides net benefits despite potentially higher interface stresses.

Figure 1.6 presents an example of specimen preparation and overlay testing configuration used to evaluate cracking performance under controlled laboratory conditions.

Figure 1.6 Example specimen preparation and overlay testing configuration used to evaluate cracking performance under controlled temperature conditions
Taken from Albayati et al., 2023

1.5 Laboratory Testing Methods

Laboratory testing methods for evaluating reflective cracking resistance and interlayer effectiveness range from fundamental material characterization tests to direct simulation of field cracking mechanisms. The choice of test method depends on the specific parameters of interest, available equipment, specimen size constraints, and intended use of results. Fundamental fracture tests provide material properties for use in mechanistic models; simulation tests directly replicate field loading and cracking mechanisms; accelerated performance tests provide rapid comparative evaluation of different materials or configurations (Cleveland et al., 2002; Zhou and Scullion, 2005).

The semi-circular bend (SCB) test has become widely adopted for characterizing fracture properties of asphalt mixtures due to its relatively simple specimen geometry and ability to provide fracture energy and crack propagation resistance parameters. Specimens are prepared by cutting semi-circular slices from cylindrical cores, creating a notch at the bottom center, and loading in three-point bending until fracture. The test can be conducted at various temperatures to characterize temperature-dependent fracture behavior. SCB test results have been correlated with field cracking performance and are increasingly used for mixture design and quality control (Li and Marasteanu, 2010).

The Texas overlay tester (OT) directly simulates reflective cracking by subjecting beam specimens to repeated opening and closing cycles representing joint or crack movements in underlying pavements. The test applies a fixed displacement amplitude (typically 0.635 mm) at a fixed cycling rate (typically 10 seconds per cycle at 25°C) and measures the number of cycles to failure, defined as a 93% reduction in peak load. The overlay tester has been adopted as the standard TxDOT procedure Tex-248-F (TxDOT, 2019) and is widely used for mixture design evaluation and specification compliance testing. Results correlate reasonably well with field overlay cracking performance in Texas conditions (Zhou and Scullion, 2005).

The crack widening device (CWD) developed by Solatiyan et al. (2023) at ÉTS provides a compact test configuration for evaluating geosynthetic-reinforced bituminous interfaces. Using specimens of manageable size (80 mm × 80 mm × 80 mm), the device simulates crack propagation through controlled horizontal crack opening displacement. The test produces force-displacement curves from which multiple performance parameters can be extracted: peak force, displacement at peak, energy dissipation, and stiffness evolution. The CWD methodology enables systematic parametric studies of temperature, displacement rate, and placement depth effects that would be impractical with larger-scale test methods.

Table 1.4 provides a comparative overview of the principal laboratory testing methods used to evaluate reflective cracking resistance and geosynthetic interlayer effectiveness, including the recently developed Crack Widening Device employed in this research.

Table 1.4 Comparison of laboratory test methods for reflective cracking evaluation

Test Method	**Specimen Geometry**	**Loading Mode**	**Parameters Measured**	**Advantages / Limitations**
Semi-Circular Bend (SCB) (Li & Marasteanu, 2010)	Semi-circular disc with notch	Three-point bending (Mode I)	K_{IC}, J_{IC}, fracture energy, flexibility index	Simple setup, low cost, AASHTO standard; limited to Mode I; small specimens

Table 1.4 Comparison of laboratory test methods for reflective cracking evaluation (continued)

Indirect Tensile Cracking Test (IDEAL-CT) (Zhou et al., 2017)	Cylindrical disc	Indirect tension at intermediate temperature	CT index, fracture energy, post-peak slope	Simple, no notching needed, ASTM D8225; intermediate-T only; lab variability
Texas Overlay Tester (OT) (Zhou & Scullion, 2005)	Rectangular beam glued to platens	Cyclic horizontal opening displacement	Cycles to failure (N_f), critical fracture energy, crack progression rate	Simulates reflective cracking; Tex-248-F standard; high COV in dense mixes
Four-Point Bending Beam (4PB) (AASHTO T 321)	Prismatic beam	Repeated flexural loading	Fatigue life, stiffness degradation, dissipated energy	Homogeneous stress zone, AASHTO T 321; time-consuming; no crack-path control
Wheel Tracking Test	Compacted slab specimen	Rolling wheel load (cyclic)	Rut depth, crack initiation time, accelerated damage	Realistic traffic loading; expensive equipment; primarily rutting-oriented
Crack Widening Device (CWD) (Solatiyan et al., 2023)	80 × 80 × 80 mm bilayer cube with interlayer	Monotonic or cyclic crack opening	Force-displacement, peak load, energy dissipation, TIF, J-integral	Compact, low-volume specimens, controlled crack path, multiple modes; recently developed for interlayer characterization

Table 1.4 Comparison of laboratory test methods for reflective cracking evaluation (continued)

Double Cantilever Beam (DCB) (ASTM D5528)	Bonded beam halves with pre-crack	Mode I opening at beam ends	G_{IC}, fracture toughness, R-curve	Pure Mode I characterization; sensitive to bonding quality; standard fracture mechanics geometry
Compact Tension (CT) (ASTM E399)	Disc or rectangular plate with notch	Direct tensile opening	K_{IC}, crack growth rate (da/dN)	Standardized fracture mechanics; large specimen requirements; limited for asphalt at intermediate T

Figures 1.7 through 1.14 illustrate representative specimen geometries, testing configurations, and experimental setups associated with the laboratory methods summarized in Table 1.4.

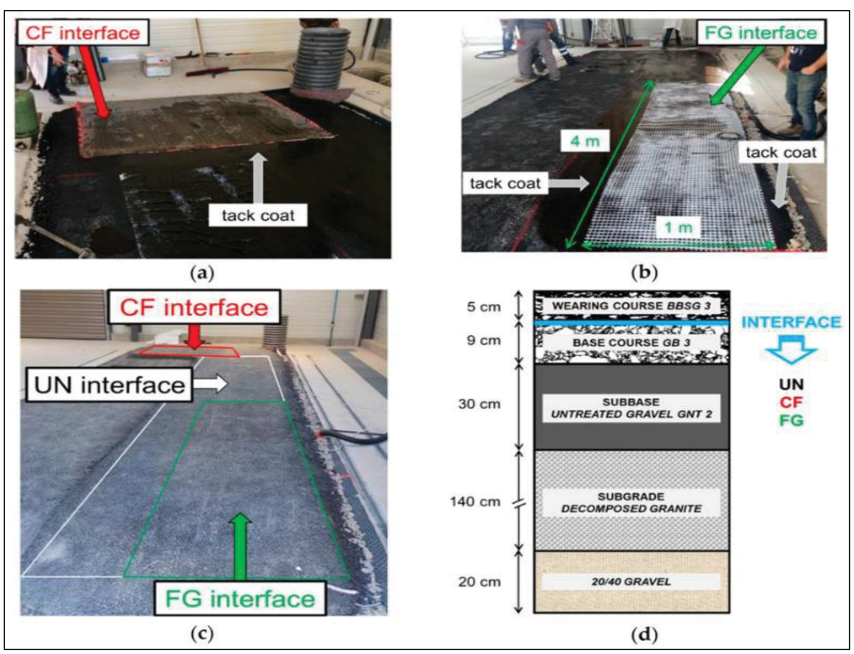

Figure 1.7 Example full-scale trial section and cross-sectional configuration for evaluating geogrid-reinforced asphalt interlayers.
Taken from Ragni et al., 2020a

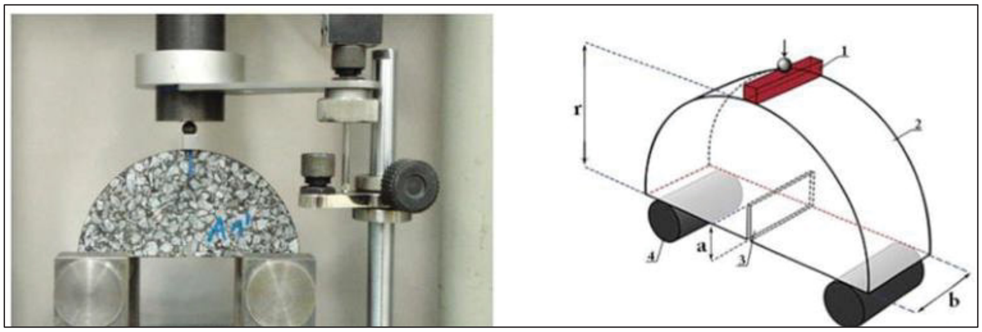

Figure 1.8 Semi-circular bending (SCB) specimen and loading configuration commonly used for fracture characterization of asphalt mixtures
Taken from Pszczola and Szydlowski, 2018

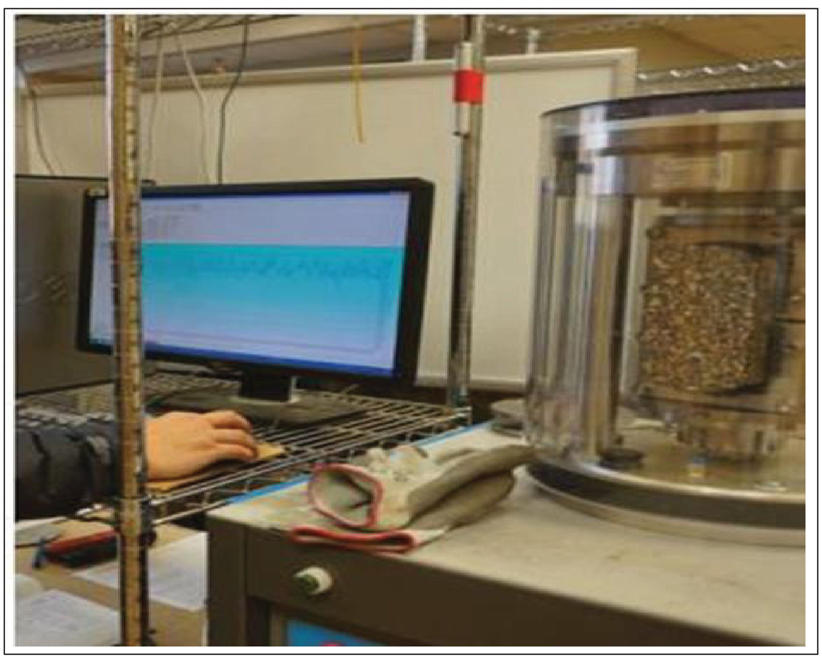

Figure 1.9 Overlay Test (OT) apparatus used to apply cyclic direct-tension displacement to asphalt mixture specimens for evaluating cracking potential.
Taken from FHWA-HIF-21-017; U.S. Government work/public domain

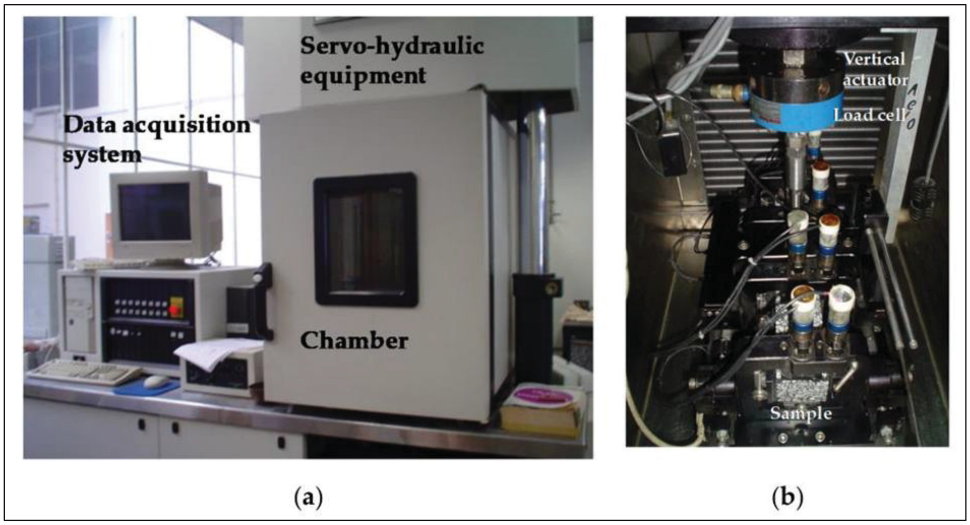

Figure 1.10 Example four-point bending (4PB) fatigue loading configuration for asphalt beam specimens.
Taken from Thives et al., 2022

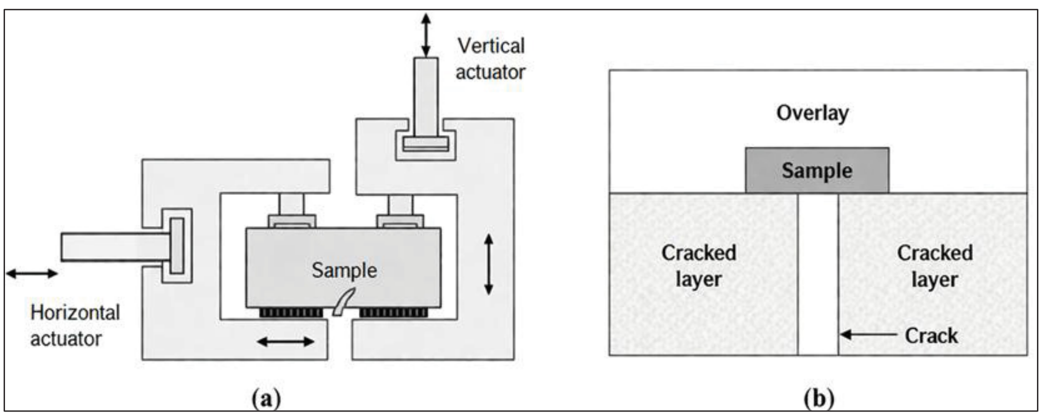

Figure 1.11 Schematic illustration of reflective cracking device concept and associated measurement approach.
After Thives et al., 2022

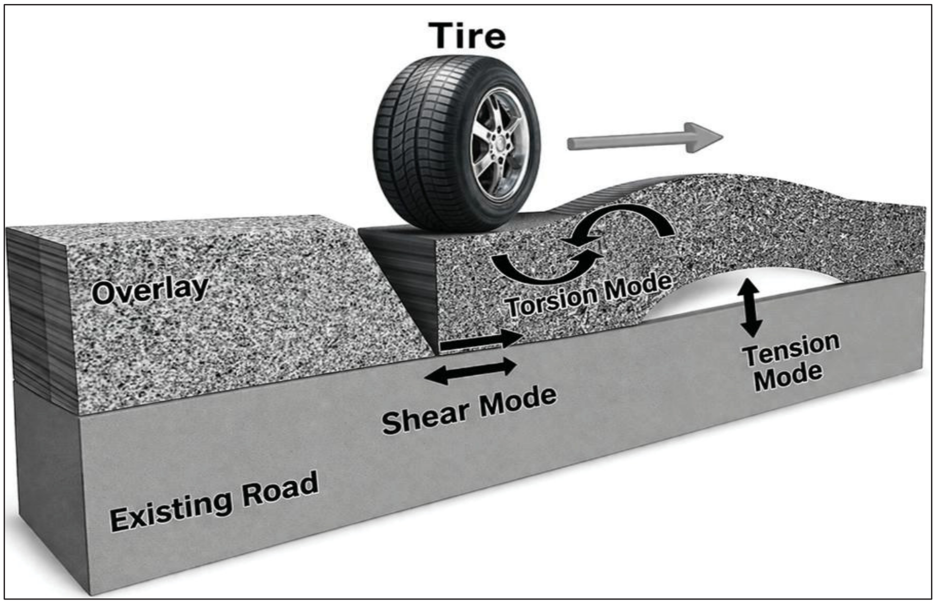

Figure 1.12 Illustration of interface shear forces and representative failure modes associated with insufficient tack coat/bonding between asphalt layers.
After Kim and Mun, 2021

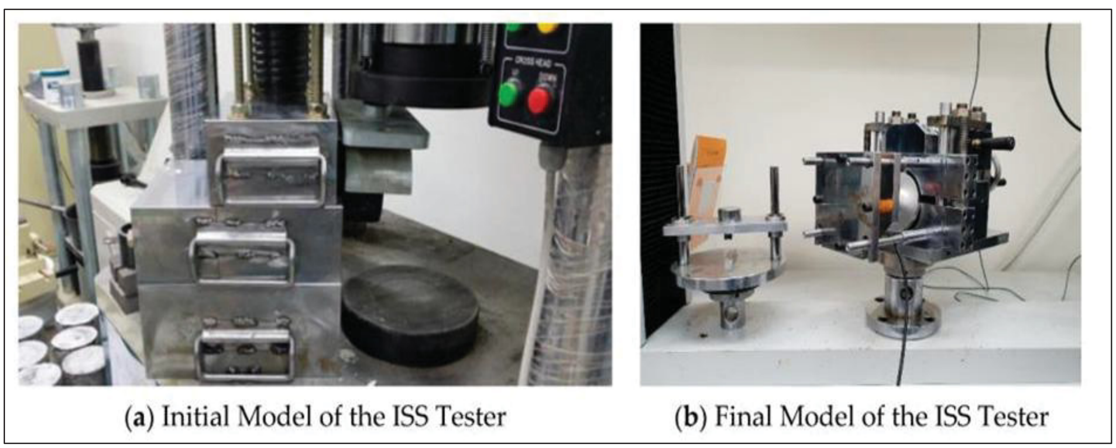

Figure 1.13 Typical experimental setup and specimen configuration for interface shear strength testing (ISST).
Taken from Kim and Mun, 2021

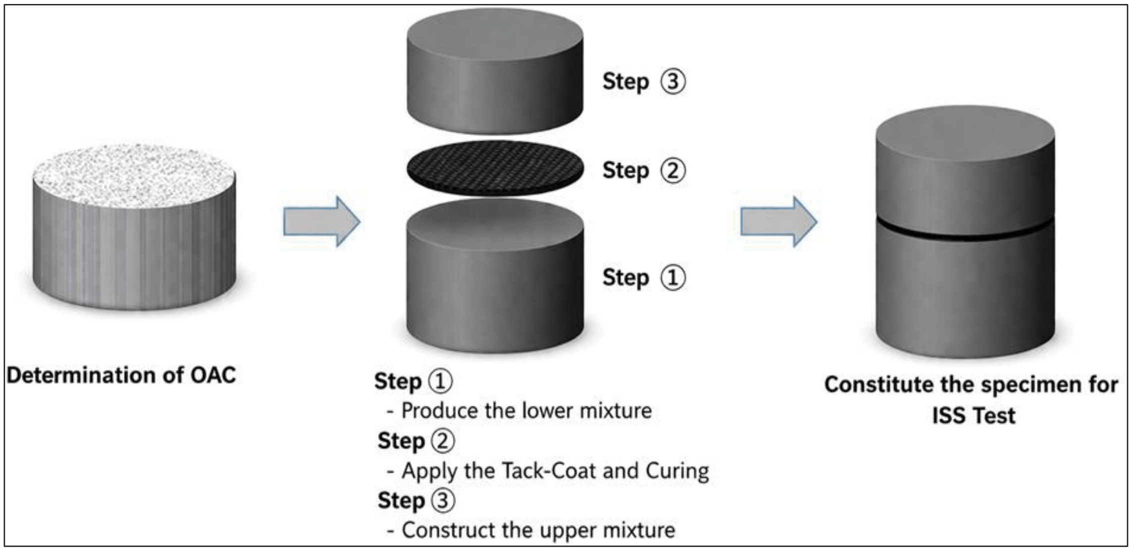

Figure 1.14 Example analysis of interface shear response and strength interpretation from ISST results.
After Kim and Mun, 2021

Standard fatigue characterization of asphalt mixtures typically employs homogeneous test geometries such as the two-point bending (2PB) trapezoidal cantilever, four-point bending (4PB) beam, and uniaxial tension-compression (TC) tests (Moreno-Navarro and Rubio-Gámez, 2016). These methods subject specimens to controlled-strain or controlled-stress sinusoidal loading at frequencies typically ranging from 10 to 30 Hz. The resulting fatigue life data are commonly analyzed using the Wöhler approach, relating applied strain amplitude to cycles to failure through a power law $N_f = K_1\ \varepsilon^{-K_2}$. In stress-controlled formulations, the equivalent Basquin law expresses the relationship as $\sigma_a = A\ (N_f)^B$, linearized in log-log space for regression analysis (Boussabnia, 2024). The characterization of geosynthetic-reinforced asphalt under cyclic loading has received comparatively limited attention. Virgili et al. (2009) conducted repeated load tests on geosynthetic-reinforced bituminous systems and found that reinforcement can significantly extend fatigue life, with effectiveness depending on the interlayer type and test configuration. Arsenie et al. (2017) modeled fatigue damage in geogrid-reinforced asphalt concrete and demonstrated that the reinforcement influence on crack propagation rate varies with loading amplitude.

The definition of fatigue failure in asphalt testing remains an active area of research with no universal consensus. The most commonly applied criterion, Nf50, defines failure as the number of load cycles at which specimen stiffness has decreased to 50% of its initial value. While Nf50 is straightforward and applicable to most test configurations, it may not accurately capture true fatigue failure in all cases, particularly for modified mixtures (Moreno-Navarro and Rubio-Gámez, 2013). Alternative criteria include phase-angle-based methods identifying the Phase II to Phase III transition, dissipated energy ratio (DER), and ratio of dissipated energy change (RDEC) approaches. Boussabnia (2024) systematically compared five failure criteria for EME-14 high-modulus asphalt using tension-compression testing and demonstrated that different criteria yield substantially different fatigue life estimates for the same material. The choice of criterion is particularly relevant when fatigue life values are low, as the distinction between true fatigue damage and quasi-static failure becomes less clear in this low-cycle regime.

Characterization of the mechanical behavior at the geosynthetic-asphalt interface requires specialized testing beyond standard mixture fatigue tests. Interface shear bond tests, including the Leutner-type Layer-Parallel Direct Shear (LPDS) test and shear-box configurations, have been widely employed to assess interlayer adhesion and aggregate-interlock effects (Raab et al., 2009; Raab et al., 2012; Canestrari et al., 2012). These tests characterize Mode II (in-plane shear) bond rather than the Mode I crack-opening response that governs reflective crack propagation. Pull-out testing complements this by assessing the tensile resistance of embedded geosynthetics, though it faces challenges in specimen preparation and confinement control. Gupta et al. (2014) found that confinement pressure and embedment length significantly influence measured pull-out resistance. Excessive confinement can cause premature geotextile tearing rather than interface debonding, complicating interpretation. Spadoni et al. (2021) evaluated both shear and flexural behavior and emphasized characterizing multiple failure modes to describe interface performance.

1.6 Field Performance Evaluation

Field performance evaluation provides the ultimate validation of reflective cracking mitigation strategies and forms the basis for developing and calibrating performance prediction models. Performance indicators for reflective cracking include the extent of cracking (percentage of pavement area or length affected), crack severity (width, spalling, secondary deterioration), crack progression rate over time, and time to first appearance of cracks at the surface. These indicators are measured through periodic distress surveys conducted using standardized protocols such as those developed for the Long-Term Pavement Performance (LTPP) program (Miller and Bellinger, 2014; Lytton et al., 2010).

Field performance of geosynthetic interlayers has been documented in numerous studies with variable outcomes. Successful installations demonstrating significant delay in reflective cracking typically share common characteristics: proper material selection matched to site conditions, excellent construction quality with attention to interface bonding, and appropriate pavement structural conditions. The typical delay in reflective cracking ranges from 2 to 7 years compared to unreinforced overlays, though results vary widely depending on site-specific factors. Cost-benefit analysis considering initial material and installation costs, extended service life, and reduced maintenance requirements generally supports economic viability for properly designed and installed geosynthetic interlayer systems (Button and Lytton, 2007; Zornberg and Thompson, 2012).

Table 1.5 provides a summary of key research studies on geosynthetic interlayer performance, showing the range of materials tested, methodologies employed, and principal findings that have shaped current understanding of interlayer behavior.

Table 1.5 Summary of key research studies on geosynthetic interlayer performance

Study	**Interlayer Type**	**Test Method**	**Key Findings**
Lytton (1989)	Geotextile	Analytical model	Established theoretical framework for geotextile reinforcement and strain-relief mechanisms in HMA overlays
de Bondt (1999)	Steel mesh, geogrid	Laboratory + numerical	Developed a design methodology for anti-reflective cracking reinforced overlays
Khodaii et al. (2009)	Polyester geogrid	Cyclic plate-load on beam (Mode I bending)	Geogrid position, temperature, and crack opening width governed reflective crack growth; one-third depth from bottom provided maximum service life
Nguyen et al. (2020)	Glass fiber grid	4-point bending + APT	Glass fiber grid characterized via 4PB lab fatigue tests; full-scale APT validated reinforcement design

Table 1.5 Summary of key research studies on geosynthetic interlayer performance (continued)

Study	**Interlayer Type**	**Test Method**	**Key Findings**
Canestrari et al. (2015)	Carbon/glass fiber grid	Shear + flexural	Combined shear and flexural laboratory characterization correlated with field distress evolution
Ragni et al. (2020a)	Geocomposite	FWD APT + laboratory	Geocomposites improved performance under accelerated FWD loading; trial section validated laboratory findings
Ragni et al. (2020b)	Geogrid (carbon, glass)	Shear-torque fatigue	Cyclic shear bonding behavior characterized; reinforcement type affected interface fatigue resistance
Ho et al. (2025)	PF, GB, GV geosynthetics	CWD monotonic	Temperature substantially affected geosynthetic interlayer crack-resistance behavior under monotonic CWD testing

Figure 1.15 illustrates an example of large-scale slab specimen fabrication and geogrid placement procedures used in laboratory evaluations of reinforced asphalt overlays.

Figure 1.15 Example large-scale slab specimen fabrication and geogrid placement for laboratory evaluation of reinforced asphalt overlays.
Taken from Rueda et al., 2023

1.7 Design Considerations and Best Practices

Overlay design for reflective cracking control requires consideration of structural adequacy, material selection, interlayer system design, and construction specifications. Current design approaches range from purely empirical methods based on experience and local performance data, to mechanistic-empirical approaches that use fracture mechanics principles to predict crack initiation and propagation rates, to fully mechanistic approaches that model the complete thermomechanical response of the pavement system. The AASHTO Mechanistic-Empirical Pavement Design Guide (MEPDG) incorporates reflection cracking prediction models based on Paris law crack growth concepts (AASHTO, 2008; Lytton et al., 2010).

Best practices for geosynthetic interlayer installation include thorough surface preparation to remove loose material and ensure good contact, application of appropriate tack coat type and rate, careful placement to avoid wrinkles and ensure full contact with the substrate, and controlled overlay placement to avoid displacement of the interlayer. Installation should be performed under suitable ambient conditions to ensure proper tack coat curing and adequate asphalt saturation of the interlayer. Surface preparation, tack coat uniformity, wrinkle-free interlayer placement, and overlay compaction should be verified as part of construction quality control (Cleveland et al., 2002).

1.8 Identified Research Gaps

Despite decades of research on reflective cracking and geosynthetic interlayers, several significant knowledge gaps persist that limit reliable design and performance prediction:

First, temperature effects on geosynthetic interlayer performance have not been fully characterized. Most laboratory studies have been conducted at single temperatures without examining how performance varies across the service temperature range. Given the strong temperature dependence of asphalt material properties and interface bonding characteristics, this represents a significant gap in understanding.

Second, displacement rate sensitivity has received limited attention. Field displacement rates vary widely depending on traffic speed, yet most laboratory tests employ fixed rates without examining rate effects. The viscoelastic nature of asphalt materials suggests that interlayer performance may depend significantly on displacement rate.

Third, placement depth optimization lacks systematic investigation. While some studies have compared discrete placement positions, systematic evaluation across multiple depths under consistent conditions is scarce. The optimal placement depth likely depends on interlayer type, overlay thickness, and service conditions.

Fourth, interactions among these variables including temperature, displacement rate, and placement depth, have not been systematically characterized. Field performance results from the combined effects of all these factors, yet most laboratory studies examine single variables in isolation.

Fifth, the fatigue behavior of geosynthetic-reinforced asphalt systems under cyclic loading has not been extensively characterized using fracture-based test configurations such as the CWD. While standard fatigue methods (4PB, 2PB, TC) are well established for homogeneous mixtures, their application to notched specimens containing geosynthetic interlayers introduces complexities related to stress concentration, crack-reinforcement interaction, and the distinction between low-cycle and high-cycle fatigue regimes. Development of monotonic-to-fatigue correlation models may offer a practical approach for estimating cyclic performance from simpler monotonic tests.

Sixth, interface characterization methods such as pull-out testing have not been systematically developed for geosynthetic-asphalt systems at realistic confinement levels representative of thin overlay applications. Existing pull-out protocols from geotechnical applications may not be directly applicable to asphalt interlayers where confinement pressures and displacement mechanisms differ fundamentally from those in soil reinforcement.

These gaps motivate the experimental investigations presented in the following chapters of this thesis, which aim to provide mechanistic understanding of how geosynthetic interlayer performance depends on temperature, displacement rate, and placement depth through systematic parametric studies using the crack widening device methodology.

1.9 Summary

This chapter has reviewed the current state of knowledge regarding reflective cracking in asphalt overlays and the use of geosynthetic interlayers for crack mitigation. The key findings from this literature review can be summarized as follows:

Reflective Cracking Mechanisms: Reflective cracking is driven by two primary mechanisms including traffic-induced loading (creating mixed Mode I and Mode II fracture conditions) and thermal movements (predominantly Mode I opening). The interaction of these mechanisms, combined with environmental factors such as moisture damage, freeze-thaw cycling, and binder aging, creates a complex deterioration process that can significantly reduce overlay service life.

Fracture Mechanics Framework: Linear elastic and viscoelastic fracture mechanics provide the theoretical foundation for understanding crack propagation in asphalt materials. The J-integral approach, Paris law for fatigue crack growth, and mixed-mode fracture criteria are essential tools for characterizing crack resistance. However, the temperature-dependent and rate-sensitive behavior of asphalt materials complicates direct application of classical fracture mechanics.

Geosynthetic Interlayer Systems: Three main categories of geosynthetic interlayers, geotextiles (paving fabrics), geogrids, and geocomposites offer different performance mechanisms including stress absorption, reinforcement, crack arrest, and moisture barrier functions. Product selection should consider the specific distress mechanisms and loading conditions anticipated in service.

Performance Mechanisms: Geosynthetic interlayers enhance crack resistance through multiple mechanisms: stress redistribution over larger areas, energy absorption during crack propagation, crack tip blunting, and horizontal crack deviation along the interlayer plane. The relative importance of these mechanisms depends on interlayer type, placement position, interface bonding quality, and loading conditions.

Laboratory Testing Methods: Various test methods have been developed to evaluate reflective cracking resistance, including beam fatigue tests, wheel tracking simulators, overlay testers, and the crack widening device. Each method has advantages and limitations in terms of specimen size, testing duration, and ability to replicate field conditions.

Field Performance Evidence: Field studies demonstrate that geosynthetic interlayers can effectively delay reflective cracking when properly designed and installed, but performance variability across projects indicates that effectiveness depends on factors beyond simple product selection.

Research Gaps: Critical gaps remain in understanding temperature effects, displacement rate sensitivity, placement depth optimization, and interactions among these variables. These gaps limit the development of reliable design guidelines and motivate the systematic experimental investigations presented in the subsequent chapters of this thesis.

CHAPTER 2

METHODOLOGY

2.1 Introduction

The literature review presented in Chapter 1 identified several persistent gaps that limit reliable design and selection of geosynthetic interlayers for reflective cracking control. Temperature effects have rarely been mapped systematically across the full range encountered in service, despite the strong temperature dependence of asphalt viscoelasticity and interface behavior. Loading-rate sensitivity has received limited attention even though field displacement rates vary widely with traffic speed and operational conditions. Placement depth is known to influence performance, yet comparative studies across multiple depths under consistent conditions remain scarce. Interactions among these variables have also not been systematically characterized.

This chapter presents the experimental methodology developed to address these gaps. All experiments were conducted at the Laboratoire de Chaussées et Matériaux Bitumineux (LCMB) of École de technologie supérieure (ÉTS) in Montreal, Canada. The following sections describe the experimental program, materials, testing apparatus, test procedures, data reduction methods, and the complete experimental matrix. Detailed analysis frameworks and results specific to each study are presented in Chapters 3, 4, and 5.

2.2 Experimental Program Overview

The overarching objective of the experimental program was to develop a mechanistic understanding of how geosynthetic interlayer performance depends on temperature, displacement rate, and placement depth in asphalt overlay systems. This objective was pursued through three interconnected studies using the Crack Widening Device (CWD), each progressively expanding the parametric scope:

Study 1 (Chapter 3): Established the CWD methodology and evaluated its ability to differentiate among interlayer types across two interface configurations with different aggregate sizes (ESG-10/ESG-14 and ESG-14/GB-20), tested at room temperature with a displacement rate of 2 mm/min.

Study 2 (Chapter 4): Expanded the investigation to three temperatures (-20 °C, 25 °C, 40 °C) with interlayers placed at two depths (one-third and two-thirds from the specimen base), using a displacement rate of 2 mm/min.

Study 3 (Chapter 5): Extended the parametric matrix to include two displacement rates (2 mm/min and 5 mm/min), three placement depths (one-third, one-half, and two-thirds), and two temperatures (25 °C and 40 °C), with advanced fracture mechanics parameters for performance characterization.

The four independent variables investigated across the three studies are: (i) interlayer type - unreinforced control, paving fabric (PF), Carbophalt GB geogrid, and Glasphalt GV geocomposite (Study 1 also tested Carbophalt GR); (ii) temperature at -20 °C, 25 °C, and 40 °C; (iii) displacement rate - 2 mm/min and 5 mm/min; and (iv) placement depth - one-third, one-half, and two-thirds from the specimen base.

2.3 Materials

2.3.1 Asphalt Mixture

The hot mix asphalt (HMA) used throughout this research program was designed to meet Transport Québec standards. Three mixture types were used across the experimental studies, differentiated by their nominal maximum aggregate size (NMAS): ESG-10 (10 mm NMAS), ESG-14 (14 mm NMAS), and GB-20 (20 mm NMAS). In Study 1 (Chapter 3), the three mixtures were produced with PG 58-28 asphalt binder. The ESG-10 used in Studies 2 and 3 (Chapters 4 and 5) was produced with PG 64E-28 performance-graded asphalt binder, which is commonly specified for Quebec climatic conditions.

ESG-10 served as the primary mixture for specimen fabrication in the temperature and displacement rate studies. Its mechanical characteristics were verified to exceed Transport Québec requirements for both water sensitivity (measured: 97.3% versus required: ≥70%) and rutting resistance (measured: 6.6% after 1,000 cycles and 8.2% after 3,000 cycles versus required: ≤10% and ≤15%, respectively). The binder content was 5.45% by mass. For the interface comparison study (Chapter 3), ESG-14 and GB-20 mixtures were also usedto evaluate the effect of aggregate size on interlayer performance. The use of multiple aggregate sizes enabled investigation of how interface texture and interlocking interact with different geosynthetic types.

2.3.2 Geosynthetic Interlayer Materials

Four commercially available geosynthetic products manufactured by TEXEL Corporation were selected for this research. These materials represent the principal categories of geosynthetic interlayers used in pavement rehabilitation:

Paving Fabric (PF): The paving fabric is a needle-punched nonwoven geotextile impregnated with PG 64-34 asphalt cement. This dual-component design combines the structural reinforcement provided by the fabric with a stress-absorbing membrane created by the asphalt saturation. The manufacturer-specified mechanical properties include grab tensile elongation of 45-105% (CAN/CGSB-148.1 No. 7.3), grab tensile strength of 550 N (CAN/CGSB-148.1 No. 7.3), Mullen burst strength of 1,585 kPa (CAN/CGSB-4.2 No. 11.1), and bitumen retention of 1.15 L/m² (ASTM D6140). The asphalt saturation provides immediate waterproofing and creates a compliant interlayer that absorbs stress concentrations at crack tips.

Carbophalt G 120/200 (GB): This is a bitumen-coated reinforcement geogrid manufactured from a combination of glass fibers (transversal direction, 120 kN strength) and carbon fibers (longitudinal direction, 200 kN strength). Both surfaces are coated with a bituminous layer, and the grid is backed by a thin plastic foil. The mesh aperture size is 20 mm × 20 mm. The dual-sided bitumen coating facilitates bonding with both the lower and upper asphalt layers, while the apertures allow aggregate interlock through the grid.

Glasphalt GV 120/120 (GV): This is a geocomposite consisting of a glass fiber grid (120 kN strength in both transversal and longitudinal directions) bonded to a nonwoven fabric backing on the bottom side. Only the top surface is coated with bitumen. The mesh aperture size is 20 mm × 20 mm. The asymmetric design, with bitumen coating on one side and fabric on the other, creates a structural configuration that differs fundamentally from both the symmetrically coated GB geogrid and the uniformly saturated PF geotextile.

Carbophalt G 200/200 (GR): This is a bitumen-coated reinforcement geogrid manufactured entirely from carbon fibers, providing 200 kN strength in both transversal and longitudinal directions, with elongation below 1.5% in both directions. Both surfaces are coated with a bituminous layer, and the grid is backed by a thin plastic foil. The mesh aperture size is 20 mm × 20 mm. The all-carbon construction offers higher tensile stiffness and lower elongation than the glass-carbon hybrid GB geogrid, while maintaining identical bitumen coating and aperture configuration. This product was evaluated in Study 1 (Chapter 3) only to assess the influence of fiber composition on crack resistance.

2.3.3 Tack Coat and Bonding Agents

Interface bonding was established using application-specific protocols. For unreinforced control specimens and GB geogrid-reinforced specimens, a slow-setting cationic asphalt emulsion (CSS-1H) was applied at a dosage of 0.18 L/m² of residual bitumen. For GV geocomposite-reinforced specimens, the emulsion dosage was increased to 0.26 L/m² following manufacturer specifications. For PF geotextile-reinforced specimens, hot PG 64-34 asphalt cement was applied at a compaction temperature of 168 °C at a dosage of approximately 0.11 L/m². These bonding protocols were established based on manufacturer recommendations and were maintained consistently throughout all experimental studies.

2.4 Specimen Fabrication

2.4.1 Slab Compaction

All specimens were produced from laboratory-compacted slabs of dimensions 500 mm × 180 mm × 100 mm. Slab compaction followed the French roller compactor protocol (LC 26-410, MTQ standard), which produces specimens with density and texture representative of field-compacted asphalt layers. Each slab was fabricated in two lifts to create the bilayer structure required for interlayer evaluation.

The bottom layer was compacted first. Because both the bottom and top asphalt layers consisted of the same ESG-10 mixture, a single slab configuration could yield both the one-third and two-thirds placement specimens through specimen orientation after cutting. For these two placement depths, the bottom layer was compacted at approximately 63 mm and the top layer at approximately 37 mm, for a total slab thickness of 100 mm. Compacting a 63 mm bottom layer required adapting the French rolling compactor, which is configured by default for a symmetric 50 mm bottom and 50 mm top. For mid-depth placement (investigated in Chapter 5), the standard symmetric 50 mm configuration was used. After compaction, the bottom slab was cured at room temperature for a minimum of 48 hours before interlayer installation.

2.4.2 Interlayer Installation

Three distinct interlayer installation procedures were employed, corresponding to the manufacturer specifications for each geosynthetic type:

For unreinforced control specimens and GB geogrid-reinforced specimens, the CSS-1H emulsion was precisely applied to the top surface of the cured bottom slab using a syringe and spatula to ensure uniform coverage at the specified dosage. The emulsion was allowed to break for approximately 3 hours in front of a fan. For GB specimens, the geogrid was then placed on the emulsified surface, and a gas blow torch with controlled movement was used to lightly activate the bitumen coating within the grid. Precautions were taken to prevent excessive aging: the torch was operated at reduced power, maintained at a 10 cm distance from the material surface, and moved at constant speed along each strand in perpendicular directions.

For GV geocomposite-reinforced specimens, the CSS-1H emulsion was applied at the higher dosage of 0.26 L/m^2, and the geocomposite was placed immediately without waiting for the emulsion to break. No blow torch activation was required due to the single-sided bitumen coating design of the GV geocomposite.

For PF geotextile-reinforced specimens, hot asphalt cement (PG 64-34) was applied at 168 °C directly to the bottom slab surface, and the pre-cut geotextile was placed immediately without delay. The hot asphalt cement saturates the fabric fibers upon contact, creating the stress-absorbing membrane interlayer.

2.4.3 Specimen Cutting and Surface Preparation

Following interlayer installation, the top layer of HMA (ESG-10) was compacted over the interlayer at 135 °C to complete the bilayer slab. After cooling, cubic specimens of 80 mm × 80 mm × 80 mm were cut from each slab using a precision diamond saw, with approximately 10 mm trimmed from both the top and bottom faces to remove surface irregularities and edge effects. For slabs compacted with the 63 mm and 37 mm lifts, trimming produced a 53 mm and 27 mm bilayer: two-thirds placement specimens retained this orientation, placing the interlayer approximately 53 mm from the base, while one-third placement specimens were inverted to place the interlayer approximately 27 mm from the base. This inversion was valid because both asphalt layers consisted of the identical ESG-10 mixture. For mid-depth slabs, the symmetric 50 mm lifts became a 40 mm and 40 mm bilayer after trimming. Figure 2.1 illustrates the key stages of the specimen fabrication process, showing the compacted bottom asphalt layer in the steel mold, the geosynthetic interlayer installed over the cured bottom layer, and the French roller compactor applying compaction to the top asphalt layer.

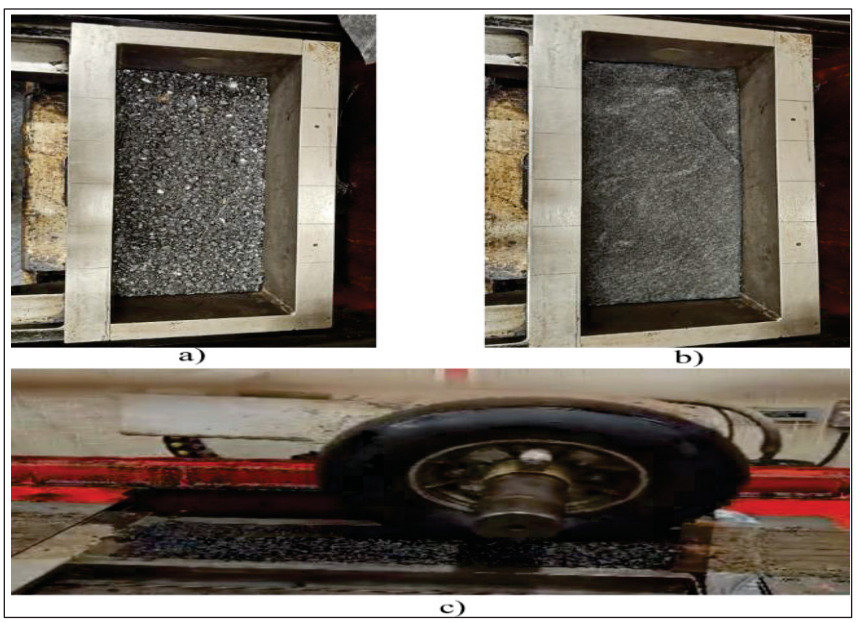

Figure 2.1 Specimen fabrication process using the French roller compactor: (a) compacted bottom asphalt layer in the steel mold, (b) paving fabric interlayer installed over the cured bottom layer, and (c) French roller compactor applying compaction to the top asphalt overlay

Prior to testing, the top and bottom surfaces of each specimen were polished using sandpaper to ensure full contact with the loading plate and the device base. This surface preparation was essential for accurate force measurement and uniform load transfer during the test.

A pre-formed notch (6 mm wide, 15 mm deep) was cut into each specimen to act as the crack initiation point. Whereas the original CWD development reported by Solatiyan et al. (2023), corresponding to Study 1 (Chapter 3), employed a 20 mm notch depth, the present studies (Chapters 4 and 5) adopted a 15 mm notch depth. The notch position (top or bottom of the specimen) was selected according to the desired interlayer placement depth relative to the crack propagation path. For a fuller interpretation of crack resistance behavior in reinforced bituminous layers, it is recommended that a minimum of three geogrid apertures be present in the specimen cross-section (Romeo et al., 2014).

2.5 Crack Widening Device (CWD)

2.5.1 Device Configuration and Mechanical Principles

The Crack Widening Device (CWD) is a laboratory apparatus designed to simulate bottom-up reflective crack propagation through geosynthetic-reinforced bituminous specimens under controlled displacement conditions. The device was developed at LCMB-ÉTS to address limitations of existing reflective cracking test methods, including the need for large specimens, complex specimen manipulation, and limited applicability for parametric evaluation of geosynthetic interlayers.

The device consists of a triangular-shaped rigid base that supports two symmetrically positioned sliding components. The bituminous specimen is placed atop these components, centered over the contact line between them. A spring-loaded screw mechanism maintains consistent initial contact between the sliding components before test initiation, preventing unintended separation or misalignment. Once the test begins, the spring mechanism is disengaged to ensure it does not contribute any resistance during testing.

The sliding components are positioned on 45-degree inclined surfaces. This geometric configuration ensures that horizontal crack opening displacement equals the vertical displacement at all times during the test. As the MTS servo-hydraulic loading system applies a downward compressive displacement to the specimen surface, the two sliding components move apart along the inclined surfaces. Protruding edges on the sliding components, precisely fitted within the pre-formed notch of the specimen, transfer the horizontal opening displacement to the crack tip, initiating and propagating a vertical crack from the notch upward through the specimen. Figure 2.2 presents a schematic diagram of the CWD, identifying all principal components and their spatial arrangement within the device assembly.

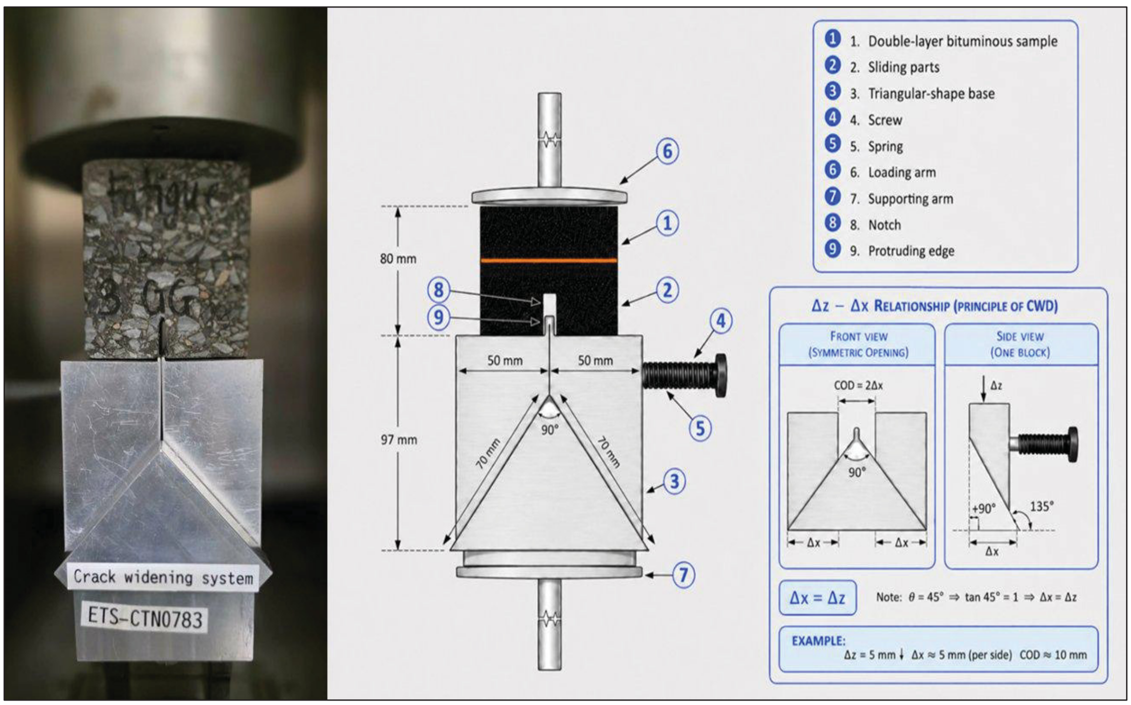

Figure 2.2 Schematic diagram of the crack widening device (CWD) showing the principal components: (1) double-layer bituminous sample, (2) sliding parts, (3) triangular-shape base, (4) screw, (5) spring, (6) loading arm, (7) supporting arm, (8) notch, and (9) protruding edge
After Solatiyan et al., 2023

The 45-degree geometry provides a direct relationship between the applied vertical displacement and the resulting horizontal crack opening. The initial compressive contact force applied to the specimen surface is up to 100 N, sufficient to maintain specimen stability without inducing damage prior to test initiation. Force and displacement data are recorded continuously throughout the test using the MTS data acquisition system.

2.5.2 Test Procedure

All tests were performed using an MTS servo-hydraulic testing machine in displacement-controlled mode. Two displacement rates were employed across the experimental program: 2 mm/min (used in Chapters 3 and 4) and 5 mm/min (used in Chapter 5). The higher displacement rate was introduced to simulate different traffic speed conditions and to evaluate rate sensitivity of the interlayer systems.

Temperature conditioning was achieved by placing specimens in the environmental chamber of the testing machine for a minimum of 4 hours prior to testing to ensure thermal equilibrium. Three temperature conditions were investigated: -20 °C ± 2 °C (low temperature, representing winter conditions), 25 °C ± 2 °C (room temperature, representing standard service conditions), and 40 °C ± 2 °C (high temperature, representing warm-season service conditions). Tests at each condition were replicated with a minimum of two specimens per interlayer type and configuration to assess repeatability.

2.5.3 Geometric Relationship: Vertical to Horizontal Displacement

The triangular wedge mechanism of the CWD transforms vertical actuator displacement into symmetric horizontal crack opening at the pre-cut notch. With wedge faces inclined at angle $\theta = 45°$, the kinematic relationships governing this transformation can be derived from the geometry of the sliding blocks.

For a single sliding block, let s denote the displacement along the inclined wedge face, Δz the vertical actuator displacement, and Δx the horizontal displacement of the sliding block. The trigonometric relations are: $\Delta z = s \times \sin(\theta)$ and $\Delta x = s \times \cos(\theta)$. Eliminating s yields $\Delta x = \Delta z \times \cot(\theta)$. For $\theta = 45°$, $\cot(45°) = 1$, therefore $\Delta x \approx \Delta z$.

Since the CWD employs two blocks that move symmetrically in opposite directions, the total Crack Opening Displacement (COD) is given by $COD = 2 \times \Delta x \approx 2 \times \Delta z$. This means the crack opening at the notch is approximately twice the vertical actuator displacement. For example, 5 mm vertical displacement produces approximately 10 mm crack opening.

2.5.4 Force Analysis and Load Cell Interpretation

Understanding the force equilibrium within the CWD is essential for interpreting load cell measurements and accounting for friction and spring effects. A free-body diagram of one sliding block reveals the following forces: N (normal force from the wedge face), $T = \mu N$ (friction force along the wedge face), Fs (horizontal spring force pulling toward the center), R (reaction from the specimen due to crack opening resistance), and V (vertical reaction measured by the load cell).

From the horizontal equilibrium condition: $N \times \cos(\theta) - T \times \sin(\theta) - Fs - R = 0$. With $T = \mu N$, solving for the normal force gives $N = (Fs + R) / [\cos(\theta) - \mu \times \sin(\theta)]$. The vertical reaction measured by the load cell is $V = N \times [\sin(\theta) + \mu \times \cos(\theta)]$. Substituting the expression for N: $V = (Fs + R) \times [\sin(\theta) + \mu \times \cos(\theta)] / [\cos(\theta) - \mu \times \sin(\theta)]$.

Under ideal conditions where the spring force is negligible ($Fs \approx 0$) and friction is minimal ($\mu \approx 0$), the expression simplifies to $V \approx R \times \tan(\theta)$. For $\theta = 45°$, $\tan(45°) = 1$, yielding $V \approx R$. This means that under ideal conditions, the load cell reading directly approximates the specimen's crack resistance force.

2.5.5 Spring Mechanism Management

The spring and screw assembly in the CWD serves to position the sliding blocks before testing. However, if the spring force Fs remains significant during testing, the load cell reading V includes both the specimen response R and the spring contribution, making it difficult to isolate the true crack resistance. Proper management of the spring mechanism is therefore critical for obtaining reliable test data.

The recommended procedure (Option B: Locking screws) involves the following steps: (1) tighten the spring screw to position the blocks and the specimen; (2) apply a seating load of up to 100 N using the actuator; (3) tighten the locking screws to create a rigid connection between the blocks and the base; (4) loosen the spring screw so the spring becomes slack. The test then proceeds with the spring disengaged, ensuring that the measured force reflects only the specimen's crack resistance.

Alternative approaches include Option A, introducing a dead-travel slot mechanism between the spring rod and sliding block such that after a small displacement of 0.3-0.5 mm, the spring becomes slack; and Option C, using a very soft spring with calibration, where blank tests without specimens are performed to verify that the spring contribution remains below 2-5% of the typical test force.

2.5.6 Validated Test Parameters

Based on validation studies conducted at ÉTS (Solatiyan et al., 2023; Ho et al., 2025; Ho et al., 2026), the following test parameters were established and adopted throughout the experimental program presented in this thesis.

Specimen dimensions were standardized at 80 × 80 × 80 mm, with a pre-cut notch of 6 mm width located at the bottom center. The notch depth was 20 mm in Study 1 (Chapter 3, following Solatiyan et al., 2023) and was refined to 15 mm in Studies 2 and 3 (Chapters 4 and 5). The specimen material was ESG-10 hot-mix asphalt. The initial compressive seating force was limited to 100 N maximum, and testing was conducted in displacement-controlled mode at two displacement rates: 2 mm/min representing quasi-static conditions and 5 mm/min representing dynamic loading.

Temperature: Three thermal conditions were examined: -20 °C (simulating severe winter conditions where asphalt becomes brittle with limited post-peak resistance), 25 °C (representing standard room temperature providing an optimal balance of stiffness and ductility), and 40 °C (simulating warm-season service where interface softening reduces interlayer effectiveness).

Interlayer placement depth: Three positions relative to the specimen base were investigated. Placement at one-third from the bottom was recommended as optimal for crack interception, as early interaction with the propagating crack enables effective stress redistribution and energy dissipation. Placement at one-half from the bottom provided intermediate performance, while placement at two-thirds from the bottom showed reduced effectiveness due to delayed crack interaction (Solatiyan et al., 2023; Ho et al., 2025; Ho et al., 2026).

2.6 Experimental Program

2.6.1 Test Variables and Conditions

The experimental program was structured as a parametric study examining the following independent variables:

Interlayer type: Four configurations were tested across all three studies: (i) unreinforced control with emulsion only, (ii) Geotextile paving fabric (PF), (iii) Geocomposite Glasphalt GV, and (iv) Geogrid Carbophalt GB. Study 1 also included a fifth configuration, Carbophalt GR (all-carbon geogrid), to evaluate the influence of fiber composition on crack resistance. The control configuration used the same emulsion application as the geogrid specimens but without any geosynthetic material, providing a baseline for quantifying the reinforcement contribution.

Placement depth: Three depths were investigated relative to the specimen base: one-third (approximately 27 mm from the bottom, placing the interlayer closer to the crack initiation point), one-half (40 mm, mid-depth), and two-thirds (approximately 53 mm, placing the interlayer closer to the loaded surface). These positions represent different overlay design scenarios and enable evaluation of how the amount of material above and below the interlayer affects crack interception and energy dissipation.

Temperature: Three thermal conditions were examined: -20 °C (simulating severe winter conditions where asphalt becomes brittle), 25 °C (representing standard room temperature conditions), and 40 °C (simulating warm-season service where asphalt viscosity is reduced).

Displacement rate: Two displacement rates were applied: 2 mm/min (representing slow traffic loading such as at intersections or in congested conditions) and 5 mm/min (representing higher speed loading). The variation in displacement rate enables evaluation of rate-dependent viscoelastic effects on interlayer performance.

2.6.2 Test Matrix

The first study (Chapter 3) tested 5 interlayer configurations × 2 interface types (ESG-10/ESG-14 and ESG-14/GB-20) at room temperature (20 ± 1 °C) with a displacement rate of 2 mm/min and interlayer placement at mid-depth. The second study (Chapter 4) tested 4 interlayer configurations × 3 temperatures (-20 °C, 25 °C, 40 °C) × 2 placement depths (one-third, two-thirds) at 2 mm/min. The third study (Chapter 5) tested 4 interlayer configurations × 2 temperatures (25 °C, 40 °C) × 2 displacement rates (2 mm/min, 5 mm/min) × 3 placement depths (one-third, one-half, two-thirds). All tests were replicated with a minimum of two specimens per condition.

Table 2.1 presents the complete experimental matrix, showing how each study progressively broadened the range of test variables while maintaining a consistent set of interlayer types across all investigations.

Table 2.1 Experimental matrix across the three studies

Study	**Interlayer Types**	**Placement Depth**	**Temperature (°C)**	**Displacement Rate (mm/min)**	**Replicates**
1 (Ch. 3)	Control, PF, GB, GR, GV	1/2	25	2	≥ 2
2 (Ch. 4)	Control, PF, GB, GV	1/3, 2/3	-20, 25, 40	2	≥ 2
3 (Ch. 5)	Control, PF, GB, GV	1/3, 1/2, 2/3	25, 40	2, 5	≥ 2

2.7 Data Analysis Framework

Multiple performance parameters were extracted from the force-displacement curves recorded during each CWD test. The analysis framework evolved across the three studies, with progressively more sophisticated fracture mechanics parameters introduced to capture different aspects of interlayer performance.

2.7.1 Force-Displacement Response

The primary output of each CWD test is a force-displacement curve that captures the complete mechanical response from initial loading through crack initiation, crack propagation across the interlayer, and final structural failure. Key descriptors extracted from these curves include maximum force (F_max), displacement at maximum force (d_max), and displacement at failure (d_f). These parameters provide direct measures of the load-bearing capacity and deformation tolerance of each interlayer system.

2.7.2 Stiffness Indices

Stiffness evolution was characterized using two complementary indices. The initial stiffness ($K_{0\text{-}4mm}$) was computed as the slope of a linear regression fit to the force-displacement data over the first 4 mm of displacement, representing the structural response before significant crack propagation reaches the interlayer. The working-range stiffness was characterized using secant stiffness values evaluated at fixed fractions of the peak force: K_{10}, K_{20}, and K_{30} denote the secant stiffness from the origin to the point on the ascending force-displacement branch where the force first reaches 10%, 20%, and 30% of the peak force, respectively, that is, $K_X = (X\% \times F_{peak}) / u_X$, where u_X is the displacement at which the force equals X% of the peak force. Their arithmetic mean, $\bar{K}_{10\text{-}30\%} = (K_{10} + K_{20} + K_{30})/3$, characterizes the effective early-loading stiffness of the system. Together, these two indices separate the pre-crack structural response from the early load-mobilization behavior of each interlayer configuration.

2.7.3 Energy Dissipation and Crack Propagation Energy

Energy dissipation during crack propagation was quantified as the area under the force-displacement curve from the origin to the point of structural failure. This energy, denoted W, represents the total mechanical work absorbed by the specimen during the fracture process and is an indicator of the interlayer system's capacity to delay crack propagation. The energy was calculated using the trapezoidal numerical integration rule applied to the recorded force-displacement data.

Crack propagation energy was further decomposed into pre-peak and post-peak contributions. The pre-peak energy represents the work required to propagate the crack from initiation to maximum load, while the post-peak energy captures the residual resistance provided by the interlayer after peak force is exceeded. This decomposition provides insight into the distinct reinforcement mechanisms operating before and after the crack fully engages the interlayer.

2.7.4 Toughness Improvement Factor (TIF)

The Toughness Improvement Factor quantifies the relative improvement in energy dissipation provided by a reinforced system compared to the corresponding unreinforced control. TIF is defined as the ratio of the energy dissipated by the reinforced specimen to the energy dissipated by the unreinforced specimen tested under the same conditions of temperature, displacement rate, and placement depth. A TIF value greater than 1.0 indicates that the interlayer improves the energy absorption capacity of the system, while values below 1.0 suggest that the interlayer introduces a structural discontinuity that reduces performance relative to the unreinforced case.

2.7.5 Fracture Toughness (G_{IC})

The critical strain energy release rate (G_{IC}) provides a fracture mechanics-based measure of the resistance to crack propagation at the interlayer interface. G_{IC} was calculated from the force-displacement data using the area method, which relates the change in potential energy to the crack surface area created during fracture. This parameter enables comparison of interlayer performance independent of specimen geometry and loading configuration, facilitating correlation with material properties and field performance data.

2.7.6 Interfacial J-integral

The J-integral at the interlayer interface was computed to characterize the crack driving force in the nonlinear regime where the viscoelastic behavior of asphalt invalidates the assumptions of linear elastic fracture mechanics. The interfacial J-integral captures the combined effects of elastic strain energy and plastic dissipation at the crack tip, providing a fuller measure of fracture resistance for viscoelastic composite systems. This parameter was calculated from the force-displacement curves following the methodology adapted for the CWD specimen geometry, accounting for the asymmetric stress distribution created by the inclined sliding mechanism.

2.8 Summary

This chapter has presented the experimental methodology employed throughout this thesis. The CWD testing approach provides a controlled, repeatable method for evaluating the crack resistance performance of geosynthetic-reinforced bituminous systems under parametric variation of temperature, displacement rate, and placement depth. The use of compact specimens and straightforward test procedures enables efficient parametric evaluation that would be impractical with larger-scale test methods, while the multiple performance parameters extracted from force-displacement data provide mechanistic insight into the fracture processes governing interlayer effectiveness.

The materials selection encompasses the three principal categories of geosynthetic interlayers used in practice, enabling systematic comparison of their distinct reinforcement mechanisms. The analytical framework, progressing from basic force-displacement descriptors through stiffness indices and energy parameters to fracture mechanics quantities (TIF, G_{IC}, J-integral), provides a sound basis for characterizing interlayer performance and establishing mechanistic relationships between material properties, placement conditions, and crack resistance behavior. The experimental results obtained using this methodology are presented and discussed in the subsequent chapters.

CHAPTER 3

EVALUATION OF CRACK DEVELOPMENT THROUGH A BITUMINOUS INTERFACE REINFORCED WITH GEOSYNTHETIC MATERIALS BY USING A NOVEL APPROACH

Ehsan Solatiyan[1], Van Thang Ho[1], Nicolas Bueche[2], Michel Vaillancourt[1] and Alan Carter[1]

[1] Department of Construction Engineering, École de technologie supérieure,
1100 Notre-Dame Ouest, Montréal, Québec, Canada H3C1K3
[2] Department of Architecture-Wood-Civil Engineering, Bern University of
Applied Sciences (BFH), Burgdorf, Bern, Switzerland

Article published in *Transportation Research Record, 2023, Vol. 2677(11), 446-457*, on May 2023.
Available at DOI: 10.1177/03611981231166002

Abstract

Using interlayers made of geosynthetic materials has proved its effectiveness with respect to postponing the appearance of reflective cracking on the surface. In this regard, in a reinforced bituminous interface, the crack first propagates from its origin upward until it reaches the interlayer. When the interlayer has higher stiffness than its surrounding bituminous material, the crack path diverts horizontally along the interlayer plane until the whole energy of the crack dissipates. Nevertheless, this mechanical improvement needs to be further studied to quantify the reinforcement effects of geosynthetic materials in mechanistic-based design of reinforced sections. This study aimed to develop a laboratory test method that not only is able to illuminate the crack resistance effect of geosynthetics but is also able to differentiate the load-displacement curves among different types of reinforced bituminous interfaces. The results led to the advent of a new test device called the crack widening device in which reproducibility and statistical variability of the outcomes were all within the acceptable range. On this ground, using paving fabric showed superior performance among others with respect to energy dissipation capability and retarding the loss in the stiffness modulus during the crack propagation stage compared with the corresponding unreinforced cases. On the other hand, using the reinforcement grids led to a higher initial stiffness of the reinforced structure, especially when embedded between coarse hot mixtures.

3.1 Introduction

A traditional pavement maintenance approach to deal with a deteriorated bituminous surface is to mill it up to a specific thickness and refill it with a new hot mix overlay. However, one of the main concerns associated with overlaying is the reflection of existing cracks caused by the movement induced by the traffic loads or moisture and temperature variations in the underlying layers or their combinations thereof. This in turn imposes massive maintenance costs on road authorities to redo their maintenance and rehabilitation measures.

Up until now, no solution has yet been documented in the literature to completely address the prevention of crack development across the overlay. Nevertheless, using interlayers made of geosynthetic materials has proved its effectiveness with respect to postponing the appearance of reflective cracks on the surface by prolonging the crack path and dissipating the energy of the crack during its propagation. In this regard, in a reinforced bituminous interface with geosynthetic materials, the crack first propagates from its origin upward until it reaches the interlayer. When the interlayer has higher stiffness than its surrounding asphaltic material, the crack path diverts horizontally along the interlayer plane until the whole energy of the crack dissipates by stretching the interlayer under the movement.

Current laboratory test devices that permit measuring the crack resistance of asphalt overlays are able to apply concurrently shear, tensile, and flexural stresses in the proximity of the crack and provide a stable state of crack propagation: the four-point bending test (Arsenie et al., 2017; Ferrotti et al., 2011; Virgili et al., 2009), wheel reflective cracking (WRC) test (Gallego and Prieto, 2006; Prieto et al., 2007), wedge splitting test method (Prieto et al., 2007), direct tensile strength test (Kumar and Saride, 2018), modified wheel tracker (Spadoni et al., 2021), Texas overlay tester (Jaskula and Rys, 2017), and UGR-FACT (Moreno-Navarro and Rubio-Gámez, 2013) are just a few. However, because of demanding large-size specimens, manipulation, and preparation of specimens, the complexity of the analysis of the results and less suitability in incorporating the reinforced structures with geosynthetics, the universal acceptability of these tests methods is limited in practice.

One of the limitations of testing specimens reinforced with geosynthetics is that a large specimen would be required to represent as best as possible the field conditions. The strength of geosynthetic materials is highly dependent on the friction and surface area. One of the objectives of the new test method was to produce and test small-size specimens. The effect of the specimen size on the results is not discussed here.

To meet this objective, four different geosynthetics, three types of geogrids, and one type of geotextile, with different physical and mechanical properties along with reference samples without the interlayer, were embedded in three different dense-graded hot mixes with respect to aggregate size to evaluate the development of the force-crack width curves from the initiation of the crack up to the failure point. This study will also address the following key points:

(a) the repeatability and variability of the proposed laboratory test device;
(b) fracture parameters that enable us to differentiate the mechanical performance of different types of interlayers during crack development;
(c) the best location of the interlayer with respect to the surrounding aggregate size.

As for the organization of the paper, a review of the literature is presented in the first section followed by a description of the materials, specimen preparation procedure, and configuration of the device and test setup. Then, the results and data analysis are discussed. Finally, a summary of the findings along with recommendations will be given.

3.2 Research Background

Many scientific proofs encourage using geosynthetic materials as an interlayer between bituminous layers to restrict fatigue cracking and rutting and to delay the appearance of reflective cracking (Solatiyan et al., 2020). This rehabilitation solution not only acts as a stress relief and reinforcement layer in the system (Saride and Kumar, 2017) but, also compared to a thick overlay, it is much more cost-effective (Steen, 2004) and sustainable since it allows lower hot mix materials as an overlay, thus decreasing the level of emissions and dissipation of natural sources of materials (Spadoni et al., 2021). However, the degree of effectiveness of the reinforced system depends mostly on the bounding condition provided at the interface (Sobhan and Tandon, 2008).

The presence of the interlayer by itself results in a discontinuity between consecutive layers in the pavement system that may lead to a loss in shear strength (Pasquini et al., 2014; Pasquini et al., 2015). Previous findings showed that a geogrid compared to paving fabric (PF) kept the integrity of the system at the interface level better by giving a higher value of the coefficient of interface bounding (CIB) (Solatiyan et al., 2021a), which stems from its meshed structure that provides more contact between its adjacent materials. This reduced bounding in the presence of the interlayer, however, plays a barrier role in growing bottom-up cracking, as already proved by the four to five times higher energy dissipated in the crack propagation stage (J-integral) in samples including PF (Solatiyan et al., 2021b).

Furthermore, the position of the geosynthetic in the pavement system is another important consideration that, with respect to the aggregate size in contact with the interlayer, affects the absorbed energy during the stretching of the geosynthetic under loading (Saride and Kumar, 2017). To take advantage of the maximum benefit from the geosynthetic, its location in the pavement structure should be selected according to the type of distress that is supposed to be addressed. With respect to reflective cracking, the minimum amount of crack propagation was observed when the geosynthetic was located at one third of the asphalt overlay thickness from the bottom (Khodaii et al., 2009). In addition, in an attempt to understand the effect of the geosynthetic on the mechanical performance of a multi-layer system under bending, the optimum location of the geosynthetic was proposed at a depth where the tensile stresses resulting from bending are high (Virgili et al., 2009). In a field study, the placement of the geosynthetic near the interface of an asphalt overlay with an underlying bituminous layer was found to be effective in limiting crack propagation (Guo and Zhang, 1993). The results from finite-element modeling of the geosynthetic-asphalt overlay showed that the minimum tensile strain required for the crack propagation over the geosynthetic is obtained when the geosynthetic is placed at one-third depth of the thickness from the bottom surface (Kuo and Hsu, 2003). However, only a few studies have been performed to evaluate the mechanical performance of geosynthetics during crack propagation when embedded between different sizes of hot mixes.

From the above-mentioned review of the literature, this study will first introduce a novel laboratory approach to differentiate the mechanical behavior of various types of geosynthetics during reflective bottom-up cracking under the displacement mode of loading, and then this behavior will be compared in two different types of interfaces composed of three hot mixes of different maximum aggregate sizes.

3.3 Method

To illuminate the evolution of the force-crack width curve in the presence of different types of geosynthetics placed at two different types of bituminous interfaces with respect to aggregate size was the main objective of this study. To reach this target, bi-layer bituminous samples with and without the interlayer were fabricated in the laboratory setting. By assuming that the friction developed between the interlayer and the bottom bituminous layer plays an important role in the crack-resistant performance of the reinforced systems, the geosynthetic was placed at two different interfaces composed of three hot mixtures. Two major criteria were considered for the comparison among the cases: the energy dissipated during crack development up to the failure point (W) and the initial modulus of the system against crack development (E) and its evolution over crack opening, as depicted in Figure 3.1. These parameters were obtained from an innovative crack development device specifically designed for this study.

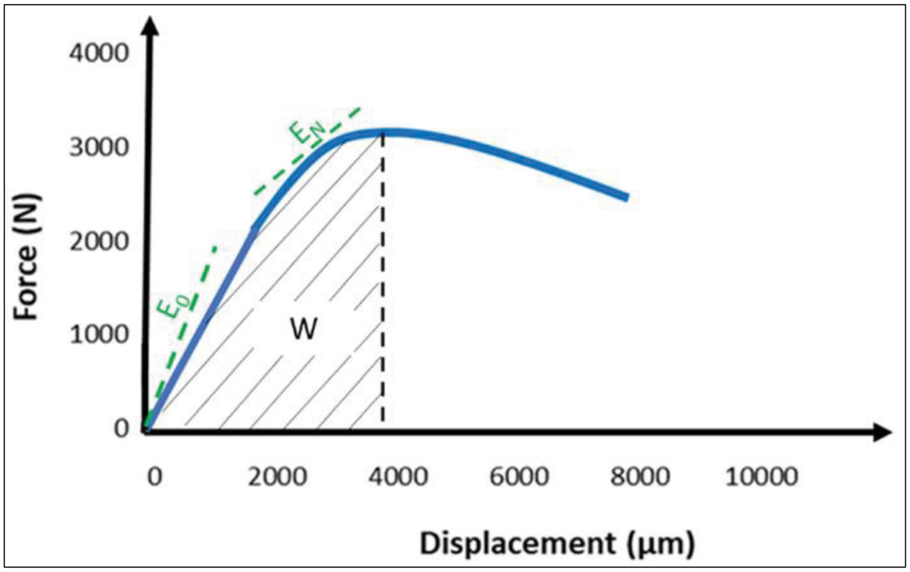

Figure 3.1 Criteria employed to differentiate among different types of geosynthetics

3.3.1 Material

In this study, three types of hot mixes normally found in Quebec (Canada) were designed to comply with Transport Quebec's standard (LC 4202) (MTQ, 2022): (I) a surface course mix with a nominal maximum aggregate size of 10 mm (ESG-10); (II) a binder course mix with a nominal maximum aggregate size of 14 mm (ESG-14); and (III) a base course mix with a nominal maximum aggregate size of 20 mm (GB-20). The mechanical specifications and the gradation curves for each type of mix are presented in Figure 3.2 and Table 3.1.

To reinforce double-layer structures, three types of reinforcement grids and one type of geotextile or PF were employed. The mechanical properties of the geogrids are shown in Table 3.2. GR and GB refer to the reinforcement grids made of carbon and a mix of glass and carbon fibers respectively, covered with bitumen on both sides, while GV is a type of geocomposite in which one side is covered with bitumen but from the bottom it is covered with a layer of fabric.

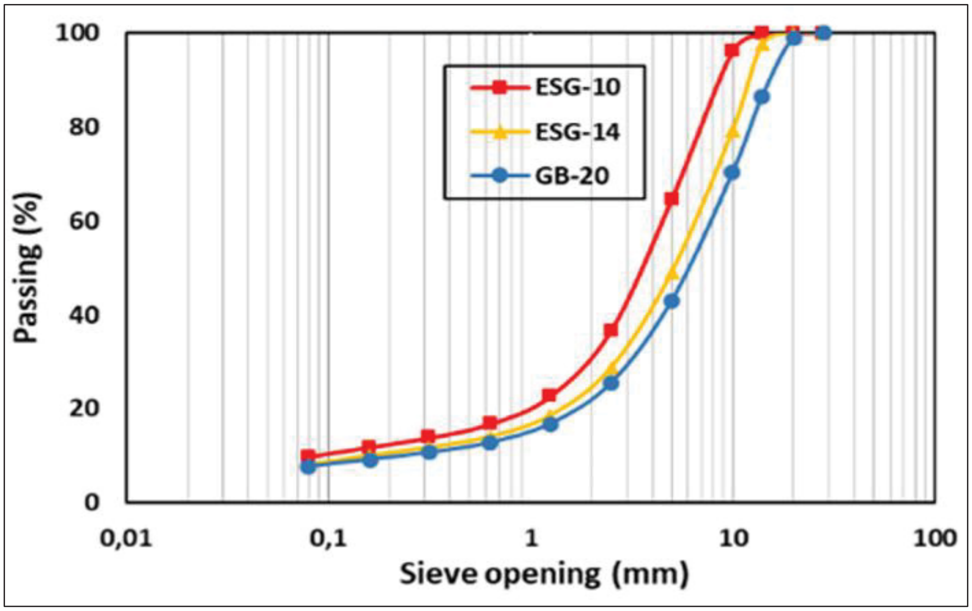

Figure 3.2 Gradation curves for each type of hot mixture. Note: ESG-10 = surface course mix (10 mm); ESG-14 = binder course mix (14 mm); GB-20 = base course mix (20 mm)

Table 3.1 The specifications of Hot Mix Asphalt

Mixture		**ESG-10**	**ESG-14**	**GB-20**
Binder Type		PG 58-28	PG 58-28	PG 58-28
Binder Content (% mass)		5.45	5.22	5.14
Mean Texture Depth (MTD) (mm) (ASTM E965)			3.6	4.4
Water Sensitivity (LC 26-001[1]) (%)	Measured	97.3	85.5	86.5
	Required	≥ 70	≥ 70	≥ 70
Rutting Resistance (LC 26-410[1]) (%)	Measured	After 1000 = 6.6 After 3000 = 8.2	7.2	9.1
	Required	(After 1000 cycles) ≤ 10 (After 3000 cycles) ≤ 15	(After 30000 cycles) ≤ 10	(After 30000 cycles) ≤ 10

Table 3.2 Technical properties of grids (provided by the geogrid supplier)

Name	**Abbreviated Name**	**Material / Transversal Strength (kN)**	**Material / Longitudinal Strength (kN)**	**Protective Layer**	**Elongation**		**Mesh size (square shape) (mm)**
					Transversal Direction	Longitudinal Direction	
Carbophalt G 120/200	GB	Glass fibers / 120	Carbon fibers / 200	Plastic foil	<3%	<1.5%	20
Carbophalt G 200/200	GR	Carbon fibers / 200	Carbon fibers / 200	Plastic foil	<1.5%	<1.5%	20
Glasphalt GV120/120	GV	Glass fibers / 120	Glass fibers / 120	non-woven	<3%	<3%	20

The PF was made of two essential elements: a needle-punched nonwoven fabric saturated with asphalt cement type PG 64-34. The main mechanical properties of the PF, supplied by the manufacturer, are given in Table 3.3.

Table 3.3 Principal mechanical specification of paving fabric (PF) (supplied by the company)

Specification	**Test Method**	**Unit**	**Value**
Grab tensile elongation	CAN/CGSB-148.1 No. 7.3	%	45-105%
Grab tensile strength	CAN/CGSB-148.1 No. 7.3	N	550
Mullen burst	CAN/CGSB-4.2 No. 11.1	kPa	1585
Bitumen retention	ASTM D6140	L/m^2	1.15

In general, 10 slabs of size 500 mm × 180 mm × 100 mm, 8 slabs reinforced with geosynthetics, and 2 unreinforced slabs were manufactured. The specimen preparation followed the procedure recommended by the producers of geosynthetic materials utilized in this study. It was started first with the production and compaction of the underlying slab (ESG 14 or GB-20) in the mold of the French roller compactor, according to LC 26-410 (MTQ standard). Thereafter, the slab was left for 48h for curing at room temperature. Then, three different procedures based on the type of the interlayer were followed as below.

- For unreinforced structures and the reinforced ones with GR and GB reinforcement grids, a slow-setting cationic asphalt emulsion, type CSS-1H, was implemented on the top surface of the bottom slab with a syringe and the edge of a spatula. The dosage of the emulsion opted for was 180 g/m² of residual bitumen, complying with the specifications provided by the manufacturer. Then after 3 h of setting time for the complete breakage of the emulsion in front of a fan, the reinforcement grid was applied on the emulsified surface with the steady-state movement of a gas blow torch to the grid to lightly melt the bitumen that the grid contains. Since the direct exposure of the binders to the flame may result in excessive aging of the material, the following precautions were adopted: not using the full power of the blow torch; keeping a 10 cm distance between the torch and the material; applying a constant-speed movement of the torch on every single strand of the grid, once in one direction and then in the other perpendicular direction.

- For the reinforced structure with the geocomposite, the same procedure as previously described for the reinforcement grid was pursued with two main differences. The dosage was selected as 270 g/m² and there was no delay between the application of the emulsion on the surface and spreading the geocomposite on the surface without using a blow torch.

- For the structure reinforced with PF, first the asphalt cement was heated up to the compaction temperature and then applied on the surface, as much as 110 g/m², followed by placing the fabric already cut at the same dimension as the slab on the bottom slab.

After the installation of the interlayer or settling the emulsion in the unreinforced case, the specimen preparation was continued by the compaction of the top bituminous layer (ESG-10 or ESG-14) over the bottom slab at 135ºC. In the final step, cubic shape samples of size 80 mm × 80 mm × 80 mm were cut from each prepared slab and their top and bottom surfaces were perfectly polished with sandpaper to have a full contact between the specimen and the loading plate from the top and the test device from the bottom. It is worth mentioning that a minimum of three openings from the geogrid structure is recommended for better interpretation of the crack resistance behavior of reinforced bituminous layers (Romeo et al., 2014). The shape, size, and number of specimens used for each structure are shown in Figure 3.3.

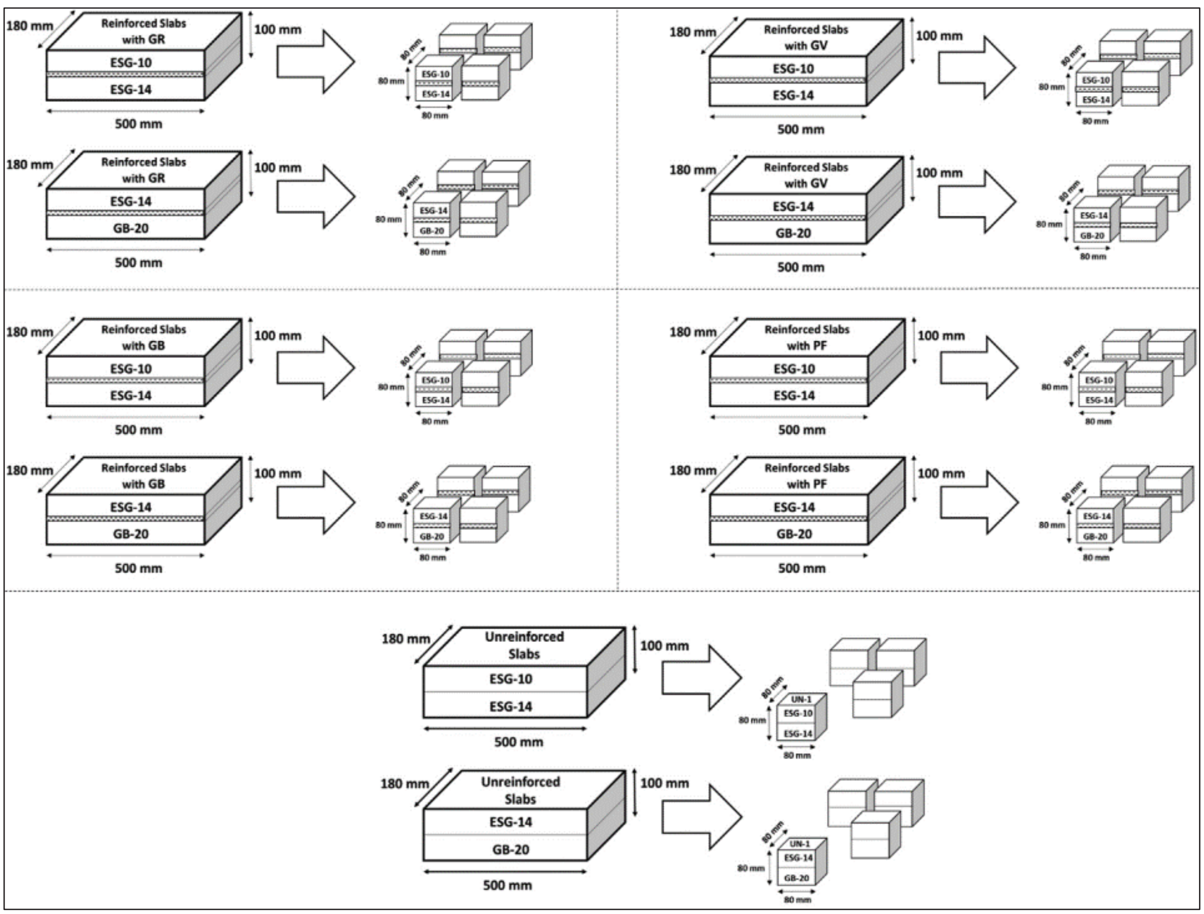

Figure 3.3 The shape, size, and dimensions of specimens

3.3.2 Test Setup

Using an interlayer between bituminous layers enhances the crack resistance performance of the whole system (Romeo et al., 2014). However, the quality of bonding provided at the interface plays a pivotal role in the level of reinforcement. To quantify this effect in mechanistic-based design methods, it is necessary to measure the level of reinforcement when the interlayer changes. To capture this mechanical effect, a crack performance tester device was designed and calibrated in the lab. This device is able to realistically simulate the loss of support from underlying layers while the crack grows from an initial notch up to the top. It was postulated that this methodology could result in having a better vision of the fracture phenomenon in reinforced and unreinforced structures. In the following section, more details are presented on the configuration of the device and test setups.

3.3.3 Crack Widening Device

In search of a test method to measure the crack resistance performance of reinforced bituminous structures that could distinguish among different types of interlayers, a crack resistance performance device was designed that has low complexity, and the time and manipulation required for the specimen preparation is competitive with other devices designed for the same purpose. It also simulates the crack propagation because of loss of support from the bottom layers under environmental and traffic loads. Figure 3.4 shows the device and the test setup.

The device is made of a triangle shape base that provides support for two sliding parts at the top and the bituminous specimen over it. The role of the screw and the spring in this configuration is to keep the sliding parts in contact with each other before the test starts. However, during the test, there should not be resistance from the spring. The test starts with an initial compressive contact force of as much as 100 N applied at the top surface via an MTS servo-hydraulic loading system and then sliding the movable parts under a constant rate of displacement. The movable parts are located on an inclined surface of 45°, which allows having the same pace of horizontal displacement as the vertical one.

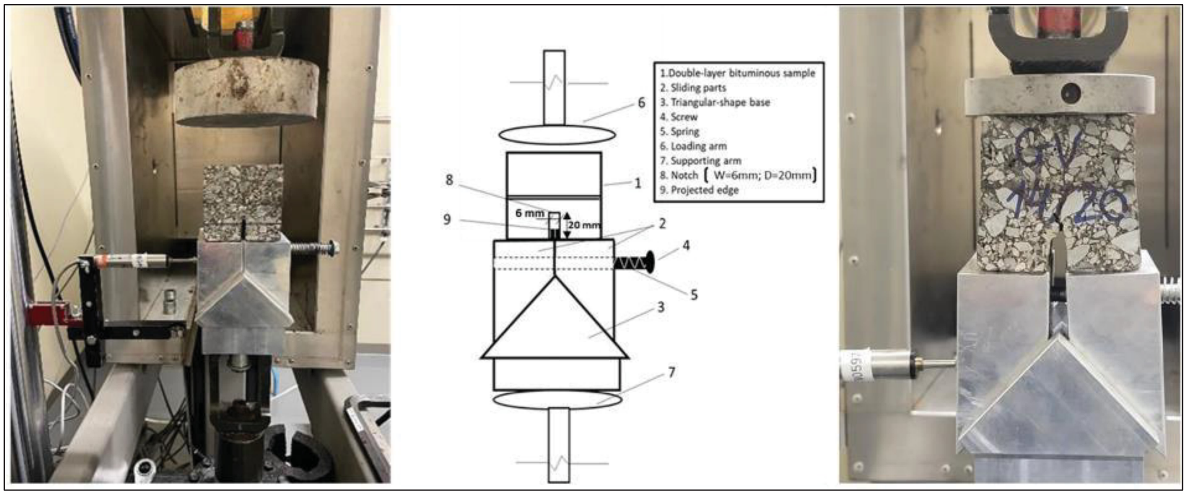

Figure 3.4 The crack widening device (CWD)

As the test starts, the movable parts slide over the inclined surface, and with the help of projected edges inserted in the notch of the specimen, of 6 mm in width and 20 mm in depth, a crack gradually starts to appear at the tip of the notch and propagates vertically upward and after crossing the interlayer reaches the top surface of the specimen, as the movable parts slide over the surface. The horizontal displacement was captured by a Linear Variable Differential Transformers (LVDT) installed horizontally in contact with the side face of the movable part. The main advantage of the device is to have more control over the temperature and rate of loading. In the course of development of the device, different combinations of temperatures and displacement rates were tested. However, there as less dispersity of results obtained at room temperature 20 ± 1ºC and a constant displacement rate of 2 mm/min. Figure 3.5 illustrates a typical result obtained from the crack performance tester device on the bituminous structure reinforced with the GR type of reinforcement grid surrounded by the ESG-10 and the ESG-14.

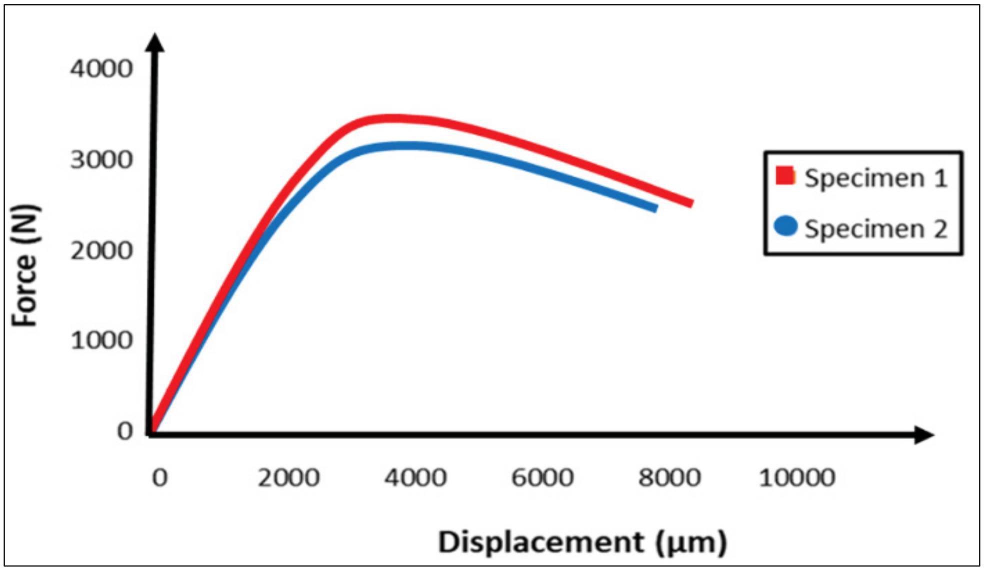

Figure 3.5 A typical force-displacement curve obtained from the crack performance tester device on two samples including the reinforcement grid made of carbon at the interface surrounded by a surface course mix with a nominal maximum aggregate size of 10 mm and a binder course mix with a nominal maximum aggregate size of 14 mm

3.4 Results and Discussion

In this section, the findings from the testing program are first presented and then analysis and discussion of the results are given. Specifically, the force-crack width curve for bituminous structures with and without reinforcements is evaluated. Afterward, based on the initial stiffness and energy dissipated by the interface during the crack development stage, the major mechanical differences among differently treated interlayers are identified.

3.4.1 Result and Discussion for Energy Dissipation

Figure 3.6 provides a comparison of the energy dissipated during the bottom-up crack propagation stage among different types of interlayers in two different structures, that is, ESG-10 over ESG-14 and ESG-14 over GB-20. These results are obtained from the area limited to the force-displacement curve up to the failure point (e.g., Figure 3.5) and averaged from two replicates for each type of interface. As can be seen, from the type of structure perspective, the interfaces reinforced with different types of reinforcement grids and PFs show improved performance when accommodated in coarse-graded mixtures. This result is in line with previous researches in which using a layer of geosynthetic interlayer resulted in an outstanding performance against reflective cracking (Prieto et al., 2007; Buttlar et al., 2000; Gonzalez-Torre et al., 2015; Zamora-Barraza et al., 2011). On the other hand, for the unreinforced structure, the energy required for the crack to propagate from the tip of the notch to the surface is noticeable when surrounded by fine-graded mixtures.

As far as the type of interlayer is concerned, the interface with the PF showed superior performance in delaying crack propagation compared with that reinforced with grids. However, in the case of the reinforcement grids, the interface reinforced with the GB grid experienced the best performance both in fine- and coarse-graded mixtures, while the GR and the GV grids only presented an improved performance in coarse mixtures and they had a comparable performance in both types of structures. The percentage of improvement in energy dissipation capability by different types of bituminous interfaces compared with corresponding unreinforced cases is shown in Figure 3.6.

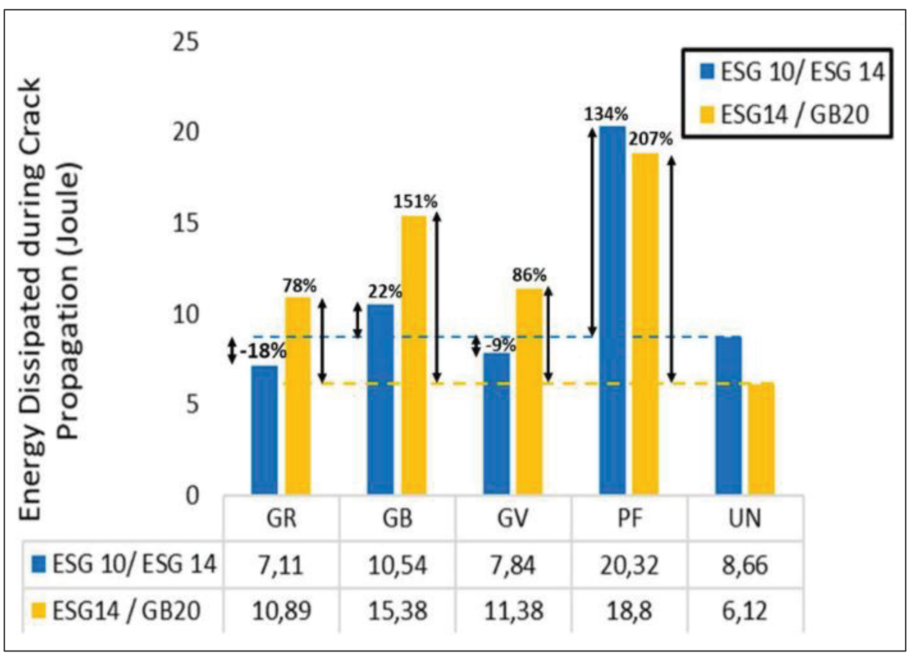

Figure 3.6 Changes in energy dissipation during the bottom-up crack propagation stage in two different double-layer structures.
Note: GR = carbon grid; GB = glass-carbon grid; GV = geocomposite; PF = paving fabric; UN = unreinforced

3.4.2 Result and Discussion for Crack Stiffness Evolution

To understand how the system including different types of interlayers reacts to the crack development, the changes in the stiffness modulus from the initiation of the test up until the failure point was studied by taking the slope of the tangent on the force-displacement curve into account. Figures 3.7 and 3.8 demonstrate the evolution of the stiffness modulus over the crack opening for different types of interfaces in two different structures.

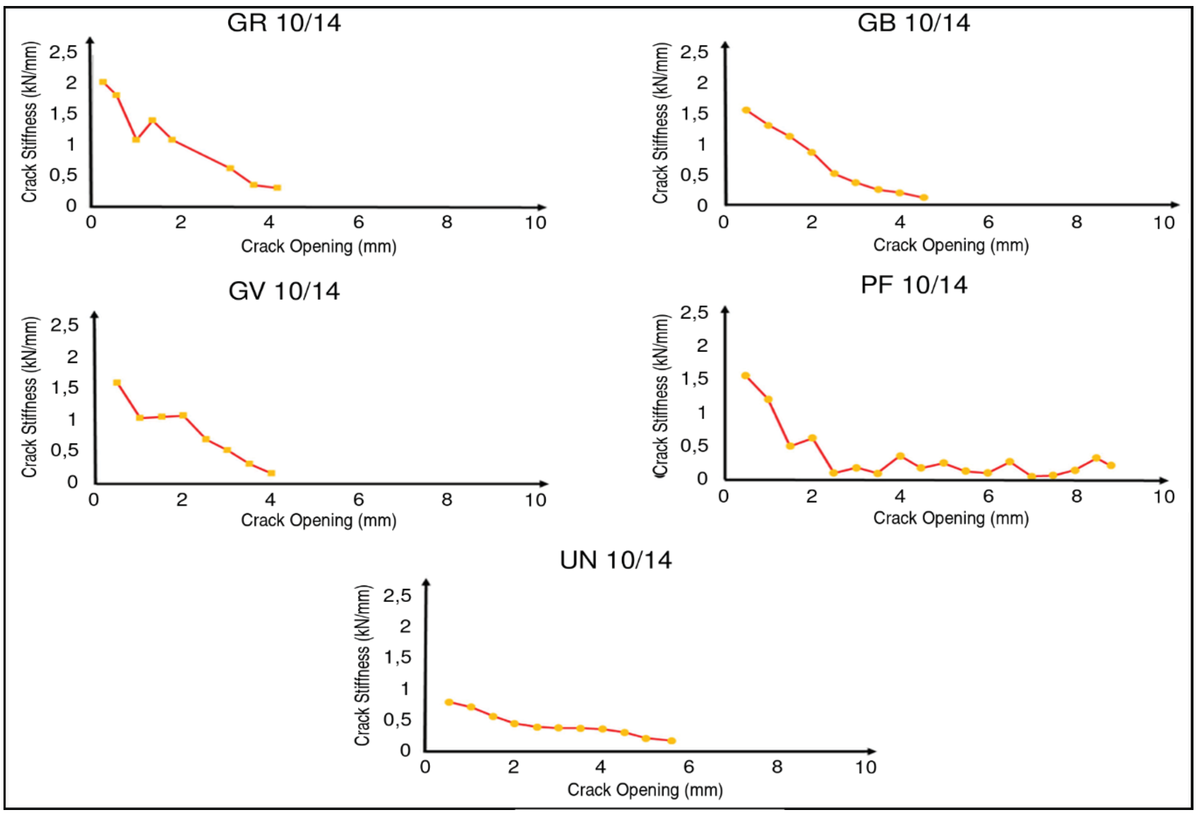

Figure 3.7 Crack stiffness evolution in double-layer structures composed of ESG-10 over ESG-14 reinforced with different types of interlayers and the unreinforced structure

In the structure composed of ESG-10 and ESG-14, a higher initial modulus was observed in the structure with the GR reinforcement grid. However, the GB reinforcement grid was able to undergo higher displacement compared with the two other reinforcement grids. Moreover, the GB reinforcement grid kept the structural integrity of the system almost unchanged, while in the GR and the GV reinforcement grids, a hardening effect was followed by a slight drop in the stiffness modulus of the system when the crack width reached 1.5-2 mm. On the other hand, in the case of the system reinforced with the PF, a sharp reduction in the stiffness of the system with respect to lower crack width was experienced. Nevertheless, the system was able to keep its structural integrity at a very large crack width because of the elasticity from the combined effect of the asphalt cement and the fabric. In addition, in an unreinforced structure, although the system showed a higher crack width before failure, the stiffness modulus of the system was the lowest.

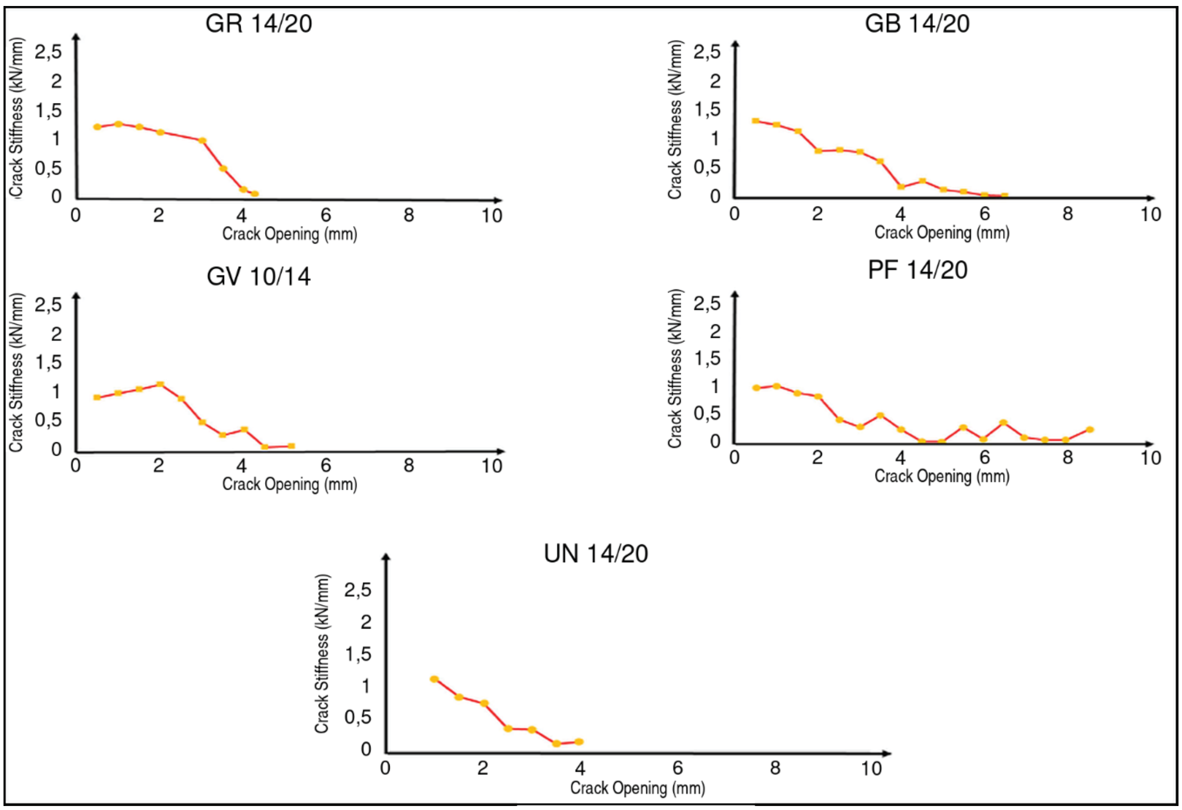

Figure 3.8 Crack stiffness evolution in double-layer structures composed of ESG-14 over GB-20 reinforced with different types of interlayers and the unreinforced structure

In the structure fabricated with ESG-14 and the GB-20, as shown in Figure 3.8, a similar trend was traced with the following differences. In the structures with the GR and GV reinforcement grids, the hardening effect was replaced by a significant improvement in the stiffness modulus of the system in the crack width between 1.5 and 2 mm. This could be referred to as the activation of the reinforcement effect, which in the presence of the coarse aggregates occurred in these two types of reinforcement grids. However, in the GB grid, the stiffness modulus was smoothly reduced from a higher initial modulus to a higher crack width. On the other hand, for the system with PF, a similar pattern as the fine-graded structure was observed. Nevertheless, the improvement in the initial stiffness modulus of the system was tangibly lower in the coarse-graded structure. Furthermore, the unreinforced structure, unlike the corresponding fine structure, showed a higher initial modulus. However, the crack width at the failure point was 30% reduced.

Figure 3.9 presents a view of changes in percentage in the mechanical performance of the bituminous interface with respect to the maximum force, maximum displacement, and initial crack stiffness when reinforced with different types of geosynthetics, compared with corresponding unreinforced cases. With respect to the maximum force, in the ESG-10/ESG-14 structure, the interface including a layer of PF had the highest resistance against shear stresses transferred from the crack during its propagation, followed by the GB, GR, and GV grids, respectively. Nonetheless, in the case of ESG-14/GB-20, it was the GB grid that showed the highest resistance, while the PF had the lowest rank.

Concerning maximum displacement at maximum force, in both types of structures, using a layer of PF at the interface led to a significant improvement in the structural integrity of the system, even in large crack openings. However, all types of reinforcement grids at the interface surrounded by ESG-10 and ESG-14 presented inferior performance compared with the unreinforced interface in a similar structure.

As for the initial crack stiffness, all types of geosynthetics induced a 2-2.5 times higher initial modulus at the interface of fine-graded mixtures compared with the unreinforced case. However, this improvement was not of great importance at the interface of coarse-graded mixtures, while in the case of the GV grid and PF, the crack stiffness on average dropped as much as 15%.

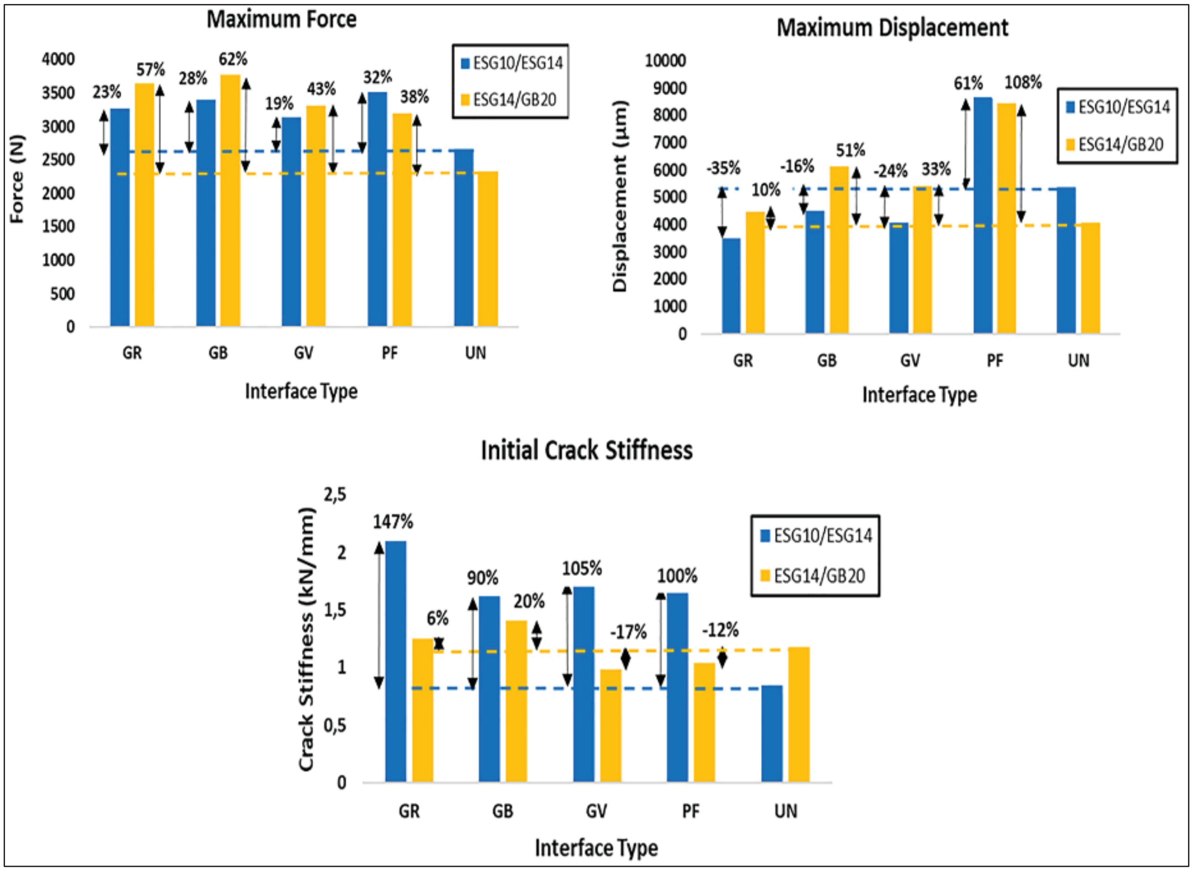

Figure 3.9 Changes in maximum force and displacement and initial crack stiffness in different interface types

3.5 Conclusions

In this study, an innovative laboratory approach was developed to investigate the crack resistance performance of double-layer bituminous structures reinforced with different types of interlayers. To have a better insight into the effect of the aggregate size used in the hot mixture on the mechanical performance of the interlayer, three different types of hot mixtures were utilized with respect to the nominal maximum aggregate size: ESG-10, ESG-14, and GB-20. Two mechanical indices were considered for understanding the differences in mechanical performance compared with the corresponding unreinforced cases: energy dissipated during the bottom-up crack propagation stage and the evolution of the stiffness modulus during the crack opening. Based on the findings from this laboratory study, the following conclusions were acquired.

- With respect to the energy required for the crack to propagate from the bottom to the top surface, the PF showed superior performance to the unreinforced one regardless of the type of the mixture it is in contact with. However, only using the GB reinforcement grid at the bituminous interface resulted in an almost two times enhanced performance compared to the corresponding unreinforced case. In the case of GR and GV reinforcement grids, the energy dissipation performance was doubled for fine-graded mixtures.

- Using the PF at the interface led to a very slow reduction in the rate of loss in the stiffness modulus of the combined system compared to the other types of interlayers.

- In all the reinforced structures, the initial modulus was remarkably higher than the corresponding unreinforced cases. This benefit was of great importance when using the carbon-made reinforcement grid (i.e., GR) at the interface. However, in the case of the geo-composite made of a layer of glass fiber grid, the improvement in the initial modulus was not tangible.

- In comparison with unreinforced structures, using reinforcement grid types GR and GB led to a higher initial modulus and smoother loss of the stiffness modulus. In the case of using a geocomposite (i.e., GV) this improvement was only associated with higher displacement when applied between coarse-graded mixtures. On the other hand, the PFs showed the lowest reduction in the loss of stiffness modulus because of yielding and significant horizontal displacement before failure under the imposed shear stresses.

- For gaining the most benefits from the reinforcement effect of the interlayers, the reinforcement grids showed improved performance while embedded between coarse-graded mixtures, namely, between a binder layer and a bituminous base layer. Nevertheless, in the case of using PF, the higher initial modulus was recorded while using it between a surface layer and a binder layer.

It is worth mentioning that, along with the current results, more experimental works are required to check the validity of the results with a larger matrix of mixes and different gradations, binder contents, geosynthetic materials, and temperatures. In addition, the evolution of the stiffness modulus of the reinforced systems can be modeled in finite-element-based modeling software to predict the appearance of reflective cracking more precisely in mechanistic-empirical pavement design methods. Furthermore, the test can be redone on one type of interlayer placed at different depths in the bituminous structure thickness to evaluate the claim that the best location for the reinforcement interlayer is one-third from the bottom of the lift.

CHAPTER 4

STUDY THE CRACK DEVELOPMENT OF GEOSYNTHETICS INTERLAYERS IN BITUMINOUS STRUCTURES UNDER DIFFERENT TEMPERATURES

Van Thang Ho[1], Celia Giani[1], Michel Vaillancourt[1], Eshan Dave[2] and Alan Carter[1]

[1] Department of Construction Engineering, École de technologie supérieure,
1100 Notre-Dame Ouest, Montréal, Québec, Canada H3C1K3
[2] Department of Civil and Environmental Engineering, University of New Hampshire,
33 Academic Way, W173 Kingsbury Hall, Durham, NH 03824-2619, USA

Article published in Journal of Testing and Evaluation, 2025, Vol. 53(5), 1291-1306, on June 2025
available at DOI: 10.1520/JTE20240285

Abstract

Overlay application is a widely used technique in pavement management systems for rehabilitation. This method proves particularly beneficial when the pavement structure retains sufficient structural integrity, allowing for the correction of visible distresses. However, the presence of deteriorated pavement poses a challenge to overlay performance, as it can lead to the upward propagation of existing cracks and joints into the overlay due to the concentration of stress and strain under the variations of loading and temperature in which those cracks, named reflective cracks, are created. This issue underscores the challenge of managing existing cracks when applying overlays. To mitigate this, interlayer systems such as geosynthetics are employed. Despite previous research in this area, a comprehensive understanding of the mechanical behavior of these composite systems is needed to enhance their effective-ness. This study investigates the effectiveness of the temperature as well as the position of reinforcement in the asphalt interface using the crack widening device. The outcomes showed that all the reinforcement can improve the performance of the system compared with the unreinforced one in most of the cases. All the reinforcement interlayers performed best at temperatures around 25°C ±2°C, regardless of the position of reinforcement, except in the case of geo-composite GV. Geo-composite GV exhibited the lowest maximum force values among others before failure at room temperature in both cases, reinforcement at one-third and two-thirds from the bottom of the samples, whereas the performance of geotextile was the best compared with

other kinds of reinforcement and unreinforcement in terms of force and displacement at both one-third and two-thirds position in most of the cases. The reinforcement or emulsion placed at one-third position always outperforms those at two-thirds in most of the cases.

4.1 Introduction

Asphalt pavements are subjected to a variety of loads that can compromise their performance, resulting in distress such as ruts and cracks. This necessitates the rehabilitation of roadways, a process that typically involves milling off the existing top layer and applying a new asphalt overlay, commonly known as “mill and fill,” at intervals throughout the pavement’s service life. Despite this method, cracks can persist in the existing asphalt layers, with the potential to rapidly propagate to the surface of the rehabilitated pavement due to horizontal and vertical movements at the crack tip (Cleveland et al., 2002). This conventional approach can be costly, requiring frequent renewal over short periods, which in turn demands additional financial and material resources. Moreover, it does not align with environmental concerns, as it releases large numbers of emissions into the air and consumes significant energy.

To mitigate these challenges, various techniques have been developed for rehabilitating cracked pavements, including stress absorption interlayers and steel meshes. Among these methods, geosynthetics have emerged as a popular antireflective cracking system. These materials are strategically placed on cracked surfaces prior to overlaying to act as a reinforcement or stress-absorbing layer, effectively delaying crack propagation (Norambuena-Contreras and Gonzalez-Torre, 2015).

The initial direction of crack growth in a geosynthetic-reinforced bituminous interface is upward, culminating at the interlayer. These interlayers enhance the performance of overlays by providing stress relief, reinforcement, and moisture control (Elseifi & Al-Qadi, 2004). However, it is crucial for the interlayer to possess sufficient cross-sectional area and modulus to enhance the strength and performance of the overlays (Nithin et al., 2015; Saride & Kumar, 2017). In cases where the interlayer is stiffer than the surrounding asphalt, cracks travel sideways along the interlayer instead of continuing upward. This horizontal movement causes the interlayer to stretch, which helps absorb and dissipate the energy driving the crack's progression.

Therefore, a comprehensive understanding of interlayer behavior in retarding reflection cracks is essential for selecting an appropriate interlayer for a given pavement system. This understanding also aids in evaluating the reinforcing effect within the context of mechanistic design for reinforced pavement sections.

4.2 Research Background

Numerous recent research studies have highlighted the significant benefits of integrating geosynthetics beneath asphalt overlays to mitigate reflective cracking (Nithin et al., 2015). This rehabilitation approach not only acts as a stress relief and reinforcement layer within the system (Marienfeld and Baker, 1999) but also presents notable cost-effectiveness compared with thicker overlays (Steen, 2004). Furthermore, it promotes sustainability by reducing the amount of hot mix material required for overlaying, thus decreasing emissions and conserving natural resources (Spadoni et al., 2021). However, the effectiveness of the reinforced system largely hinges on the conditions established at the interface (Sobhan & Tandon, 2008).

The addition of an interlayer creates a boundary between pavement layers that can weaken the overall structure's resistance to shear forces since it interrupts the continuous bond between layers (Pasquini et al., 2015; Pasquini et al., 2013). Geogrids have been observed to exhibit minimal reduction in shear resistance, attributed to their apertures (Brown et al., 2001), whereas geotextile interlayers are found to be less resistant to shearing (Brown et al., 2001; Zamora-Barraza et al., 2011). Previous studies have demonstrated that compared with paving fabric (PF), geogrids maintain better interface integrity, evidenced by a higher coefficient of interface bonding (Solatiyan et al., 2021a). This is due to the meshed structure of geogrids, facilitating greater contact between adjacent materials.

A critical factor in geosynthetic performance is its location within the pavement. This placement directly affects the energy absorption during loading-induced stretching, especially regarding the aggregate size present at the interlayer (Saride & Kumar, 2017). To fully leverage the benefits of geosynthetics, their placement should align with the type of distress being addressed. For instance, when the reinforcement was placed at one-third from the bottom of the asphalt overlay to mitigate the reflective cracking, minimal crack propagation was observed (Gonzalez-Torre et al., 2015). Research from actual pavement installations has confirmed that positioning geosynthetics between an asphalt overlay and the existing bituminous layer below produces optimal results - the material helps restrict crack growth, extends the pavement's resistance to repeated loading, and improves its ability to withstand bending forces (Guo & Zhang, 1993; Moayedi et al., 2009).

Quantifying the reduction of reflective cracking in pavement structures presents a complex challenge due to the multitude of mechanical and environmental variables at play. In an effort to measure the enhancement of cracking resistance in pavements with the inclusion of geosynthetics between layers, various laboratory test devices have been developed. These include the four-point bending test (Ferrotti et al., 2011; Virgili et al., 2009), University of Granada-Fatigue Asphalt Cracking Test (Moreno-Navarro & Rubio-Gámez, 2013), direct tensile strength test (Kumar & Saride, 2018), wheel reflective cracking test (Gallego & Prieto, 2006), wedge splitting test method (Gharbi et al., 2017), modified wheel tracker (Spadoni et al., 2021), and Texas overlay tester (Jaskula and Rys, 2017; Leiva-Padilla et al., 2016).

However, practical limitations such as the requirement for large-size specimens, intricate specimen manipulation and preparation, complex result analysis, and limited applicability for reinforced structures with geosynthetics have hindered widespread adoption of these testing methods. This study addresses these challenges by embedding geosynthetics (two types of grids and one type of geotextile) at two positions - one-third and two-thirds from the bottom - under varying temperature conditions (−20°C, 25°C, and 40°C).

The objective of this study is to evaluate the force-crack width curves from crack initiation to failure under these specified thermal conditions. This approach aims to provide valuable insights into the effectiveness of geosynthetics in improving the cracking resistance of asphalt overlays in a range of temperature scenarios.

4.3 Methodology

The aim of this study was to investigate the performance of geosynthetics in bituminous structures under different temperature and placement depth. The study involved analyzing the evolution of the force-displacement curve. Two sets of laboratory specimens for testing were created: one group of two-layer bituminous samples that included the interlayer material and a control group without it. The same hot mixture has been used for the top and bottom layers of the sample to better fit the reality of pavement rehabilitation. To investigate the hypothesis that interface friction between the interlayer and lower bituminous layer governs crack-resistant performance, geosynthetic materials were strategically positioned at one-third and two-thirds heights from the specimen base, enabling systematic evaluation of the frictional mechanisms that influence reinforcement effectiveness. In the control test, the placement position of emulsion was similar to the placement of geosynthetics in the samples for a perspective comparison of how geosynthetics can improve the performance of a pavement structures. In the comparison of specimens, the energy dissipated during crack development up to the point of failure was examined. A customized crack propagation testing apparatus was developed and implemented to measure these critical parameters.

4.3.1 Materials

This study focused on designing one specific type of hot mix commonly used in Quebec, Canada, to meet Transport Quebec's standard. Both the surface and binder courses in this study were constructed using a mix with a 10-mm nominal maximum aggregate size, designated ESG-10. The mechanical characteristics of ESG-10 surpassed the required benchmark for both water sensitivity and resistance to rutting as outlined in detail in Table 4.1. The binder type employed in this study was PG 64E-28.

The evaluation of reinforced interface performance incorporated three distinct interlayer materials: two types of grids and a geotextile (designated as PF). The PF interlayer featured a dual-component design, consisting of a needle-punched nonwoven fabric impregnated with PG 64-34 asphalt cement. The manufacturer-specified mechanical properties of the PF are outlined in Table 4.2.

Table 4.1 The specification of hot mix asphalt

Specification		Value
Mixture		ESG-10[a]
Binder type		PG 64E-28
Binder content, % mass		5.45
Water sensitivity (LC 26-001), %	Measured	97.3
	Required	≥70
Rutting test (LC 26-410), %	Measured	After 1,000 = 6.6; After 3,000 = 8.2
	Required	After 1,000 ≤10; After 3,000 ≤15

Note: [a] ESG-10 = a mix for the surface course and binder course with a maximum aggregate size of 10 mm.

Table 4.2 The mechanical properties of paving fabric (PF)

Specification	Test Method	Unit	Value
Grab tensile elongation	CAN/CGSB-148.1 No. 7.3	%	45-105
Grab tensile strength	CAN/CGSB-148.1 No. 7.3	N	550
Mullen burst	CAN/CGSB-4.2 No. 11.1	kPa	1,585
Bitumen retention	ASTM D6140	L/m²	1.15

Note: ASTM D6140, Standard Test Method to Determine Asphalt Retention of Paving Fabrics Used in Asphalt Paving for Full-Width Applications.

The mechanical properties of the geogrids are presented in Table 4.3, where "GB" refers to bitumen-coated reinforcement grids manufactured from two different fiber compositions: one made purely of carbon fibers and another combining both glass and carbon fibers, with bituminous coating applied to both surfaces. On the other hand, “GV” represents a type of geo-composite where one side is bitumen-coated and the bottom side is covered with a fabric layer.

Table 4.3 The mechanical properties of geosynthetics

Name	**Name in Abbreviation**	**Type/ Transversal Strength, kN**	**Type/Longitudinal Strength, kN**	**Covered Layer**	**Elongation**		**Mesh Size (Square Shape), mm**
					Transversal Direction	Longitudinal Direction	
Carbophalt G120/200	GB	Glass fibers/120	Carbon fibers/200	Plastic foil	<3%	<1.5%	20
Glasphalt GV 120/120	GV	Glass fibers/120	Glass fibers/120	Non-woven	<3%	<3%	20

In general, 12 slabs of size 500 by 180 by 100 mm were manufactured in a laboratory: 6 slabs were reinforced with grids, 3 slabs reinforced with geotextile, and 3 slabs were unreinforced. The specimens were prepared meticulously, following the procedures recommended by the manufacturers of the geosynthetic materials used in this study. Initially, the bottom layer of the slab was constructed and compacted using the French roller compactor, as per LC 26-410 (MTQ standard), ensuring adherence to the one-third and two-third sample proportions by applying the initial layer of ESG-10 at a precisely measured 63-mm thickness. The next steps are to cure all slabs within 48 h under room temperature, with three distinct procedures being conducted after that depending on the type of interlayer used.

- For structures without reinforcement and those reinforced with GB reinforcement grids, a slow-setting cationic asphalt emulsion, type CSS-1H, was precisely applied to the top surface of the bottom slab. This application was carried out using a syringe and the edge of a spatula, ensuring accuracy. The emulsion dosage used was 0.18 L/m² of residual bitumen, meeting the manufacturer’s specifications. After allowing 3 h for the emulsion to fully break in front of a fan, the reinforcement grid was then placed on the emulsified surface. A gas blow torch with controlled, steady movement was used to lightly melt the bitumen within the grid. To prevent excessive aging of the material due to direct flame exposure, precautions were taken: the blow torch was operated at reduced power, maintaining a 10-cm distance between the torch and the material, and a constant-speed movement was applied to each strand of the grid, first in one direction and then perpendicular.

- For structures reinforced with a geo-composite, a similar procedure to that of the reinforcement grid was followed with two main distinctions. The emulsion dosage was increased to 0.26 L/m², with no wait time between applying the emulsion and laying the geo-composite on the surface. The use of a blow torch was omitted in this process.
- In the case of the paving fabric, the asphalt cement was heated to the compaction temperature of 168°C and carefully applied to the surface of the bottom slab. The selected dosage was approximately 0.11 L/m², following the manual instructions provided by the company. Unlike the previous methods, there was no delay between the application of the cement and the placement of the precut geotextile, which matched the dimensions of the slab.

After the interlayer was installed or the emulsion settled in the unreinforced case, the specimen preparation advanced with the compaction of a 37-mm top bituminous layer of ESG-10. This compaction was meticulously conducted to complete the slab over the bottom layer, using a temperature of 135°C. For the final step, cubic-shaped samples, each measuring 80 by 80 by 80 mm, were carefully cut from every prepared slab. Edges were precisely trimmed to eliminate any potential edge-distraction, as illustrated in Figure 4.1.

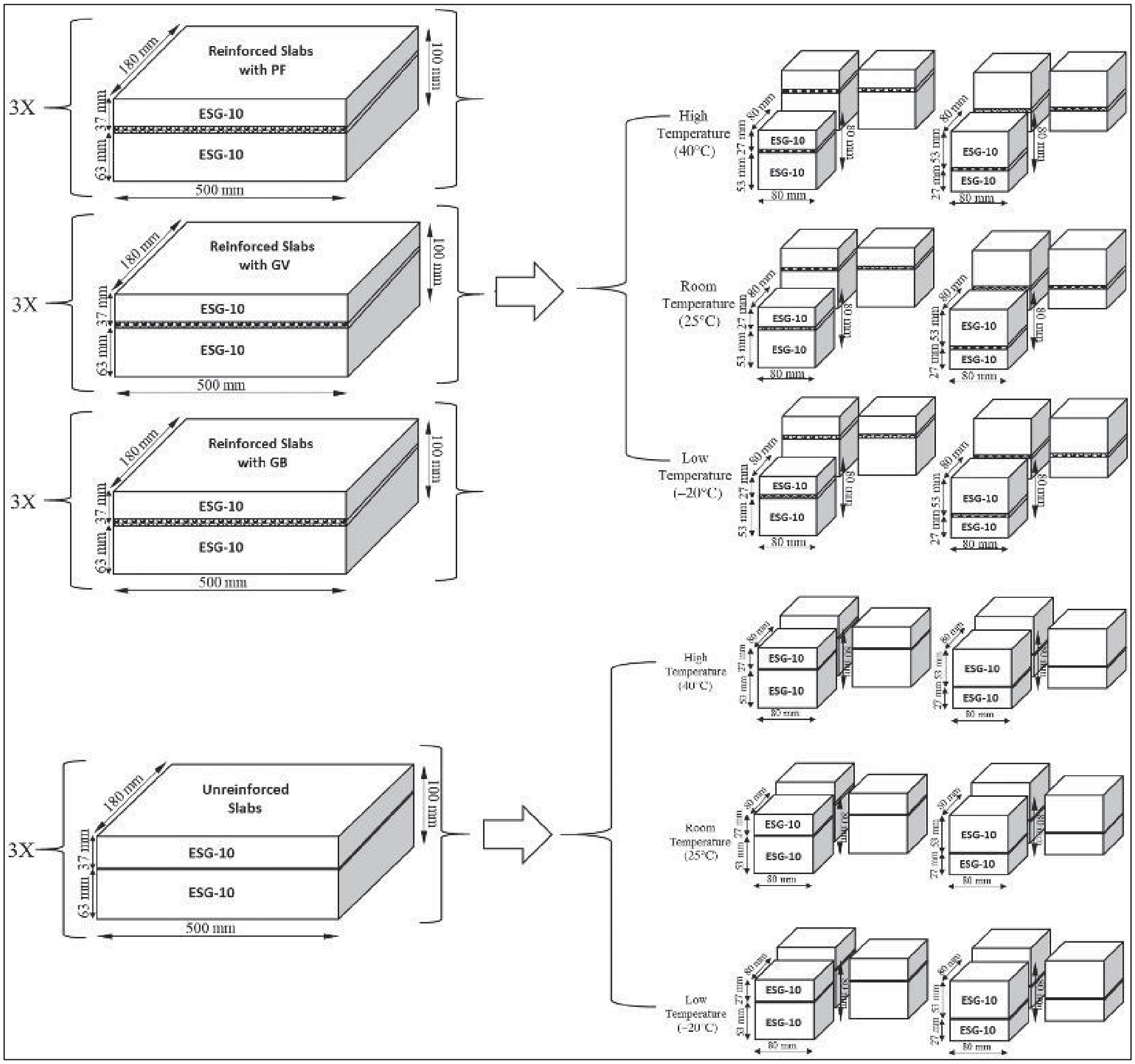

Figure 4.1 Schematic of shape, size, and dimensions of specimens

Ahead of conducting the tests, both the top and bottom surfaces of the samples underwent a thorough polishing process using sandpaper. This precise procedure aimed to establish seamless and full contact between the top of each sample and the loading plate, as well as ensuring optimal contact with the test device's bottom surface. Such meticulous preparation was paramount for guaranteeing the accuracy and reliability of results during the experimental evaluation.

It is essential to highlight that for a more comprehensive interpretation of the crack resistance behavior of reinforced bituminous layers, it is recommended to have a minimum of three opening apertures from the geogrid structures (Solatiyan et al., 2023). This guideline is crucial for obtaining insightful and meaningful results from the conducted tests.

4.3.2 Test Setup

The incorporation of an interlayer between bituminous layers significantly improves the crack resistance performance of the entire system. However, the effectiveness of reinforcement largely depends on the quality of bonding established at this interface. To accurately quantify this impact within mechanistic-based design methodologies, it is essential to evaluate the level of reinforcement under various interlayer conditions.

In addressing this mechanical aspect, a crack performance testing device was meticulously developed and calibrated in a laboratory setting. This innovative apparatus effectively simulates the loss of support from underlying layers due to environmental and traffic loads, allowing cracks to propagate from an initial notch to the surface. The hypothesis was that this method would offer a more comprehensive understanding of the fracture phenomenon in both reinforced and unreinforced structures. Figure 4.2 illustrates the device and the test setup.

The device consists of a triangular-shaped base that provides sturdy support for two sliding components positioned at the top, with the bituminous specimen placed atop them. The screw and spring mechanism ensures consistent contact between the sliding components before test initiation, preventing any unintended separation or misalignment during the experimental procedure. However, once the test begins, the spring should not introduce any resistance. The testing process initiates with an initial compressive contact force of up to 100 N, which is applied to the top surface using an MTS servo-hydraulic loading system. Subsequently, the movable components start sliding under a constant rate of displacement. These movable components are positioned on a 45° inclined surface, allowing them to move horizontally at the same pace as their vertical displacement. At the onset of the test, the components are set in motion along the inclined surface. The geometry of the protruding edges, precisely fitted within the specimen’s notch (6 mm in width and 15 mm in depth), facilitates the gradual development of a crack at the notch tip. This notch has been made at the top or bottom of the cube depending on the desired depth of the reinforcement. This crack then proceeds to propagate vertically upward, crossing the interlayer, until it reaches the top surface as the movable parts continue their movement over the surface.

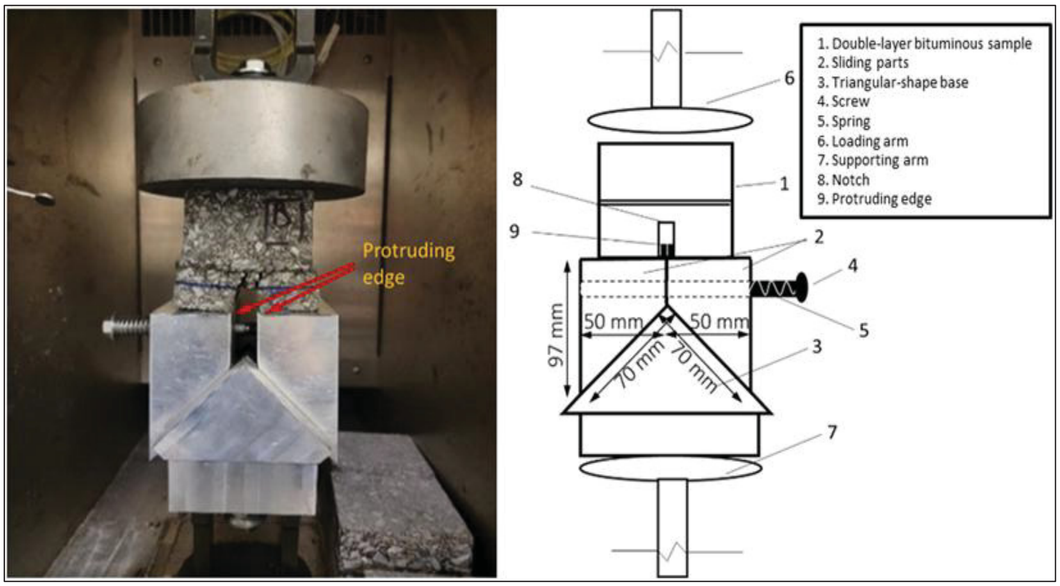

Figure 4.2 A view of crack widening device and how it works

Samples have been tested at 40°C ± 2°C, room temperature 25°C ± 2°C and −20°C ± 2°C. To ensure the samples were at the appropriate temperature, they were placed in the thermal chamber of the press for 4 h before testing to keep the temperature inside the chamber and the samples stable.

4.4 Results and Discussion

Our primary focus is on evaluating force-crack width curves for bituminous structures with reinforcement placed at two different positions in samples and under different temperatures. Subsequently, we identify significant mechanical differences based on interlayer positioning and temperature variations during the crack development stage. All the results presented were averaged from two replicates for each type of interface.

4.4.1 Performance of Reinforcement at Different Positions

Figure 4.3 compares the results between reinforced and unreinforced samples when tested at three different temperatures in which the position of reinforcement for reinforced samples as well as the position of emulsion for unreinforced samples was placed at the height at one-third from the bottom of the samples. As can be seen at high temperature, maximum forces at failure point for samples reinforced with geosynthetics were higher than those unreinforced. This can be explained as all the reinforced samples start mobilizing when the crack propagation reaches the reinforcement layer and that they presented more resistance in force. However, since the bituminous coating of the geogrids and the tack coat applied under the geogrids loses its resistance at high temperature, it thus experiences less deflection and showed less displacement compared with the unreinforced samples. On the other hand, the emulsion CSS-1H applied on control samples as a bonding agent contributes to delaying the crack propagation and leads to higher displacement as a result. Moreover, those samples with PF performed best compared with other reinforcement samples in terms of force and displacement, in which the maximum displacement of PF was nearly twice that of the maximum displacement for samples reinforced with Glasphalt GV. This benefit of PF came from the fact that the geotextile has a fabric layer saturated with high-performance asphalt cement that helps to postpone the crack propagation.

At room temperature, however, samples reinforced with Carbophalt G (GB) presented highest resistance before failure, whereas Glasphalt GV exhibited the lowest value among others before failure. In terms of displacement, however, the PF showed the highest displacement, which means it needed more energy for the sample to reach the failure point. In fact, the geo-composite Glasphalt GV has a layer of fabric between the apertures that prevent good interlocking between two layers of bitumen, whereas the PF was also manufactured with a layer of fabric that, however, was saturated with high-performance asphalt cement inside. On the other hand, Carbophalt GB with coated-bitumen on both sides contributes a good interlocking between two asphalt layers. In the case of the control test, the emulsion layer plays as a bonding agent linking the two asphalt layers and helps to delay the crack development in which it helps to improve the stiffness of the unreinforced samples. Those reasons could result in the lowest value in terms of force for Glasphalt GV under room temperature.

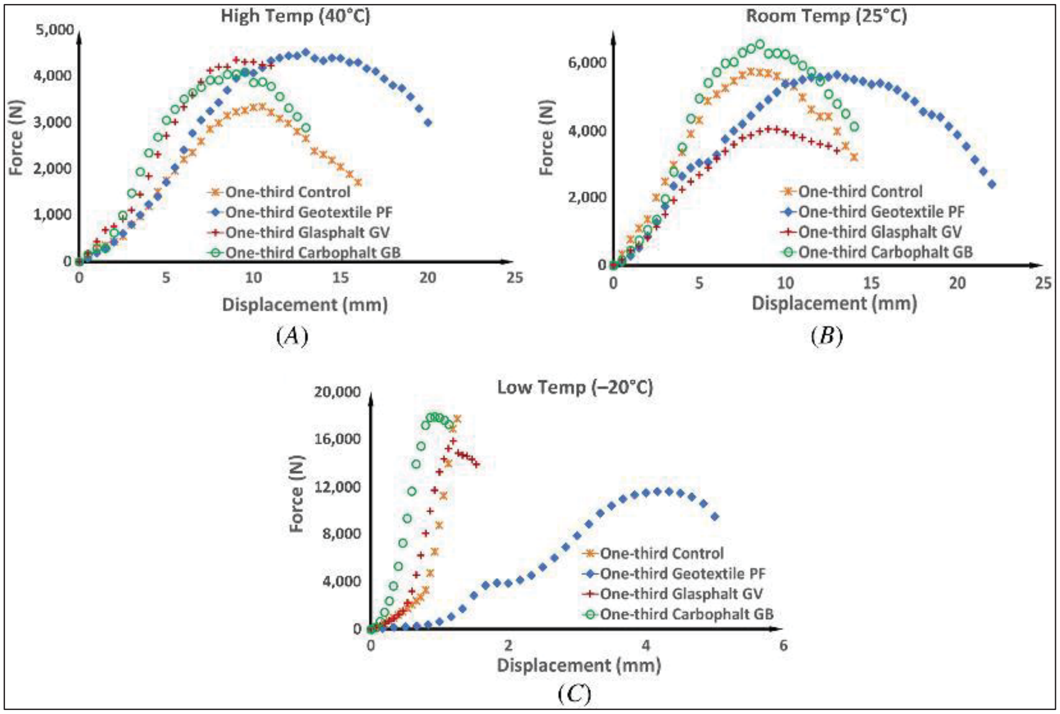

Figure 4.3 Force-displacement relationship for all samples with reinforcement and emulsion placed at one-third from the bottom of specimens underwent different temperatures: (A) high temperature (40°C), (B) room temperature (25°C), and (C) low temperature (−20°C)

At low temperature, samples with PF continued to outperform compared with others in terms of displacement in which the PF maintained the resistance even though all samples became brittle and those unreinforced did not contribute in resistance against cracking after reaching maximum force at this level of temperature.

For those samples with the reinforcement as well as emulsion interlayers located at two-thirds from the bottom subjected to a high temperature at 40°C, the behavior was similar among those specimens in which PF exhibited slightly lower in terms of force and slightly greater in terms of displacement (Figure 4.4). Two distinct stages were observed. The first stage was the contribution of the asphalt in the system where the asphalt mostly resists crack development before it reaches the reinforcement layer. The second stage is when the reinforcement layer starts mobilizing; hence, the structure has less integrity to perform resistance compared with the case of one-third and that all the curves for this case were similar among each other for the first stage following different development in displacement depends on reinforcement type or emulsion in the second stage that have been shown in the results for high and room temperature conditions at two-thirds. At room temperature, GV samples continued their lowest performance in terms of force and displacement among others, whereas PF performed best in those terms.

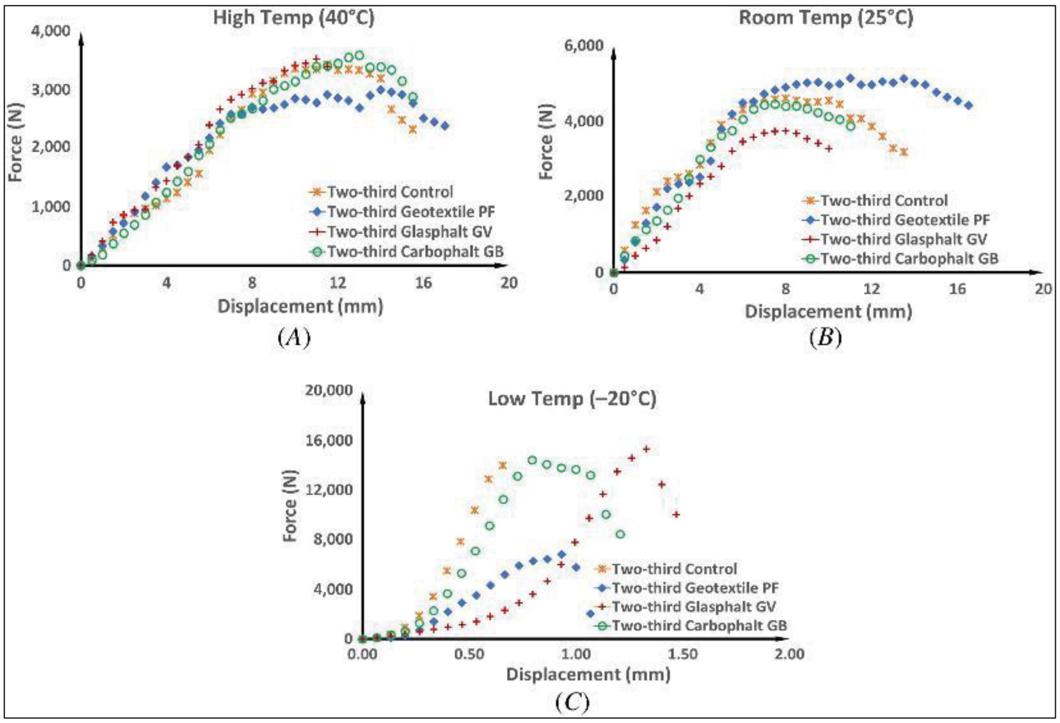

Figure 4.4 Force-displacement relationship for all samples with reinforcement and emulsion placed at two-thirds from the bottom of the specimens underwent different temperatures: (A) high temperature (40°C), (B) room temperature (25°C), and (C) low temperature (−20°C)

At low temperature, all samples presented the contractive behavior in which the maximum displacement was exceptionally low compared with those observed at high temperature and room temperature. The PF, however, exhibited the lowest value in terms of force and displacement among others, whereas Glasphalt GV performed best in terms of force and unreinforced samples continued to have consistent behavior, as is similar to that observed in the case of one-third at this temperature.

4.4.2 The Effectiveness of Temperature on Performance of Geosynthetics

The performance of asphalt pavement reinforcement systems exhibits significant temperature-dependent behavior (Figure 4.5). As can be seen in most of the cases, at room temperature, the reinforcement showed best performance compared to the cases of high and low temperature in both one-third and two-third position, in which it required more energy dissipation for the crack propagation for all samples at room temperature. This can be explained as at high temperatures (40°C), the reduced viscosity of asphalt cement leads to interface delamination, weakening the bond between layers and compromising overall system integrity. The bituminous coating within the geogrids and geotextiles loses cohesion, further diminishing the reinforcement's ability to integrate with the asphalt matrix. Although the material becomes more ductile, it also becomes less resistant to deformation, reducing its capacity to effectively distribute and withstand applied loads. In contrast, at room temperature (25°C), the asphalt cement maintains an optimal viscosity, ensuring strong interface bonding and better interlocking between the reinforcement and asphalt layers. This balanced material behavior allows for both strength and flexibility, making it the most effective temperature for reinforcement mobilization. The reinforcement can distribute loads efficiently and delay crack propagation, enhancing the overall pavement performance. However, at low temperatures (−20°C), the materials become brittle and rigid, significantly limiting their ability to deform and absorb energy. The increased stiffness leads to higher stress concentrations at crack tips, accelerating crack propagation and reducing the effectiveness of stress transfer between layers. As a result, the reinforcement's ability to improve pavement durability is diminished under extreme cold conditions.

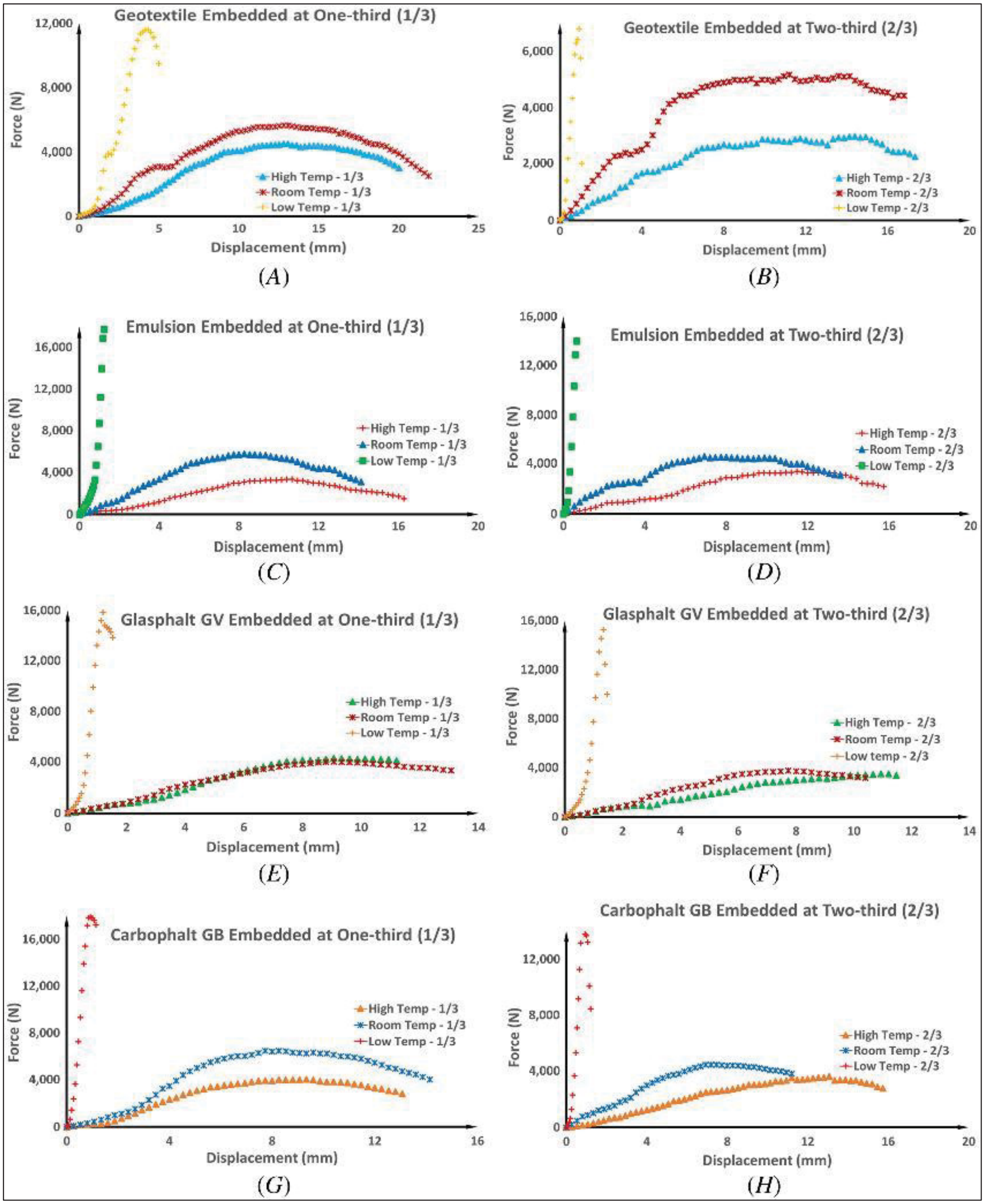

Figure 4.5 The influence of temperature on performance of reinforced and unreinforced samples: (A) at one-third, (B) at two-thirds, (C) at one-third, (D) at two-thirds, (E) at one-third, (F) at two-thirds, (G) at one-third, and (H) at two-thirds

The only deviation from the temperature-dependent performance trends was observed in samples reinforced with Glasphalt GV at one-third depth under high and room temperature conditions, where their maximum force values remained similar. This inconsistency is primarily attributed to the presence of a non-saturated fabric layer interspersed between apertures, which hinders optimal interlocking with the surrounding asphalt matrix and compromises overall composite integrity. Additionally, the single-sided bitumen coating on Glasphalt GV weakens interface bonding, resulting in suboptimal adhesion between the reinforcement and adjacent layers. This structural limitation disrupts effective stress transfer mechanisms within the pavement system, reducing the reinforcement's capacity to distribute loads efficiently. As a result, Glasphalt GV demonstrates a diminished ability to mobilize its reinforcement properties, leading to a less effective contribution to the pavement's structural performance compared with alternative reinforcement solutions. However, displacement was higher in tests conducted at room temperature, a trend that aligns with the observations detailed in the preceding section.

4.4.3 Energy Dissipation

Figure 4.6 illustrates the comparative energy dissipation during the bottom-up crack propagation phase, plotted against temperature and reinforcement position. The data represent the pre-peak region of the force-displacement curves, terminating at structural failure. Samples with reinforcement or emulsion placed at one-third depth required more energy to delay crack propagation compared with those at two-thirds, with geotextile at one-third consistently outperforming other reinforced and unreinforced samples. This superior performance is attributed to earlier crack interception, improved energy absorption, and better use of reinforcement properties due to an optimal stress state.

Additionally, the greater material volume above the reinforcement at one-third enhances load distribution and crack bridging effectiveness. In contrast, reinforcement at two-thirds exhibited reduced effectiveness, as the limited material above it resulted in a more concentrated stress state, later crack interception, and less efficient energy dissipation. Furthermore, high and room temperatures provided the most favorable conditions for geotextile performance, reinforcing its advantage over other reinforcements at both one-third and two-thirds positions. Notably, in unreinforced samples, the position of the emulsion did not influence energy dissipation, as control tests at both depths yielded similar results across different temperature conditions.

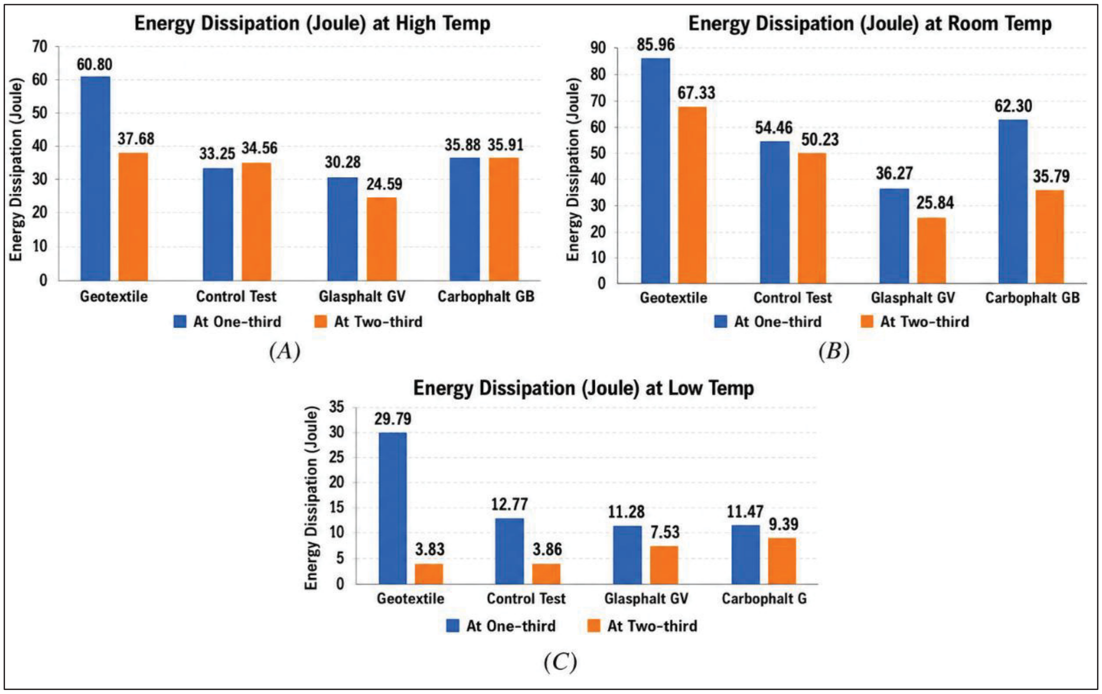

Figure 4.6 Energy dissipation under different temperatures and positions of reinforcement for reinforced and unreinforced samples: (A) high temperature (40°C), (B) room temperature (25°C), and (C) low temperature (-20°C)

4.4.4 Relation between Force and Time

Figure 4.7 presents the time needed for a sample to reach the maximum force under different positions and temperatures for reinforced and unreinforced tests. It is of interest that at high temperature, all the samples with reinforcement or emulsion at one-third need less time to reach the maximum forces compared with those at two-thirds. However, in the case of room temperature, it needs a longer time to reach the maximum forces for the samples with reinforcement or emulsion located at one-third compared with two-thirds. This is due to the fact that at high temperatures, the viscosity of asphalt cement is reduced, leading to a delamination of the reinforced interface and a loss of bituminous coating within the geogrids/geotextile. Consequently, this results in a shorter time to attain maximum force resistance for reinforcements or emulsions located at one-third. When the crack reaches the reinforcement or emulsion layer at one-third, the reinforcement layer with the delamination of interface as well as the bitumen with the loss of viscosity starts to resist the crack and reaches the maximum forces soon.

In the case where the reinforcement is positioned at two-thirds, the structure loses its integrity upon crack development. This loss persists until the crack reaches the reinforcement layer, where it begins mobilizing to counter crack propagation, which results in a longer time for obtaining maximum force. However, the competence of resistance for reinforcement layer is similar to those at one-third above.

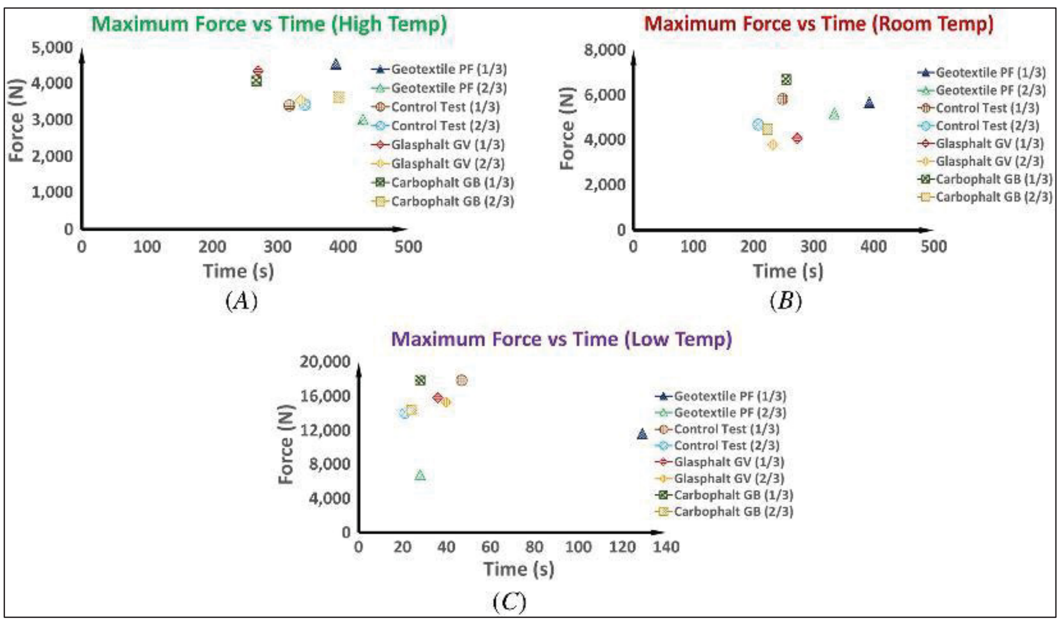

Figure 4.7 Relationship between maximum force and time for reinforced and unreinforced samples: (A) high temperature (40°C), (B) room temperature (25°C), and (C) low temperature (-20°C)

On the other hand, under room temperature conditions, as previously mentioned, reinforcement located at one-third consistently outperformed reinforcement placed at two-thirds in terms of force and displacement. That means when the crack reaches the reinforcement at one-third, the resistance not only comes from the asphalt system with full viscosity but also comes from the reinforcement or emulsion layer, and all together would enhance the resistance time in which it takes more time to reach maximum force before destroying the whole system. All samples under low temperature follow similar behavior to those in room temperature in all the cases in which those reinforcement or emulsion layer at one-third need longer time to reach maximum force compared with those at two-thirds, except in the case of Glasphalt GV; however, the difference is not that much. It should be noted that at low temperatures, the samples become brittle and the reinforcement or emulsion layer at one-third becomes rigid; thus, the whole structure becomes stiffer when combining both constituents and it needs a bit more time to reach the maximum force. In the case of two-thirds, due to the brittleness of the sample, when crack develops, the whole system already failed before reaching the reinforcement or emulsion layer, which means the maximum resistance time is shorter than those at one-third. It is also very interesting that the PF located at one-third shows an exceptional performance to resist the force where it needs a significant time to reach the maximum force compared with all other samples; hence, PF continues to outperform even at low temperatures when the position of reinforcement is at one-third.

When the forces apply, cracks develop slowly in the samples until reaching the maximum force, followed by a faster pace in crack development until the samples completely fail. The speed of crack development can be evaluated based on the duration of time after reaching maximum force until failure as shown in Figure 4.8.

As can be seen at high temperatures, crack develops faster for those reinforcements or emulsions located at two-thirds compared with those at one-third, which means that after reaching the maximum force, the reinforcement or emulsion located at two-thirds cannot resist force as much as those at one-third. Similar behavior was also observed in the case of room temperature except in the case of control test where the emulsion located at one-third shows less resistance against crack after reaching maximum force compared with those at two-thirds; however, the difference was not that much. In general, Glasphalt GV shows least resistance against crack under room and high temperature, whereas PF located at one-third always shows best resistance in all three cases of temperature. Another important thing is that control samples do not show any resistance after reaching maximum force at low temperature in both one-third and two-thirds position of emulsion compared with all other reinforced samples regardless of the position of reinforcement. This is in agreement with the section above.

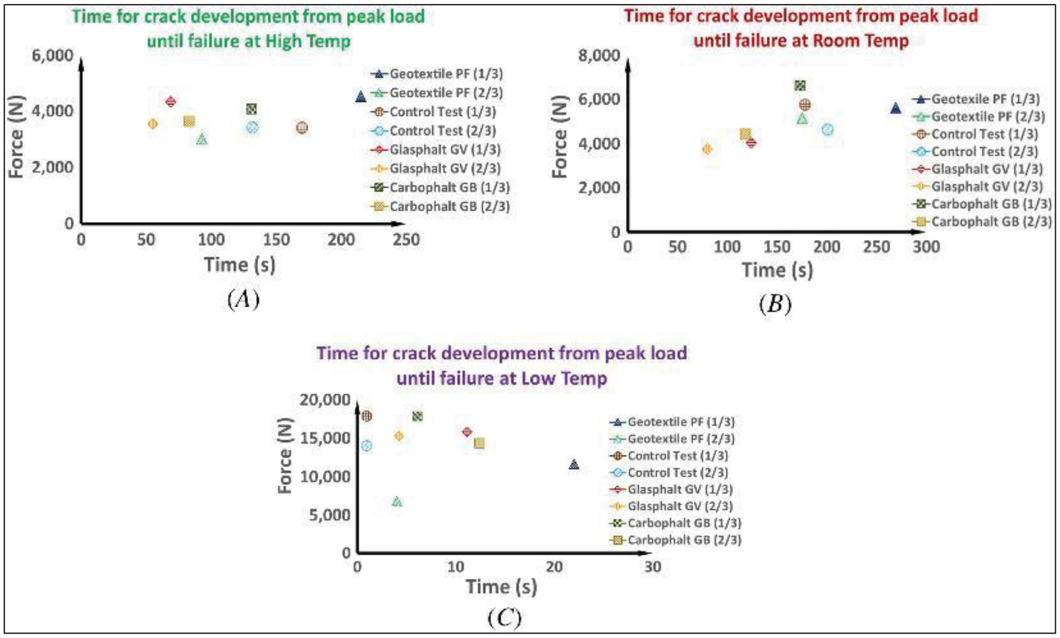

Figure 4.8 Maximum force and time between peak load and failure: (A) high temperature (40°C), (B) room temperature (25°C), and (C) low temperature (−20°C)

4.5 Conclusion

Based on the outcomes of our laboratory investigation, several conclusions can be drawn. Introducing reinforcement generally improved the performance of the pavement system in most cases. The reinforcement interlayers exhibited optimal performance at room temperature, with the exception of GV. Geotextiles showed superior performance compared with other types of reinforcement and unreinforced samples in terms of force and displacement at both one-third and two-thirds positions in most scenarios. Furthermore, reinforcement or emulsion placed at the one-third position consistently outperformed those at the two-thirds position in the majority of cases.

When considering the energy required for cracks to propagate from the bottom to the top surface, samples with reinforcement or emulsion at the one-third position demonstrated superior performance compared with those at the two-thirds position. It is also noteworthy that both high and room temperatures maintained the best performance of geotextiles compared with other types of reinforcements and unreinforced samples at both the one-third and two-thirds positions.

Temperature notably influenced the performance of both reinforced and unreinforced samples, especially when the reinforced interlayer was subjected to critical temperatures. High temperatures (40°C) resulted in delamination of the reinforced interface due to asphalt cement losing viscosity, whereas low temperatures (−20°C) caused brittleness, resulting in interfacial stress condition behavior. At room temperature, all specimens exhibited outstanding performance compared with those at high and low temperatures.

Samples with reinforcement or emulsion at the one-third position required less time to reach maximum forces compared with those at the two-thirds position. Conversely, at room temperature, samples with reinforcement or emulsion at the one-third position required more time to reach maximum forces compared with those at the two-thirds position. However, at high and room temperatures, cracks developed faster for reinforcements or emulsions located at the two-thirds position compared with those at the one-third position.

These findings highlight the need for further experiments to validate these results across varying binder contents, incorporating different geosynthetic materials, and examining the initial modulus of the system against crack development. Especially when using GV, it should be noted to choose appropriate coarse-graded mixtures to investigate the performance of this kind of reinforcement. All together will enable more accurate predictions of reflective cracking onset, particularly within the context of mechanistic-empirical pavement design methodologies.

4.5.1 Optimal Reinforcement Position

The placement of geosynthetics at one-third depth from the bottom of the asphalt overlay consistently outperformed the two-thirds position across all tested temperatures. This superior performance is attributed to earlier crack interception, enhanced stress distribution, and improved load transfer facilitated by the greater volume of asphalt material above the interlayer. Reinforcement at one-third depth demonstrated higher energy dissipation, delayed crack propagation, and prolonged structural integrity compared to two-thirds placement, which exhibited reduced effectiveness due to concentrated stress states and delayed crack interception.

4.5.2 Temperature-Dependent Performance

Geosynthetics exhibited peak performance at room temperature (25°C), where the asphalt binder maintained optimal viscosity for interlayer bonding and stress transfer. At high temperatures (40°C), reduced binder viscosity caused interface delamination, weakening reinforcement effectiveness. At low temperatures (−20°C), material brittleness accelerated crack propagation, though geotextiles (PF) still provided marginal resistance. These findings underscore the critical role of temperature in pavement design and highlight the need for climate-specific interlayer selection.

4.5.3 Geotextile Superiority Over Geogrids

The geotextile (PF), saturated with high-performance asphalt cement, outperformed geogrids (GB and GV) in all scenarios. PF's fabric structure enhanced crack bridging and energy absorption, whereas geo-composite GV underperformed due to poor interlocking from its non-woven fabric layer and single-sided bitumen coating. Carbophalt GB, with dual-sided bitumen coating, showed moderate performance but lagged behind PF. This emphasizes the importance of material composition and interface bonding in reinforcement efficacy.

4.5.4 Unreinforced Samples and Emulsion Limitations

In some cases, unreinforced samples with emulsion matched or exceeded reinforced samples in displacement resistance, particularly at high temperatures. This anomaly arose from delamination in reinforced interfaces, where weakened bonding negated reinforcement benefits. However, at room and low temperatures, geosynthetics consistently outperformed unreinforced systems, validating their role in crack mitigation under moderate conditions.

4.5.5 Implications for Pavement Engineering

The study validates the crack widening device as a practical tool for evaluating reflective cracking resistance. Engineers should prioritize geotextile placement at one-third depth in temperate climates, while avoiding geo-composites like GV in high-stress environments. Future work should expand testing to diverse asphalt mixes, binder types, and additional reinforcement depths (e.g., mid-layer) to refine mechanistic-empirical design models.

Additionally, optimizing interlayer adhesion techniques could address high-temperature delamination challenges, further enhancing pavement durability.

By integrating these findings, pavement rehabilitation strategies can achieve longer service life, reduced maintenance costs, and improved sustainability through targeted use of geosynthetic interlayers.

CHAPTER 5

FRACTURE-ENERGY-BASED ASSESSMENT OF GEOSYNTHETIC INTERLAYERS IN ASPHALT OVERLAYS UNDER VARIABLE TEMPERATURE, DISPLACEMENT RATE, AND PLACEMENT DEPTH

Van Thang Ho[1], Michel Vaillancourt[1], Eshan Dave[2] and Alan Carter[1]

[1] Department of Construction Engineering, École de technologie supérieure,
1100 Notre-Dame Ouest, Montréal, Québec, Canada H3C1K3
[2] Department of Civil and Environmental Engineering, University of New Hampshire,
33 Academic Way, W173 Kingsbury Hall, Durham, NH 03824-2619, USA

Article submitted to the International Journal of Pavement Engineering on June 22, 2026.

Abstract

Reflective cracking causes premature asphalt overlay failure, necessitating effective mitigation. This study evaluates three geosynthetic interlayers - paving fabric (PF), Carbophalt GB geogrid, and Glasphalt GV geocomposite - using a Crack Widening Device at two temperatures (25 °C, 40 °C), two displacement rates (2, 5 mm/min), and three placement depths. Performance was characterised through stiffness indices, energy dissipation, Toughness Improvement Factor (TIF), fracture energy (G_{IC}), interfacial J-integral, and crack-interlayer interaction analysis. PF consistently achieved superior performance with TIF of 1.36-1.54 at 2 mm/min and 1.08-1.21 at 5 mm/min, G_{IC} of 38-40 kJ/m², and highest J-integral values at one-third depth, exhibiting low rate-sensitivity through progressive fibre activation. Glasphalt GV showed dramatic rate sensitivity: poor performance at 2 mm/min (TIF = 0.54-0.57) reversed to excellent results at 5 mm/min (TIF = 1.12-1.29), indicating its glass fibre network requires dynamic loading for activation. Carbophalt GB demonstrated moderate, stable performance (TIF ≈ 1.0). One-third placement enabled earlier crack interception and superior energy dissipation across all materials. Unreinforced controls were stiffer but brittle; reinforced systems traded stiffness for ductility. At 40 °C, reduced viscosity limited force development despite increased deformation capacity. These observations collectively highlight that apparent stiffness alone is insufficient to characterise reflective-cracking resistance. The proposed multi-metric framework - integrating stiffness indices, dissipated energy, TIF, G_{IC},

and interfacial J-integral - provides a mechanistic basis for interpreting the coupled effects of interlayer type, temperature, displacement rate, and placement depth in geosynthetic-reinforced asphalt overlay systems.

5.1 Introduction

Bituminous pavements deteriorate under combined traffic loading and environmental conditions, with cracking being particularly problematic as it compromises pavement integrity and allows water infiltration, accelerating structural damage (Tutumluer et al., 2024; Norambuena-Contreras and Gonzalez-Torre, 2015). Asphalt overlays offer a practical rehabilitation solution, restoring ride quality and extending service life without complete reconstruction (Sobhan and Tandon, 2008; Button and Lytton, 2007). However, cracks in the underlying pavement tend to propagate upward through the overlay - known as reflective cracking - due to stress concentrations at existing crack locations under traffic loads or thermal movements (Amini, 2005; Elseifi and Al-Qadi, 2004). Once these cracks reach the surface, they create pathways for moisture infiltration, leading to accelerated deterioration (Lytton, 1989; Cleveland et al., 2002).

Conventional maintenance strategies such as mill-and-fill operations address surface distresses but fail to eliminate underlying cracks, causing the problem to reappear within a few years and requiring repeated costly interventions (Cleveland et al., 2002; Nithin et al., 2015). To address this limitation, geosynthetic interlayers have emerged as a promising solution (Nithin et al., 2015). Installed between existing cracked pavement and new overlay, these materials absorb and redistribute stresses, slow crack progression, and can redirect crack growth laterally rather than vertically (Steen, 2004; Li et al., 2022; Sudarsanan et al., 2018; Brown et al., 2001).

Different geosynthetic types offer distinct performance characteristics (Guo and Zhang, 1993; Wang et al., 2023). Geogrids provide structural reinforcement through rigid apertures, geotextiles offer flexibility with asphalt saturation for enhanced bonding, and geocomposites combine elements of both. Effectiveness depends on material type, placement depth, interface bonding quality, and environmental conditions (Spadoni et al., 2021; Gonzalez-Torre et al., 2015; Ferrotti et al., 2011; El-Hakim and Tighe, 2014; Saride and Kumar, 2017).

Understanding interlayer behaviour under realistic conditions is essential for effective application (Jaskula and Rys, 2017). Temperature and displacement rate are particularly important variables, as asphalt properties change significantly across service conditions (Cleveland et al., 2002; Jaskula and Rys, 2017).

5.2 Research Background

The application of geosynthetics beneath asphalt overlays to reduce reflective cracking has been extensively studied (Saride and Kumar, 2017; Leiva-Padilla et al., 2016; Moayedi et al., 2009). This rehabilitation approach serves as both stress-relief and reinforcement layer while offering cost savings compared to thicker overlays (Moreno-Navarro and Rubio-Gámez, 2016; Buttlar et al., 2000). However, system effectiveness depends critically on interface conditions (Nithin et al., 2015). The interlayer creates a discontinuity that can affect shear strength and overall performance (Norambuena-Contreras and Gonzalez-Torre, 2015). Geogrids exhibit minimal reduction in shear resistance due to aggregate interlock through apertures, whereas geotextiles show somewhat lower shear resistance (Pasquini et al., 2013). Recent research has examined the influence of tack coats on interlayer shear bond strength (Pasquini et al., 2015; Gharbi et al., 2017; Raab and Partl, 2004). The characterisation of interlayer bonding has benefited from systematic evaluations of shear test devices (Raab et al., 2009), model-material studies of aggregate interlock and shear stiffness (Raab et al., 2012), comprehensive interlaboratory investigations comparing different test procedures across 14 laboratories on 1,400 cores (Canestrari et al., 2012), and long-term field investigations demonstrating that interlayer bond strength generally improves under traffic-induced compaction and settlement but may deteriorate when the pavement develops distress (Raab and Partl, 2008).

Understanding geosynthetic-reinforced pavement behaviour requires integrating field monitoring, computational modelling, and laboratory experiments. Field investigations using Falling Weight Deflectometer testing have demonstrated that conventional backcalculation procedures must be recalibrated to account for interlayer effects (Carret and Carter, 2022). Analogous long-term monitoring of geosynthetic-reinforced soil structures has confirmed measurable settlement reductions (Kazimierowicz-Frankowska and Kulczykowski, 2021), supporting the broader effectiveness of geosynthetic reinforcement. These observations have motivated overlay design frameworks incorporating service life predictions, ranging from empirical methods (Roodi et al., 2025) to fracture-based approaches (Sobhan and Tandon, 2008). Finite element analyses employing cohesive zone formulations have shown that thermal-induced joint movements govern crack patterns in asphalt overlays (Dave and Buttlar, 2010).

Laboratory digital image correlation (DIC) investigations have revealed detailed crack propagation mechanisms in geosynthetic-reinforced systems (Romeo et al., 2014). Recent work combining DIC with scaled trafficking devices demonstrated how reinforcement grids alter both interlayer debonding behaviour and vertical crack-growth patterns under repeated loading (Raab and Arraigada, 2025; Correia et al., 2025). These studies reveal that paving fabrics excel in energy absorption, whereas reinforcement grids primarily enhance stiffness (Zamora-Barraza et al., 2011; Ho et al., 2025). Multiaxial geocomposite effects on fatigue performance and crack propagation delay have also been documented (Virgili et al., 2009). The interaction between reflective crack resistance and interlayer bonding has been systematically examined using accelerated pavement testing, revealing that reinforcement type significantly influences bonding properties (Raab et al., 2017).

Placement depth is critical: positioning geosynthetics at one-third depth significantly reduces crack propagation (Khodaii et al., 2009). Field case studies such as the Texas State Highway 21 project have provided practical installation guidance (Kumar et al., 2023). Ho et al. (2025) demonstrated that one-third placement consistently outperformed two-thirds across all temperature conditions.

Temperature significantly influences performance. Ho et al. (2025) found that all interlayers performed best at 25 °C; at 40 °C, reduced viscosity caused interface delamination, while at -20 °C, brittleness limited deformation and energy absorption (Molenaar, 1983; Dave and Buttlar, 2010). These observations emphasise the need for temperature-resilient solutions in pavement rehabilitation.

5.3 Problem Statement

Despite significant advances in geosynthetic interlayer research, critical gaps remain in understanding their behaviour under varying field conditions. Conventional laboratory test methods such as four-point bending (Gonzalez-Torre et al., 2015; Virgili et al., 2009) and wheel reflective cracking tests (Gallego and Prieto, 2006) require large specimens, complex apparatus, and extended testing durations, hindering systematic parametric studies across multiple variables.

Research on placement depth has generally been limited to discrete comparisons between one-third and two-thirds positions (Gonzalez-Torre et al., 2015), while interface bond strength studies have focused primarily on tack coat optimisation rather than reinforcement positioning (Correia et al., 2024; Correia and Zornberg, 2016). Perhaps more critically, displacement rate effects remain largely unexplored, as most laboratory evaluations employ fixed rates (Kumar and Saride, 2018) without examining sensitivity to the widely varying loading conditions encountered in field pavements.

To address these limitations, Solatiyan et al. (2023) developed a crack widening device (CWD) using compact specimens (80 mm × 80 mm × 80 mm) to evaluate crack propagation resistance. That investigation, focused on validating the CWD method, was performed at a single room temperature (20 ± 1 °C), a single displacement rate (2 mm/min), and with reinforcement at mid-depth only, and used force-displacement and stiffness measures as the only performance indicators. Ho et al. (2025) subsequently applied the CWD method to assess temperature effects across three thermal conditions (-20 °C, 25 °C, 40 °C) with reinforcement positioned at one-third and two-thirds depths; however, the displacement rate was again fixed at 2 mm/min, the intermediate one-half depth was omitted, and a mechanistic fracture-mechanics interpretation was not pursued.

The present study advances this body of work along three axes that have not been jointly examined in previous CWD-based investigations. First, displacement rate is introduced as a primary controlled variable, with each configuration tested at both 2 mm/min and 5 mm/min to quantify the rate sensitivity of each interlayer type. Second, the one-half placement depth is added to the one-third and two-thirds positions used in earlier work, enabling identification of an optimum depth rather than a binary comparison. Third, a three-metric mechanistic framework combining the Toughness Improvement Factor (TIF), the Mode I fracture energy (G_{IC}), and the interfacial J-integral is applied jointly for the first time to geosynthetic-reinforced asphalt overlays evaluated under CWD loading, moving the analysis from product ranking towards interpretation of the underlying fracture and interface mechanisms that govern rate-dependent behaviour.

Accordingly, the objective of this study is not merely to rank interlayer products, but to develop a fracture- and interface-based framework for interpreting how interlayer type, temperature, displacement rate, and placement depth jointly govern crack resistance in asphalt overlay systems. To this end, three geosynthetic interlayers - a paving fabric (PF), Carbophalt GB geogrid, and Glasphalt GV geocomposite - were evaluated using a crack widening device at three placement depths (one-third, one-half, and two-thirds), two temperatures (25 °C and 40 °C), and two displacement rates (2 mm/min and 5 mm/min). By combining stiffness indicators ($K_{0\text{-}4mm}$, $\bar{K}_{10\text{-}30\%}$) with dissipated energy, Toughness Improvement Factor (TIF), fracture energy (G_{IC}), interfacial J-integral, and crack-interlayer interaction metrics, this study aims to clarify the mechanical trade-offs between stiffness, ductility, crack interception, and post-peak resistance in geosynthetic-reinforced asphalt systems.

5.4 Methodology

This study systematically evaluated crack resistance of geosynthetic-reinforced bituminous specimens using a Crack Widening Device, examining three interlayer types across multiple placement depths, temperatures, and displacement rates with energy-based fracture parameters to provide mechanistic insight into reflective crack mitigation. The experimental programme examined the following variables: (i) three placement depths (one-third, one-half, and two-thirds from the specimen bottom), (ii) two test temperatures (25 °C and 40 °C), and (iii) two displacement rates (2 mm/min and 5 mm/min). Force-displacement curves were recorded throughout each test, from which stiffness indices ($K_{0\text{-}4mm}$ and $\bar{K}_{10\text{-}30\%}$), Toughness Improvement Factor (TIF), fracture energy (G_{IC}), and J-integral values were extracted.

5.4.1 Materials

Laboratory-made bilayer bituminous specimens (80 mm × 80 mm × 80 mm) were prepared using ESG-10 hot mix asphalt with PG 64E-28 asphalt binder for both the top and bottom layers. The same mixture was intentionally used for both layers rather than the conventional ESG-10 over GB-20 configuration specified in Quebec standards. This design choice isolates the geosynthetic interlayer effect by eliminating confounding variables such as stiffness mismatch and differential thermal contraction between dissimilar mixtures. By maintaining identical material properties above and below the reinforcement, observed differences in crack resistance can be attributed directly to the interlayer system. This homogeneous configuration also better represents rehabilitation scenarios where the existing aged pavement may differ substantially from fresh mixture specifications. Three geosynthetics, a geotextile (paving fabric, PF), a geogrid (Carbophalt GB), and a geocomposite (Glasphalt GV), were evaluated alongside unreinforced controls. The PF is a needle-punched nonwoven fabric saturated with PG 64-34 asphalt binder, while the GB is a glass-carbon geogrid with bitumen coating on both sides, and the GV is a fiberglass geocomposite featuring bitumen coating on one side and a fabric layer on the bottom. Specimen preparation followed manufacturer recommendations and established laboratory procedures. Unreinforced control specimens with CSS-1H cationic asphalt emulsion tack coat only were also prepared for comparison. The mechanical properties of all materials are detailed in Tables 5.1-5.3.

Table 5.1 The specifications of Hot Mix Asphalt

Specification		Value
Mixture		ESG-10[1]
Asphalt Binder Grade		PG 64E-28
Binder Content (% mass)		5.45
Water Sensitivity (LC 26-001) (%)	Measured	97.3
	Required	≥70
Rutting Test (LC 26-410) (%)	Measured	After 1,000 = 6.6; After 3,000 = 8.2
	Required	After 1,000 ≤10; After 3,000 ≤15

[1]ESG-10= a mix for the surface course and binder course with a maximum aggregate size of 10 mm

Table 5.2 The mechanical properties of paving fabric (PF) (supplied by the company)

Specification	Test Method	Unit	Value
Grab tensile elongation	CAN/CGSB-148.1 No. 7.3	%	45-105
Grab tensile strength	CAN/CGSB-148.1 No. 7.3	N	550
Mullen burst	CAN/CGSB-4.2 No. 11.1	kPa	1,585
Bitumen retention	ASTM D6140	L/m²	1.15

Note: ASTM D6140, Standard Test Method to Determine Asphalt Retention of Paving Fabrics Used in Asphalt Paving for Full-Width Applications

Table 5.3 The mechanical properties of geosynthetics

Name	Name in Abbreviation	Type/ Transversal Strength, kN	Type/Longitudinal Strength, kN	Covered Layer	Elongation		Mesh Size (Square Shape), mm
					Transversal Direction	Longitudinal Direction	
Carbophalt G120/200	GB	Glass fibres/120	Carbon fibres/200	Plastic foil	<3%	<1.5%	20
Glasphalt GV 120/120	GV	Glass fibres/120	Glass fibres/120	Non-woven	<3%	<3%	20

5.4.2 Specimen Preparation

All slabs were constructed in the laboratory with dimensions of 500 mm × 180 mm × 100 mm following geosynthetic manufacturer recommendations. The bottom slab layer was formed and compacted using a French roller compactor in accordance with LC 26-410 (MTQ standards), then cured at room temperature for 48 hours. Three installation methods were applied depending on interlayer type.

To investigate placement depth, the interlayer (or tack coat for the control) was installed at three interface heights measured from the specimen bottom: one-third (≈27 mm), one-half (≈40 mm), and two-thirds (≈53 mm) of the 80 mm specimen height. These interface locations were achieved by compacting the bottom ESG-10 layer to the target thickness prior to interlayer installation, then compacting the remaining thickness as the top layer.

For unreinforced slabs and GB grid-reinforced slabs, CSS-1H cationic asphalt emulsion was applied at 0.18 L/m² residual bitumen. After three hours drying, the reinforcement grid was placed and a controlled blow torch was used to lightly melt the bitumen within the grid while maintaining 10 cm distance for even heating. For geocomposite reinforcement, emulsion was applied at 0.26 L/m² without wait time or blow torch treatment. For paving fabric installation, heated bitumen at 168 °C was applied at 0.11 L/m², and the pre-cut geotextile was immediately placed onto the slab.

After interlayer installation, a top ESG-10 layer was compacted at 135 °C. From each slab, 80 mm × 80 mm × 80 mm specimens were carefully cut with all edges trimmed to prevent edge effects (Figure 5.1). Before testing, specimen surfaces were polished with sandpaper to achieve a smooth finish ensuring full contact with the loading plate and testing apparatus base. Each geogrid structure incorporated at least three open apertures following Romeo et al. (2014) to ensure reliable crack resistance assessment.

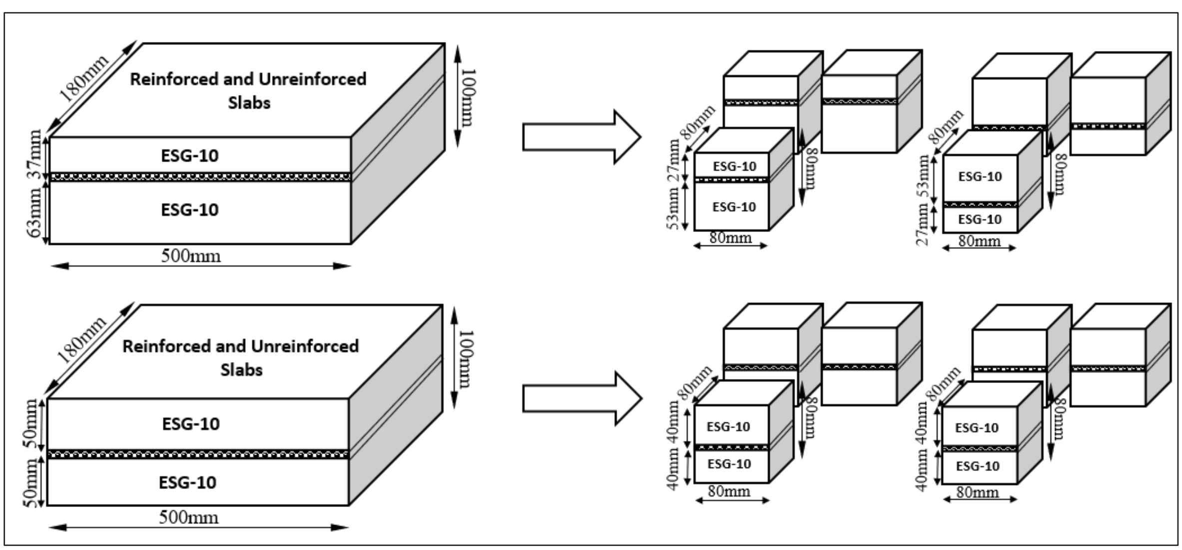

Figure 5.1 Schematic of shape, size, and dimensions of specimens

5.4.3 Test Setup

A laboratory-designed crack performance testing device was used to evaluate crack propagation in bituminous specimens (Figure 5.2). The setup consists of two inclined sliding components engaging a pre-cut notch in the specimen, inducing controlled crack initiation and upward propagation towards the surface under displacement-controlled loading. A preset compressive force of up to 100N was applied using an MTS servo-hydraulic system prior to testing.

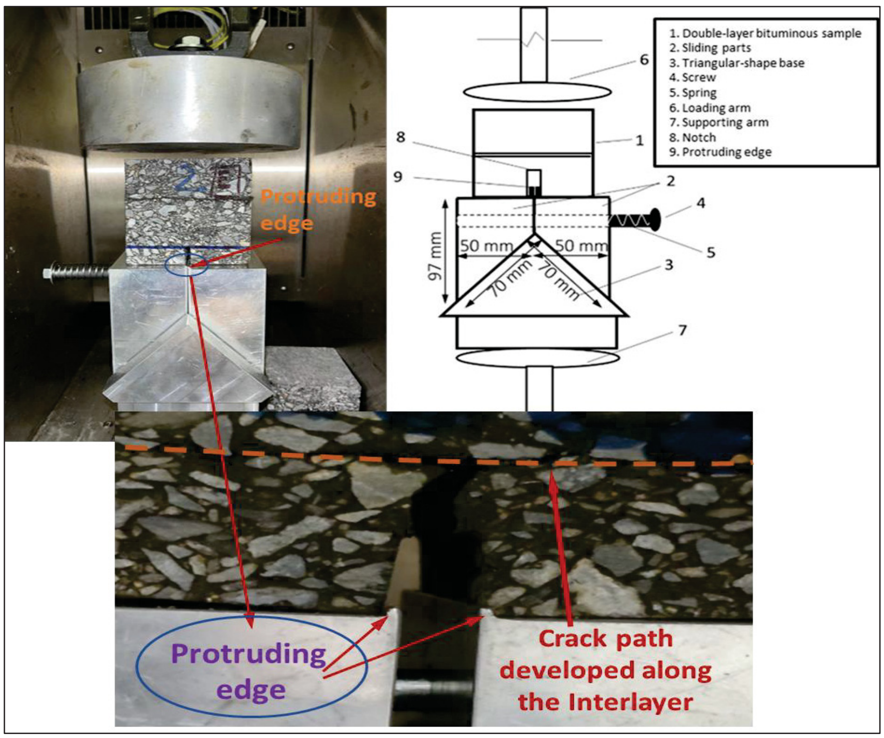

Figure 5.2 Sketch of the crack widening apparatus with detail components

It should be noted that the contact between the asphalt specimen and the two triangular pieces is intentionally unbonded. No adhesive or tack coat was applied at this interface; the boundary condition is a dry contact that transmits compressive reactions while allowing relative sliding. This avoids shear locking at the supports and prevents an artificial increase in the measured fracture response due to unintended shear transfer. As highlighted in Figure 5.2 (photo and close-up view), the protruding edge of the triangular piece locally concentrates tensile opening near the notch and promotes a splitting-type crack initiation; the crack may then develop along the interlayer plane, consistent with the intended reflective-cracking mechanism captured by the test.

Specimens were notched (6 mm wide, 15 mm deep) on the bottom face to initiate a crack that propagates upward towards the specimen surface, consistent with a reflective-cracking mechanism. Tests were conducted at 25 ± 2 °C and 40 ± 2 °C after four hours of thermal conditioning. Reinforcement (or tack coat in control specimens) was placed at one-third, one-half, or two-thirds of the specimen depth from the bottom, and displacement rates of 2 mm/min and 5 mm/min were applied (Figure 5.3).

a) At One-third from the bottom

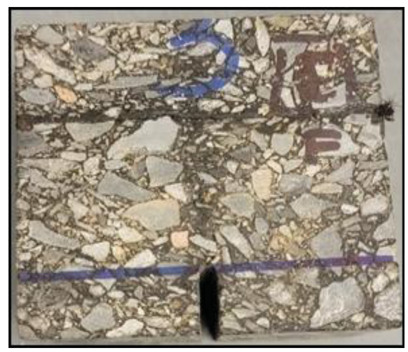

b) At Two-thirds from the bottom

c) At One-half from the bottom

Figure 5.3 Placement depth of reinforcement/emulsion within the specimens.

5.4.4 Data Analysis

For each specimen, the test records actuator displacement u_i (mm) and applied force F_i (N) at discrete sampling points. Several performance parameters were extracted from these force-displacement records to characterise crack resistance behaviour.

Two stiffness indicators were derived using least-squares regression. The initial stiffness $K_{0\text{-}4mm}$ was obtained from all data points with $0 \leq u_i \leq 4$ mm, capturing the quasi-linear response before the interlayer is fully mobilised. The working-range stiffness $\bar{K}_{10\text{-}30\%}$ was defined as the arithmetic mean of the secant stiffnesses evaluated where the force reaches 10%, 20%, and 30% of the peak force on the ascending branch of the force-displacement curve, reflecting the effective early-loading stiffness of the system.

Energy dissipation was calculated as the total area under the force-displacement curve using trapezoidal integration: $\Sigma\Delta E = \Sigma((y_i + y_{i+1})/2) \times \Delta x$, where y_i represents consecutive force values and Δx is the displacement increment. The Toughness Improvement Factor (TIF) was computed as TIF = $U_{reinforced}/U_{control}$, quantifying reinforcement effectiveness relative to unreinforced specimens under identical conditions. Values greater than 1 indicate improved toughness; values below 1 signify reduced performance.

Fracture energy ($G_{IC} = W/A$) was determined as the energy required to propagate a crack per unit area of fracture surface, where W is the absorbed energy and A is the ligament area. The interfacial J-integral ($J_{inter} = W_{int}/A_{lig}$) characterises the mechanical work required for crack propagation from the notch root to the target interface, normalised by the fracture area created across the ligament.

The time to interlayer ($T_{interlayer}$) represents the elapsed time from loading initiation until the crack first reaches the reinforcement plane. To identify this moment, raw force histories were smoothed using an 11-point centred moving average to remove high-frequency noise while preserving critical features. The force derivative was computed via central difference method, and the first peak was identified when the derivative transitioned from positive to negative for at least seven consecutive points, ensuring genuine peak detection rather than spurious fluctuations.

5.5 Results and Discussion

This section presents the mechanical response of reinforced and unreinforced bituminous specimens tested using the Crack Widening Device. Building upon our previous investigations (Ho et al., 2025) that established temperature effects at a single displacement rate, the present analysis explicitly examines the interaction between displacement rate, temperature, and interlayer placement depth. Replicate specimens were tested for each configuration, and the response patterns discussed below are based on the valid tests retained for analysis. Where replicate behaviour was consistent, mean curves and summary values were used to represent the configuration. The findings are interpreted comparatively within the limits of the present laboratory matrix, specimen geometry, and experimental repeatability.

5.5.1 Stiffness Analysis Framework

Force-displacement responses were obtained at 40 °C and 25 °C under displacement rates of 5 mm/min and 2 mm/min, with interlayers placed at one-third and two-thirds from the specimen bottom. Results at -20 °C were excluded due to brittle behaviour and absence of measurable post-peak resistance in control samples (Ho et al., 2025). Four interface configurations were evaluated: CSS-1H tack coat only (control), and three reinforced systems with Geotextile PF, Glasphalt GV, or Carbophalt GB.

For each specimen, the test provides a discrete record of actuator displacement u_{ii} (mm) and applied force F_i (N) at sampling points i = 1, ..., n within the displacement interval of interest. The local tangent stiffness K (in N/mm) is defined as the slope of the best-fit linear regression of force versus displacement over a specified displacement interval:

$$K = \frac{\sum_{i=1}^{n}(u_i - \bar{u})(F_i - \bar{F})}{\sum_{i=1}^{n}(u_i - \bar{u})^2} \tag{5.1}$$

In this expression, the numerator is the covariance between displacement and force in the selected interval, the denominator is the variance of displacement, and their ratio gives the slope of the regression line that best represents the local force-displacement trend.

Two stiffness indicators are derived from Eq. (5.1). The initial stiffness $K_{0\text{-}4mm}$ is calculated from data within the displacement range 0-4 mm, capturing the quasi-linear response associated with crack initiation before full interlayer mobilisation. To characterise the effective early-loading stiffness, secant stiffness values are evaluated where the force reaches 10%, 20%, and 30% of the peak force on the ascending branch, and their arithmetic mean is reported as $\bar{K}_{10\text{-}30\%}$ (Eq. 5.2).

$$\bar{K}_{10-30\%} = \frac{K_{10} + K_{20} + K_{30}}{3} \tag{5.2}$$

The use of two stiffness indices allows separation of the early elastic-dominated response from the post-initiation behaviour governed by crack-interlayer interaction. This distinction is essential because higher stiffness does not necessarily imply improved resistance to reflective cracking.

5.5.1.1 Effect of Temperature on Stiffness Response

Stiffness response at 40°C

At 40 °C, the initial stiffness $K_{0\text{-}4mm}$ shows no consistent ranking among the systems (Figs. 5.4b, 4e, 4h, 4k): the stiffest system differs from one condition to another, with no systematic difference between reinforced and control specimens. This is expected, as the crack has not yet intersected the interlayer, so the early response is dominated by the softened asphalt and CSS-1H bond rather than the reinforcement. Differences emerge in $\bar{K}_{10\text{-}30\%}$: the control records the highest value only at one-third depth under the faster rate (Figure 5.4c), but this reflects localised crack opening producing steep, short-lived load response followed by abrupt failure. Reinforced specimens show lower $\bar{K}_{10\text{-}30\%}$ but allow distributed slip along the interlayer, displaying broader plateaus and gradual post-peak decay. At 40 °C, reinforcement primarily improves ductility rather than stiffness.

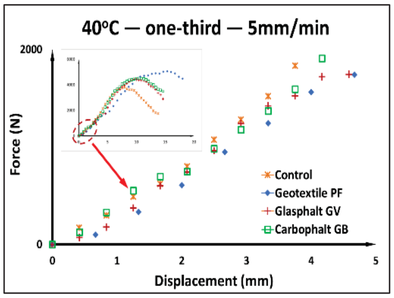

a) One-third depth, 5 mm/min

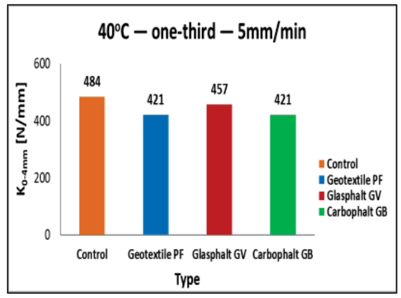

b) Initial $K_{0\text{-}4mm}$

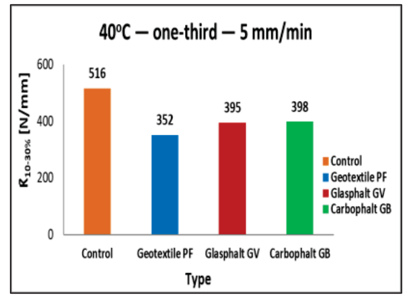

c) Average Initial $\bar{K}_{10\text{-}30\ \%}$

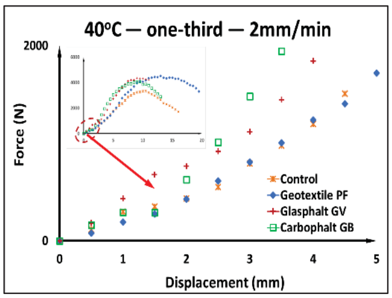

d) One-third depth, 2 mm/min

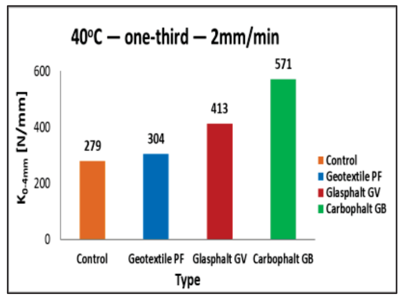

e) Initial $K_{0\text{-}4mm}$

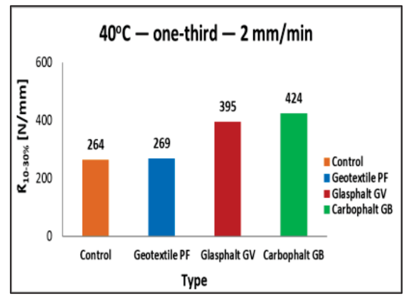

f) Average Initial $\bar{K}_{10\text{-}30\ \%}$

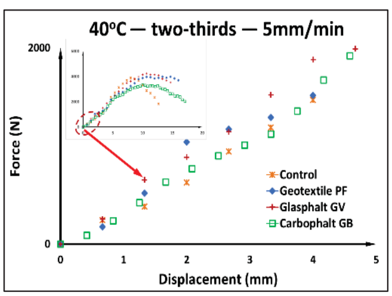

g) Two-thirds depth, 5 mm/min

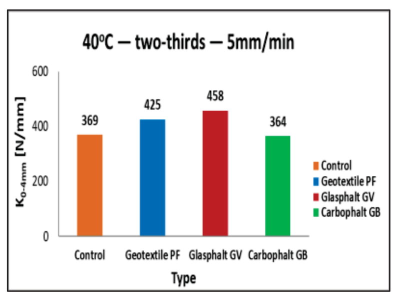

h) Initial $K_{0\text{-}4mm}$

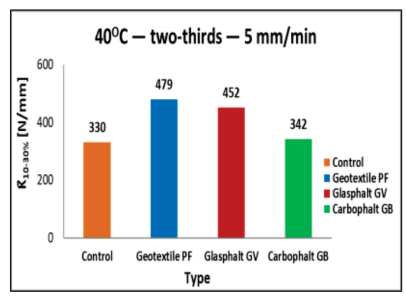

i) Average Initial $\bar{K}_{10\text{-}30\ \%}$

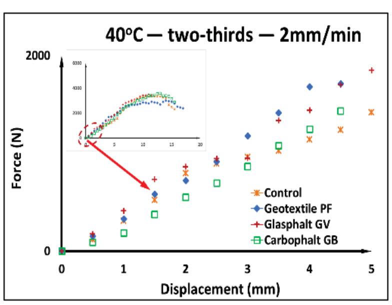

j) Two-thirds depth, 2 mm/min

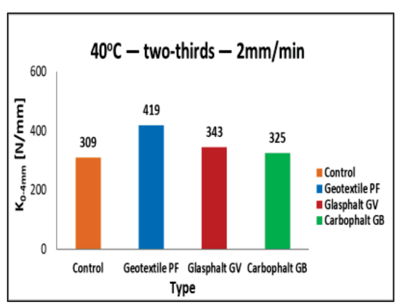

k) Initial $K_{0\text{-}4mm}$

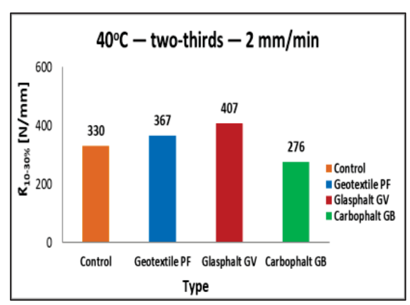

l) Average Initial $\bar{K}_{10\text{-}30\ \%}$

Figure 5.4 Initial and working-range stiffness parameters at 40 °C for one-third and two-thirds placement depths under displacement rates of 5 and 2 mm/min

Stiffness response at 25°C

At room temperature, control specimens achieve generally higher $K_{0\text{-}4mm}$ and $\bar{K}_{10\text{-}30\%}$ than reinforced systems (Figs. 5.5b, 5.5e, 5.5h, 5.5k and 5.5c, 5.5f, 5.5i, 5.5l). Inserting a geosynthetic introduces a compliant membrane and slip plane within the rigid assembly, reducing apparent stiffness. However, control specimens lose capacity rapidly after peak load - a brittle failure signature - whereas reinforced specimens maintain force over wider displacement windows with progressive crack bridging. The high stiffness of the control thus indicates a stiffer but less damage-tolerant system. The stiffness contrast between control and reinforced systems is more pronounced at 25 °C than at 40 °C.

5.5.1.2 Effect of Displacement Rate on Stiffness Response

Two displacement rates (2 mm/min and 5 mm/min) were evaluated - an aspect not addressed in previous work. Increasing the displacement rate from 2 to 5 mm/min generally increased peak force, reflecting asphalt's viscoelastic nature: faster loading reduces time for stress relaxation, resulting in higher apparent stiffness and strength.

Material-specific rate sensitivity varied considerably. Glasphalt GV exhibited dramatic dependence: at 2 mm/min, it performed poorly with reduced post-peak load retention; whereas at 5 mm/min, it demonstrated substantially improved performance with extended load-bearing capacity. This reversal suggests Glasphalt GV's reinforcement mechanism requires dynamic loading to activate effectively. In contrast, Geotextile PF demonstrated consistent performance across both rates, with the asphalt-saturated fabric engaging progressively through distributed fibre stretching regardless of displacement rate. Carbophalt GB showed intermediate rate sensitivity. These findings have practical implications for material selection: for applications dominated by slow, repeated loading (urban intersections, bus stops, low-speed roadways), Geotextile PF offers the most reliable performance. Glasphalt GV may be suitable for high-speed highways involving dynamic loading, but its poor slow-loading performance represents a significant limitation. The low rate-sensitivity of Geotextile PF makes it the more robust choice across the range of loading conditions encountered in typical pavement applications.

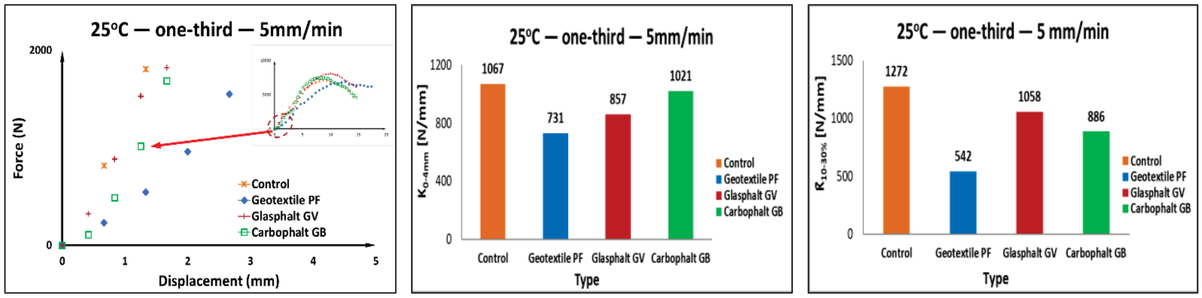

a) One-third depth, 5 mm/min b) Initial $K_{0\text{-}4\ mm}$ c) Average $\bar{K}_{10\text{-}30\%}$

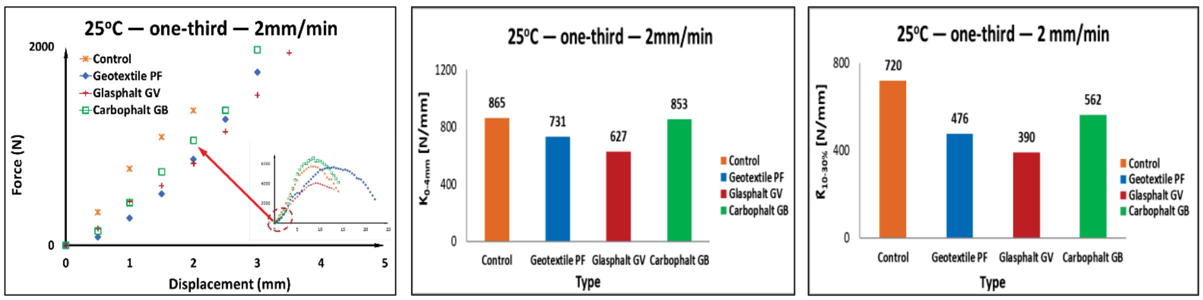

d) One-third depth, 2 mm/min e) Initial $K_{0\text{-}4\ mm}$ f) Average $\bar{K}_{10\text{-}30\%}$

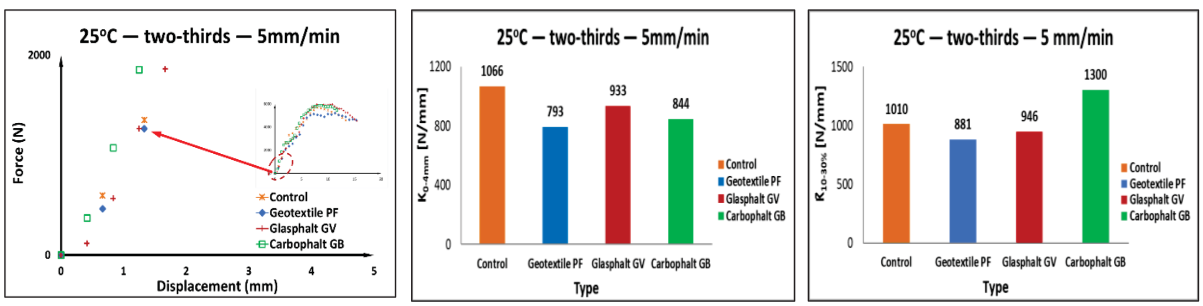

g) Two-thirds depth, 5 mm/min h) Initial $K_{0\text{-}4\ mm}$ i) Average $\bar{K}_{10\text{-}30\%}$

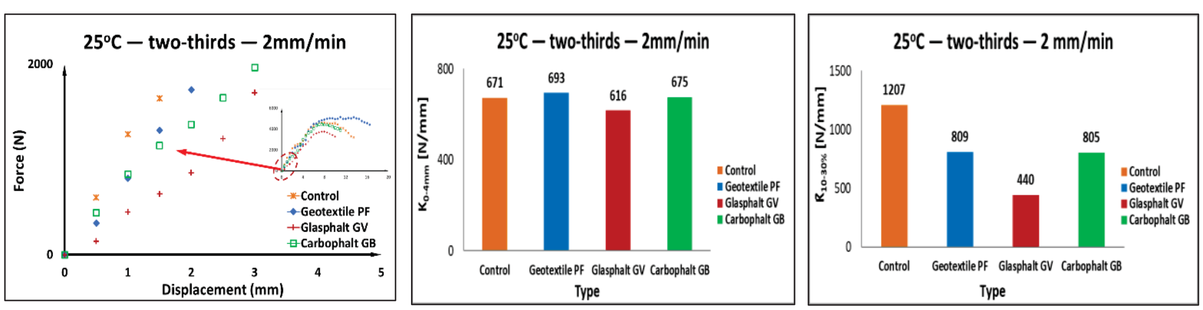

j) Two-thirds depth, 2 mm/min k) Initial $K_{0\text{-}4\ mm}$ l) Average $\bar{K}_{10\text{-}30\%}$

Figure 5.5 Initial and working-range stiffness parameters at 25 °C for one-third and two-thirds placement depths under displacement rates of 5 and 2 mm/min

5.5.1.3 Effect of Placement Depth

Interlayer placement at one-third versus two-thirds from the bottom was evaluated to match and extend the configurations used by Ho et al. (2025). At one-third depth, the propagating crack encounters reinforcement early, enabling effective bridging and stress redistribution before significant upper-layer damage accumulates. Force-displacement curves consistently show broader post-peak plateaus and extended load-bearing capacity. The greater asphalt volume above the reinforcement at this position supports system stability, enabling specimens to withstand larger deformations before ultimate failure.

At two-thirds depth, the crack propagates through larger unreinforced volume before reaching the interlayer, delaying mobilisation and reducing effectiveness. Specimens display shorter post-peak plateaus and steeper load decline compared to one-third placement. The reduced material volume above the reinforcement and delayed activation promote stress concentration and greater tendency for brittle fracture once the crack breaches the interlayer. These results confirm that one-third placement consistently outperforms two-thirds placement regardless of temperature or displacement rate, reinforcing the practical recommendation to position geosynthetics closer to the crack initiation zone.

The observed trade-off between local interlayer bond strength and global crack resistance aligns with findings from accelerated pavement testing conducted at Empa, where Raab et al. (2017) combined two complementary methods: a Layer-Parallel Direct Shear (LPDS) test for interlayer bond strength and a Model Mobile Load Simulator (MMLS3) for reflective crack propagation. The LPDS measurements indicated that geosynthetic insertion reduced field-core bond strength by approximately 30 to 60 per cent relative to the unreinforced asphalt-asphalt reference, while still satisfying the Swiss minimum requirement of 15 kN. Despite this local bond reduction, the same reinforcement systems applied to slabs substantially extended the number of MMLS3 load cycles to failure: glass-carbon and polyester grids reached on average 950,000 and 680,000 cycles respectively, compared to 370,000 cycles for the unreinforced reference, representing improvements of approximately 2.6 and 1.8 times, whereas one system using a SAMI installation underperformed and is excluded from this generalisation. The present study's observation that control specimens achieve higher stiffness but fail in a more brittle manner is consistent with this body of work: the Empa studies similarly found that unreinforced specimens displayed higher initial shear strength values but experienced more rapid crack propagation once failure initiated. This convergence of findings across different testing methodologies (Crack Widening Device versus accelerated traffic simulation) strengthens the conclusion that energy dissipation capacity, rather than peak stiffness, governs geosynthetic interlayer effectiveness.

5.5.1.4 Summary of Stiffness Analysis

The analysis of $K_{0\text{-}4mm}$ and $\bar{K}_{10\text{-}30\%}$ reveals that high stiffness does not translate into better crack resistance. The control system is stiffer yet more brittle, whereas reinforced systems trade stiffness for improved ductility - precisely the objective of geosynthetic interlayers. One-third placement mobilises the interlayer earlier and yields more pronounced post-peak benefits than two-thirds configuration. displacement rate introduces additional complexity, with Glasphalt GV showing dramatic rate sensitivity while Geotextile PF maintains consistent behaviour. The energy-based parameters presented in following sections provide additional insight into these relationships.

It is worth noting that the present finding - control specimens exhibiting higher $K_{0\text{-}4\ mm}$ than reinforced systems - appears to contrast with Solatiyan et al. (2023), who reported 2-2.5 times higher initial stiffness in reinforced bilayers. This apparent discrepancy arises from two key differences. First, the present study uses a homogeneous ESG-10/ESG-10 configuration, whereas Solatiyan et al. (2023) employed dissimilar bilayers (ESG-10/ESG-14 and ESG-14/GB-20) where the unreinforced control already contained a weak emulsion-bonded interface between two different mixtures, suppressing its apparent initial stiffness. Second, the stiffness indices defined here ($K_{0\text{-}4\ mm}$ via least-squares regression over a fixed 4 mm window) capture both the pre- and early post-mobilisation response, whereas Solatiyan et al. (2023) reported a tangent modulus at the very onset of loading. When the control eliminates the material-mismatch interface, the geosynthetic insertion clearly introduces a compliant slip plane, and the trade-off between stiffness and ductility becomes evident. Both studies therefore remain consistent in their core conclusion that energy dissipation, not stiffness, governs reinforcement effectiveness.

5.5.2 Effect of Displacement Rate on Force-Displacement Response

The effect of displacement rate on crack propagation is further illustrated by the force-displacement responses obtained at 2 mm/min and 5 mm/min (Figure 5.6).

At 40 °C (Figs. 5.6a, 5.6c, 5.6e, 5.6g), Geotextile PF exhibits higher peak forces at 5 mm/min than at 2 mm/min, accompanied by reduced displacement capacity, indicating a stiffer but less ductile response. Control specimens show nearly identical peak forces at both displacement rates, with only minor differences in deformation, reflecting the largely rate-insensitive and brittle behaviour of the CSS-1H bond at elevated temperature. Glasphalt GV displays limited gains in peak resistance with increasing displacement rate but greater displacement capacity at 5 mm/min; a notably lower failure force at 2 mm/min for the two-thirds position confirms its strong rate sensitivity under slow loading. Carbophalt GB shows minimal differences between displacement rates, indicating limited rate dependence at 40 °C.

At 25 °C (Figs. 5.6b, 5.6d, 5.6f, 5.6h), the displacement-rate effect is more pronounced than at 40 °C, consistent with the higher stiffness of the asphalt matrix, although its magnitude varies considerably between materials, with peak forces at 5 mm/min ranging from comparable to those at 2 mm/min up to roughly twice as high. Glasphalt GV shows the strongest rate sensitivity, with force-displacement curves confirming limited reinforcement mobilisation at slow displacement rates. Geotextile PF exhibits more proportional increases in both peak force and displacement capacity, indicating a more stable response across displacement rates. Overall, the results demonstrate that displacement rate affects both resistance and deformation capacity, with material-specific implications for reflective cracking performance.

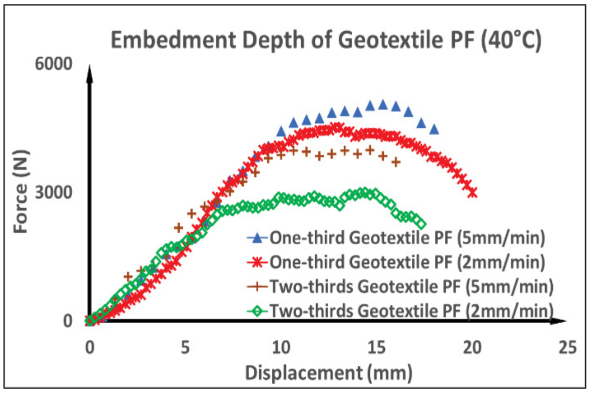

a) Performance of Geotextile PF under 40°C

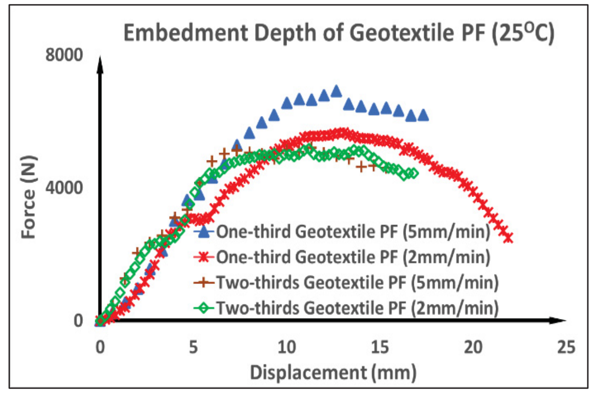

b) Performance of Geotextile PF under 25°C

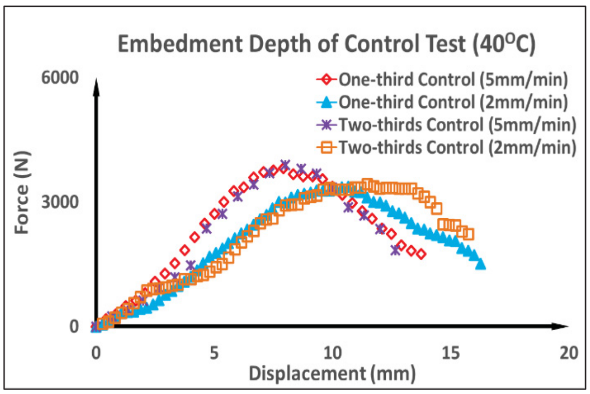

c) Performance of Control test under 40°C

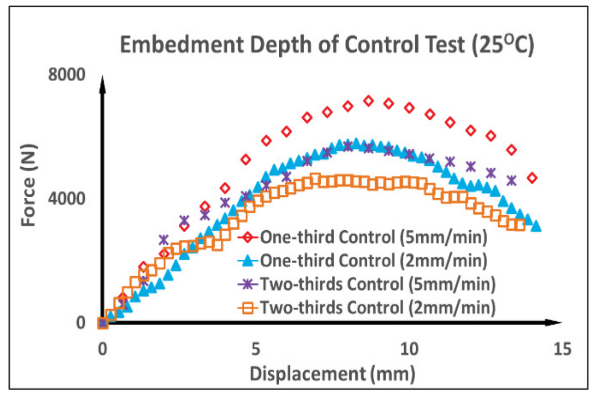

d) Performance of Control test under 25°C

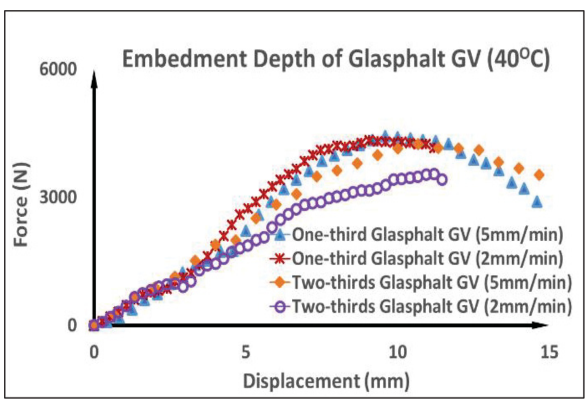

e) Performance of Glasphalt GV under 40°C

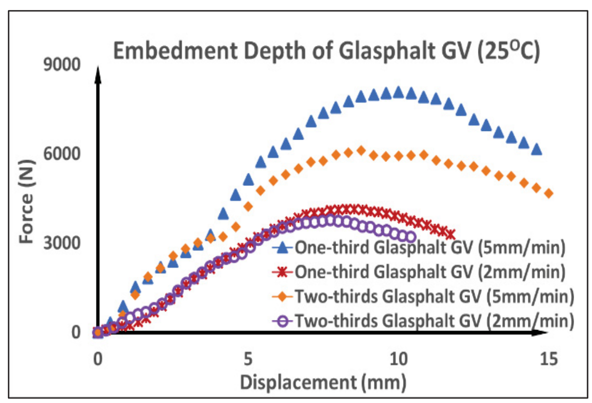

f) Performance of Glasphalt GV under 25°C

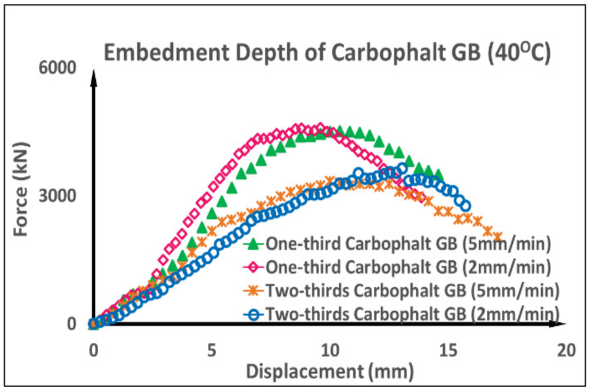

g) Performance of Carbophalt GB under 40^{o}C

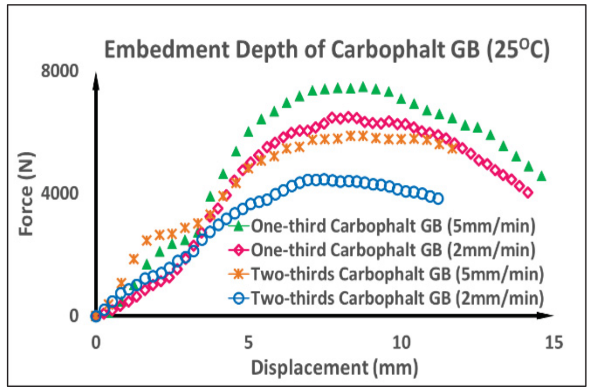

h) Performance of Carbophalt GB under 25^{o}C

Figure 5.6 Effect of displacement rate on the force-displacement response of Geotextile PF, Control test, Glasphalt GV and Carbophalt GB at one-third and two-thirds embedment depths under 25 °C and 40 °C.

5.5.3 Optimum Placement Depth for Reinforcement in Asphalt Systems

The previous sections demonstrated optimal performance at room temperature and a strong dependence on displacement rate; therefore, the influence of interlayer placement depth was evaluated by positioning reinforcements or emulsion at one-third, one-half, and two-thirds of the overlay depth and testing at 25 °C under displacement rates of 5 and 2 mm/min (Figure 5.7).

Across all materials, placement at one-third depth consistently provided the highest crack resistance, as the propagating crack intercepted the interlayer at an early stage, enabling effective stress redistribution, enhanced crack-bridging action, broader post-peak plateaus, and delayed failure. For Geotextile PF, the one-third position achieved the highest peak force and displacement capacity at both displacement rates, while placements farther from the crack initiation zone exhibited reduced resistance and earlier post-peak degradation.

Control specimens with CSS-1H tack coat alone showed a similar depth effect but failed in a brittle manner with rapid post-peak load reduction. Glasphalt GV displayed pronounced sensitivity to both placement depth and displacement rate: the one-third position maximised peak force and displacement capacity at 5 mm/min, whereas slower loading substantially reduced peak forces for all depths, particularly at two-thirds depth, indicating delayed and limited reinforcement mobilisation. In contrast, Carbophalt GB exhibited relatively uniform behaviour across placement depths and displacement rates, with only minor post-peak advantages for one-third placement. At two-thirds depth, the crack propagated through a larger unreinforced asphalt volume before engaging the interlayer, delaying mobilisation and reducing effectiveness. Overall, the results confirm that proximity to the crack initiation zone is the dominant factor governing interlayer effectiveness, while material-specific sensitivity to placement depth and displacement rate controls the magnitude and stability of the reinforcement response.

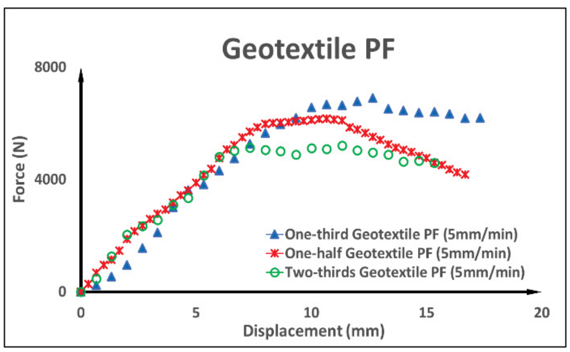

a) At 5 mm/min

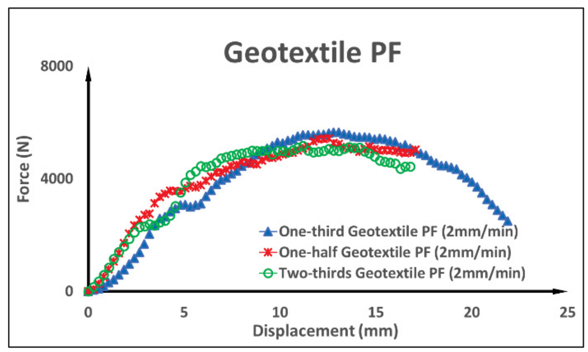

b) At 2 mm/min

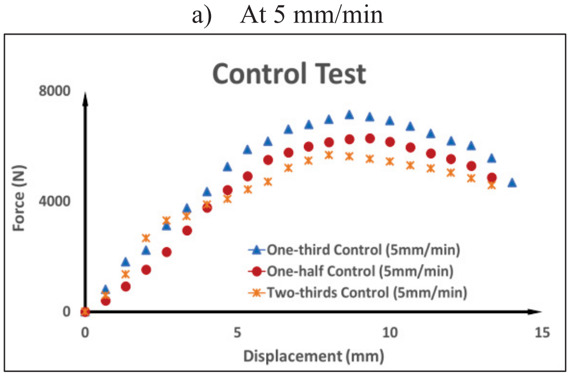

c) At 5 mm/min

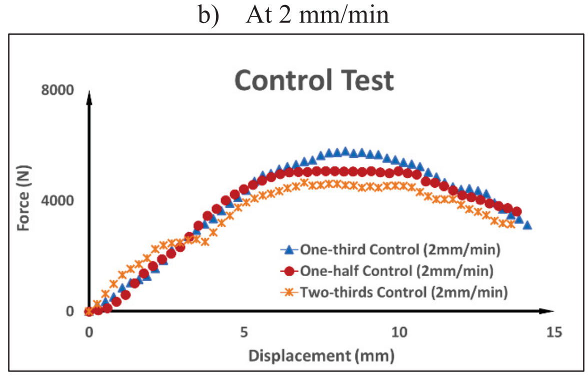

d) At 2 mm/min

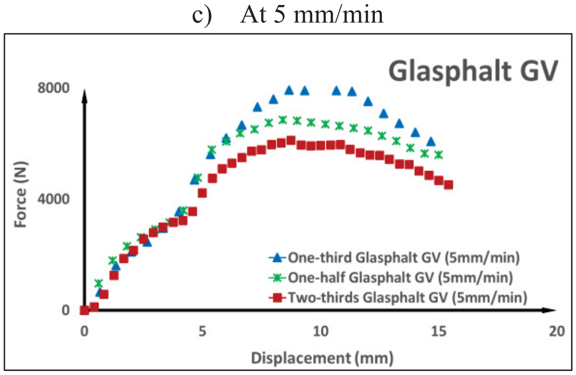

e) At 5 mm/min

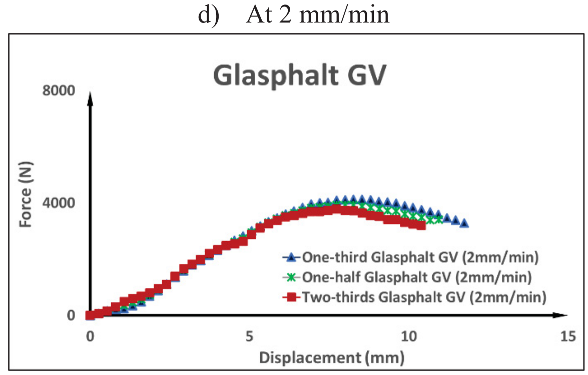

f) At 2 mm/min

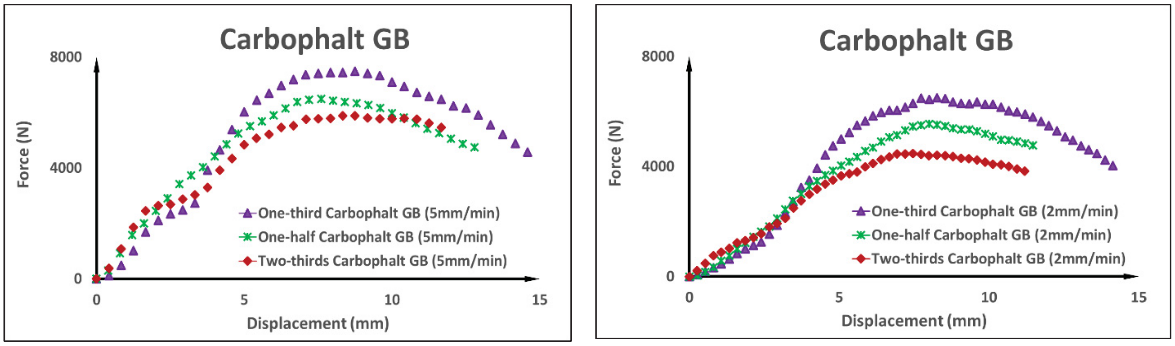

g) At 5 mm/min

h) At 2 mm/min

Figure 5.7 Force-displacement response of Geotextile PF, Control, Glassphalt GV, and Carbophalt GB at one-third, one-half, and two-thirds placement depths at 25°C under displacement rates of 5 and 2 mm/min.

5.5.4 Energy Dissipation

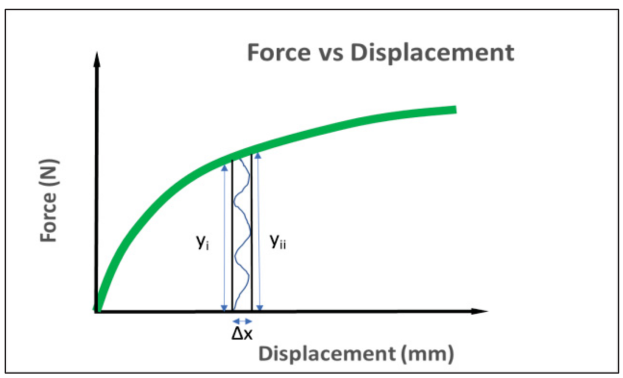

Figure 5.8 Calculation for energy dissipation

The Complementing stiffness and force-displacement-based assessments, crack propagation energy was used to quantify the capacity of each interlayer system to absorb mechanical work during fracture. The energy was calculated as the total area under the force-displacement curve (Figure 5.8) using the trapezoidal rule (Eq. 5.3):

$$\sum \Delta E = \left(\frac{y_{ii} + y_i}{2}\right) * \Delta x \tag{5.3}$$

where y_i and y_{ii} represent consecutive force values and Δx is the displacement increment. This cumulative energy (in Joules) reflects the total mechanical work absorbed by the specimen from crack initiation to complete failure. Figure 5.9 presents the energy dissipation results for all tests during bottom-up crack propagation, comparing two displacement rates (5 mm/min and 2 mm/min) and three reinforcement positions at room temperature.

Energy dissipation at 5 mm/min (Figure 5.9a). At the higher displacement rate, specimens with reinforcement or emulsion placed at one-third from the bottom consistently required the highest energy to propagate cracks. Geotextile PF at one-third position achieved the maximum energy dissipation (~82 J), with Carbophalt GB (~75 J) and the control (~73 J) recording lower values at this position. Glasphalt GV at one-third position required comparable energy (~82 J) to Geotextile PF, demonstrating that this material can perform effectively when combined with optimal placement depth and sufficient displacement rate - consistent with the rate sensitivity findings in Section 5.5.2.

At one-half and two-thirds positions, energy dissipation decreased progressively for all materials. Geotextile PF showed values of approximately 72 J at one-half and 62 J at two-thirds. Glasphalt GV declined only modestly, retaining the highest energy among all materials at these deeper positions (~78 J at one-half and ~69 J at two-thirds). Carbophalt GB showed the widest variation in absolute energy, from ~75 J at one-third to ~61 J at one-half and ~51 J at two-thirds. However, other metrics (e.g., peak force retention and TIF under slow loading) still indicate that placement nearer the crack initiation zone is beneficial, particularly when loading is quasi-static.

Energy dissipation at 2 mm/min (Figure 5.9b). At the slower displacement rate, Geotextile PF at one-third position achieved the highest energy dissipation across all test configurations (~86 J), surpassing both other reinforced specimens and unreinforced control samples. This outstanding performance confirms Geotextile PF's low rate-sensitivity identified in Section 5.5.1.2 - the asphalt-saturated fabric engages progressively across both displacement rates, providing reliable energy absorption through distributed fibre stretching and pull-out mechanisms.

Control specimens showed consistent energy dissipation across all three emulsion positions (~55 J at one-third, ~53 J at one-half, ~51 J at two-thirds), suggesting that emulsion placement depth does not significantly impact energy absorption in unreinforced samples. The relatively uniform control values provide a baseline against which reinforcement effectiveness can be assessed.

Glasphalt GV exhibited dramatically reduced energy dissipation at 2 mm/min compared to 5 mm/min, with values dropping to approximately 36 J at one-third, 28 J at one-half, and 26 J at two-thirds. At this slower rate, Glasphalt GV required the least energy to resist deformation among all materials tested, indicating lower capacity for energy absorption under quasi-static loading conditions. This poor performance at 2 mm/min confirms the rate sensitivity mechanism discussed earlier: Glasphalt GV's reinforcement mechanism fails to activate effectively under slow loading, resulting in interfacial discontinuities rather than crack bridging. Carbophalt GB showed intermediate performance, declining from ~63 J at one-third to ~47 J at one-half and ~36 J at two-thirds, with values reduced compared to 5 mm/min.

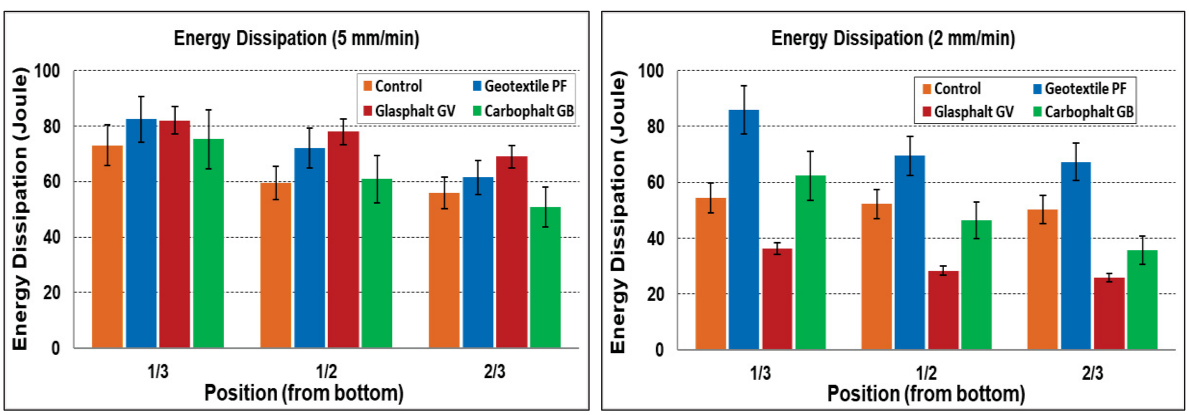

a) At 5 mm/min

b) At 2 mm/min

Figure 5.9 Dissipated energy at 25 °C for different placement depths and displacement rates.

Overall, the energy-based results reinforce the trends identified in the mechanical response analyses: placement at one-third depth maximised crack resistance across both displacement rates, Geotextile PF provided the most robust performance, Glasphalt GV was highly sensitive to displacement rate and placement depth, and Carbophalt GB exhibited moderate but consistent energy absorption.

5.5.5 Crack-Interlayer Interaction Analysis

The time to interlayer $T_{\text{interlayer}}$ is defined as the elapsed time between the start of loading and the instant when the main crack first reaches the reinforcement/emulsion plane. Under fixed geometry and displacement rate, this quantity reflects the crack-propagation rate through the asphalt cover and thus the ability of each interlayer system to delay the onset of reflective cracking.

Raw force histories $F(t)$ were smoothed using an 11-point centred moving average,

$$\tilde{F}_i = \frac{1}{11}\sum_{j=i-5}^{i+5} F_j \tag{5.4}$$

where $\tilde{F}_i$ is the smoothed force at data point i, and F_j represents the raw force values. This window size effectively removes high-frequency noise while preserving critical features such as peaks and transitions.

The force derivative was computed using the central difference method:

$$\left.\frac{dF}{dt}\right|_i = \frac{\tilde{F}_{i+1} - \tilde{F}_{i-1}}{2\Delta t} \tag{5.5}$$

where Δt is the time step between consecutive measurements. This derivative, denoted as D_i, serves as the primary indicator for identifying phase transitions. Positive values ($D_i > 0$) indicate increasing force as the crack approaches the interlayer, while negative values ($D_i < 0$) indicate decreasing force in the post-peak phase. These two regimes are designated as the contractive phase (the rising-force stage in which the system progressively resists crack growth as the reinforcement engages) and the dilative phase (the post-peak softening stage as the crack breaches the interlayer plane), respectively.

The first peak in the force curve, corresponding to the moment when the crack reaches the interlayer, was identified when the derivative transitioned from positive to negative and remained negative for at least seven consecutive points:

$$D_{i-1} > 0 \text{ and } D_i \leq 0 \text{ for all } j \in [i, i+6]$$

This sustained negative slope criterion ensures the identified peak represents a genuine transition rather than a spurious local fluctuation. Once the peak was identified at index i_{peak}, the time to interlayer and corresponding crack opening displacement were calculated:

$$T_{\text{interlayer}} = t_{\text{peak}} - t_0 \text{ and } \delta_{\text{interlayer}} = \upsilon \times T_{\text{interlayer}}$$

where t_0 is the test start time (typically zero) and υ is the constant displacement rate (2 mm/min or 5 mm/min). The force at this critical moment ($F_{interlayer} = \tilde{F}_{i(peak)}$) completes the characterisation of the pre-interlayer phase.

The experimental data provide critical insights into crack-interlayer interaction dynamics across different reinforcement positions and displacement rates (Figure 5.10). At the one-third depth position (closest to crack initiation), Carbophalt GB exhibited the shortest time to interlayer engagement (98.0 s at 5 mm/min), demonstrating its immediate stress transfer capability through its stiff glass-carbon composite structure. However, this advantage diminished at reduced displacement rates (238.0 s at 2 mm/min), where viscoelastic relaxation effects became pronounced. The geotextile (PF) showed contrasting behaviour, requiring 121.0 s for crack interception at 5 mm/min but maintaining superior force retention (6590.1 N vs. 7459.1 N for Carbophalt GB), attributable to its asphalt-saturated fabric's energy dissipation through distributed fibre stretching. This performance gap widened significantly at 2 mm/min loading, where PF's time-to-interlayer increased to 367.0 s while sustaining 5539.7 N force - a 32% greater force retention than Carbophalt GB under comparable conditions, highlighting its low rate-sensitivity in toughness.

Mid-depth (one-half) placements revealed transitional behaviour, with Geocomposite GV showing unexpected force reduction (6770.7 N at 5 mm/min vs. 7973.8 N at one-third), suggesting interfacial shear failure mechanisms dominate when reinforcement is positioned away from maximum tensile stress zones. The control samples' progressive performance decline from one-third (7147.7 N) to two-thirds (5521.6 N) positions underscores emulsion's limited crack-bridging capacity compared to structural geosynthetics. Notably, at two-thirds depth, all materials exhibited time-dependent performance degradation, with the geotextile requiring 381.0 s at 2 mm/min - 2.3× longer than at one-third position - indicating delayed activation of its reinforcement mechanism when placed near the surface.

Cross-comparison of energy dissipation pathways shows Carbophalt GB's 5836.9 N force at two-thirds position represents only 78% of its one-third capacity, while Geotextile retained

79% (5197.8 N vs. 6590.1 N), indicating that both flexible (PF) and grid (GB) reinforcement systems retain similar load capacity at two-thirds depth. The inverse relationship between displacement rate and force capacity was most pronounced in Geocomposite GV (4129.2 N at 2 mm/min vs. 7973.8 N at 5 mm/min), exposing its temperature-sensitive interfacial bonding limitations. These findings collectively demonstrate that optimal crack mitigation requires balancing early stress interception (favoured by reinforcement nearer the crack initiation zone) with sustained damage tolerance (enhanced by ductile materials like PF), with one-third positioning providing the most effective compromise across loading scenarios.

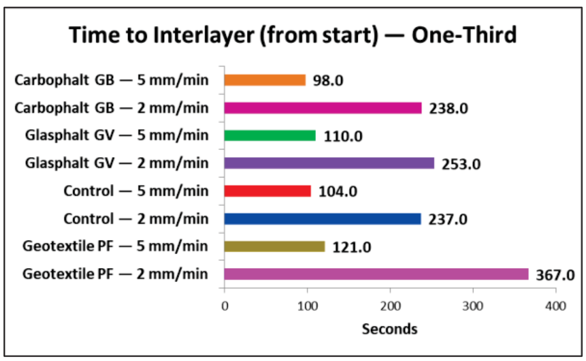

a) Time to reach the interlayer (one-third case)

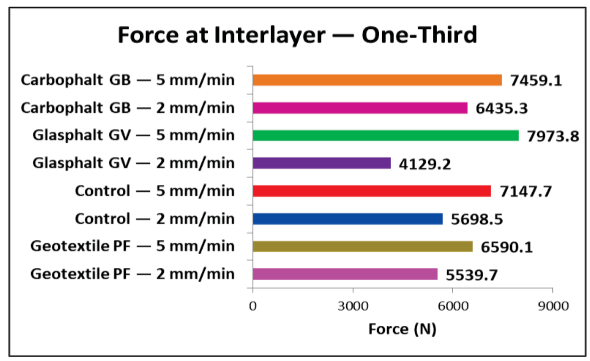

b) Force at interlayer (one-third case)

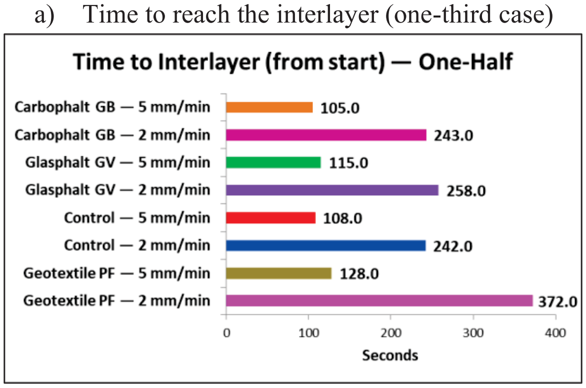

c) Time to reach the interlayer (one-half case)

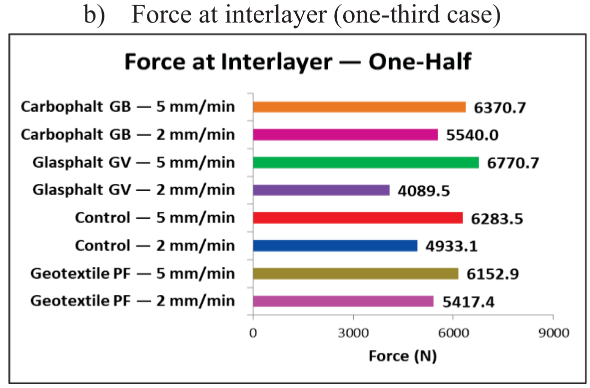

d) Force at interlayer (one-half case)

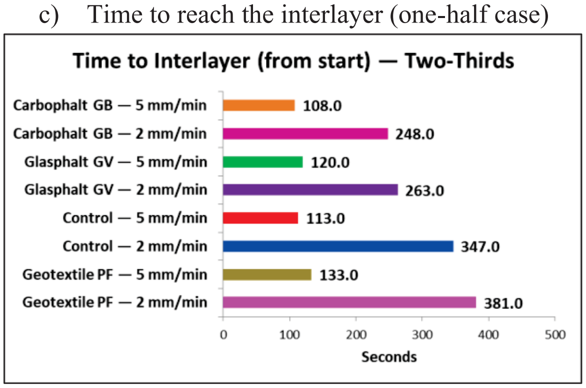

e) Time to reach the interlayer (two-thirds case)

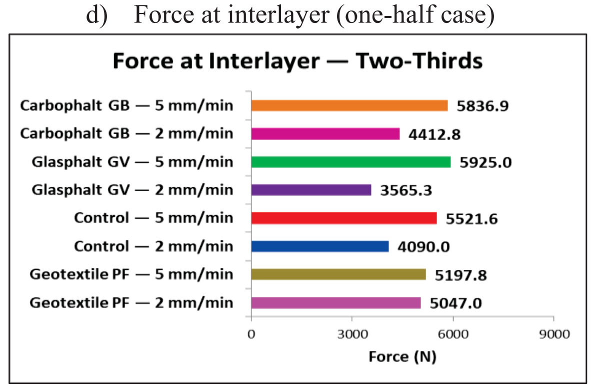

f) Force at interlayer (two-thirds case)

Figure 5.10 Time to interlayer and force at interlayer for different placement depths.

5.5.6 Influence of Reinforcement Type and Placement on Toughness Improvement Factor

The Toughness Improvement Factor (TIF) is a dimensionless measure of how much a reinforcement improves an asphalt composite's crack resistance relative to an unreinforced control (the control is set to TIF = 1). It is defined as the ratio of the energy absorbed by a reinforced specimen during fracture to that absorbed by an unreinforced specimen under identical test conditions. Mathematically, it can be expressed as:

$$TIF = \frac{U_{reinforced}}{U_{control}} \tag{5.6}$$

where U_(reinforced) and U_(control) denote the total energy absorbed (i.e., the area under the force-displacement curve) for the reinforced and unreinforced samples under identical conditions, respectively. This area corresponds to the mechanical work done during loading, encompassing both elastic deformation and post-peak fracture energy dissipation. Values greater than 1 indicate that the reinforcement enables the material to absorb and redistribute more energy before failure; a value near 1 implies no change, and values below 1 signify reduced toughness.

Figure 5.11 compares three reinforcement types including geotextile (PF), Carbophalt GB, and Glasphalt GV at displacement rates of 2 mm/min and 5 mm/min. The results reveal pronounced rate-dependency with distinct behavioural patterns across materials and placement depths.

At 2 mm/min, geotextile achieved the highest TIF of 1.54 at one-third depth, maintaining values of 1.44 and 1.36 at one-half and two-thirds depths, respectively. This consistent performance reflects the geotextile's ability to progressively mobilise fibre capacity regardless of placement position. Carbophalt GB showed moderate performance, with TIF declining from 1.12 at one-third to 0.76 at two-thirds depth, indicating strong dependence on proximity to the crack front. Glasphalt GV performed poorly across all positions (TIF = 0.54-0.57), suggesting that its stiffness characteristics are incompatible with the ductile deformation mechanisms dominating at slower displacement rates.

At 5 mm/min, the performance landscape shifted substantially. Geotextile maintained strong TIF values of 1.08-1.21 with reduced position sensitivity, indicating more uniform engagement under rapid loading. Carbophalt GB improved markedly, approaching unity at all placements (TIF = 0.91-1.03). Most notably, Glasphalt GV reversed from detrimental to beneficial performance, achieving TIF values of 1.12-1.29 which is the highest occurring at mid-depth. This mid-depth maximum reflects the relative nature of the TIF metric rather than an absolute optimum, since TIF normalises each specimen against its depth-matched control and can therefore peak where the control baseline is comparatively weak; on an absolute basis, the energy dissipation of Glasphalt GV at 5 mm/min still favoured one-third placement (approximately 78 J at one-third versus 61 J at one-half), consistent with the overall finding that proximity to the crack initiation zone governs interlayer effectiveness. This transformation indicates that Glasphalt GV's glass fibre network requires dynamic loading for effective activation.

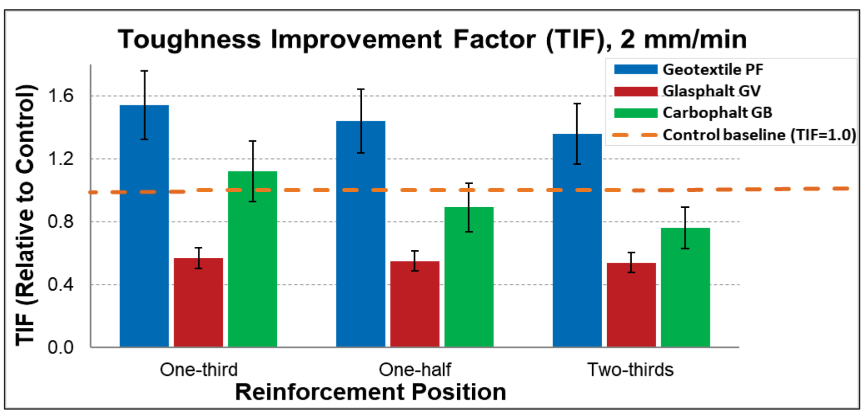

a) At 2 mm/min

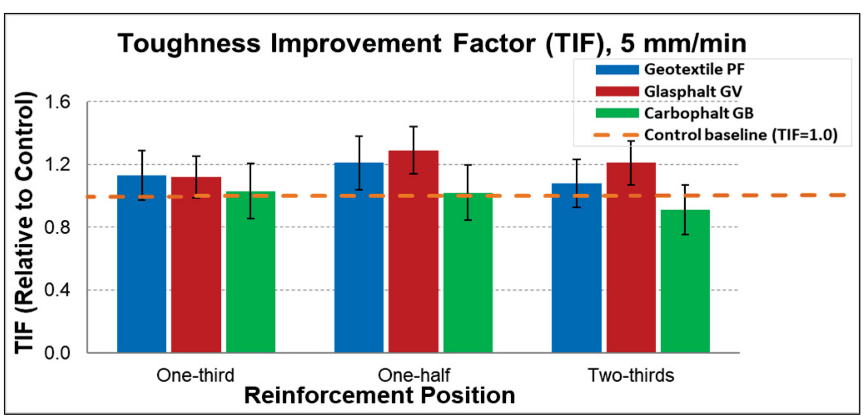

b) At 5 mm/min

Figure 5.11 Toughness Improvement Factor Comparison

The observed rate dependency reflects asphalt's viscoelastic nature: at slower rates, ductile materials like geotextiles benefit from extended engagement time, while stiffer interlayers cannot deform sufficiently. At higher rates, the asphalt matrix behaves more brittlely, favoring reinforcements with rapid stress transfer capability.

These findings carry practical implications for material selection. For applications dominated by slow, repeated loading - such as urban intersections - geotextile offers reliable performance across placement depths. For high-speed highways involving dynamic loading, Glasphalt GV may provide superior performance. Carbophalt GB represents an intermediate option requiring careful placement near the crack initiation zone. The interaction between material properties, placement depth, and displacement rate must be considered to optimise reinforcement effectiveness.

5.5.7 Fracture Toughness G_{IC}

Fracture energy (G_{IC}), also known as Mode I fracture toughness, is a critical parameter used to evaluate a material's resistance to crack initiation and propagation under tensile opening forces. In asphalt materials, G_{IC} is defined as the energy required to propagate a crack per unit area of fracture surface. The formula for calculating G_{IC} is commonly expressed as:

$$G_{IC} = \frac{W}{A} \tag{5.7}$$

where W is the energy absorbed during fracture (i.e., the area under the force-displacement curve, in N·mm or J), and A is the ligament area (in mm^2) across which the crack propagates. Higher G_{IC} values indicate greater crack resistance and durability of the asphalt system. While the Toughness Improvement Factor (TIF) provides a relative measure of reinforcement effectiveness compared to the control baseline, the absolute G_{IC} values reveal the fundamental energy dissipation mechanisms governing fracture behaviour under different loading conditions.

Figure 5.12 presents the absolute fracture energy (G_{IC}) for specimens reinforced with geotextile (PF), Carbophalt GB, and Glasphalt GV at displacement rates of 2 mm/min and 5 mm/min across three placement depths. These measurements complement the TIF analysis by quantifying actual energy absorption capacity rather than relative effectiveness alone.

At 2 mm/min, geotextile reinforcement at one-third depth achieved approximately 40 kJ/m², consistent with its superior TIF of 1.54. The geotextile's progressive fibre activation mechanism enables effective crack arrest when positioned near the initiation zone. Although G_{IC} decreased at placements farther from the crack initiation zone, values remained above control levels at all positions. Both grid-type materials performed poorly at this displacement rate: Glasphalt GV recorded only 7 kJ/m² at two-thirds depth (TIF = 0.54), while Carbophalt GB showed similarly diminished capacity. Notably, unreinforced controls often exceeded grid reinforcement performance at positions farther from the crack initiation zone, suggesting that improperly positioned rigid interlayers may introduce stress concentrations that compromise fracture resistance.

The performance hierarchy shifted substantially at 5 mm/min. Geotextile maintained stable G_{IC} values of approximately 38-40 kJ/m² at one-third depth with little change from the lower rate, reflecting its low rate-sensitivity, although values still decreased at deeper placements (approximately 23 and 15 kJ/m² at one-half and two-thirds depths). More significantly, Glasphalt GV exhibited dramatic improvement, reaching approximately 38 kJ/m² at one-third depth - a transformation consistent with its TIF reversal from 0.57 to 1.12. This rate sensitivity indicates that Glasphalt GV's glass fibre network requires dynamic loading to mobilise effectively; under rapid deformation, the material provides immediate crack resistance as the asphalt matrix responds in a more brittle manner. Carbophalt GB similarly improved, with G_{IC} values approaching control levels at most positions.

The correlation between absolute G_{IC} and relative TIF illuminates an important distinction. Glasphalt GV at 2 mm/min illustrates this clearly: despite TIF values suggesting modest relative performance, the absolute G_{IC} of 7-15 kJ/m² indicates genuinely poor fracture resistance. Conversely, at 5 mm/min, elevated TIF values correspond to substantially higher absolute energy absorption, confirming genuine performance improvement rather than merely favourable comparison to a weak baseline.

These findings reinforce the material selection principles established in the TIF analysis.

Geotextile provides consistent toughness enhancement regardless of loading conditions, whereas grid-based systems exhibit strong rate dependence. For field applications, material choice must account for anticipated displacement rates: geotextile suits general conditions, while Glasphalt GV may benefit applications dominated by rapid, dynamic loading.

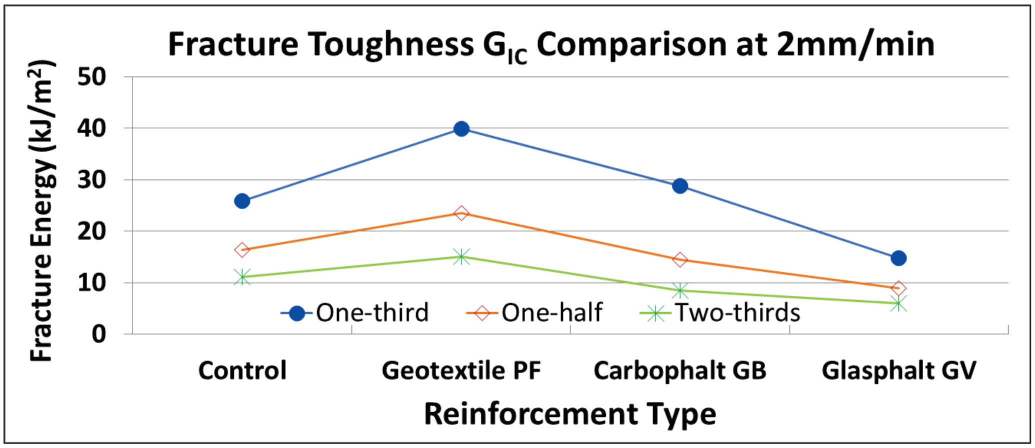

a) At 2 mm/min

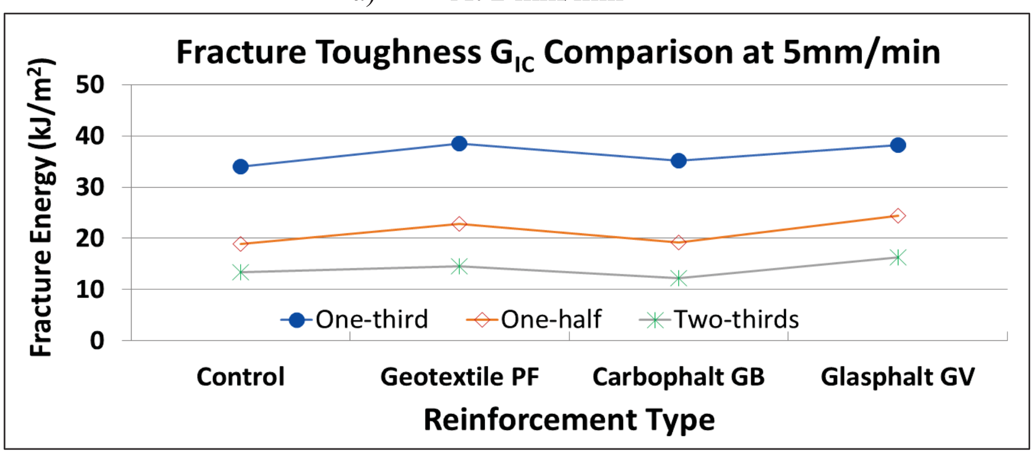

b) At 5 mm/min

Figure 5.12 Fracture Toughness Comparison

5.5.8 Effect of Reinforcement/Emulsion Position on J-Integral

Figure 5.13 presents the interfacial J-integral, J_{inter}, for each material system and interface position at two displacement rates. The quantity is defined as the mechanical work required for the crack to travel from the notch root to the target interface, normalised by the fracture area created across the ligament. From the measured force-displacement record $P(\delta)$, the work up to interface interception is as follow:

$$U(\delta_{\text{int}}) = \int_0^{\delta_{\text{int}}} P(\delta)d\delta \approx \sum_{i=1}^{n-1} \frac{P_{i+1}+P_i}{2}(\delta_{i+1}-\delta_i) \tag{5.8}$$

Where P(δ) is the measured load [N] as a function of crosshead displacement δ [mm]; $\delta_{int}=\upsilon\, t^*/60$ is the displacement at the moment the crack front meets the interface, where υ is the imposed rate [mm/min] and t* the time-to-interlayer marker [s]; P_i, δ_i are the sampled values used in the trapezoidal sum; and n is the number of samples up to δ_{int}. The ligament that the crack must traverse has length $\ell_{lig}=|y_{int}-a_0|$ (interface depth minus initial notch) and fracture area $A_{lig}=b\,\ell_{lig}$, with b the specimen thickness [mm], y_{int} the interface depth [mm], and a_0 the initial notch length [mm]. The plotted quantity is therefore making explicit that the normalisation uses only the area actually created while the crack crosses the ligament.

$$\boxed{J_{inter} = \frac{U(\delta_{\text{int}})}{A_{lig}} = \frac{U(\delta_{\text{int}})}{bl_{lig}}} \quad [\text{N mm}^{-1}] \tag{5.9}$$

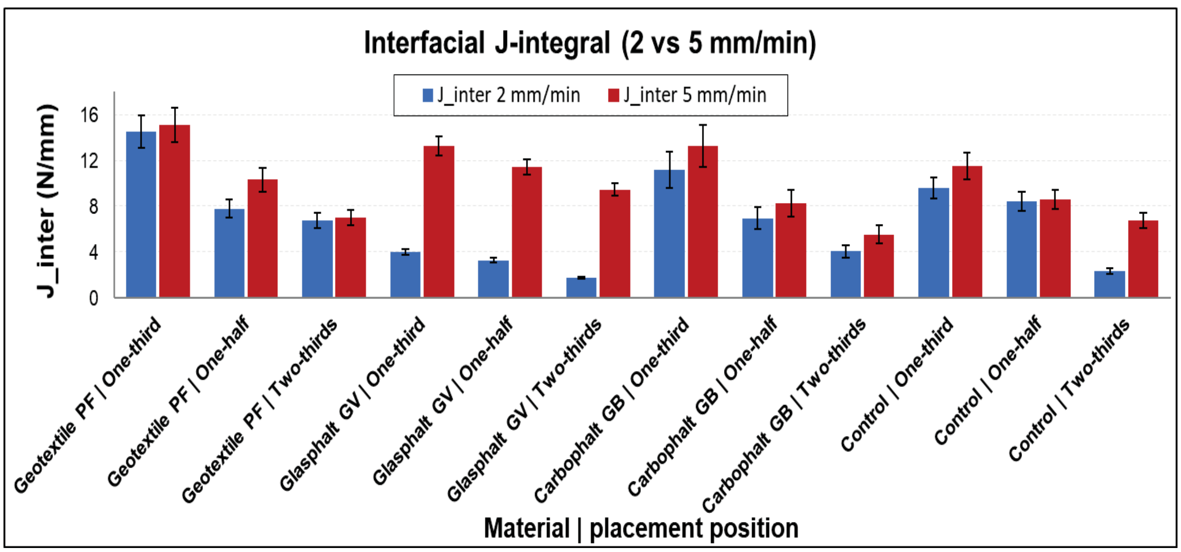

Figure 5.13 The J-integral at the interface according to displacement rate and placement of reinforcement/emulsion

Interpreting the figure, the higher displacement rate (5 mm/min) generally produces larger J_{inter} than the lower rate (2 mm/min), consistent with a rate-dependent increase in the work needed to carry the crack across the ligament. The asphalt-saturated paving fabric (PF) attains the highest values - most pronounced when the interface is located at one-third of the height - because the reinforcement is engaged earlier and provides effective crack bridging. Carbophalt GB shows intermediate levels with clear rate sensitivity and a gradual drop as the interface is moved upward (one-half → two-thirds), indicating reduced ligament engagement. Glasphalt GV records the lowest J_{inter} (work to reach the interface), suggesting limited resistance prior to interface interception; its toughness gains observed at 5 mm/min occur mainly in the post-interception stage once the glass-fibre network is mobilised. Unreinforced controls fall between PF and GV, the emulsion delays crack advance and raises J_{inter} relative to the weakest reinforced case, but does not sustain bridging to the extent observed for PF. Overall, interfacial toughness depends jointly on the imposed rate and the ligament geometry used in the normalisation; deeper interfaces and asphalt-saturated fabrics demand measurably more energy for the crack to traverse the interface.

5.6 Conclusion

This study evaluated the fracture response of three geosynthetic interlayers - paving fabric (PF), Carbophalt GB, and Glasphalt GV - using a Crack Widening Device under three placement depths, two temperatures, and two displacement rates.

Displacement rate influenced reinforcement effectiveness. Peak forces were generally higher at 5 mm/min than at 2 mm/min, with the magnitude of the effect depending on interlayer type. Within the investigated matrix, PF showed the most stable response across the two displacement rates, with TIF values of 1.36-1.54 at 2 mm/min and 1.08-1.21 at 5 mm/min attributable to progressive fibre engagement across both displacement rates. Glasphalt GV exhibited pronounced rate sensitivity, with TIF values of 0.54-0.57 at 2 mm/min reversing to 1.12-1.29 at 5 mm/min, indicating that its glass fibre network requires dynamic loading for effective activation. Carbophalt GB showed intermediate behaviour with TIF approaching unity at both rates.

Placement closer to the crack initiation zone generally produced more favourable performance. In the three-depth comparison conducted at 25 °C, one-third placement from the bottom - the position nearest to the crack tip - generally produced the strongest force-displacement and energy-based response across materials and displacement rates. Energy dissipation confirmed this hierarchy: PF at one-third depth achieved 82-86 J compared to 62-67 J at two-thirds depth, with corresponding G_{IC} values of approximately 40 kJ/m². The crack-interlayer interaction analysis further supported this finding: one-third placement consistently produced the highest interfacial J-integral values, reflecting greater work required to carry the crack through the ligament, and earlier time-to-interlayer contact. Carbophalt GB exhibited the shortest time to crack interception at 5 mm/min but this advantage diminished substantially at 2 mm/min due to viscoelastic relaxation effects, while PF maintained superior force retention at the moment of interception across both rates.

Temperature modulated interlayer activation. Room temperature (25 °C) provided the most favourable balance between interface integrity and deformability, whereas at 40 °C softening of the asphalt system limited force development despite increased deformation capacity.

Stiffness alone did not provide an adequate measure of reflective-cracking resistance. Control specimens frequently exhibited higher $K_{0\text{-}4mm}$ and $\bar{K}_{10\text{-}30\%}$ values than reinforced systems, particularly at 25 °C, yet failed more abruptly. Reinforced specimens traded stiffness for ductility - precisely the intended function of geosynthetic interlayers - demonstrating that energy-based metrics including TIF, G_{IC}, and interfacial J-integral provide more meaningful characterisation than stiffness indices alone.

Within the limits of the present laboratory configuration, specimen geometry, and mixture system, PF provided the most consistent performance across the investigated conditions and is suited for applications where displacement rates are variable or unpredictable. Glasphalt GV may be considered where dynamic loading at higher displacement rates dominates, but should be used with caution where slow repeated loading prevails. Carbophalt GB offers moderate and relatively stable behaviour but still benefits from placement closer to the crack initiation zone. One-third placement from the overlay bottom is recommended for all geosynthetic types evaluated. Laboratory testing protocols should incorporate multiple displacement rates, as single-rate evaluation may misrepresent the rate-dependent behaviour identified in this study.

Overall, the results show that geosynthetic interlayer effectiveness is governed by the coupled influence of material type, placement depth, temperature, and displacement rate. These findings provide a fracture- and interface-based framework - combining stiffness indices, dissipated energy, TIF, G_{IC}, and interfacial J-integral - for mechanistic interpretation and comparative evaluation of geosynthetic-reinforced asphalt overlay systems.

CHAPTER 6

SUPPLEMENTARY INVESTIGATION: PULL-OUT RESISTANCE OF GEOTEXTILE INTERLAYER IN ASPHALT SPECIMENS

6.1 Introduction

The preceding chapters used the Crack Widening Device (CWD) to characterize geosynthetic-reinforced overlays under mode I loading, where the interlayer carries tensile stresses perpendicular to the crack plane as the underlying crack opens. In service, however, a geosynthetic interlayer must also resist mode II loading: when traffic-induced horizontal shear acts on the asphalt-fabric interface, the interlayer is subjected to pull-out forces. The pull-out resistance governs how well the interlayer is anchored in the asphalt matrix and therefore how effectively it can bridge a propagating crack and redistribute stress to the surrounding material. The CWD program addresses crack opening; this supplementary chapter complements it by isolating the mode II response.

This chapter presents a supplementary experimental investigation of the pull-out behavior of a paving fabric (nonwoven geotextile) interlayer embedded within asphalt concrete specimens, using a custom pull-out test apparatus designed and fabricated in-house at the LCMB. As a first-generation prototype, the apparatus enabled a preliminary evaluation of the pull-out test methodology for asphalt-geosynthetic systems. A mechanistic analysis shows that the current apparatus configuration resulted in an incorrect failure mode, where the geotextile experienced tensile tearing rather than interface debonding. The underlying mechanics are discussed in detail, the expected response corresponding to true interface debonding is proposed conceptually, and a quantitative comparison between the actual and expected behaviors is provided. The findings establish clear design guidelines for refining the apparatus toward a reliable interface characterization tool.

6.2 Test Setup and Procedure

6.2.1 Specimen Configuration

A bilayer asphalt specimen was fabricated following the same procedure described in Chapter 2 (Section 2.4). The specimen consisted of a paving fabric (needle-punched nonwoven geotextile) placed at the interface between two layers of ESG-10 asphalt mixture. The ESG-10 is a dense-graded (semi-coarse) asphalt mixture with a nominal maximum aggregate size of 10 mm, commonly used as a surface course material in Quebec. This mixture was selected to ensure consistency with CWD specimens and to isolate interfacial behavior under comparable material conditions. The geotextile was positioned with a portion extending beyond the mold opening for gripping by the MTS loading frame. The tack-coat application rate and curing conditions were consistent with those used in the CWD test specimens.

6.2.2 Pull-out Test Apparatus

Pull-out tests were conducted using an MTS 810 servo-hydraulic testing system at the LCMB laboratory. To address the lack of standardized pull-out test equipment for bituminous interlayer systems, a custom apparatus was designed and fabricated in-house by the author and Professor Carter as a first-generation prototype. The apparatus consists of a steel holder assembly comprising a rigid base plate, lateral side plates, and a top plate fastened with bolts to provide confinement of the asphalt specimen, with the protruding geotextile fabric gripped by the upper hydraulic jaw of the MTS loading frame.

The test configuration applied a vertical tensile displacement to the geotextile while the asphalt specimen remained stationary within the holder, thereby inducing tensile loading in the geotextile and interfacial stresses at the asphalt-geotextile interface. This configuration does not reproduce a pure interface pull-out condition. The applied loading introduces large tensile stresses within the geotextile itself, and the resulting failure mode is controlled jointly by the interface bond and the fabric tensile capacity, as detailed in the following sections. Figure 6.1 shows the specimen preparation and assembly sequence.

Figure 6.1 Specimen preparation sequence showing geotextile insertion between asphalt layers, positioning of the interlayer, and assembled specimen in the steel mold

Figure 6.2 presents the complete test setup with the steel mold assembly and a schematic illustration showing the key components of the clamping arrangement.

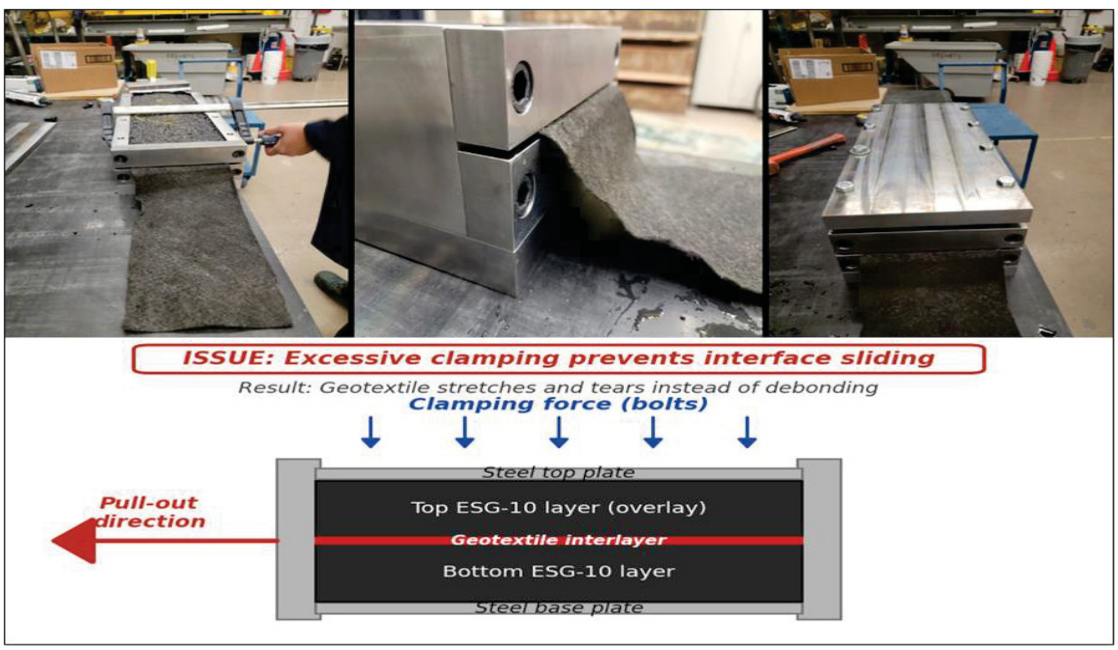

Figure 6.2 Pull-out test setup: laboratory photographs showing specimen with geotextile extending from mold, clamping assembly, and top view (top); schematic illustration showing the excessive clamping issue at the interface (bottom)

6.2.3 Testing Protocol

The pull-out test was performed under displacement-controlled conditions at a constant rate of 2 mm/min at room temperature (approximately 25 ± 2 °C). The selected displacement rate (2 mm/min) is consistent with the quasi-static loading conditions used in CWD testing; however, its relevance to field-induced interfacial shear rates remains limited. Axial force and axial displacement were recorded continuously throughout the test using the MTS data acquisition system. The test continued past the peak load until it was terminated at a displacement of 134 mm, once tensile failure of the geotextile had developed.

6.2.4 Finite Element Visualization of the Pull-out Configuration

To complement the experimental program, a three-dimensional finite element model of the pull-out configuration was built in Abaqus. The model reproduces the specimen assembly as three deformable parts: the lower and upper asphalt lifts, meshed with 4,500 eight-node linear brick elements each (C3D8R), and the geotextile interlayer between them, meshed with 900 four-node shell elements (S4R), for a total of about 12,600 nodes. The construction of the model is shown in Figure 6.3, and its discretization is summarized in Table 6.1. The materials are described by linear-elastic properties: $E = 3.45$ GPa and $\nu = 0.35$ for the asphalt, taken as the long-term modulus of its viscoelastic definition, and $E = 10$ MPa and $\nu = 0.20$ for the geotextile. That viscoelastic definition is a four-term Prony series with nominal constants; because it is entered in the frequency domain while the analysis step is quasi-static in time, it does not act, and both lifts respond at the long-term modulus. The interaction between the geotextile and each asphalt lift is represented by surface-to-surface contact with a penalty friction formulation ($\mu = 0.3$), so that normal pressure and frictional shear can develop on both faces of the fabric. The asphalt block is fully restrained, and the pull-out action is applied in a single static step by prescribing a total axial displacement of 5 mm at the free end of the geotextile; as the step is static, no loading rate is represented, and the analysis completed in four increments.

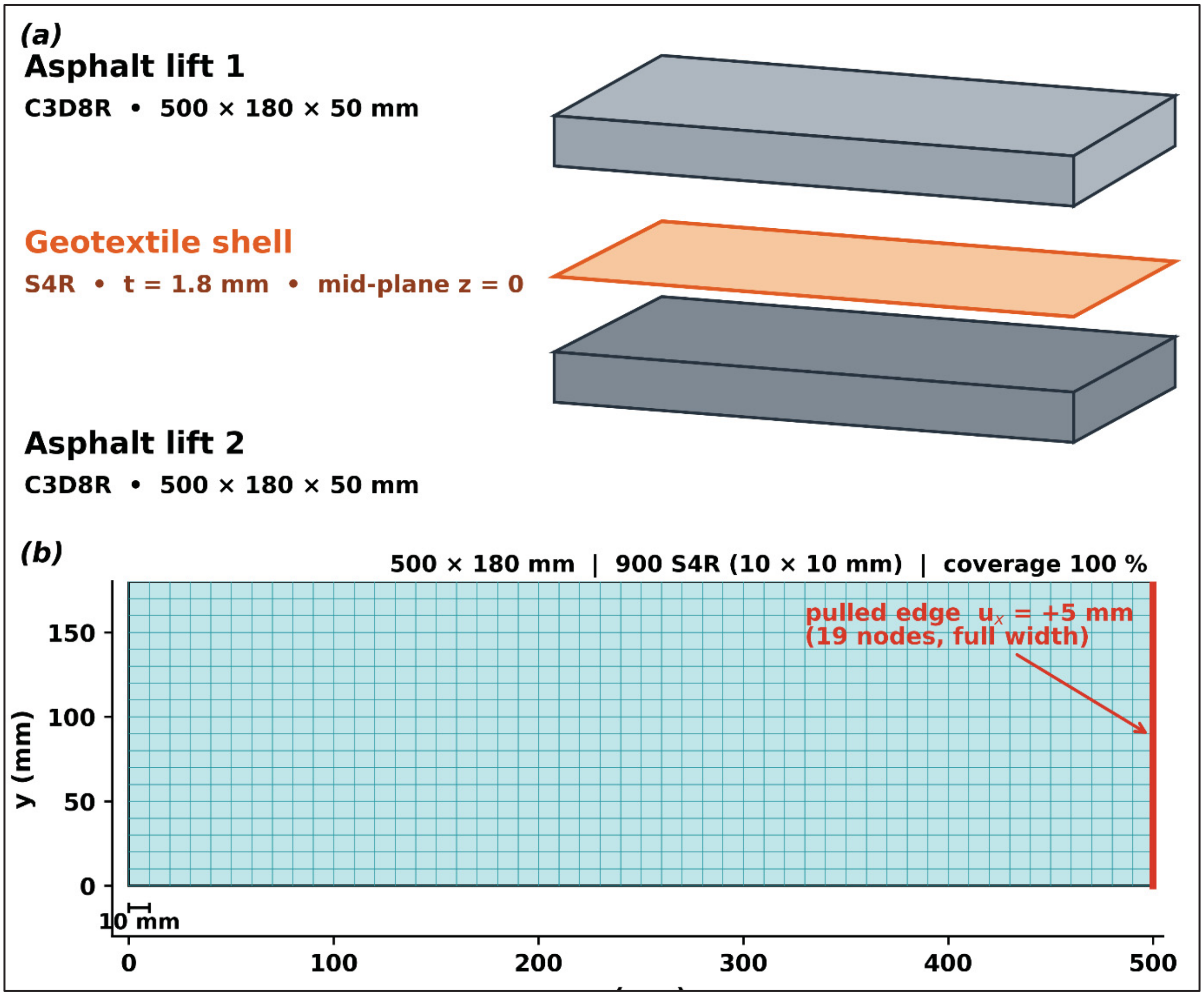

Figure 6.3 Construction of the pull-out finite element model: (a) exploded view of the asphalt lifts and the geotextile interlayer shell; (b) geotextile mesh (10 mm grid) with the loaded edge

Table 6.1 Discretization of the pull-out finite element model

Component	**Element type**	**Elements**	**Nodes**	**Element size**
Asphalt lift (×2)	C3D8R solid	4,500 per lift	5,814 per lift	10 mm cubes
Geotextile sheet	S4R shell, t = 1.8 mm	900	969	10 × 10 mm
Total		9,900	12,597	

The purpose of this model is strictly illustrative: it visualizes how displacement and stress distribute within the specimen and along the geotextile under the pull-out action, as shown in Figure 6.4. Its contact parameters and material constants are nominal input values, so no quantitative conclusions are drawn from it. The quantitative modeling is presented separately: after the tensile-tearing failure mode was identified, this model was extended and calibrated against the measured load-displacement response, and the calibration procedure and its results are reported in Section 6.6.

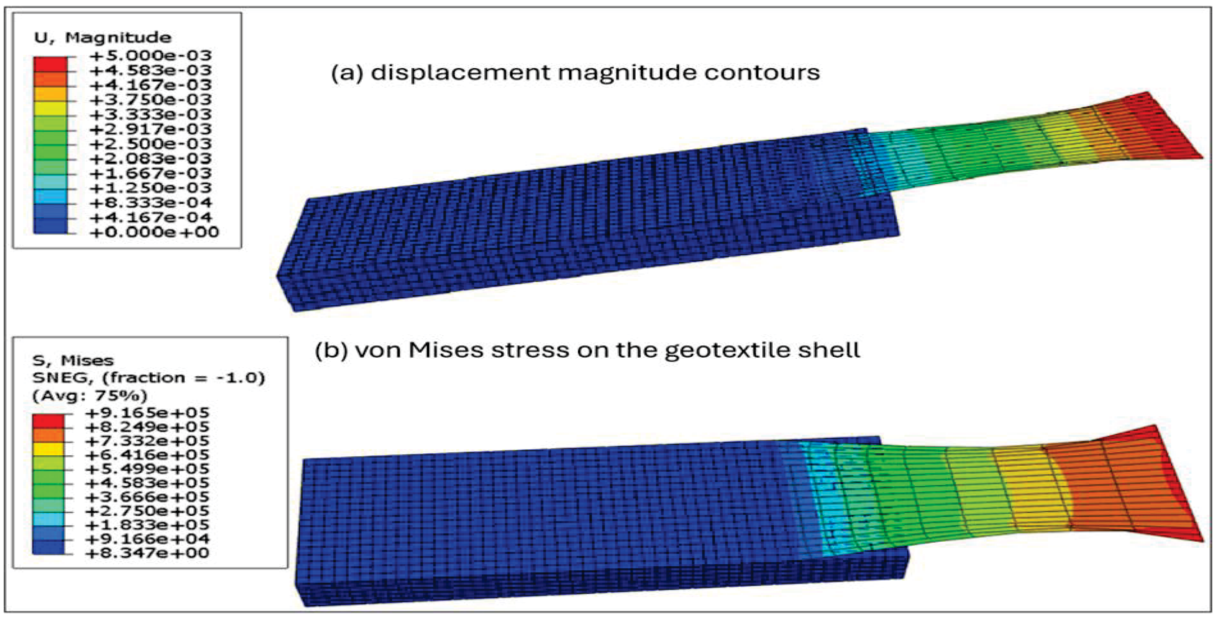

Figure 6.4 Finite element visualization of the pull-out configuration (illustrative, uncalibrated model): (a) displacement magnitude contours showing the prescribed 5 mm pull-out of the geotextile relative to the fixed asphalt block; (b) von Mises stress on the geotextile shell, increasing toward the loaded end

6.3 Test Results and Failure Mode Identification

6.3.1 Load-Displacement Response

Figure 6.5 gives the load-displacement curve obtained from the pull-out test. The curve can be divided into four distinct phases, each corresponding to a specific deformation mechanism within the geotextile.

Phase I - Fiber alignment (0-30 mm): The initial portion of the curve shows a gradual, nearly linear increase in force with an apparent stiffness of approximately 0.014 kN/mm over the

Phase I window. This low stiffness reflects the mechanics of nonwoven geotextile deformation: randomly oriented fibers progressively rotate and align in the direction of the applied load. The force required during this phase is primarily consumed in overcoming inter-fiber friction and reorienting the fiber network, not in mobilizing interface shear resistance.

Phase II - Strain hardening (30-110 mm): As more fibers become aligned with the loading direction, the effective cross-section carrying the load increases, resulting in a strain-hardening response. The curve shows a concave-upward shape characteristic of extensible materials undergoing large deformations. The force increases from approximately 0.45 kN at 30 mm to the peak of 2.013 kN at 110 mm displacement.

Phase III - Peak (110 mm): The force reaches its maximum recorded value of 2.013 kN at a displacement of 110 mm. This peak marks the transition between strain-hardening (Phase II) and progressive rupture (Phase IV) and represents the maximum tensile capacity of the geotextile in the bitumen-impregnated, confined configuration. The peak is reached when the most-aligned fibers attain their ultimate tensile strength near-simultaneously, beyond which the load-bearing cross-section begins to deteriorate through fiber-by-fiber failure rather than further re-orientation.

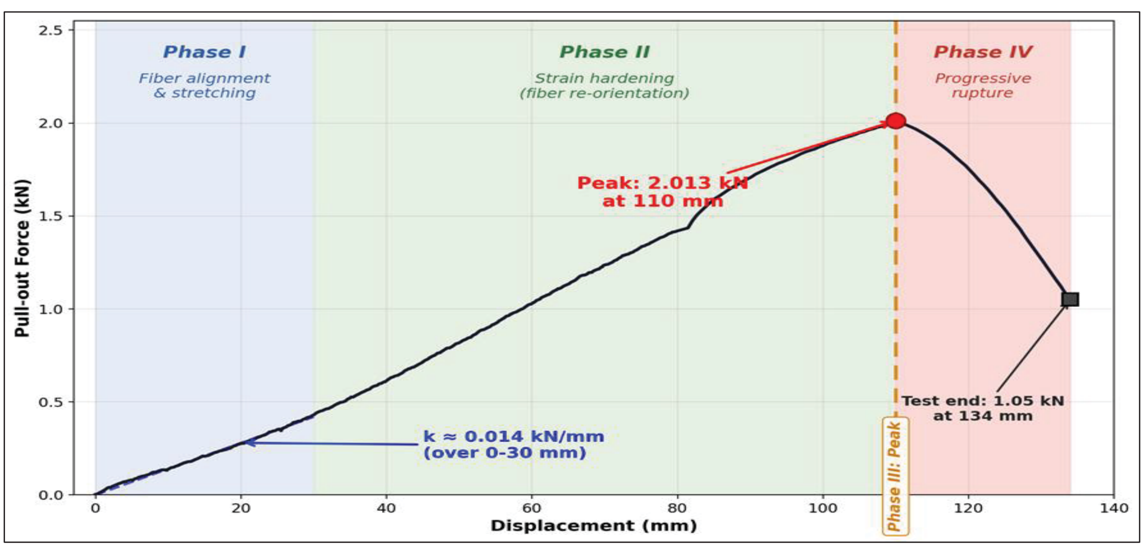

Figure 6.5 Load-displacement curve from the pull-out test on paving fabric (nonwoven geotextile) in ESG-10 asphalt, showing four phases of tensile deformation leading to tearing failure

Phase IV - Progressive rupture (110-134 mm): Beyond the peak, the force decreases gradually from 2.013 kN at 110 mm to 1.05 kN at 134 mm, the displacement at which the test was terminated. This 24 mm post-peak descent corresponds to progressive fiber-by-fiber rupture through the necked cross-section of the geotextile, which is characteristic of nonwoven fabric tensile failure. The total recorded displacement of 134 mm corresponds to a tensile strain on the order of 100 percent, relative to an initial free (gauge) length of approximately 130 mm. Because the fabric remained bonded and did not slide at the interface, the full crosshead displacement is taken up as elongation of this free length. This is corroborated by the 26.5 cm final stretched length measured post-test (about 130 mm of initial length plus 134 mm of elongation). A strain of this magnitude is consistent with the manufacturer's rated grab-tensile elongation of 45-105 percent for this fabric (Table 3.3).

6.3.2 Identification of Failure Mode

The pull-out test conducted in this study resulted in tensile failure (tearing) of the geotextile rather than interface debonding. Post-test examination revealed severe necking of the geotextile near the mold opening, with a measured deformed length of 26.5 cm. The necking pattern (hourglass shape with progressive narrowing toward a central tearing point) is characteristic of tensile failure in nonwoven geotextiles, where randomly oriented fibers progressively align in the loading direction before ultimate rupture. The geotextile remained fully bonded to the asphalt surfaces within the mold; no evidence of interface sliding was observed. Figure 6.6 assembles the visual evidence of the tensile failure mode, with post-test photographs documenting the progressive geotextile deformation observed during pull-out.

To further clarify the distinction between the observed and intended failure mechanisms, Figure 6.7 presents a schematic comparison of load transfer, deformation, and geotextile response between the actual tensile tearing mode and the expected interface debonding mode.

a) Stretching and necking near mold edge b) Necking and rupture at mold edge

Figure 6.6 Evidence of tensile failure mode: (a) geotextile being pulled from mold showing stretching, (b)post-test specimen showing severe necking

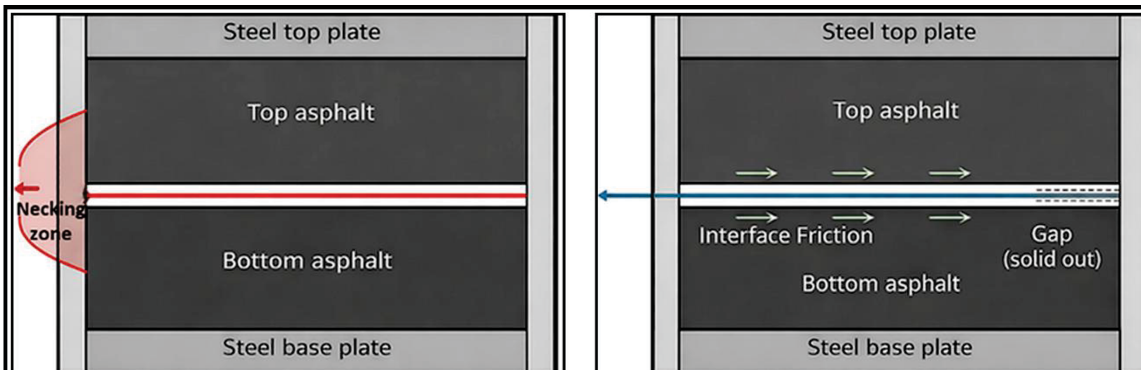

a) Actual: Geotextile tearing **b) Expected: Interface debonding**

Figure 6.7 Schematic illustration of (a) the observed tensile-tearing failure, in which the geotextile elongates and ruptures while remaining bonded to the asphalt, and (b) the intended interface debonding failure, in which the geotextile slides as an intact body relative to the asphalt

6.4 Expected Interface Debonding Behavior

To provide a benchmark for comparison, the expected load-displacement response for a true interface pull-out test (debonding failure) was estimated by adapting the experimental results of Noory et al. (2017) to the geometry of the present specimen. Noory et al. developed a dedicated double-shear and pull-out apparatus for asphalt-geocomposite interfaces and tested specimens at two temperatures (15 °C and 30 °C) with tack-coat application rates of 0-1.5 kg per square meter.

From their reported tension-displacement curves, four key parameters can be extracted: peak pull-out tensions in the range of 25-72 kPa (with the upper end corresponding to cold temperatures and aggressive bond conditions, and the lower end to warm temperatures and weak bond conditions); peak displacements between approximately 7 and 12 mm depending on temperature and bond conditions, with the upper end of this range observed at 15 °C and the lower end at 30 °C; an average Phase II tension-displacement slope of 5 to 8 kPa/mm; and Phase IV post-peak tensions that decline to approximately 20-25 kPa at the maximum tested displacement of ~22 mm. Because Noory's tests were terminated at this displacement, a true steady-state residual plateau is not directly observable in their data, so Phase IV is characterized here by the end-of-test tension range rather than a stable residual value. The narrow peak-displacement window of 7-12 mm is a consistent signature of interface debonding regardless of the absolute strength: the bond breaks through shear failure at the interface plane, and once it is broken, the geotextile slides as an intact body.

Noory's response is described in four phases: apparatus-specific gripping slip, elastic mobilization, progressive geocomposite mobilization (in which the geocomposite begins to slide as a whole within the asphalt matrix), and post-peak decline. The gripping-slip phase is specific to Noory's gripping system and does not exist in the present specimen, so it is omitted. The remaining three phases (elastic mobilization, progressive geocomposite mobilization, post-peak decline) are renumbered Phases I, II, and III for the expected response described below. Note that this Phase numbering refers to the expected debonding behavior and is independent of the four-phase decomposition used earlier (Section 6.3) for the actual fiber-stretching response, where Phase I-IV referred to fiber alignment, strain hardening, peak, and progressive rupture.

The expected pull-out forces, stiffness, and residual force for the present specimen were derived from Noory's tensions in four steps. The derivation converts each tension value (kPa) into a force (kN) by multiplying by the active bonded area, allowing direct comparison with the measured force in the present test.

Step 1: Active bonded area. The geotextile was embedded over the full slab length L = 500 mm with width w = 180 mm. Because both faces of the fabric are in contact with the asphalt (one with the upper layer, one with the lower layer), the active bonded area is the sum of the two interface contact areas:

$$A = 2 \times L \times w = 2 \times 500\ mm \times 180\ mm = 180{,}000\ mm^2 = 0.18\ m^2 \tag{6.1}$$

The present specimen has a bonded interface area approximately 9.5 times larger than Noory's pull-out specimens (147 × 65 mm, $A \approx 0.019\ m^2$). Applying Noory's tension values (kPa) directly to the larger area of the present specimen implicitly assumes that the shear bond stress is uniformly distributed across the interface and scales linearly with specimen geometry. This is a reasonable first-order assumption in the linear-elastic regime, but it does not capture potential edge effects, non-uniform stress distribution along the embedment length, or progressive debonding-front propagation that may become more pronounced at larger scales. The expected values derived in Steps 2-4 should be interpreted as order-of-magnitude benchmarks rather than precise predictions.

Step 2: Representative pull-out tension. Noory's reported peak tension range of 25-72 kPa reflects the combined effects of temperature and tack-coat application rate. The 72 kPa upper end corresponds to cold temperatures (15 °C) and aggressive bond conditions, whereas the 25 kPa lower end corresponds to warm temperatures (30 °C) and weak bond conditions. The present test was conducted at ambient laboratory temperature (25 ± 2 °C) with a tack-coat application rate consistent with typical Quebec construction practice, conditions that fall in the middle of Noory's range. A midrange representative peak tension was adopted:

$$\tau_{peak} = 50\ kPa \tag{6.2}$$

Step 3: Expected peak pull-out force. Applying the representative peak tension uniformly over the active bonded area gives the expected peak pull-out force:

$$F_{peak} = \tau_{peak} \times A = 50\ kPa \times 0.18\ m^2 = 9\ kN \tag{6.3}$$

This calculation assumes that the full embedded length is simultaneously active at the instant of peak load, which corresponds to the upper-bound estimate of the bond capacity. In reality, peak force during interface debonding occurs when the maximum mobilized length is engaged; a propagating debonding front may engage somewhat less than the full embedded area, so the true expected peak could be somewhat lower than 9 kN. This upper-bound estimate is appropriate for the present benchmarking, however, because the comparison aim is to demonstrate that the test did not reach the bond capacity, and any downward correction to the expected value would only strengthen the diagnostic conclusion (the actual 2.013 kN remains a small fraction of even the lower-bound expected value).

Step 4: Expected initial stiffness and residual force. The expected initial stiffness K_{exp} is obtained by multiplying Noory's Phase II tension-displacement slope by the active bonded area:

$$K_{exp} = (d\tau / d\delta) \times A = (5\ \text{to}\ 8\ kPa/mm) \times 0.18\ m^2 = 0.9\ \text{to}\ 1.4\ kN/mm \tag{6.4}$$

The expected residual force at large displacement, after the adhesive bond is fully broken and only sliding friction remains, is estimated from the end-of-test tension values reported by Noory et al. (2017), which lie in the range of approximately 20-25 kPa at displacements of ~22 mm. Adopting a representative value of 22 kPa from this range:

$$F_{res} = \tau_{res} \times A = 22\ kPa \times 0.18\ m^2 = 3.96\ kN \approx 4\ kN \tag{6.5}$$

Independent qualitative support for the existence of a substantial bond reduction at geosynthetic-asphalt interfaces is provided by Raab et al. (2017). Using a Layer-Parallel Direct Shear (LPDS) test on cores extracted from full-scale test sections trafficked with the MLS10 simulator, they reported maximum shear forces of approximately 16 to 28 kN at reinforced interfaces (glass-fiber with SAMI, glass-carbon, and polyester grids), compared to 38 to 40 kN at the unreinforced asphalt-asphalt reference, corresponding to reductions of roughly 30 to 60 percent depending on the system. Although LPDS shear results are not directly comparable to the interface shear mobilized in a pull-out test, both bodies of evidence consistently indicate that geosynthetic insertion lowers interfacial coupling relative to a fully bonded asphalt-asphalt interface. This qualitative agreement supports the order of magnitude of the 50 kPa value derived from Noory and adopted for the present benchmark.

The expected peak bond capacity of approximately 9 kN substantially exceeds the rated dry grab tensile strength of the paving fabric (550 N per CAN/CGSB-148.1 No. 7.3, Table 3.3). Although the narrow-jaw grab geometry is not directly comparable to the wide-width mobilization of the present configuration, even the bitumen-impregnated peak of 2.013 kN measured here remains far below the 9 kN expected bond. In a properly designed apparatus, debonding would mobilize well before the geotextile reached its tensile capacity, ensuring that the failure mode characterizes the interface bond rather than the fabric material. Figure 6.8 shows the expected curve, which differs from the actual test result in both shape and magnitude.

Phase I - Elastic interface response (0-8 mm): The initial response is characterized by a steep, nearly linear increase in pull-out force, reflecting the high initial stiffness of the asphalt-geotextile bond given by Equation (6.4) (K_{exp} = 0.9-1.4 kN/mm). This expected stiffness is approximately seventy times higher than the actual test value of 0.014 kN/mm. The gap has a simple cause. A rigid bonded interface transmits load immediately upon application, whereas a nonwoven fabric requires extensive deformation to align its randomly oriented fibers before measurable load can develop.

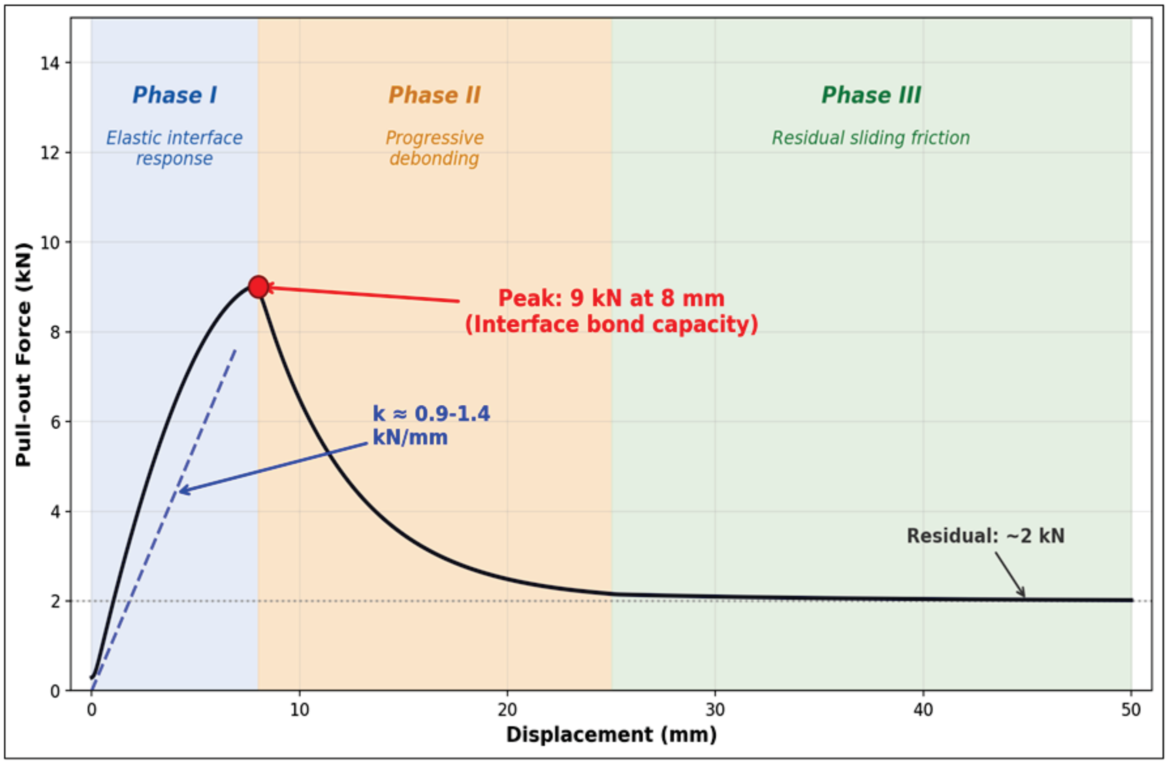

Figure 6.8 Expected load-displacement response for true interface debonding behavior of geotextile from ESG-10 asphalt layers

Phase II - Progressive geocomposite mobilization (8-25 mm): After the peak of approximately 9 kN given by Equation (6.3) is reached at a displacement on the order of 8 mm (within Noory's 7-12 mm peak-displacement range), the force decreases gradually. Following Noory's observation, this softening corresponds to the initiation of bulk movement of the geocomposite/geotextile within the asphalt matrix rather than purely progressive failure of an adhesive bond.

Phase III - Residual sliding friction (beyond 25 mm): Once the adhesive bond is fully broken along the entire embedded length, the pull-out resistance is governed solely by sliding friction between the geotextile and the asphalt surfaces. The expected residual force is approximately 4 kN given by Equation (6.5) ($F_{res} \approx 22$ kPa × 0.18 m² ≈ 4 kN). Although Noory's tests did not reach a fully stable residual plateau within the displacement range tested, the descending trend toward sliding-friction tension values of approximately 20-25 kPa is a defining feature of debonding behavior and is absent from the actual test response, where the post-peak descent reflects fabric rupture rather than sliding.

The peak force of approximately 9 kN expected for interface debonding is around four and a half times higher than the 2.013 kN peak measured in the actual test. This is mechanistically diagnostic: the test reached only about 22 percent of the expected interface bond capacity before the geotextile ruptured. Because the bonded interface, over its large bonded area and under the bolt-clamped confinement, was stronger than even the bitumen-impregnated geotextile could withstand, failure was forced to occur within the fabric material rather than at the interface. In a properly configured test, the interface bond strength would be lower than the tensile strength of the geotextile so that debonding governs failure; the present configuration violated this hierarchy.

6.5 Comparative Analysis

Figure 6.9 presents a direct overlay of the actual and expected pull-out curves; Table 6.2 consolidates the corresponding quantitative parameters.

The largest difference is the displacement at peak force: roughly 14× larger in the actual test. Interface debonding in asphalt systems is inherently a small-displacement phenomenon because the bond breaks through shear failure at the interface plane, with peak displacements of 7-12 mm reported by Noory et al. (2017) across the tested temperature and tack-coat conditions. The large displacement observed here is a direct consequence of the high elongation capacity of nonwoven geotextiles (typically 50-150 percent strain at break), which was fully mobilized because the interface bond remained intact.

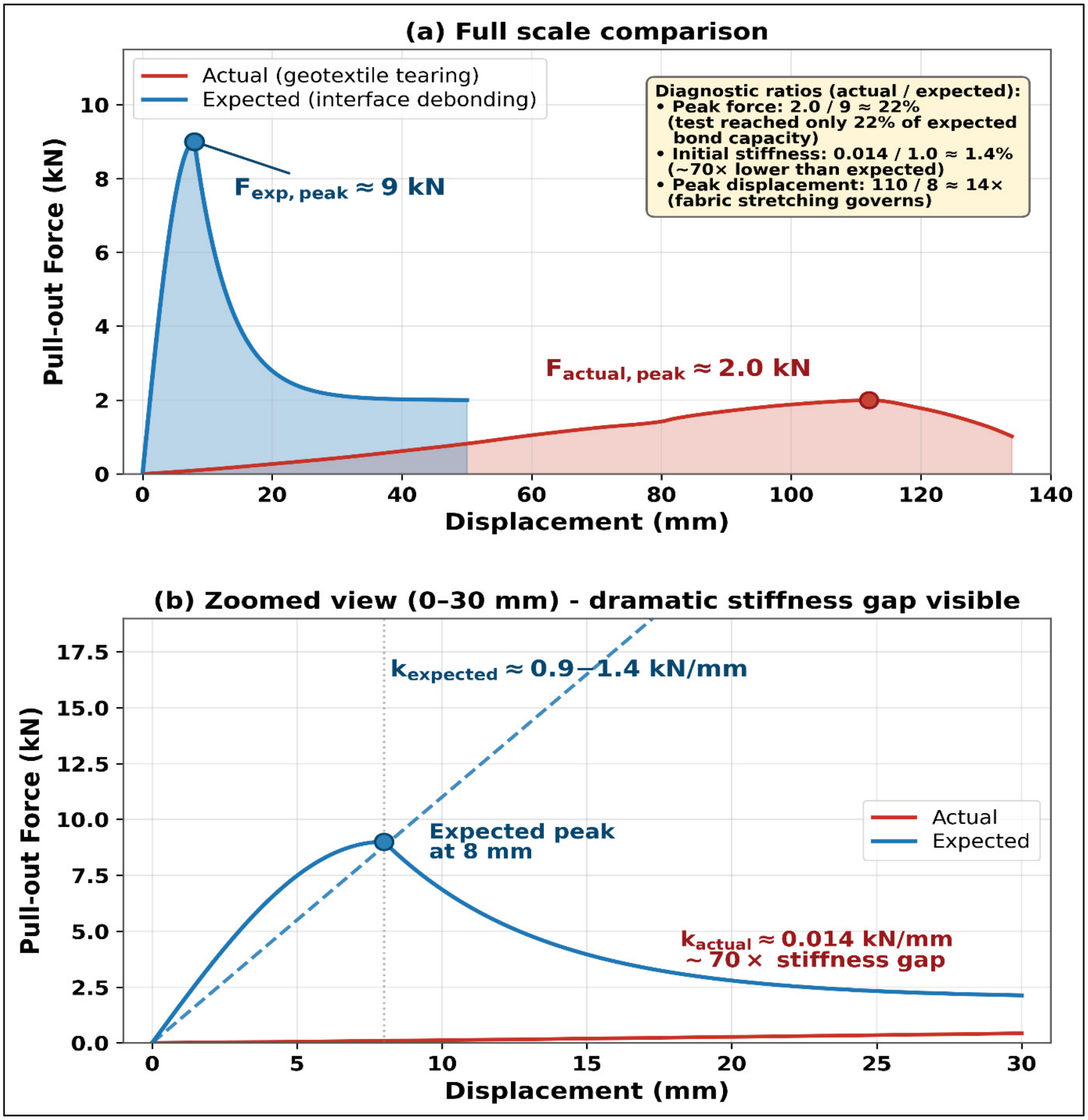

Figure 6.9 Comparison of actual pull-out response (geotextile tearing) and expected response (interface debonding): (a) full scale; (b) zoomed view showing initial stiffness contrast

Table 6.2 Quantitative comparison of actual versus expected pull-out test response

Parameter	Actual response (geotextile tearing)	Expected response (interface debonding)	Ratio (actual / expected)	Diagnostic
Peak force (kN)	2.013	~9 (upper bound)	~22%	✓✓
Displacement at peak (mm)	110	~8	~14× larger	✓✓✓
Initial stiffness (kN/mm)	0.014	0.9-1.4	~70× lower	✓✓✓
Initial-response mechanism	Fiber alignment (0-30 mm)	Elastic interface bond (0-8 mm)	-	✓
Post-peak window (mm)	24 (110-134)	~17 (8-25)	-	-
Residual force (kN)	1.05 (test terminated)	~4 (sliding friction)	-	✓
Total energy (kN·mm)	~144, spread over 134 mm	similar magnitude, narrow window	narrow vs broad	✓
Failure mode	Tensile rupture (~100% strain; width necked 180→93 mm)	Interface debonding (sliding)	different	✓✓✓
Reference / source	Direct MTS measurement	Noory et al. (2017): 50 kPa × 0.18 m²	-	-

The initial stiffness provides another diagnostic indicator. The actual test exhibited a stiffness of approximately 0.014 kN/mm in the Phase I region, characteristic of the compliant response of a nonwoven fabric being stretched. The expected interface response, derived from Noory's Phase II slope applied to the present specimen geometry of 0.18 square meters, would be on the order of 0.9-1.4 kN/mm. The actual stiffness is therefore less than two percent of the expected range, which corresponds to a reduction of roughly seventy-fold (a factor of 64 to 100 across the expected stiffness range). This gap is direct evidence that no genuine interface bond mobilization occurred during the test: had the bolt-clamped specimen permitted any meaningful interface response, the early load-displacement slope would have been at least one to two orders of magnitude steeper than what was measured.

The total energy absorbed during the actual test (the area under the load-displacement curve) is on the order of 144 kN·mm, a magnitude of broadly the same order as an idealized debonding response would produce. The spatial distribution of that energy, however, is very different. In the actual test the energy is spread thinly over 134 mm of large-displacement fabric stretching, whereas the expected debonding response would concentrate higher peak forces over a much narrower 8-25 mm displacement window. This shift from a tall-narrow response to a low-broad response is the signature of a failure mode that has migrated from the interface into the geotextile material. While the high energy absorption capacity of geotextiles is beneficial for crack retardation in service, the pull-out test should characterize the interface bond rather than the material tensile properties.

6.6 Calibration of the Finite Element Model Against the Measured Response

The finite element model introduced in Section 6.2.4 was extended to reproduce the measured pull-out response. Because the post-test examination showed no sliding at the interface, the embedded portion of the geotextile is effectively fixed between the asphalt blocks. The calibration analyses used a reduced model consisting of the free fabric length only, clamped along the mold-exit line. The full-specimen model of Section 6.2.4 is retained for stress visualization; the reduced model gives the same pull response at a small fraction of the computational cost.

The geotextile is represented by four-node conventional shell elements (S4R) lying on the interface plane between the two asphalt lifts. The shell section is 1.8 mm thick, the thickness of the impregnated fabric, with five integration points through the thickness. Shell elements suit this problem because the fabric works in membrane tension; at 1.8 mm its bending stiffness contributes nothing measurable to the pull response. In the full model of Section 6.2.4 the sheet is meshed with a 10 mm grid (900 elements over the 500 × 180 mm plan) and both faces exchange load with the asphalt lifts through surface-to-surface contact with hard normal behavior and a friction coefficient of 0.3. In the calibration model the embedded portion is replaced by the clamped mold-exit line, as explained above, and the free length is meshed at 5 mm in the pull direction so that the necking zone near the exit is resolved. The nineteen nodes of the grip line are driven together: the pull displacement is prescribed in the loading direction while the transverse, out-of-plane, and rotational degrees of freedom are held, reproducing the rigid grip of the test.

The free length between the mold exit and the grip was taken as 120 mm. This value was not measured directly before the test; it was derived from the post-test stretched length of the pulled fabric (26.5 cm) and the displacement at the end of the test, and it is consistent, within the uncertainty of that post-test measurement, with the approximately 130 mm back-calculated in Section 6.3.1. The calibrated material parameters are tied to this value. The grip line was displaced at constant rate to 165 mm under displacement control, mirroring the test. The analysis used the quasi-static explicit procedure with element removal at full damage; the kinetic energy remained below 0.3 percent of the internal energy up to the peak.

The impregnated fabric was represented by an elastic-plastic law with ductile damage. Four parameters control the structural response: the elastic modulus, the stress cap at which damage begins, the plastic strain at damage onset, and the displacement over which the material degrades to zero stress. Starting values were obtained in closed form from the measured anchors (peak force 2.013 kN at 110 mm, dissipated work 144.4 kN·mm) on an idealized uniaxial strip. A first analysis with these values reproduced the failure displacement within 5 percent but overestimated the peak force by 50 percent, because the clamped ends prevent the lateral contraction assumed in the closed-form estimate. The two governing parameters were then updated once, using the ratio between the first-run response and the targets. The final set is: elastic modulus 11.6 MPa, stress cap 7.95 MPa (true stress), damage onset at a plastic strain of 0.005, and a damage displacement of 43 mm obtained from the work balance of the measured curve.

Table 6.3 compares the calibrated model with the measurement. The model reaches a peak of 1.984 kN at 111.5 mm, against 2.013 kN at 110 mm measured, and dissipates 141.2 kN·mm against 144.4 kN·mm. Damage initiates and grows in the element row at the mold exit, the fabric necks there, and the section separates at that location - the same failure mode and location observed in the test (Section 6.3).

Figure 6.10 overlays the two curves. The model matches the measured peak, the displacement at peak, and the dissipated work. The two paths to the peak differ in shape: the measured curve is concave upward, because load is first carried by progressive fiber realignment, whereas the elastic-plastic law gives a concave-downward path. Past the peak the model drops within a few millimeters, while the measured force decreased progressively to 1.05 kN at 134 mm, where the test was terminated.

The difference in curvature has a physical origin. The paving fabric is a needle-punched nonwoven. At low load, most fibers are slack or inclined to the loading direction, and only a small fraction of them is straight and in tension. As the displacement grows, fibers straighten and rotate toward the loading direction, and more fibers are recruited into tension. The apparent stiffness increases with elongation, which produces the J-shaped, concave-upward measured curve. An isotropic elastic-plastic law behaves in the opposite way by construction: it starts at its full elastic stiffness and can only soften as the stress approaches the plastic cap and necking develops. No parameter set of this law can reproduce recruitment hardening. Because the two curves were calibrated to share the same peak point and the same area under the curve, and their curvatures are opposite, they necessarily cross. The model runs above the measurement over most of the rising branch and is caught near the peak. The crossing follows from the calibration targets. It is not an additional model error.

The shape difference does not indicate slip. Slip at the asphalt-fabric interface would produce the debonding response of Section 6.4: a peak near 9 kN at about 8 mm, followed by a frictional plateau near 4 kN. Neither feature appears in the measured curve, and the interface was loaded to only about 22 percent of its estimated bond capacity. The post-test observations agree: the fabric tore and necked at the mold exit, and the embedded portion remained bonded in the asphalt (Section 6.3.2). The length balance closes as well: the post-test stretched length of 26.5 cm equals the initial free length of approximately 130 mm plus the actuator travel of 134 mm, so the machine displacement is fully accounted for by fabric elongation. Slip at the hydraulic grip cannot be excluded completely, because no strain was measured directly on the fabric, but the closed length balance and the smooth, continuous measured curve indicate that any grip slip was minor.

The elongation of the fabric is also not uniform, at two scales. At the fiber scale, only part of the fibers are in tension at any load level, and the impregnating bitumen redistributes load locally at the fiber crossings. The progressive recruitment of the remaining fibers is what generates the concave-upward curve. At the specimen scale, the deformation localized at the mold exit, where the clamped boundary concentrates stress, and the width necked from 180 mm to about 93 mm. The stretching is therefore non-uniform both along the free length and across the width. A single strain value can describe the fabric only on average.

Three limitations bound the calibration. First, the free gauge length was derived rather than measured, and the elastic modulus and stress cap scale with it; a direct measurement of the mold-exit-to-grip distance would remove this uncertainty. Second, the initial stiffness of the model (0.026 kN/mm) exceeds the measured toe stiffness (0.014 kN/mm), because the fiber-realignment stage of a nonwoven fabric is not represented by an elastic-plastic law. A fabric material model driven by the full measured curve would be required to capture it. Third, the post-peak drop is abrupt in the model because the damage localizes in a single element row, while the real rupture progressed over a long-necked zone. Because the damage localizes in this way, the post-peak branch is also mesh-dependent; the peak force and the pre-peak response are governed by the elastic-plastic parameters and the geometry and are not mesh-dependent.

Table 6.3 Calibrated model versus measured pull-out response

Quantity	**Measured**	**FE model**	**Deviation**
Peak force (kN)	2.013	1.984	-1.4%
Displacement at peak (mm)	110	111.5	+1.4%
Dissipated work (kN·mm)	144.4	141.2	-2.2%
Failure mode	tensile tearing	tensile tearing	-
Failure location	mold exit	mold-exit element row	-

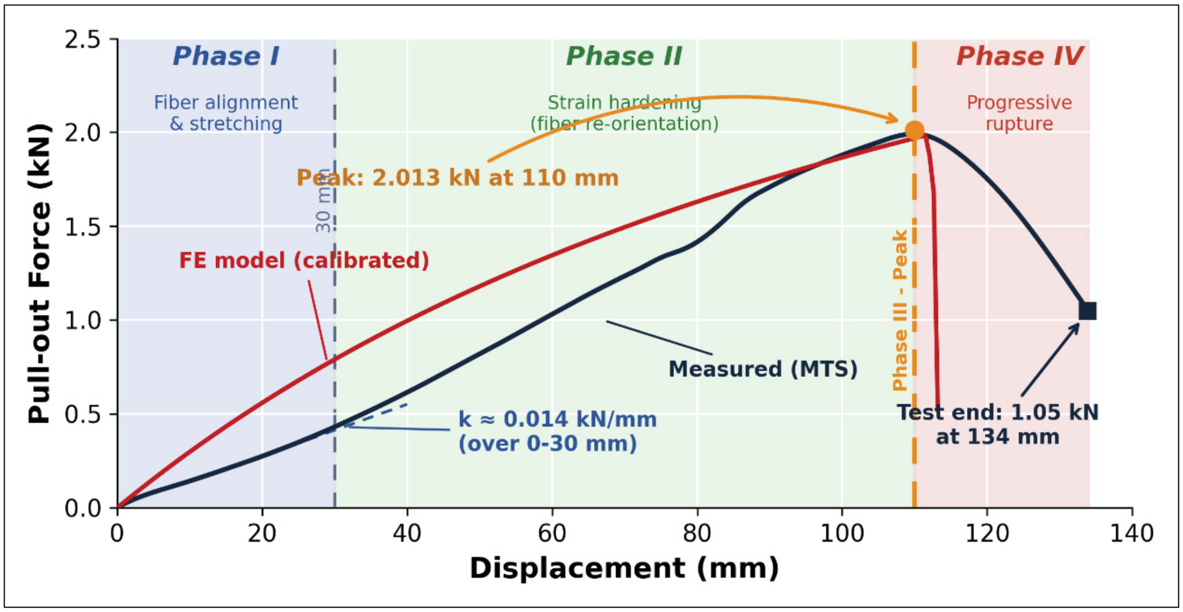

Figure 6.10 Measured pull-out response compared with the calibrated finite element model: the model reproduces the peak force (-1.4%), the displacement at peak (+1.4%), and the dissipated work (-2.2%), and tears at the mold exit; the rising-branch shape and the post-peak rate are outside the scope of the elastic-plastic material law (see text).

Within these limits, the calibrated model reproduces the three measured anchors within 3 percent and places the failure at the observed location. It gives quantitative support to the tensile-tearing interpretation of Sections 6.3 and 6.5 and provides a working numerical basis for the next-generation apparatus of Section 6.8: once a test produces interface debonding, the same framework can be recalibrated to extract interface parameters instead of fabric parameters.

6.7 Mechanistic Interpretation of the Failure Mode

6.7.1 Fundamental Differences: Soil vs. Asphalt Pull-out

The mechanics of pull-out resistance differ fundamentally between soil-geosynthetic and asphalt-geosynthetic systems. In soil systems, pull-out resistance is primarily governed by interface friction on both surfaces of the geosynthetic and passive bearing resistance for geogrids with transverse ribs. The confining soil is granular and can rearrange as the geosynthetic displaces, allowing progressive mobilization of friction along the embedded length (Gupta et al., 2014). The failure mode is typically sliding of the geosynthetic through the soil, and the peak pull-out force is reached at relatively small displacements (typically 5-25 mm depending on embedded length and normal stress).

In asphalt overlay systems, the pull-out resistance mechanism involves three distinct components that act simultaneously. First, adhesion from the tack coat creates a chemical/physical bond between the asphalt matrix and the geotextile fibers. During overlay placement at elevated temperatures (140-160 °C), the bitumen penetrates into the nonwoven fabric structure, creating an impregnation zone that strengthens the bond upon cooling. Second, mechanical interlock occurs as aggregate particles from the ESG-10 mixture embed into the geotextile surface, creating physical anchorage points. Third, confinement pressure from the overlying asphalt layer generates normal stress-dependent friction at the interface.

At service temperatures (below 40 °C), the asphalt layers exhibit viscoelastic behavior with relatively high stiffness, unlike the compliant granular soil in conventional pull-out tests. This means that the combined adhesion, interlock, and friction forces at the asphalt-geotextile interface can potentially exceed the tensile strength of the geotextile itself, particularly for nonwoven fabrics which have relatively low tensile strength and high elongation at break.

6.7.2 The Role of Clamping Configuration

The clamping configuration of the steel mold governs the failure mode of the pull-out test. The bolt-tightened design was originally selected to ensure the structural integrity of the specimen during loading, but tightening the top plate against the specimen creates an external confinement that is superimposed on the natural interface bond. This mechanical confinement (i) raises the normal stress on the geotextile far beyond what would exist in a real pavement, (ii) suppresses the vertical separation that would normally accompany debonding, and (iii) effectively clamps the asphalt layers together so that the geotextile cannot slide between them.

In a real pavement structure, the static confinement on the geosynthetic interlayer comes only from the overlay self-weight. For a typical 40-60 mm overlay this corresponds to roughly 1-1.5 kPa. Transient traffic loading superimposes higher stress pulses, but these act only momentarily as each wheel passes, whereas the confinement relevant to a slow, quasi-static pull-out is the sustained component, which remains on the order of 1-1.5 kPa. The bolt-tightened steel plates in the present apparatus impose a sustained normal stress well above this field value; although the clamping force was not instrumented, the rigid bolted assembly both elevates the interface normal stress and, more decisively, suppresses the vertical separation and interfacial sliding that an interface debonding requires. Under this over-confinement, the combined adhesion, interlock, and friction resistance at the interface exceeds the tensile capacity of the nonwoven geotextile. The failure mechanism therefore migrates from the interface to the fabric itself, as illustrated schematically in Figure 6.11.

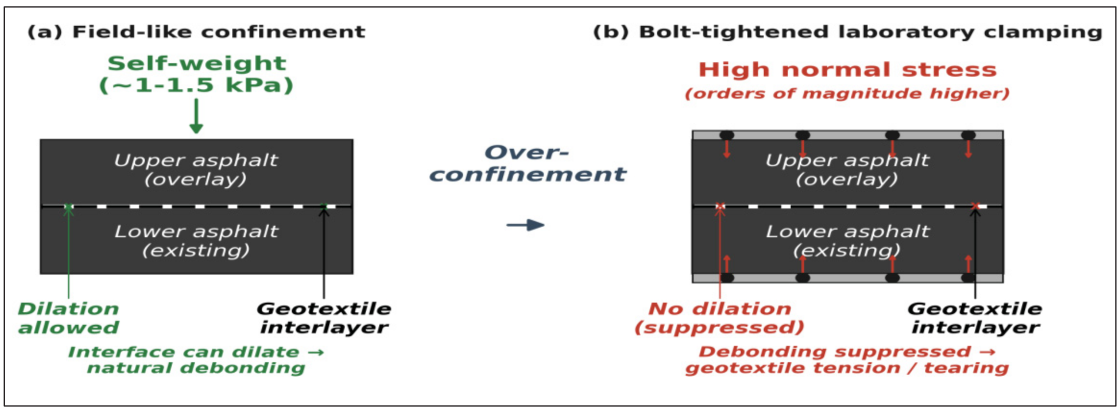

Figure 6.11 Effect of confinement system on the failure mode: (a) field-like overlay self-weight (~1-1.5 kPa) allows interface dilation and natural debonding; (b) bolt-tightened laboratory clamping imposes normal stresses well above field levels and suppresses debonding, forcing tensile failure of the geotextile

Figure 6.11(a) represents field service conditions, where the geotextile interlayer is subjected only to the self-weight of the asphalt overlay and any traffic surcharge. Under these modest normal stresses (typically 1-5 kPa), the interface plane retains the freedom to dilate vertically, which is the kinematic prerequisite for debonding to initiate and propagate.

Figure 6.11(b) depicts the laboratory configuration. The bolted top plate transmits a confinement pressure to the specimen that exceeds the field stress by orders of magnitude, preventing any vertical separation at the bond plane and pushing the friction and interlock components of the interface resistance well beyond the tensile capacity of the geotextile material. The result is a complete migration of the failure mechanism: rather than sliding at the interface, the geotextile is forced to elongate and tear within its own cross-section, as confirmed by the post-test observations described in Section 6.3.2.

6.8 Discussion and Recommendations

The analysis shows that the first-generation pull-out test apparatus, designed and fabricated in-house at the LCMB, identified a design limitation in its current configuration. While the bolt-tightened steel clamping system provides firm specimen confinement, this investigation revealed that the excessive mechanical confinement, compounded by the large, bonded area of the specimen, transforms the test from an interface characterization method into a tensile test of the geotextile material. The measured peak force of 2.013 kN therefore represents the confined tensile strength of the paving fabric, not the pull-out resistance at the asphalt-geotextile interface.

The measured value of 2.013 kN is several times the manufacturer's rated dry grab tensile of 550 N (CAN/CGSB-148.1 No. 7.3, Table 3.3); although the two are not measured under comparable geometries, the elevation above the dry rated value is consistent with the well-established effect of bitumen impregnation, which transforms the nonwoven fabric into a composite in which the bitumen matrix contributes additional resistance through fiber-matrix friction and viscous drag. The post-test necking (26.5 cm stretched length, narrowing from the 180 mm specimen width to about 142 mm at the specimen edge and 93 mm at the neck, elongation-at-failure on the order of 100 percent) provides direct physical confirmation of tensile failure, consistent with the 45-105 percent grab-tensile elongation rated for this fabric (Table 3.3).

These observations leave no ambiguity about the failure mode. The main lesson from this prototype is the sensitivity of pull-out test outcomes to the boundary conditions imposed by the clamping system: an apparatus that confines the specimen too tightly does not measure interface bond, even when load and displacement are recorded with high precision. This sensitivity is rarely quantified in the published literature on asphalt-geosynthetic pull-out testing and represents a transferable contribution: future apparatus designs must explicitly verify the failure mode before reporting pull-out strength.

These results also reinforce the distinction drawn in Section 6.7.1 between the two families of pull-out systems. In soil, the geosynthetic is embedded in a discrete granular medium:

resistance is essentially frictional, mobilized progressively along the embedded length as particles rearrange, and failure occurs by sliding of the inclusion through the soil. In an asphalt overlay, by contrast, the geotextile is bonded within a continuous viscoelastic matrix: frictional resistance acts together with a cohesive component created by tack-coat adhesion and bitumen impregnation, so that any sliding must overcome both friction and the rupture of this cohesive bond. The 2.013 kN anchorage force measured here, several times the rated dry grab tensile strength of the fabric, is a direct manifestation of this cohesive contribution. Consequently, test procedures and interpretation frameworks developed for soil-geosynthetic pull-out cannot be transposed directly to asphalt systems: in a cohesive, continuous medium the governing question is not the frictional sliding capacity of the interface, but the competition between interface debonding and tensile failure of the geotextile, which the confinement conditions of the apparatus decide.

Secondly, geometric factor reinforces this conclusion and qualifies the role attributed to confinement above. The expected bond capacity of approximately 9 kN was derived in Section 6.4 from the interface shear strength under representative ambient conditions applied over the bonded area of the present specimen; it is a property of the bond strength and the specimen size rather than of the over-confined clamping. This benchmark already exceeds the tensile capacity of the nonwoven fabric by a wide margin: the fabric capacity is fixed by the material at the order of 0.55 kN dry on a grab basis, rising only to the roughly 2 kN measured here once bitumen-impregnated, whereas the 9 kN figure is the product of the interface shear strength and the relatively large, bonded area of 0.18 square meters (some 9.5 times that of Noory's specimens). Because the total bond force scales with the bonded area, reducing the confinement toward field levels would lower the friction component of the interface shear strength but would not by itself bring the bond capacity below the fabric tensile capacity over an embedment of this size. Over-confinement thus aggravated an outcome that the specimen geometry alone already made likely. Restoring the necessary bond-below-tensile hierarchy consequently requires the specimen geometry to be addressed jointly with the confinement, most directly by shortening the embedded (bonded) length, or by lowering the interface shear strength through elevated-temperature testing, as reflected in the recommendations below.

Based on the analysis above, the following refinements are proposed for a next-generation pull-out apparatus to achieve valid interface characterization of asphalt-geosynthetic systems:

(a) Replace bolt-tightened clamping with dead-weight or pneumatic confinement applying a field-representative stress (1-5 kPa, including transient traffic surcharge above self-weight).

(b) Add multiple LVDTs along the embedded length to monitor frontal and internal displacement and track the debonding front.

(c) Implement a systematic failure-mode validation protocol after each test by examining whether the geotextile slid out of the interface (debonding) or experienced material damage (tensile failure).

(d) Design the apparatus to accommodate testing at elevated temperatures (40-60 °C) to reduce the asphalt stiffness and bond strength sufficiently to promote interface failure before geotextile tensile failure.

(e) Size the bonded (embedded) area so that the resulting bond capacity remains below the tensile capacity of the interlayer being tested. For a weak nonwoven fabric this implies a substantially shorter embedded length than the full 500 mm slab used here, or alternatively the use of an interlayer with a higher tensile capacity, such as a geocomposite or grid, for a given bonded area.

(f) Consider using complementary direct shear tests such as the Leutner shear test (EN 12697-48) for reliable interface bond characterization, as recommended in the literature (Correia et al., 2024; Canestrari et al., 2012).

With these refinements, the prototype can become a reliable, standardized tool for characterizing interface bond properties of geosynthetic interlayers in asphalt overlay systems.

6.9 Summary

This chapter presented a supplementary pull-out investigation of a paving fabric interlayer using a first-generation apparatus developed in-house at the LCMB. The mechanistic analysis showed that the bolt-tightened clamping configuration forced failure into the geotextile material rather than at the asphalt-geotextile interface, identifying an apparatus design limitation. Benchmarking against the published debonding behavior of Noory et al. (2017) confirmed that the test reached only a fraction of the expected interface bond capacity. Section 6.8 presents six design refinements for the next generation of the apparatus. A finite element model calibrated against the measured response reproduced the peak force, the displacement at peak, and the dissipated work within 3 percent, with tearing at the mold exit.

CHAPTER 7

CORRELATION BETWEEN MONOTONIC AND CYCLIC FATIGUE LOADING BEHAVIOR OF GEOSYNTHETIC-REINFORCED ASPHALT INTERLAYERS

7.1 Introduction

This chapter presents an analysis of the empirical correlation between monotonic test parameters and cyclic fatigue loading behavior for four asphalt interlayer configurations tested using the Crack Widening Device (CWD). The primary objective is to explore empirical correlations between quasi-static monotonic test parameters and fatigue life, providing a diagnostic framework for evaluating consistency between monotonic and fatigue performance trends.

The four configurations investigated include: (i) unreinforced control specimens, (ii) specimens reinforced with Carbophalt GB geogrid (GB), (iii) specimens reinforced with Glasphalt GV 120/120 geocomposite (GV), and (iv) specimens reinforced with paving fabric geotextile (PF). All specimens were 80 x 80 x 80 mm cubic asphalt samples with the geosynthetic interlayer placed at the one-half depth position (40 mm from the specimen bottom).

One observation from the experimental program needs attention: the PF geotextile fatigue results appear inconsistent with the monotonic loading behavior. While PF performs best under monotonic loading - particularly at lower displacement rates - its measured fatigue life values are comparable to or only marginally better than the unreinforced control. This chapter develops an exploratory diagnostic framework, calibrated on the three consistent datasets (Control, GB, GV), to test whether the PF fatigue measurements are consistent with the trend established by the other materials. The framework is intended as a residual analysis on the PF observation and not as a generalized predictive model; both the calibration logic and its limitations are reported in detail in Sections 7.6 and 7.7.

7.2 Cyclic Test Protocol

Cyclic loading tests were performed on the same specimen configuration as the monotonic tests: 80 × 80 × 80 mm CWD specimens with a 15 mm starter notch and the reinforcement placed at the one-half position, giving a 25 mm gauge length between the notch tip and the interlayer. The tests were load-controlled at room temperature (25 °C): the vertical load was cycled in a haversine (compression-only sinusoidal) pattern between the preset compressive load (up to 100 N) and the target load level, at target levels of 1 to 5 kN for the reinforced configurations (1 to 4 kN for the Control) and at loading frequencies of 1 Hz and 2 Hz. The axial force, axial displacement, and cycle count were recorded continuously and reduced to per-cycle quantities: the force and displacement extrema, the load and displacement amplitudes, the cyclic stiffness and the corresponding dynamic modulus, the dissipated energy per cycle, the accumulated permanent displacement, and the phase angle. The stress amplitude assigned to each test was computed as the average load amplitude over cycles 3 to 10 divided by the specimen cross-section (6,400 mm^2). The specimen configuration - including the dry, unbonded contact between the specimen and the two triangular pieces of the CWD apparatus described in Chapter 5 - was identical to that of the monotonic tests, and a preset compressive load of up to 100 N was applied prior to each test as in the monotonic protocol. Failure (Nf) was defined as a 50% reduction in peak force relative to the initial stabilized value, or complete fracture of the specimen, whichever occurred first. Figure 7.1 shows the loading history of a representative test (GV geocomposite, 1 Hz, 3 kN): panel (a) shows the loading waveform over cycles 50 to 54, panel (b) confirms that the per-cycle load envelope remains essentially constant throughout the test, and panel (c) shows the displacement envelope accumulating progressively until failure at Nf = 244 cycles.

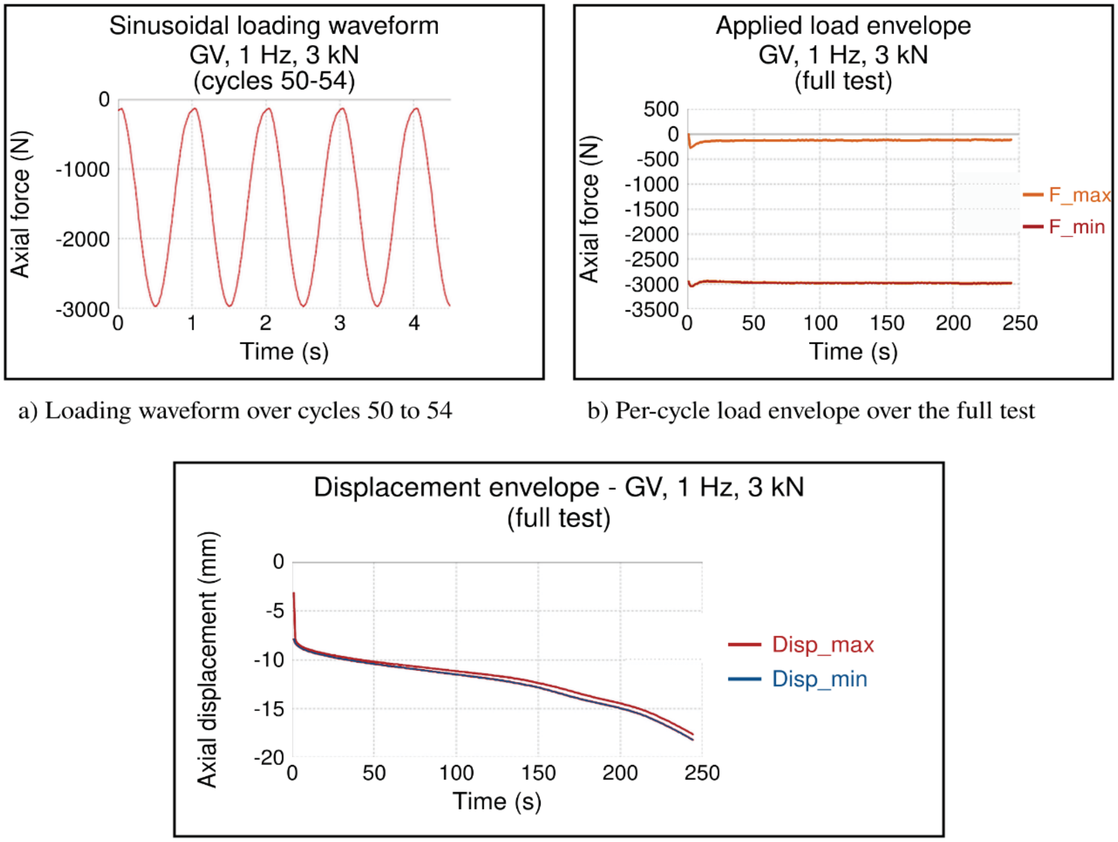

a) Loading waveform over cycles 50 to 54

b) Per-cycle load envelope over the full test

c) Per-cycle displacement envelope up to failure at $N_f = 244$ cycles

Figure 7.1 Loading history of a representative cyclic test (GV geocomposite, 1 Hz, 3 kN target load, one-half placement): (a) applied sinusoidal loading waveform over cycles 50 to 54; (b) per-cycle envelope of the maximum and minimum applied force, showing a constant load amplitude over the full test; (c) per-cycle envelope of the axial displacement, showing progressive accumulation up to failure at $N_f = 244$ cycles.

7.3 Monotonic Loading Test Results

7.3.1 Force-Displacement Response at 5 mm/min

Monotonic loading tests were conducted at two displacement rates, 5 mm/min and 2 mm/min, so that the rate dependence of each interlayer could be assessed. Figure 7.2 curves at 5 mm/min for all four configurations.

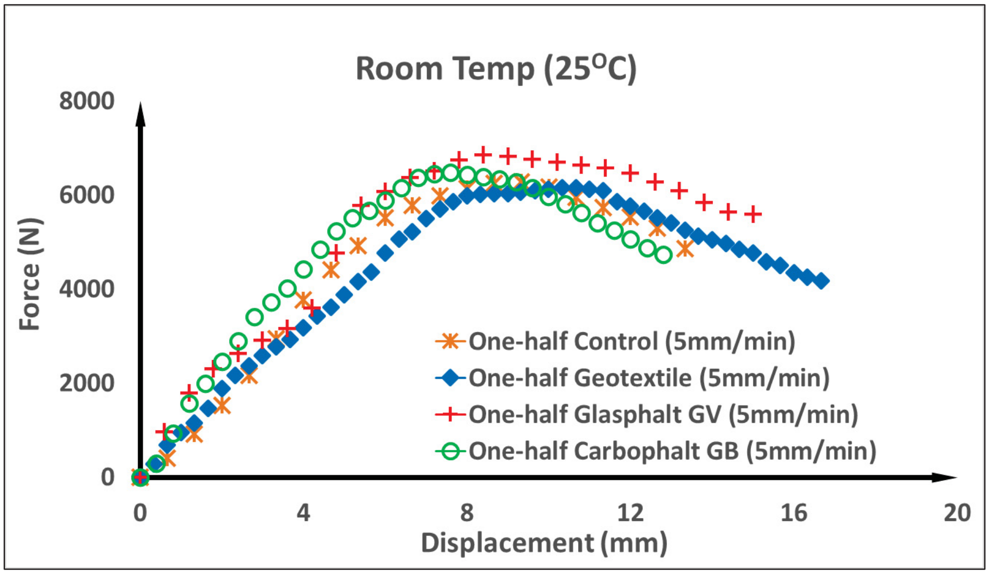

Figure 7.2 Monotonic force-displacement curves at 5 mm/min loading rate (one-half placement)

At this faster rate the four peak forces fell within a narrow band: the GV geocomposite recorded the highest peak (6,856 N), followed by the GB geogrid (6,490 N), the unreinforced control (6,302 N), and the PF geotextile (6,162 N). The two stiff reinforcements led on peak force, while the PF geotextile carried the lowest peak, marginally below the control. The PF specimen, however, showed the most gradual post-peak softening and the longest time to failure (128 s versus 110 s for the control), indicating that at this rate its contribution lies in ductility and energy absorption rather than in peak load.

7.3.2 Force-Displacement Response at 2 mm/min

At the slower rate of 2 mm/min the ranking changed markedly. The corresponding force-displacement curves are given in Figure 7.3.

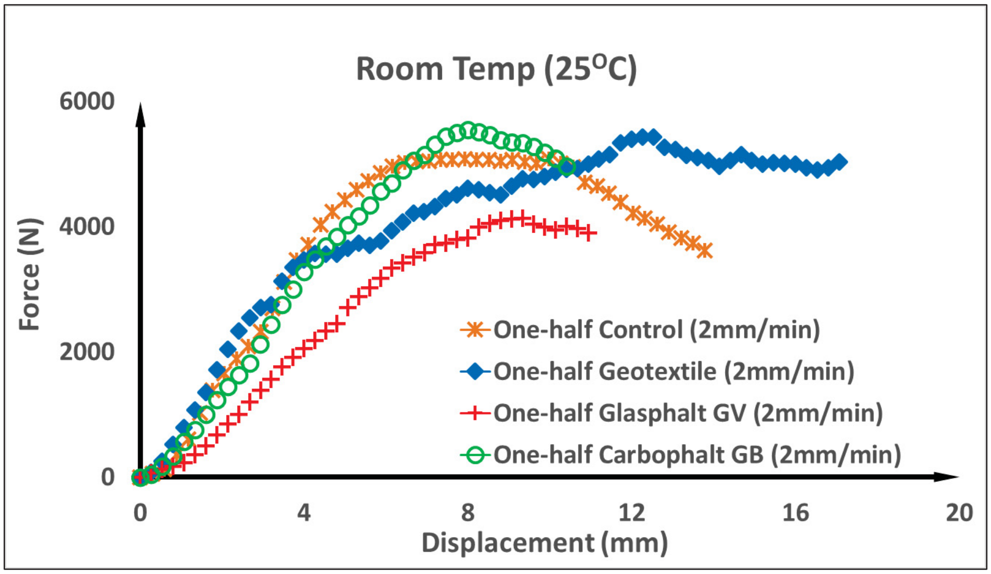

Figure 7.3 Monotonic force-displacement curves at 2 mm/min loading rate (one-half placement)

The peak-force order reversed relative to 5 mm/min: the PF geotextile rose from last to second (5,454 N), now exceeding the control (5,083 N) by 7.3%, while the GV geocomposite fell from first to last (4,148 N), 18% below the control; the GB geogrid remained the strongest (5,560 N). The ductility advantage of the PF geotextile, already visible at 5 mm/min, became pronounced at this rate: its time to failure reached 367 s against 235 s for the control, a 56.2% increase and the longest of the four materials. As the loading rate decreased, the PF geotextile thus rose in the peak-force ranking and widened its time-to-failure margin over the control, whereas the GV geocomposite dropped from first to last, a divergence that testing at a single rate would not reveal.

7.3.3 Summary of Monotonic Test Parameters

Two observations emerge from the monotonic tests. First, every configuration reached a higher peak force at the faster rate, consistent with viscoelastic stiffening of the asphalt matrix. Second, the ranking among the interlayers was not fixed but rate-dependent: the PF geotextile was weakest on peak force at 5 mm/min yet second strongest at 2 mm/min, the GV geocomposite moved in the opposite direction, and the GB geogrid stayed comparatively stable. No single monotonic rate characterizes these materials, and peak force alone can rank them in contradictory orders. This rate dependence motivates the loading-rate sensitivity index introduced in the next section and underpins the monotonic-to-fatigue correlation developed later in the chapter.

Figure 7.4Table 7.1 the time to failure, peak force, and displacement at failure for all four configurations at both rates. Panel (c) shows that the PF geotextile sustains the largest deformation before failure at both rates (16.7 mm at 5 mm/min and 17.3 mm at 2 mm/min), whereas the GV geocomposite shows the largest reduction at the slower rate (from 15.3 mm to 11.2 mm, a 27% drop), consistent with its pronounced rate sensitivity.

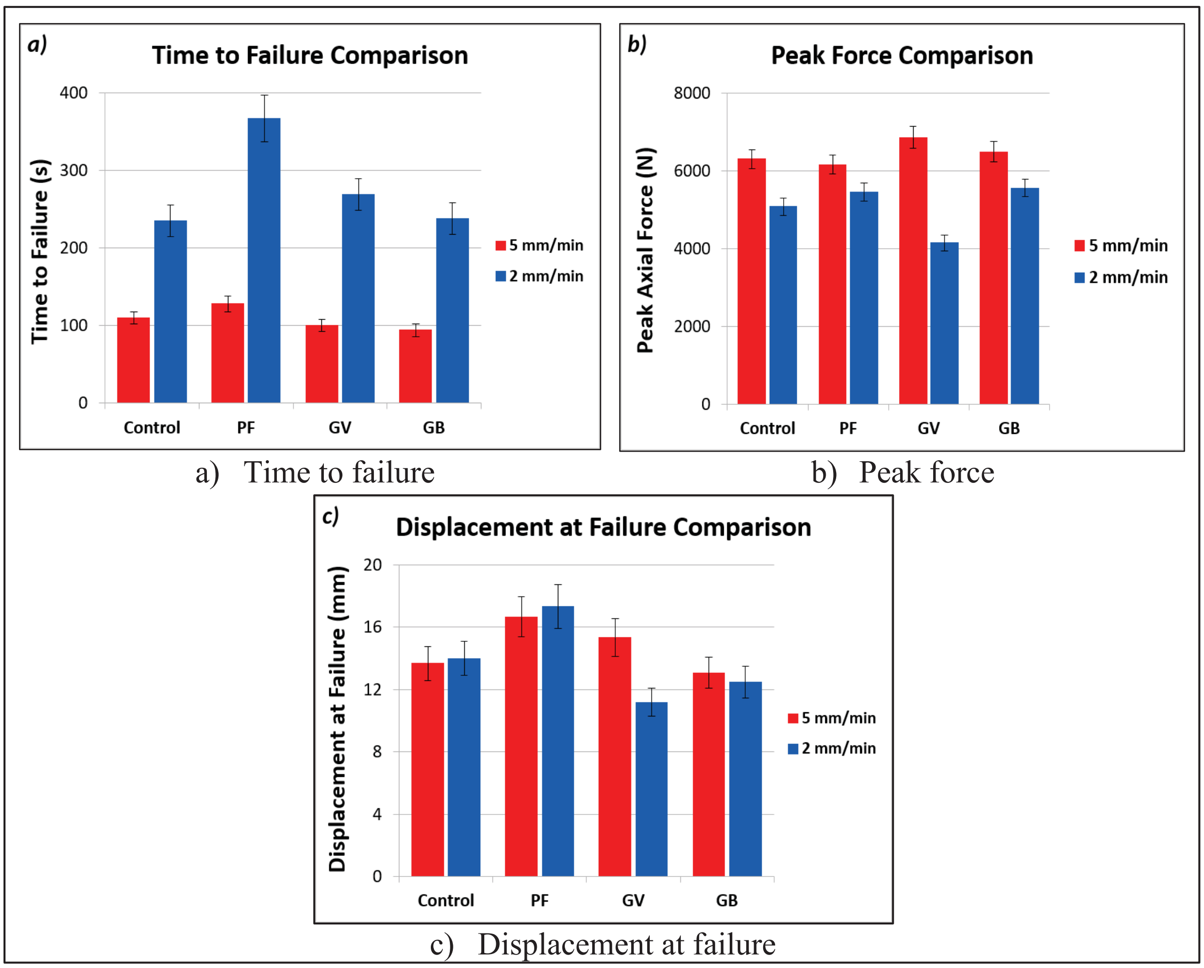

a) Time to failure

b) Peak force

c) Displacement at failure

Figure 7.4 Effect of displacement rate on the monotonic response of the four interlayer configurations at the one-half placement, comparing 5 mm/min and 2 mm/min: (a) time to failure; (b) peak axial force; (c) displacement at failure. Error bars represent ±1 SD estimated from the coefficient of variation observed across placement positions within the same testing campaign (~8% for time and displacement; ~4% for peak force).

Table 7.1 Monotonic test parameters at one-half placement (percentage values at 2 mm/min relative to Control)

Material	Time 5mm (s)	Force 5mm (N)	Time 2mm (s)	Force 2mm (N)	% Time	% Force
Control	110	6,302	235	5,083	-	-
Geotextile PF	128	6,162	367	5,454	+56.2%	+7.3%
Geocomposite GV	100	6,856	269	4,148	+14.5%	-18.4%
Carbophalt GB	94	6,490	238	5,560	+1.3%	+9.4%

7.4 Loading Rate Sensitivity Analysis

The ratio of time to failure at 2 mm/min to that at 5 mm/min provides a quantitative measure of each material's apparent loading rate sensitivity. This parameter matters because fatigue loading at 1-2 Hz involves effective strain rates much lower than 5 mm/min monotonic tests. Figure 7.5 plots this index for all four configurations.

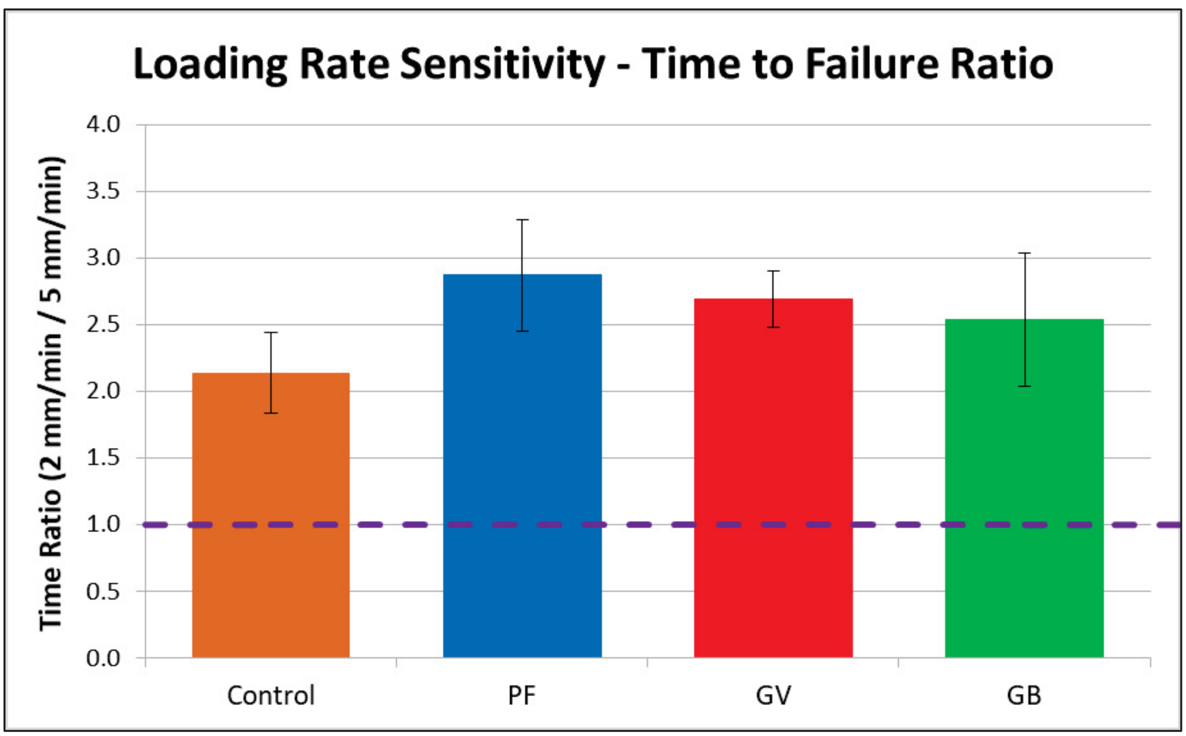

Figure 7.5 Loading rate sensitivity index (time ratio 2 mm/min to 5 mm/min)

The PF geotextile possesses the highest rate sensitivity index of 2.87, compared to GV (2.69), GB (2.53), and Control (2.14). This index quantifies the time-to-failure ratio between two monotonic loading rates, which is conceptually distinct from the energy retention ratio analyzed in Section 7.8 (ratio of energy at slow rate to energy at fast rate for the same specimen) and from the Toughness Improvement Factor (TIF) defined in Chapter 5 (energy of reinforced specimen relative to unreinforced control at the same rate). Under the time-based metric, PF stretches out longer at slow rates (more time to failure). The energy retention ratio shows PF retains nearly the same total absorbed energy at both rates (0.97). The two metrics are consistent: PF is rate-stable in absolute energy absorption but rate-sensitive in time-to-failure. This elevated rate sensitivity can be attributed to the continuous paving fabric providing distributed stress transfer across the crack face, which becomes increasingly effective as the loading rate decreases.

The physical mechanism is related to the viscoelastic nature of the bitumen-geotextile interface. At lower loading rates, the paving fabric has more time to develop adhesive bonding and frictional resistance along its continuous surface area.

7.5 Cyclic Fatigue Loading Test Results

7.5.1 S-N Curves and Basquin Regression

The fatigue data were fitted using the Basquin power law relationship, which relates the applied stress amplitude to the number of cycles to failure:

$$\sigma_a = A * (N_f)^\wedge B \tag{7.1}$$

where σ_a is the applied stress amplitude (MPa), N_f is the number of cycles to failure, A is the fatigue strength coefficient (intercept), and B is the Basquin exponent (slope in log-log space). The exponent B is always negative, indicating decreasing fatigue life with increasing stress amplitude. The magnitude |B| quantifies the material's sensitivity to stress level changes - a higher |B| indicates steeper decline in fatigue life with increasing stress.

In logarithmic form, Equation (7.1) becomes:

$$\log(N_f) = (1/B) * \log(\sigma_a) - (1/B) * \log(A) \tag{7.2}$$

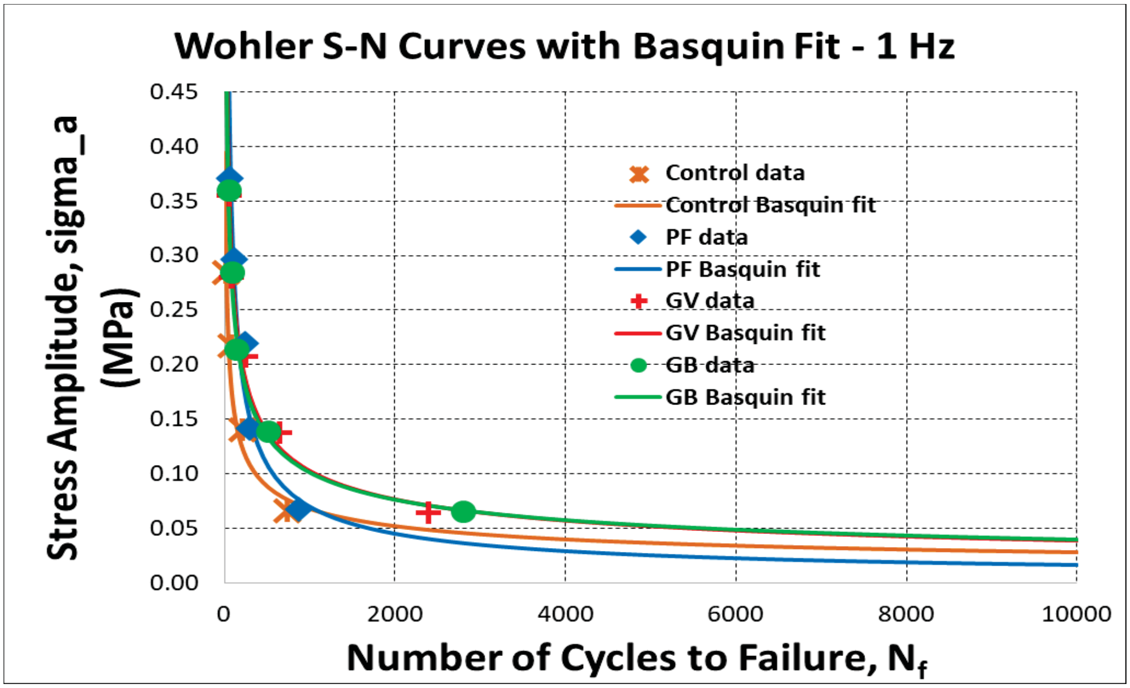

Figure 7.6 Wöhler S-N curves with Basquin fit at 1 Hz

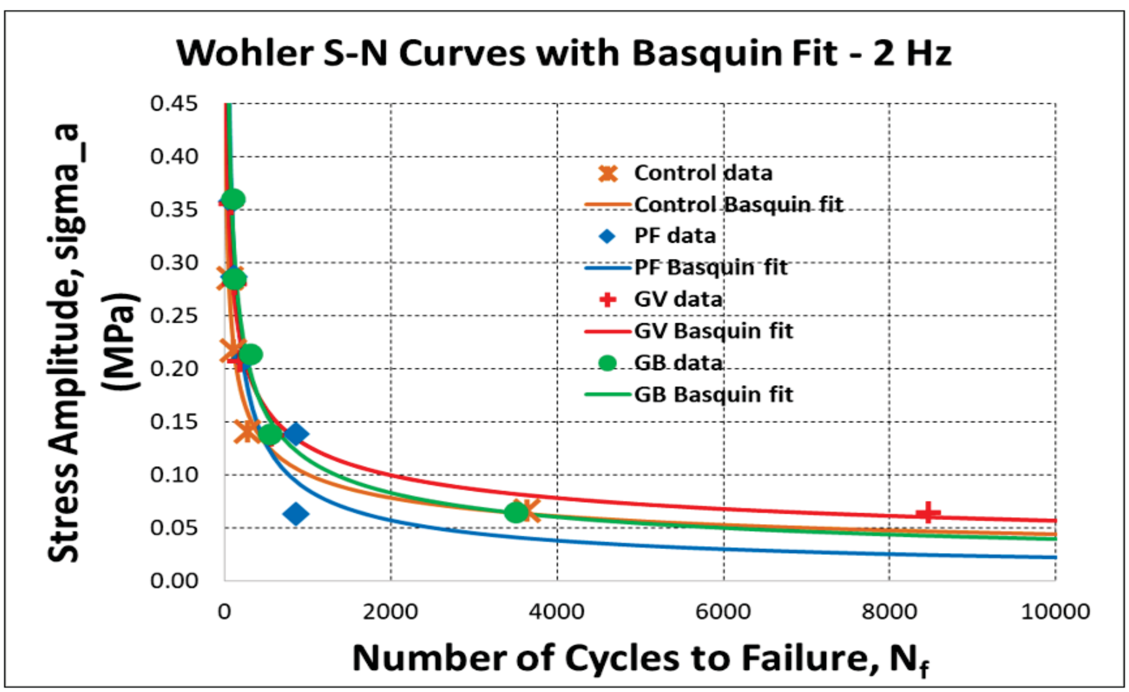

Figure 7.7 Wöhler S-N curves with Basquin fit at 2 Hz

This linearized form enables direct regression analysis of the experimental data. For each material-frequency combination, the Basquin parameters A and B were determined by least-squares regression of $\log(N_f)$ versus $\log(\sigma_a)$. The fitted Basquin curves for each configuration are shown in Figures 7.6 and 7.7, and the slope magnitudes are compared in Figure 7.9.

7.5.2 Fatigue Improvement Factor

The Fatigue Improvement Factor (FIF), defined as the ratio of reinforced to control fatigue life, provides a direct measure of reinforcement effectiveness. Because the Control configuration was tested only up to 4 kN, all mean fatigue lives and improvement factors are computed over the common 1 to 4 kN load range.

The FIF is defined as:

$$\mathrm{FIF} = N_{f,\mathrm{reinforced}} / N_{f,\mathrm{control}} \tag{7.3}$$

where $N_{f,\mathrm{reinforced}}$ is the number of cycles to failure for the reinforced specimen, and $N_{f,\mathrm{control}}$ is the corresponding value for the unreinforced control at the same load amplitude and frequency. A FIF greater than 1.0 indicates that the reinforcement extends fatigue life relative to the unreinforced configuration.

Figure 7.8 gives the FIF values for each reinforced configuration (PF, GB, GV) at the four load amplitudes (1, 2, 3, 4 kN) and at both test frequencies, with (a) showing results at 1 Hz and (b) showing results at 2 Hz. The FIF values are displayed as grouped bar charts with the horizontal reference line at FIF = 1.0 marking the threshold above which reinforcement provides a measurable fatigue benefit relative to the unreinforced control.

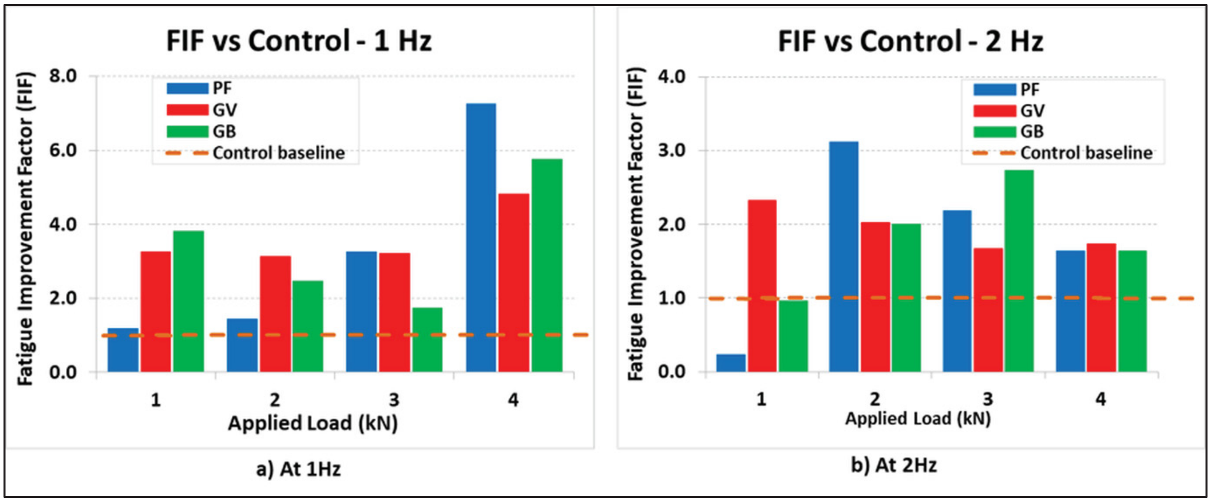

Figure 7.8 Fatigue Improvement Factor (FIF) relative to control at (a) 1 Hz and (b) 2 Hz

At 1 Hz, GB provides FIF of 3.80 at 1 kN, GV achieves 3.24, while PF shows only 1.19. This ranking (GB > GV >> PF) is inconsistent with the monotonic test results.

At 2 Hz, GB achieves FIF values ranging from 0.96 to 2.73, while GV ranges from 1.67 to 2.32. The PF geotextile shows FIF values below 1.0 at several load levels at 2 Hz, meaning it performs worse than the unreinforced control - a result that contradicts the mechanistic expectation based on its superior monotonic performance. This discrepancy provides the primary motivation for developing the correlation model presented in Section 7.6.

7.5.3 Basquin Slope Analysis

The magnitude of the Basquin exponent |B| quantifies the steepness of the S-N relationship in log-log space and is an indicator of a material's sensitivity to stress amplitude. A steeper slope (higher |B|) indicates that fatigue life decreases more rapidly with increasing stress, reflecting greater stress-level dependence of the fatigue response. Figure 7.9 compares the Basquin slope magnitude |B| for all four configurations at both test frequencies, enabling a direct assessment of how interlayer type and loading frequency influence the stress-life gradient.

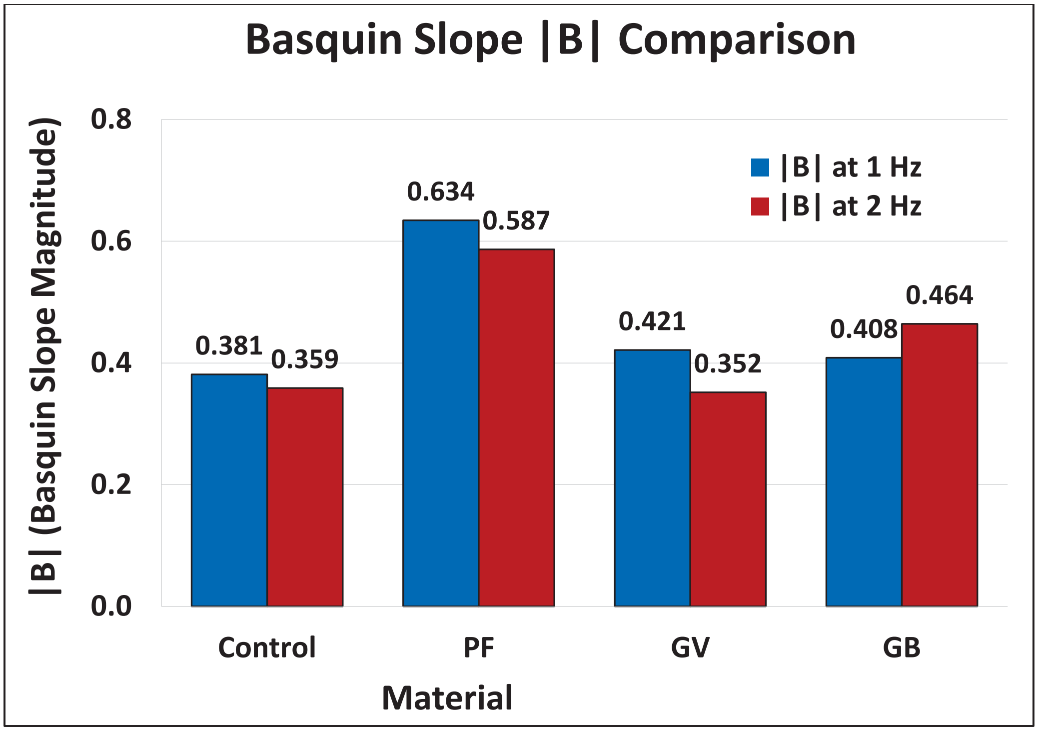

Figure 7.9 Basquin slope magnitude |B| comparison

PF exhibits the steepest Basquin slope (|B| = 0.634 at 1 Hz), higher than GV (0.419), GB (0.406), and Control (0.381). This is consistent with the material's strong sensitivity to loading rate and stress amplitude.

7.6 Monotonic-Fatigue Correlation Model

7.6.1 Methodology

A preliminary exploratory correlation framework was developed to investigate whether the unexpectedly low PF fatigue measurements are consistent with the broader monotonic-fatigue relationship established by the three other materials. The framework uses log-linear regression calibrated on three consistent datasets (Control, GB, GV) and is intended as a diagnostic tool, not a validated predictive model. With only three calibration points, the framework cannot establish a generalizable correlation; it can, however, indicate whether PF lies within or outside the trend defined by the other materials. Four monotonic parameters were evaluated as candidate predictors: (a) dissipated energy at 2 mm/min, (b) time to failure at 2 mm/min, (c) loading rate sensitivity index, and (d) peak force at 2 mm/min. The primary purpose of this section is to demonstrate the framework itself: the observations that follow are preliminary and based on the limited dataset of this study, and the approach is intended to be repeated with larger datasets in future research to develop a reliable predictive model.

The rationale for selecting the 2 mm/min loading rate parameters as primary predictors is that the slower rate better represents the sustained loading conditions experienced during cyclic fatigue. At 2 mm/min, viscoelastic relaxation mechanisms have more time to develop, producing material response characteristics that are more representative of the repeated loading conditions at 1-2 Hz. The loading rate sensitivity index bridges both rates and captures the material's time-dependent behavior.

The correlation model assumes a log-linear relationship between the monotonic parameter X and the mean fatigue life N_f:

$$\log(N_f) = m * \log(X) + c \tag{7.4}$$

where X represents the monotonic predictor variable (energy, time, rate sensitivity, or peak force), m is the regression slope, and c is the intercept. This functional form was chosen because both fatigue life and monotonic parameters span several orders of magnitude, and the log-log transformation linearizes the expected power-law relationship between material properties and fatigue resistance.

The diagnostic procedure follows the residual-analysis logic standard in outlier detection: the suspect observation (PF) is excluded from the fit so that the regression line is not pulled toward it, the regression is then constructed from the three remaining observations (Control, GB, GV), and the position of PF relative to that regression is reported as the diagnostic output. Step one extracts the mean fatigue life at 1 Hz, averaged across all four load amplitudes, for the three calibration materials: Control (N_f = 258 cycles), GB (N_f = 880 cycles), and GV (N_f = 837 cycles). Step two extracts the corresponding monotonic parameter value for each material from the 2 mm/min test data. Step three obtains the regression parameters m and c by least-squares fitting of the three calibration points in log-log space. Step four computes the PF position on this regression by substituting the PF monotonic parameter value, and reports it as a diagnostic indicator. The output is therefore a measure of consistency between the PF measurement and the trend defined by the other three materials, not a forecast of the true PF fatigue life.

Excluding PF from the calibration is essential to the diagnostic logic. The PF measurement is the observation under test; if PF were included in the fit, the regression line would be pulled toward the PF point and any deviation between the measurement and the trend would be artificially reduced. This is the same reason that, in standard outlier diagnostics, the candidate outlier is excluded from the regression before its residual is examined. Within this framing, the four candidate predictors yield four diagnostic positions for PF, and the spread among those positions is itself part of the output: when the candidate predictor mechanisms disagree on where the PF point should lie, no single diagnostic can be elevated above the others without an independent reason.

7.6.2 Correlation Results

A leave-one-out sensitivity check was performed on each of the four candidate models to quantify how strongly the predicted PF position depends on any single calibration material. Each calibration material in turn (Control, GB, GV) was removed from the regression, the line was refitted through the two remaining points, and the PF position on the refitted line was recomputed. With only three calibration points, the resulting two-point fit collapses to a deterministic line through those two points, so the leave-one-out exercise does not yield a conventional cross-validation statistic, but it does reveal the stability of the framework. Removing one material changed the predicted PF value by factors of three (rate sensitivity), five (peak force), and seventy (energy), and produced unbounded results for the time model when GV was removed, because the two remaining time-to-failure values were nearly identical. This sensitivity is itself the principal quantitative output. It shows that the framework cannot forecast a single PF value. The wide range of full-fit predictions (285 to 4,246 cycles) is a structural property of the three-point dataset, not a numerical artefact.

The models show variable goodness-of-fit, with R^2 ranging from 0.03 (peak force) to 0.91 (rate sensitivity), reflecting the limited calibration dataset of only three points. The time-based model predicts PF fatigue life of 4,246 cycles, far exceeding the measured value of 382 cycles.

Figure 7.10shows the energy-based correlation, where the dissipated energy at 2 mm/min is the predictor. The three calibration points (Control, GB, GV) show moderate scatter around the regression line with R-squared = 0.390, and the regression slope is negative, indicating higher monotonic energy does not necessarily correspond to longer fatigue life in this limited dataset. The model predicts a PF fatigue life of only 285 cycles based on PF's dissipated energy of 69.5 J, which is the highest among all materials at 2 mm/min.

Figure 7.10 shows the time-based correlation, using time to failure at 2 mm/min as the predictor. This model achieves R-squared = 0.294, a weak fit caused by the very narrow range of calibration time values (Control 235 s versus GB 238 s), which leaves the regression slope poorly constrained. Time to failure does not, on its own, explain fatigue life in this three-point dataset. The model nonetheless predicts a PF fatigue life of 4,246 cycles, about 11 times the measured value of 382 cycles. This gap arises from extrapolating PF's long time to failure (367 s) far beyond the calibration range and should be read as the size of the divergence, not as a reliable estimate.

Figure 7.10displays the rate sensitivity correlation. The loading rate sensitivity index, defined as the ratio of time to failure at 2 mm/min to that at 5 mm/min, captures the material's viscoelastic response characteristics. PF possesses the highest rate sensitivity (2.87), and the model predicts 1,408 cycles with R-squared = 0.91.

Figure 7.10shows the peak force correlation at 2 mm/min. This model achieves R-squared = 0.033, indicating essentially no linear correlation between peak force and fatigue life in this three-point dataset. The regression slope is negative, and the predicted PF fatigue life from this model is 525 cycles. Table 7.2 summarizes the fitted parameters and the resulting PF predictions for all four correlation models.

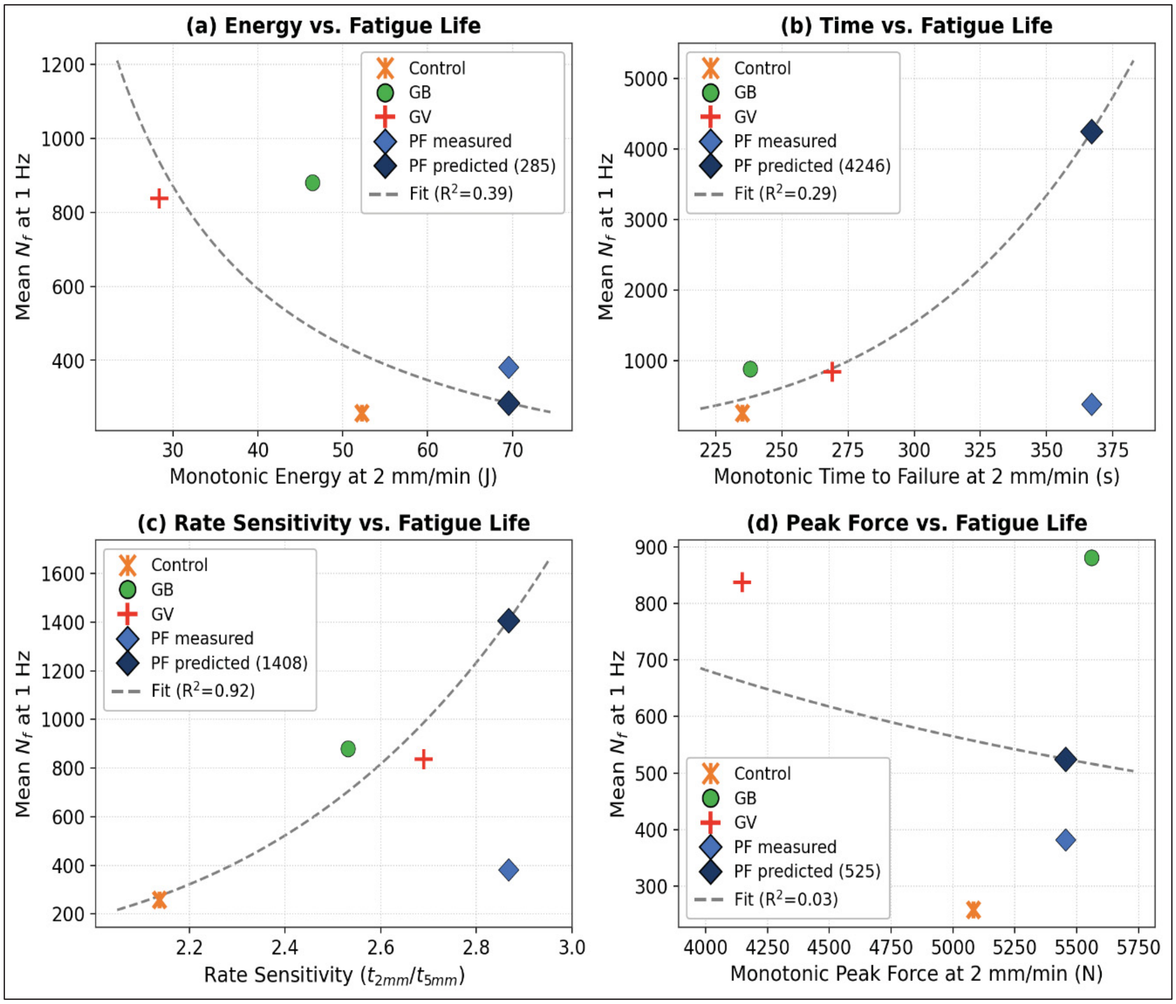

Figure 7.10 Monotonic-fatigue correlation models: (a) energy, (b) time, (c) rate sensitivity, (d) peak force

Table 7.2 Correlation model parameters and PF predictions (mean N_f at 1 Hz)

Predictor	Slope (b)	Intercept (a)	R²	PF Predicted	PF Measured
Energy (2 mm)	-1.33	4.90	0.39	285	382
Time (2 mm)	5.04	-9.30	0.29	4,246	382
Rate Sensitivity	5.57	0.60	0.91	1,408	382
Peak Force (2 mm)	-0.85	5.88	0.03	525	382

Across all four models, the predicted PF fatigue life ranges from 285 (energy) to 4,246 cycles (time), with an average of approximately 1,616 cycles. The time-based and rate sensitivity models predict PF well above the measured value of 382 cycles and above GB (880 cycles) and GV (837 cycles), while the energy and peak force models yield predictions near or below the measured value. The two models with the highest R^2 (rate sensitivity at 0.91 and energy at 0.39) diverge widely, reflecting the sensitivity of three-point calibration to the specific predictor chosen.

7.6.3 Per-Load Level Predictions

Beyond the mean-life predictions summarized in the previous section, the time-based correlation model was applied at each individual load amplitude to generate per-load fatigue life estimates for the PF geotextile. This resolution enables a direct comparison between measured and predicted values across the entire tested load range.

Predictions are presented in two complementary formats: Figure 7.11 presents the predicted PF fatigue life (navy diamonds) overlaid on the measured fatigue data for all four configurations at both test frequencies (1 Hz and 2 Hz) across the 1-4 kN load range, and Table 7.3 reports the corresponding numerical values at 1 Hz together with the predicted Fatigue Improvement Factor (FIF) defined as the ratio of predicted PF fatigue life to Control fatigue life at the same load level.

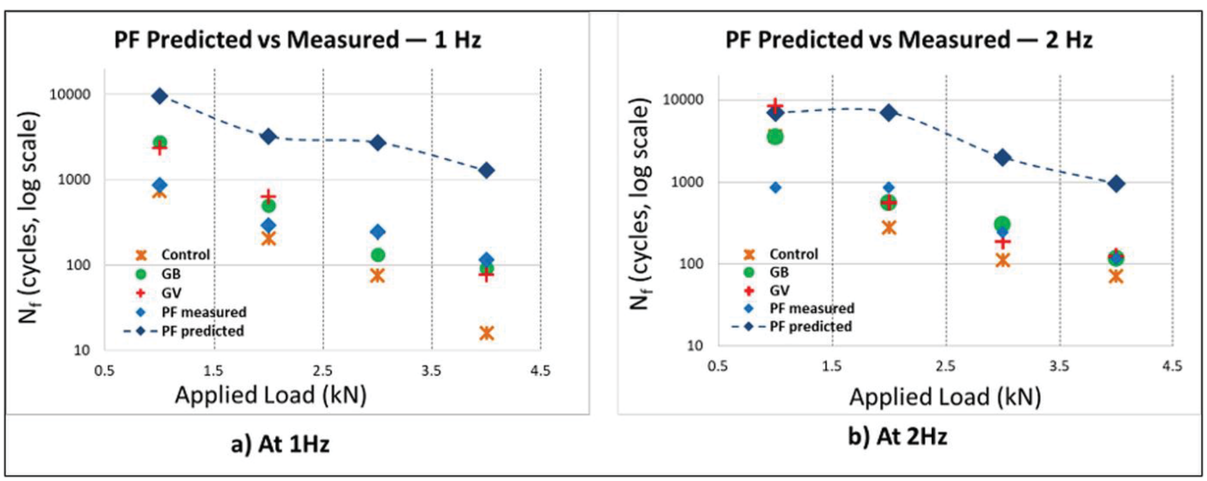

Figure 7.11 PF predicted (navy) versus measured (blue) fatigue life at each applied load level: (a) 1 Hz and (b) 2 Hz loading frequency

Table 7.3 Per-load PF predictions at 1 Hz (time-based model)

Load (kN)	Control	GB Geogrid	GV Geocomp.	PF Measured	PF Predicted	Pred. FIF
1	735	2,794	2,386	873	9,698	13.19
2	205	504	642	293	3,255	15.88
3	76	132	244	247	2,744	36.10
4	16	92	77	116	1,289	80.54

Within the time-based diagnostic framework, the per-load predictions place PF substantially above all other materials at the lower load levels. At 1 kN, the diagnostic indicates a predicted FIF of 13.19 against the measured 1.19. These values are extrapolations from a three-point calibration and outside the calibration envelope; they are reported here only to indicate the magnitude of the divergence between the diagnostic and the measurement, not as design values. Any conclusion about the actual PF fatigue performance under correctly prepared specimens would require dedicated re-testing.

7.7 Predicted S-N Curves for PF Geotextile

Applying the time-based diagnostic at each load level yields a predicted S-N curve for the PF geotextile that lies well above those of the other materials. This position is a direct consequence of PF's long monotonic time to failure propagated through the diagnostic; it is a projection of the diagnostic, not an observed result. The measured PF fatigue data are presented below for comparison.

Figure 7.12 the predicted PF data points (navy diamonds) onto the measured S-N curves for all materials. The predicted PF Basquin regression line (dashed navy) lies consistently above all other materials at both 1 Hz and 2 Hz. The faded blue diamonds represent the actual PF measured data, which cluster near or below the control curve. The visual contrast between predicted and measured PF positions quantifies the magnitude of the experimental discrepancy.

At 1 Hz, the predicted Basquin fit places PF at approximately 9,698 cycles at 1 kN against 873 measured cycles (factor of 11.1), and at 1,289 cycles versus 116 measured cycles at 4 kN (factor of 11.1). As elsewhere in this section, these numerical values are diagnostic indicators rather than validated predictions.

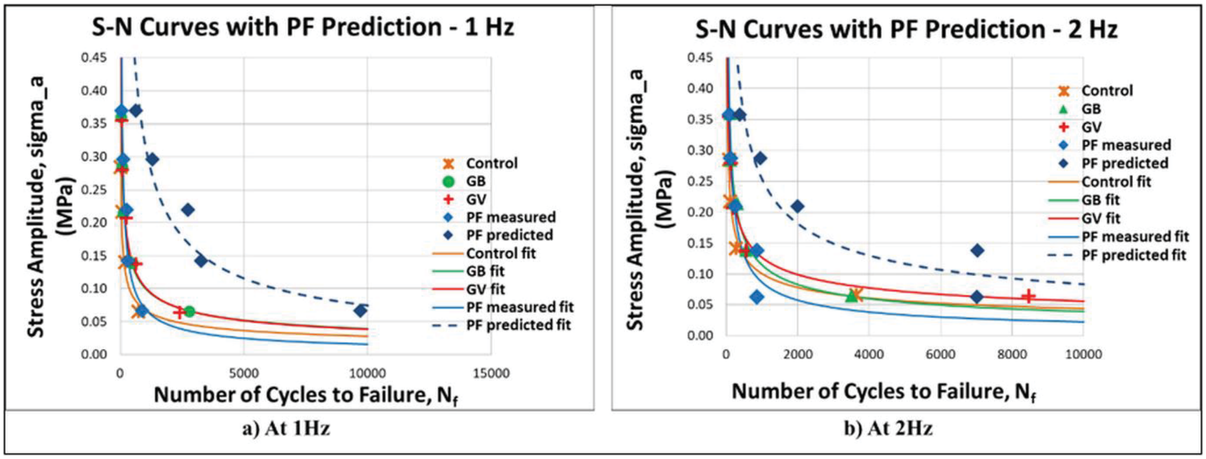

Figure 7.12 S-N curves at (a) 1 Hz and (b) 2 Hz with PF predicted Basquin regression (dashed navy). Faded points show PF measured data

7.8 Dissipated Energy Analysis

Dissipated energy provides a complementary measure of interlayer performance by capturing the total work done on the specimen before failure. It is calculated as the area under the force-displacement curve from initial loading to the end of the test, expressed in joules, and integrates both load-bearing and deformation capacity into a single quantity. The sensitivity of dissipated energy to loading rate reveals the viscoelastic character of the interlayer: rate-independent energy absorption indicates a stable, well-bonded interface, whereas a pronounced reduction at the slower rate indicates rate-sensitive weakening, typically associated with progressive debonding or viscoelastic relaxation.

Figure 7.13 presents the dissipated energy analysis for the four configurations, with (a) showing the monotonic dissipated energy at both loading rates (5 mm/min and 2 mm/min) and (b) displaying the energy ratio E_{2mm}/E_{5mm} that quantifies the rate-dependence of energy absorption, and (c) plotting the monotonic energies at the two rates against each other, where proximity to the 1:1 line indicates rate-insensitive energy dissipation: PF lies closest to the line while GV falls farthest below it. The complete numerical values for dissipated energy and peak displacement at both loading rates are summarized in Table 7.4. The PF geotextile exhibits the highest energy retention ratio (0.97), followed by Control (0.88), GB (0.76), and GV (0.36), establishing a clear hierarchy of rate-stability that mirrors the rate sensitivity patterns observed in the rate sensitivity analysis of Section 7.4. This energy-based hierarchy is also consistent with the TIF rate-sensitivity findings reported in Chapter 5, in which GV exhibited the most pronounced rate dependence.

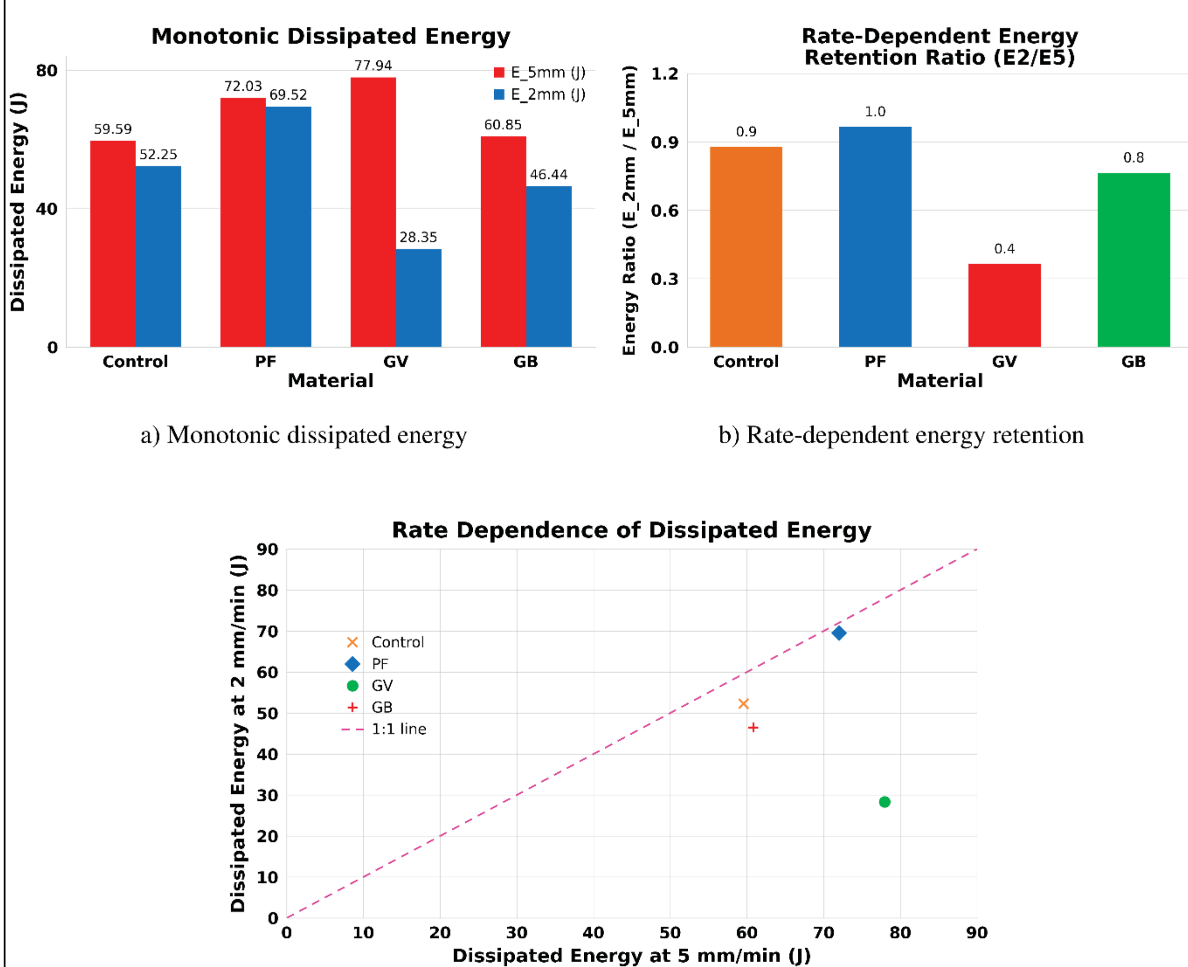

a) Monotonic dissipated energy

b) Rate-dependent energy retention

c) Dissipated energy: 2 mm/min versus 5 mm/min

Figure 7.13 Dissipated energy at the one-half placement: (a) monotonic dissipated energy at 5 mm/min and 2 mm/min for the four configurations, (b) the energy-retention ratio E_{2mm}/E_{5mm} (1.0 = full retention), and (c) the monotonic dissipated energy at 2 mm/min plotted against 5 mm/min with the 1:1 line

Table 7.4 Monotonic dissipated energy and displacement parameters

Material	E 5mm (J)	E 2mm (J)	E Ratio	Disp 5mm (mm)	Disp 2mm (mm)
Control	59.59	52.2	0.88	13.67	14.00
PF Geotextile	72.03	69.5	0.97	16.67	17.34
Geocomposite Glassphalt GV	77.94	28.35	0.36	15.33	11.17
Carbophalt GB Geogrid	60.85	46.4	0.76	13.08	12.47

The PF energy ratio ($E_{2\ mm}/E_{5\ mm}$) of 0.97 is the highest among all materials, indicating that the PF maintains nearly its full energy absorption capacity even at lower loading rates. In contrast, GV shows a large energy loss (ratio = 0.36).

The energy ratio indicates how well a material maintains its crack bridging capacity across different loading rates. A ratio close to 1.0 means the material absorbs nearly the same energy regardless of loading rate, suggesting stable interface behavior. PF's ratio of 0.97 indicates strong rate independence - the paving fabric maintains its energy absorption mechanism even when the loading rate is reduced by 60%. This behavior is consistent with the continuous fabric coverage providing uniform stress transfer regardless of loading rate.

GV's low energy ratio (0.36) indicates that the geocomposite loses 64% of its energy absorption capacity at the slower rate. This rate-dependent weakness is likely related to the nonwoven backing, which may undergo progressive debonding at slower loading rates. GB shows an intermediate ratio of 0.76, consistent with the mechanical interlock mechanism of the geogrid providing more stable but less extensive stress transfer compared to the geotextile.

7.9 Discussion

7.9.1 Mechanistic Interpretation of PF Geotextile Behavior

Three key mechanistic factors support the expectation that PF should outperform all other configurations within the tested conditions. First, the continuous fabric coverage ensures uniform stress transfer across the entire crack face. Second, the highest rate sensitivity (2.87x) among the tested materials indicates progressively stronger bonding at lower strain rates representative of fatigue loading. Third, the high energy retention ratio (0.97) confirms a stable, rate-independent energy absorption mechanism.

7.9.2 Possible Sources of Experimental Error

Two procedural limitations in specimen preparation were identified during post-test review and are documented here as candidate contributors to the deviation between predicted and measured PF fatigue life. Both are related to the cutting and orientation of the 80 x 80 x 80 mm cubic specimens extracted from the larger 500 x 180 x 100 mm compacted slabs. They are presented as possible mechanisms, not as proven causes; verification would require a re-test under a controlled procedure, which is recommended as future work.

The first limitation concerns specimen orientation. The compacted slabs were not marked to distinguish the substrate face (bottom) from the overlay face (top) before being cut into specimens, and the cutting protocol did not include a verification step to preserve this distinction.

For geogrid and geocomposite reinforcements, the mechanical response is largely symmetric across the two faces of the interlayer, so any inadvertent inversion has limited effect on the recorded fatigue life. For the paving fabric geotextile, however, the two faces differ in their bonding characteristics: the substrate face receives the tack coat emulsion before fabric placement, whereas the overlay face bonds primarily through asphalt penetration during compaction. If a specimen is inverted, the weaker overlay-side bond is placed at the critical crack propagation zone, which can promote premature debonding instead of the gradual crack bridging that the fabric is intended to provide.

The second limitation concerns notch orientation relative to the compaction direction. The slabs were compacted using a French roller compactor, which applies unidirectional loading along the rolling axis and induces anisotropy in both the asphalt matrix and the geosynthetic interlayer.

For the paving fabric in particular, the continuous fibers tend to align preferentially along the rolling direction, producing higher tensile strength and crack bridging capacity in that direction. The rolling direction was not transferred from the slab to the cut specimens, so the notch could have been positioned perpendicular to, rather than parallel with, the compaction axis. In specimens affected by this misalignment, crack propagation would proceed along the direction of lower fiber resistance, reducing the measured fatigue life.

The two limitations compound each other when both occur simultaneously: a specimen that is both inverted and notch-misaligned would carry a weakened interface at the critical location and would propagate the crack along the direction of lower fiber resistance. This compound effect offers a plausible mechanism for the observed deviation between the higher PF predictions and the measured PF response. The GB geogrid and GV geocomposite are intrinsically less sensitive to these procedural factors, because (a) grid-based reinforcements have more symmetric top-bottom bonding characteristics, and (b) the open grid structure provides similar crack resistance regardless of the orientation relative to the rolling direction.

7.9.3 Limitations of the Correlation Model

Several limitations of the present diagnostic framework should be acknowledged before its results are used in any design or specification context. A leave-one-out sensitivity analysis was applied to each candidate predictor and is reported in Section 7.6; removing any single calibration material changes the PF diagnostic position by factors of three (rate sensitivity), five (peak force), and seventy (energy), and produces an unbounded result for the time predictor. This sensitivity is the most immediate quantitative limitation and informs the structural points listed below. First, the regression is calibrated on only three data points (Control, GB, GV); with this sample size, the goodness-of-fit metrics span a wide range (R-squared from 0.03 to 0.91), which is itself diagnostic that the framework is exploratory rather than predictive. Second, predicting PF behavior from the calibrated regression is by construction an extrapolation: the PF monotonic parameter values lie outside or near the boundary of the Control-GB-GV envelope, and extrapolation magnifies any model misspecification. Third, the assumed log-linear relationship has no independent physical justification for the specific load and frequency range investigated and may not hold across a wider range of material properties or test conditions. Fourth, the framework does not propagate measurement uncertainty into the predicted values; reported predictions should be read as point estimates without confidence bounds. The Basquin slope estimates underlying Figure 7.10 carry standard errors of 0.019 to 0.153 (4.6% to 26.0% of the slope magnitude), reflecting the four to five load levels available per S-N fit. Confirmation of any predicted PF value would require both an enlarged calibration dataset and a re-test of PF specimens prepared under a documented and verified procedure.

7.10 Summary

This chapter examined the relationship between monotonic loading parameters and cyclic fatigue life for four geosynthetic-reinforced asphalt configurations. An exploratory log-linear correlation framework was developed using the three consistent datasets (Control, GB, GV) and applied as a diagnostic tool to interpret the PF measurements. In the monotonic experiments, the PF paving fabric had the highest loading rate sensitivity index (2.87), the highest energy retention ratio (0.97), and the longest time to failure at 2 mm/min, indicating mechanical characteristics that would generally be associated with strong fatigue performance.

The four candidate correlation models predict PF mean fatigue life in the range of 285 to 4,246 cycles at 1 Hz (mean of approximately 1,616 cycles), depending on the predictor variable used. The time-based and rate-sensitivity models, which capture the time-dependent character of the loading, predict values that substantially exceed the measured 382 cycles, whereas the energy-based model predicts a value below the measurement. The wide spread among predictions reflects the limited three-point calibration and is itself a quantitative indication that the present dataset cannot fix a single expected value. If dissipated energy is taken as the controlling parameter, the energy-based diagnostic positions PF at 285 cycles, which is comparable to the measured 382 cycles and would indicate consistency between the PF measurement and the broader trend; if the time-dependent character of the response is taken as controlling, the time and rate-sensitivity diagnostics position PF an order of magnitude higher and would indicate substantial deviation. The chapter does not select between these readings on internal grounds. Two specimen preparation procedures identified during post-test review are discussed in Section 7.9.2 as candidate contributors only relevant under the time-dependent reading.

The correlation framework provides a practical methodology for estimating fatigue life from monotonic test data, though the model should be validated with additional materials before design application.

CONCLUSION

This thesis presented a mechanistic investigation of the performance of three geosynthetic interlayer systems - a nonwoven paving fabric (PF), a fiberglass geocomposite (GV), and a carbon-glass fiber geogrid (GB) - in asphalt overlay systems, using the Crack Widening Device (CWD) developed at the Laboratoire de Chaussées et Matériaux Bitumineux of École de technologie supérieure. The research program addressed the fundamental question of how geosynthetic interlayers modify the fracture toughness, stiffness response, and fatigue life of asphalt overlay systems under controlled laboratory conditions. The program progressed systematically from comparative material evaluation, through the study of placement depth, temperature, and loading rate effects, to the development of empirical correlations between monotonic and cyclic fatigue loading behavior, and a supplementary investigation of interface pull-out resistance. The findings from these investigations are synthesized below around four cross-cutting themes that emerged across the experimental program, followed by a statement of the original contributions of the work and a set of recommendations for future research.

Comparative Material Behavior and Rate-Sensitivity Mechanisms

All three geosynthetic systems improved the crack resistance of asphalt overlays relative to unreinforced control specimens, but the mechanism through which each system acted differed significantly. The paving fabric PF dissipated energy primarily through fiber pull-out and progressive deformation, the geocomposite GV retained higher initial stiffness through its fiberglass grid, and the geogrid GB exhibited intermediate behavior. Aggregate size influenced the response, with coarser-graded mixtures producing greater crack-opening displacement before peak force due to enhanced aggregate interlock with the reinforcement. The comparative investigation also established the CWD as a reliable tool for characterizing geosynthetic interlayer performance under controlled laboratory conditions.

The temperature and loading-rate study revealed that these mechanism differences also produce qualitatively different rate-sensitivity behaviors. The geocomposite GV exhibited significant rate sensitivity, with a Toughness Improvement Factor (TIF) ratio of approximately 2.0 between the 5 mm/min and 2 mm/min conditions, attributable to the viscoelastic contribution of the fiberglass grid under rapid loading. PF exhibited a rate-stable benefit, with TIF remaining above unity at both rates (1.36-1.54 at 2 mm/min and 1.08-1.21 at 5 mm/min), while GB showed intermediate rate sensitivity with TIF values approaching unity at both rates. Temperature affected the absolute stiffness of all systems through reduced binder viscosity at 40 degrees C, but the relative ranking among systems and the rate-sensitivity classification were preserved across temperatures. Taken together, the comparative and rate-sensitivity findings establish that PF, GV, and GB are not interchangeable reinforcement options but represent three distinct strategies - energy dissipation, viscoelastic stiffening, and intermediate rigidity - each suited to different loading regimes.

Placement Depth as a Geometric Design Variable

Placement at one-third and two-thirds depth from the bottom of the overlay specimen produced fundamentally different crack-reinforcement interaction timing. Both placements exhibited the contractive-to-dilative phase transition defined in Section 5.5.5, but with markedly different timing and force retention: the one-third position engaged the reinforcement earlier and sustained higher force at the interlayer plane, with the two-thirds position retaining only about 78-79 per cent of the one-third force (consistent across both geotextile PF and grid GB), yielding greater energy dissipation in the contractive phase (82-86 J for PF at one-third versus 62-67 J at two-thirds). The two-thirds position delayed activation of the reinforcement mechanism, shifting the contractive-to-dilative transition to a stage where stress concentration and brittle fracture predominate. The intermediate one-half position produced transitional behaviour between these two extremes, with the geocomposite GV in particular showing an unexpected force reduction at mid-depth, consistent with interfacial shear effects becoming dominant when the reinforcement sits away from the zone of maximum tensile stress. The geometric relationship between the crack-tip trajectory and the geosynthetic plane governs the timing of the contractive-to-dilative transition rather than its presence. This mechanistic understanding provides a rational basis for selecting placement depth as a design variable in reflective-cracking mitigation, and demonstrates that the structural position of the interlayer within the overlay cross-section is as critical as the intrinsic material properties of the geosynthetic itself.

A Diagnostic Framework Linking Monotonic and Fatigue Behavior

The TIF methodology introduced in Chapter 5 provides a normalized metric for comparing geosynthetic performance across different testing conditions and temperatures, and forms the basis of the monotonic-fatigue correlation framework developed in Chapter 7. Four log-linear correlation models were constructed by regressing mean fatigue life on a single monotonic predictor (energy, time-to-failure, rate sensitivity, and peak force), calibrated on three materials (Control, GB, GV), with R-squared values ranging from 0.03 (peak force) to 0.91 (rate sensitivity). The rate-sensitivity and time-based models provided meaningful relationships; the energy and peak-force models showed weak or negligible correlations within the limited calibration set. When the framework was applied to PF - a material deliberately excluded from calibration to act as an independent test - the four models produced a wide spread of predicted fatigue lives, ranging from 285 to 4,246 cycles at 1 Hz against a measured value of 382 cycles. The energy-based model agreed closely with the measured value, whereas the time-based and rate-sensitivity models placed PF an order of magnitude higher. The spread between predictors, rather than any single point estimate, constitutes the principal output of the framework, since it identifies which monotonic descriptors are reliable predictors and which are not for each material class. The framework is therefore proposed as a diagnostic and calibration tool for future research rather than as a predictive instrument ready for design adoption.

Lessons from the First-Generation Apparatus

Two lessons emerged from the experimental program that warrant explicit mention because they shape the interpretation of the quantitative results above and inform the recommendations for future testing. The supplementary pull-out investigation conducted with a custom-designed first-generation apparatus did not produce valid interface bond data: testing of the PF geotextile resulted in tensile material failure rather than the intended interface debonding, as evidenced by an excessively large displacement at peak force (110 mm), a very low initial stiffness (approximately 0.014 kN/mm), visible necking of the geotextile, and a gradual post-peak descent characteristic of progressive fiber rupture. Comparison against the expected debonding response derived from the published pull-out data of Noory et al. (2017), adapted to the present specimen geometry of 0.18 square meters bonded area, showed that the test reached only 22 per cent of the expected bond capacity before fabric rupture, with a stiffness less than two per cent of the expected value. The excessive confinement pressure generated by the bolt-tightened clamping system was identified as the root cause. Although the first-generation test did not achieve its primary objective, the mechanistic interpretation of the failure mode provides a precise design roadmap for a next-generation apparatus.

In parallel, two procedural limitations in specimen preparation for the cyclic fatigue tests of Chapter 7 (specimen-orientation inversion and notch-direction misalignment relative to the French-roller compaction axis) were identified during post-test review and are presented as candidate contributors to the order-of-magnitude deviation observed under the time-based PF prediction. The methodological recommendation arising from both investigations is the inclusion of explicit face-marking and rolling-direction transfer steps in any future geosynthetic-reinforced CWD specimen preparation protocol, together with the introduction of a dead-weight or pneumatic confinement system at field-representative stress levels in the next-generation pull-out apparatus. These methodological lessons do not invalidate the quantitative findings of the thesis, but they delimit the conditions under which those findings hold and define the procedural improvements that would extend the framework to broader application.

Original Contributions

The principal original contributions of this thesis to the field of pavement engineering are the following:

(1) The first systematic comparative evaluation of three structurally different geosynthetic interlayer types (paving fabric, fiberglass geocomposite, carbon-glass fiber geogrid) under a single, controlled fracture-mechanics test protocol (the CWD), yielding a coherent performance ranking that links failure mechanism to material architecture.

(2) The introduction of the Toughness Improvement Factor (TIF) as a normalized comparative metric for geosynthetic-reinforced asphalt mixtures, validated across two temperatures

and two loading rates and shown to discriminate strongly rate-sensitive (GV) from less rate-sensitive (PF, GB) reinforcement.

(3) The mechanistic interpretation of placement depth as a geometric design variable that governs the timing of the contractive-to-dilative transition in crack-reinforcement interaction, providing a rational basis for placement-depth optimization in overlay design.

(4) The development of a four-predictor monotonic-fatigue correlation framework with a calibration-and-application protocol that uses the inter-predictor spread as a diagnostic signal, applicable to future studies that seek to predict cyclic fatigue life from short-duration monotonic tests.

(5) A documented methodological roadmap for next-generation interface pull-out testing of geosynthetic interlayers, derived from the first-generation apparatus failure mode and quantitative comparison against expected debonding responses from the published literature, and supported by a finite element model calibrated to the measured response.

Recommendations for Future Research

Based on the findings and limitations identified throughout this research program, the following recommendations are proposed for future investigations:

(1) Validation of the monotonic-fatigue correlation model across a broader range of geosynthetic types, asphalt mixture compositions, and testing temperatures, to establish the generality and boundary conditions of the proposed Nf correlation framework before it can be adopted in pavement design practice.

(2) Development of a second-generation pull-out apparatus incorporating a dead-weight or pneumatic confinement system applying field-representative stress levels (1 to 5 kPa for typical overlay thicknesses), multiple displacement transducers along the embedded specimen length to track the debonding front, and a temperature-controlled testing environment to promote interface bond failure before geotextile tensile failure.

(3) Standardization of CWD specimen preparation protocols, with particular attention to establishing clear top-bottom face marking conventions and notch orientation alignment relative to the compaction direction, to eliminate the preparation errors identified in Chapter 7 and to enable valid inter-laboratory comparison of results.

(4) Field validation of the laboratory-derived performance rankings by monitoring reflective cracking progression in instrumented pavement sections incorporating PF, GV, and GB interlayers under real traffic and climatic loading in Quebec, to bridge the gap between laboratory fracture mechanics parameters and field pavement performance.

(5) Extension of the rate-depth parametric framework of Chapter 5 (TIF, fracture energy, and interfacial J-integral) and of the cyclic fatigue program of Chapter 7 to sub-zero temperatures (-10 degrees C to -20 degrees C). Chapter 4 established the monotonic response at -20 degrees C at a single displacement rate; the combined rate-depth interaction and the fatigue behavior under thermal cracking conditions, which represent a critical and dominant distress mode in Quebec's subarctic climate, remain uncharacterized below the 25 degrees C and 40 degrees C used in Chapters 5 and 7.

(6) Integration of the CWD test parameters into mechanistic-empirical pavement design frameworks, such as the MEPDG, by establishing transfer functions between laboratory fracture mechanics metrics (TIF, initial stiffness K, energy ratio) and field reflective cracking progression rates, thereby enabling geosynthetic interlayer selection to be incorporated directly into pavement rehabilitation design procedures.

LIST OF BIBLIOGRAPHIC REFERENCES

AASHTO. (2008). *Mechanistic-empirical pavement design guide: A manual of practice.* American Association of State Highway and Transportation Officials, Washington, DC.

AASHTO. (2013). *Standard method of test for determining the fracture energy of asphalt mixtures using the semicircular bend geometry (SCB) (AASHTO TP 105-13).* American Association of State Highway and Transportation Officials, Washington, DC.

AASHTO. (2021). *Standard method of test for determining the fracture potential of asphalt mixtures using the Illinois Flexibility Index Test (I-FIT) (AASHTO T 393-21).* American Association of State Highway and Transportation Officials, Washington, DC.

AASHTO. (2022). *Standard method of test for determining the fatigue life of compacted asphalt mixtures subjected to repeated flexural bending (AASHTO T 321-22).* American Association of State Highway and Transportation Officials, Washington, DC.

Albayati, A. H., Ajool, Y. S., & Allawi, A. A. (2023). Comparative analysis of reinforced asphalt concrete overlays: Effects of thickness and temperature. *Materials, 16(17), 5990.* https://doi.org/10.3390/ma16175990

Amini, F. (2005). *Potential applications of paving fabrics to reduce reflective cracking.* Report No. FHWA/MS-DOT-RD-05-174, Jackson State University, Mississippi.

Anderson, T. L. (2005). *Fracture mechanics: Fundamentals and applications (3rd ed.).* CRC Press, Boca Raton, FL.

Arsenie, I. M., Chazallon, C., Duchez, J.-L., & Mouhoubi, S. (2017). Modelling of the fatigue damage of a geogrid-reinforced asphalt concrete. *Road Materials and Pavement Design, 18(1), 250-262.* https://doi.org/10.1080/14680629.2016.1159973

ASTM. (2019). *Standard test method for determination of cracking tolerance index of asphalt mixture using the indirect tensile cracking test at intermediate temperature (ASTM D8225-19).* ASTM International, West Conshohocken, PA.

ASTM. (2021). *Standard test method for Mode I interlaminar fracture toughness of unidirectional fiber-reinforced polymer matrix composites (ASTM D5528/D5528M-21).* ASTM International, West Conshohocken, PA.

ASTM. (2022). *Standard test method to determine asphalt retention of paving fabrics used in asphalt paving for full-width applications (ASTM D6140-22).* ASTM International, West Conshohocken, PA.

ASTM. (2024). *Standard test method for linear-elastic plane-strain fracture toughness of metallic materials (ASTM E399-24).* ASTM International, West Conshohocken, PA.

Baek, J., & Al-Qadi, I. L. (2006). Finite element method modeling of reflective cracking initiation and propagation: Investigation of the effect of steel reinforcement interlayer on retarding reflective cracking in hot-mix asphalt overlays. *Transportation Research*

Record: Journal of the Transportation Research Board, 1949(1), 32-42. https://doi.org/10.1177/0361198106194900104

Baek, J., & Al-Qadi, I. L. (2008). Mechanism of overlay reinforcement to retard reflective cracking under moving vehicular loading. In I. L. Al-Qadi, T. Scarpas, & A. Loizos (Eds.), *Pavement Cracking: Mechanisms, Modeling, Detection, Testing and Case Histories, 6th RILEM International Conference on Cracking in Pavements (pp. 563-573).* CRC Press.

Bondt, A. H. de. (1999). *Anti-reflective cracking design of (reinforced) asphaltic overlays.* PhD Thesis, Delft University of Technology, Netherlands.

Boussabnia, M. M. (2024). *Comportement en fatigue d'un enrobé à module élevé adapté aux régions froides : influence de la température, de la fréquence de sollicitation et relation entre les résultats obtenus à partir de différentes méthodes d'essai*. PhD Thesis, École de technologie supérieure, Montréal.

Brown, S. F., Thom, N. H., & Sanders, P. J. (2001). A study of grid reinforced asphalt to combat reflection cracking. *Journal of the Association of Asphalt Paving Technologists, 70, 543-569.*

Buttlar, W. G., Bozkurt, D., & Dempsey, B. J. (2000). Cost-effectiveness of paving fabrics used to control reflective cracking. *Transportation Research Record, 1730(1), 139-149.* https://doi.org/10.3141/1730-17

Button, J. W., & Lytton, R. L. (2007). Guidelines for using geosynthetics with hot-mix asphalt overlays to reduce reflective cracking. *Transportation Research Record, 2004(1), 111-119.* https://doi.org/10.3141/2004-12

Canadian General Standards Board. (1992). *Methods of testing geotextiles and geomembranes: Grab tensile test for geotextiles (tensile strength and elongation at break) (CAN/CGSB-148.1 No. 7.3-92).* Canadian General Standards Board, Gatineau, QC.

Canadian General Standards Board. (1994). *Textile test methods: Bursting strength - Diaphragm pressure test (CAN/CGSB-4.2 No. 11.1-94).* Canadian General Standards Board, Gatineau, QC.

Canestrari, F., Ferrotti, G., Lu, X., Millien, A., Partl, M. N., Petit, C., Phelipot-Mardelé, A., Piber, H., & Raab, C. (2012). Mechanical testing of interlayer bonding in asphalt pavements. In M. N. Partl, H. U. Bahia, F. Canestrari, C. de la Roche, H. Di Benedetto, H. Piber, & D. Sybilski (Eds.), *Advances in Interlaboratory Testing and Evaluation of Bituminous Materials* (RILEM State-of-the-Art Reports, Vol. 9, pp. 303-360). Springer, Dordrecht. https://doi.org/10.1007/978-94-007-5104-0_6

Canestrari, F., Belogi, L., Ferrotti, G., & Graziani, A. (2015). Shear and flexural characterization of grid-reinforced asphalt pavements and relation with field distress evolution. *Materials and Structures, 48(4), 959-975.* https://doi.org/10.1617/s11527-013-0207-1

Carret, J.-C., & Carter, A. (2022). Effects of adding a geotextile into a pavement structure on FWD experimental data and estimated pavement remaining service life. In *Proceedings of the RILEM International Symposium on Bituminous Materials (ISBM Lyon 2020)* (pp. 639-645). Springer International Publishing, Cham. https://doi.org/10.1007/978-3-030-46455-4_81

Cleveland, G. S., Button, J. W., & Lytton, R. L. (2002). *Geosynthetics in flexible and rigid pavement overlay systems to reduce reflection cracking.* Report No. FHWA/TX-02/1777-1, Texas Transportation Institute, College Station, TX.

Correia, N. S., & Zornberg, J. G. (2016). Mechanical response of flexible pavements enhanced with geogrid-reinforced asphalt overlays. *Geosynthetics International, 23(3), 183-193.* https://doi.org/10.1680/jgein.15.00041

Correia, N. S., Silva, M. P. S., & Shahkolahi, A. (2024). Optimum tack coat rate for different asphalt geosynthetic interlayers to achieve optimum shear bond strength. *Geotextiles and Geomembranes, 52(4), 778-789.* https://doi.org/10.1016/j.geotexmem.2024.04.004

Correia, N. S., Bernardinelli, A. L. C. S., Santos, K. M., & Shahkolahi, A. (2025). Influence of different paving geosynthetics on crack growth phases and strain behavior in asphalt overlays. *E3S Web of Conferences, 644, 03012.* https://doi.org/10.1051/e3sconf/202564403012

Dave, E. V., & Buttlar, W. G. (2010). Thermal reflective cracking of asphalt concrete overlays. *International Journal of Pavement Engineering, 11(6), 477-488.* https://doi.org/10.1080/10298430903578911

El-Hakim, M., & Tighe, S. L. (2014). Impact of freeze-thaw cycles on mechanical properties of asphalt mixes. *Transportation Research Record, 2444(1), 20-27.* https://doi.org/10.3141/2444-03

Elseifi, M. A., & Al-Qadi, I. L. (2004). A simplified overlay design model against reflective cracking utilizing service life prediction. *Road Materials and Pavement Design, 5(2), 169-191.* https://doi.org/10.1080/14680629.2004.9689968

Ferrotti, G., Canestrari, F., Virgili, A., & Grilli, A. (2011). A strategic laboratory approach for the performance investigation of geogrids in flexible pavements. *Construction and Building Materials, 25(5), 2343-2348.* https://doi.org/10.1016/j.conbuildmat.2010.11.032

Gallego, J., & Prieto, J. N. (2006). New laboratory equipment for study of reflective cracking in asphalt overlays. *Transportation Research Record, 1970, 215-222.* https://doi.org/10.3141/1970-25

Gharbi, M., Nguyen, M. L., Trichet, S., & Chabot, A. (2017). Characterization of the bond between asphalt layers and glass fiber grid with help of a Wedge Splitting Test. In A. Loizos, I. Al-Qadi, & T. Scarpas (Eds.), *Bearing Capacity of Roads, Railways and Airfields: Proceedings of the 10th International Conference on the Bearing Capacity of*

Roads, Railways and Airfields (BCRRA 2017) (pp. 1517-1524). CRC Press, London. https://doi.org/10.1201/9781315100333-201

Gonzalez-Torre, I., Calzada-Perez, M. A., Vega-Zamanillo, A., & Castro-Fresno, D. (2015). Evaluation of reflective cracking in pavements using a new procedure that combine loads with different frequencies. *Construction and Building Materials, 75, 368-374.* https://doi.org/10.1016/j.conbuildmat.2014.11.030

Guo, Z., & Zhang, Q. (1993). Prevention of cracking progress of asphalt overlayer with glass fabric. In J. M. Rigo, R. Degeimbre, & L. Francken (Eds.), *Reflective Cracking in Pavements: State of the Art and Design Recommendations, Proceedings of the Second International RILEM Conference* (RILEM Proceedings 20, pp. 398-405). E & FN Spon, Liege, Belgium.

Gupta, R., Swan, R. H., & Zornberg, J. G. (2014). Laboratory pullout equipment for testing soil-geosynthetic interface for reinforced flexible pavement design. In *Geo-Congress 2014: Geo-characterization and Modeling for Sustainability, Geotechnical Special Publication No. 234* (pp. 2543-2557). ASCE, Atlanta, GA. https://doi.org/10.1061/9780784413272.246

Ho, V. T., Giani, C., Vaillancourt, M., Dave, E., & Carter, A. (2025). Study the crack development of geosynthetics interlayers in bituminous structures under different temperatures. *Journal of Testing and Evaluation, 53(5), 1291-1306.* https://doi.org/10.1520/JTE20240285

Ho, V. T., Vaillancourt, M., Dave, E. V., & Carter, A. (2026). Fracture-energy-based assessment of geosynthetic interlayers in asphalt overlays under variable temperature, displacement rate, and placement depth. Manuscript submitted to *International Journal of Pavement Engineering*, 2026.

Hu, S., Zhou, F., & Scullion, T. (2010). Reflection cracking-based asphalt overlay thickness design and analysis tool. *Transportation Research Record, 2155(1), 12-23.* https://doi.org/10.3141/2155-02

Jacobs, M. M. J., Hopman, P. C., & Molenaar, A. A. A. (1996). Application of fracture mechanics principles to analyze cracking in asphalt concrete. *Journal of the Association of Asphalt Paving Technologists, 65,* 1-39.

Jaskula, P., & Rys, D. (2017). Effect of interlayer bonding quality of asphalt layers on pavement performance. *IOP Conference Series: Materials Science and Engineering, 236(1), 012005.* https://doi.org/10.1088/1757-899X/236/1/012005

Jayawickrama, P. W., & Lytton, R. L. (1987). Methodology for predicting asphalt concrete overlay life against reflective cracking. In *Proceedings, 6th International Conference on Structural Design of Asphalt Pavements* (Vol. I, pp. 912-924). Ann Arbor, Michigan.

Kazimierowicz-Frankowska, K., & Kulczykowski, M. (2021). Deformation of model reinforced soil structures: Comparison of theoretical and experimental results.

Geotextiles and Geomembranes, 49(5), 1176-1191. https://doi.org/10.1016/j.geotexmem.2021.03.011

Khodaii, A., Fallah, S., & Moghadas Nejad, F. (2009). Effects of geosynthetics on reduction of reflection cracking in asphalt overlays. *Geotextiles and Geomembranes, 27(1), 1-8.* https://doi.org/10.1016/j.geotexmem.2008.05.007

Kim, D., & Mun, S. (2021). Development of an interface shear strength tester and a model predicting the optimal application rate of tack coat. *Construction Materials, 1(1), 22-38.* https://doi.org/10.3390/constrmater1010002

Koerner, R. M. (2012). *Designing with geosynthetics (6th ed.).* Xlibris Corporation, Bloomington, IN.

Kumar, V. V., & Saride, S. (2018). Evaluation of cracking resistance potential of geosynthetic reinforced asphalt overlays using direct tensile strength test. *Construction and Building Materials, 162, 37-47.* https://doi.org/10.1016/j.conbuildmat.2017.11.158

Kumar, V. V., Roodi, G. H., Subramanian, S., & Zornberg, J. G. (2023). Installation of geosynthetic interlayers during overlay construction: Case study of Texas State Highway 21. *Transportation Geotechnics, 43, 101127.* https://doi.org/10.1016/j.trgeo.2023.101127

Kuo, C. M., & Hsu, T. R. (2003). Traffic induced reflective cracking on pavements with geogrid reinforced asphalt concrete overlay. In 82nd Annual TRB Meeting, Washington, DC.

Leiva-Padilla, P., Loria-Salazar, L., Aguiar-Moya, J. P., & Leiva-Villacorta, F. (2016). Reflective cracking in asphalt overlays reinforced with geotextiles. In *8th RILEM International Conference on Mechanisms of Cracking and Debonding in Pavements* (RILEM Bookseries, Vol. 13, pp. 219-226). Springer, Dordrecht. https://doi.org/10.1007/978-94-024-0867-6_31

Li, X., & Marasteanu, M. O. (2010). Using semi-circular bending test to evaluate low temperature fracture resistance for asphalt concrete. *Experimental Mechanics, 50(7), 867-876.* https://doi.org/10.1007/s11340-009-9303-0

Li, Q., Yang, G., Wang, H., & Yue, Z. (2022). The direct and oblique shear bond strength of geogrid-reinforced asphalt. *Coatings, 12(4), 514.* https://doi.org/10.3390/coatings12040514

Lytton, R. L. (1989). Use of geotextiles for reinforcement and strain relief in asphalt concrete. *Geotextiles and Geomembranes, 8(3), 217-237.* https://doi.org/10.1016/0266-1144(89)90004-6

Lytton, R. L., Tsai, F. L., Lee, S. I., Luo, R., Hu, S., & Zhou, F. (2010). *Models for predicting reflection cracking of hot-mix asphalt overlays.* NCHRP Report 669, Transportation Research Board, Washington, DC. https://doi.org/10.17226/14410

Marienfeld, M. L., & Baker, T. L. (1999). Paving fabric interlayer system as a pavement moisture barrier. *Transportation Research Circular E-C006,* Transportation Research Board, Washington, DC.

Miller, J. S., & Bellinger, W. Y. (2014). *Distress identification manual for the long-term pavement performance program (5th revised ed.).* Report No. FHWA-HRT-13-092, Federal Highway Administration, McLean, VA.

Ministère des Transports du Québec. (n.d.). *Résistance à la déformation des enrobés à l'essai d'orniérage (LC 26-410).* Recueil des méthodes d'essai LC, Les Publications du Québec, Québec, Canada.

Moayedi, H., Kazemian, S., Prasad, A., & Huat, B. B. K. (2009). Effect of geogrid reinforcement location in paved road improvement. *Electronic Journal of Geotechnical Engineering, 14, 1-11.*

Molenaar, A. A. A. (1983). Structural performance and design of flexible road constructions and asphalt concrete overlays (PhD thesis). Delft University of Technology, Delft, The Netherlands.

Moreno-Navarro, F., & Rubio-Gámez, M. C. (2013). UGR-FACT test for the study of fatigue cracking in bituminous mixes. *Construction and Building Materials, 43, 184-190.* https://doi.org/10.1016/j.conbuildmat.2013.02.024

Moreno-Navarro, F., & Rubio-Gámez, M. C. (2016). A review of fatigue damage in bituminous mixtures: Understanding the phenomenon from a new perspective. *Construction and Building Materials, 113, 927-938.* https://doi.org/10.1016/j.conbuildmat.2016.03.126

MTQ. (2022). *Bilan de l'état du réseau routier du Québec.* Ministère des Transports du Québec, Québec, Canada.

Nguyen, M. L., Chazallon, C., Sahli, M., Koval, G., Hornych, P., Doligez, D., Chabot, A., Le Gal, Y., Brissaud, L., & Godard, E. (2020). Design of reinforced pavements with glass fiber grids: From laboratory evaluation of the fatigue life to accelerated full-scale test. In A. Chabot, P. Hornych, J. Harvey, & L. G. Loria-Salazar (Eds.), *Accelerated Pavement Testing to Transport Infrastructure Innovation, Lecture Notes in Civil Engineering, Vol. 96 (pp. 329-338).* Springer. https://doi.org/10.1007/978-3-030-55236-7_34

Nithin, S., Rajagopal, K., & Veeraragavan, A. (2015). State-of-the-art summary of geosynthetic interlayer systems for retarding the reflective cracking. *Indian Geotechnical Journal, 45(4), 472-487.* https://doi.org/10.1007/s40098-015-0161-7

Noory, A., Moghadas Nejad, F., & Khodaii, A. (2017). Evaluation of shear bonding and reflective crack propagation in a geocomposite reinforced overlay. *Geosynthetics International, 24(4), 343-361.* https://doi.org/10.1680/jgein.17.00007

Norambuena-Contreras, J., & Gonzalez-Torre, I. (2015). Influence of geosynthetic type on retarding cracking in asphalt pavements. *Construction and Building Materials, 78, 421-429.* https://doi.org/10.1016/j.conbuildmat.2014.12.034

Ozer, H., Al-Qadi, I. L., Lambros, J., El-Khatib, A., Singhvi, P., & Doll, B. (2016). Development of the fracture-based flexibility index for asphalt concrete cracking potential using modified semi-circle bending test parameters. *Construction and Building Materials, 115, 390-401.* https://doi.org/10.1016/j.conbuildmat.2016.03.144

Paris, P. C., & Erdogan, F. (1963). A critical analysis of crack propagation laws. *Journal of Basic Engineering, 85(4), 528-533.* https://doi.org/10.1115/1.3656900

Pasquini, E., Bocci, M., Ferrotti, G., & Canestrari, F. (2013). Laboratory characterisation and field validation of geogrid-reinforced asphalt pavements. *Road Materials and Pavement Design, 14(1), 17-35.* https://doi.org/10.1080/14680629.2012.735797

Pasquini, E., Bocci, M., & Canestrari, F. (2014). Laboratory characterisation of optimised geocomposites for asphalt pavement reinforcement. *Geosynthetics International, 21(1), 24-36.* https://doi.org/10.1680/gein.13.00032

Pasquini, E., Pasetto, M., & Canestrari, F. (2015). Geocomposites against reflective cracking in asphalt pavements: Laboratory simulation of a field application. *Road Materials and Pavement Design, 16(4), 815-835.* https://doi.org/10.1080/14680629.2015.1044558

Prieto, J. N., Gallego, J., & Pérez, I. (2007). Application of the wheel reflective cracking test for assessing geosynthetics in anti-reflection pavement cracking systems. *Geosynthetics International, 14(5), 287-297.* https://doi.org/10.1680/gein.2007.14.5.287

Pszczola, M., & Szydlowski, C. (2018). Influence of bitumen type and asphalt mixture composition on low-temperature strength properties according to various test methods. *Materials, 11(11), 2118.* https://doi.org/10.3390/ma11112118

Raab, C., & Partl, M. N. (2004). Effect of tack coats on interlayer shear bond of pavements. In *Proceedings of the 8th Conference on Asphalt Pavements for Southern Africa (CAPSA'04)* (pp. 847-855). Sun City, South Africa, 12-16 September 2004.

Raab, C., & Partl, M. N. (2008). Investigation into a long-term interlayer bonding of asphalt pavements. *Baltic Journal of Road and Bridge Engineering, 3(2), 65-70.* https://doi.org/10.3846/1822-427X.2008.3.65-70

Raab, C., Partl, M. N., & Abd El Halim, A. O. (2009). Evaluation of interlayer shear bond devices for asphalt pavements. *Baltic Journal of Road and Bridge Engineering, 4(4), 186-195.* https://doi.org/10.3846/1822-427X.2009.4.186-195

Raab, C., Abd El Halim, A. O., & Partl, M. N. (2012). Interlayer bond testing using a model material. *Construction and Building Materials, 26(1), 190-199.* https://doi.org/10.1016/j.conbuildmat.2011.06.009

Raab, C., Arraigada, M., Partl, M. N., & Schiffmann, F. (2017). Cracking and interlayer bonding performance of reinforced asphalt pavements. *European Journal of Environmental and Civil Engineering, 21(sup1), 14-26.* https://doi.org/10.1080/19648189.2017.1306462

Raab, C., & Arraigada, M. (2025). *Towards a better understanding of crack propagation in asphalt pavements with reinforcement grids (using laboratory-scaled traffic load and interlayer shear test). Road Materials and Pavement Design, 26(sup1), 39-54.* https://doi.org/10.1080/14680629.2025.2482878

Ragni, D., Montillo, T., Marradi, A., & Canestrari, F. (2020a). Fast Falling Weight Accelerated Pavement Testing and Laboratory Analysis of Asphalt Pavements Reinforced with Geocomposites. *In Asphalt Pavements and Environment, Lecture Notes in Civil Engineering, 48, 417-430.* https://doi.org/10.1007/978-3-030-29779-4_41

Ragni, D., Canestrari, F., Allou, F., Petit, C., & Millien, A. (2020b). Shear-Torque Fatigue Performance of Geogrid-Reinforced Asphalt Interlayers. *Sustainability, 12(11), 4381.* https://doi.org/10.3390/su12114381

Rice, J. R. (1968). A path independent integral and the approximate analysis of strain concentration by notches and cracks. *Journal of Applied Mechanics, 35(2), 379-386.* https://doi.org/10.1115/1.3601206

Romeo, E., Freddi, F., & Montepara, A. (2014). Mechanical behaviour of surface layer fiberglass-reinforced flexible pavements. *International Journal of Pavement Engineering, 15(2), 95-109.* https://doi.org/10.1080/10298436.2013.828838

Roodi, G. H., Kumar, V. V., Subramanian, S., & Zornberg, J. G. (2025). *Modified AASHTO empirical pavement design method for geosynthetic-reinforced asphalt.* Geosynthetics International, 33(2), 326-344. https://doi.org/10.1680/jgein.25.00056

Rueda, E. J., Bastidas-Martínez, J. G., Ruge, J. C., Alayón, Y., & Olivos, J. (2023). Laboratory analysis of an asphalt mixture overlay reinforced with a biaxial geogrid. *Coatings, 13(1), 99.* https://doi.org/10.3390/coatings13010099

Saride, S., & Kumar, V. V. (2017). Influence of geosynthetic-interlayers on the performance of asphalt overlays on pre-cracked pavements. *Geotextiles and Geomembranes, 45(3), 184-196.* https://doi.org/10.1016/j.geotexmem.2017.01.010

Schapery, R. A. (1984). Correspondence principles and a generalized J-integral for large deformation and fracture analysis of viscoelastic media. *International Journal of Fracture, 25(3), 195-223.* https://doi.org/10.1007/BF01140837

Sobhan, K., & Tandon, V. (2008). Mitigating reflection cracking in asphalt overlays using geosynthetic reinforcements. *Road Materials and Pavement Design, 9(3), 367-387.* https://doi.org/10.1080/14680629.2008.9690124

Solatiyan, E., Bueche, N., & Carter, A. (2020). A review on mechanical behavior and design considerations for reinforced-rehabilitated bituminous pavements. *Construction and Building Materials, 257, 119483.* https://doi.org/10.1016/j.conbuildmat.2020.119483

Solatiyan, E., Bueche, N., & Carter, A. (2021a). Laboratory evaluation of interfacial mechanical properties in geogrid-reinforced bituminous layers. *Geotextiles and Geomembranes, 49(4), 895-909.* https://doi.org/10.1016/j.geotexmem.2020.12.014

Solatiyan, E., Bueche, N., & Carter, A. (2021b). Experimental measurements of interfacial mechanical properties between rehabilitated bituminous layers using innovative approaches. *Journal of Materials in Civil Engineering, 33(5), 04021077.* https://doi.org/10.1061/(ASCE)MT.1943-5533.0003697

Solatiyan, E., Ho, V. T., Bueche, N., Vaillancourt, M., & Carter, A. (2023). Evaluation of crack development through a bituminous interface reinforced with geosynthetic materials by using a novel approach. *Transportation Research Record, 2677(11), 446-457.* https://doi.org/10.1177/03611981231166002

Spadoni, S., Ingrassia, L. P., Paoloni, G., Virgili, A., & Canestrari, F. (2021). Influence of geocomposite properties on the crack propagation and interlayer bonding of asphalt pavements. *Materials, 14(18), 5310.* https://doi.org/10.3390/ma14185310

Steen, E. S. (2004). Reflective cracking and the use of non-woven interlayers to arrest crack propagation. In Proceedings, 8th Conference on Asphalt Pavements for Southern Africa (CAPSA), Sun City, South Africa.

Sudarsanan, N., Karpurapu, R., & Amrithalingam, V. (2018). An investigation on the interface bond strength of geosynthetic-reinforced asphalt concrete using Leutner shear test. *Construction and Building Materials, 186, 423-437.* https://doi.org/10.1016/j.conbuildmat.2018.07.010

Texas Department of Transportation (TxDOT). (2019). *Test procedure for overlay test, TxDOT designation: Tex-248-F.* Materials and Tests Division, Austin, TX.

Thives, L. P., Pais, J. C., Pereira, P. A. A., Minhoto, M. C., & Trichês, G. (2022). Performance of asphalt rubber mixture overlays to mitigate reflective cracking. *Materials, 15(7), 2375.* https://doi.org/10.3390/ma15072375

Tutumluer, E., Kang, M., & Qamhia, I. I. A. (2024). Geosynthetic stabilization of road pavements, railroads, and airfields. *Transportation Geotechnics, 48, 101345.* https://doi.org/10.1016/j.trgeo.2024.101345

Virgili, A., Canestrari, F., Grilli, A., & Santagata, F. A. (2009). Repeated load test on bituminous systems reinforced by geosynthetics. *Geotextiles and Geomembranes, 27(3), 187-195.* https://doi.org/10.1016/j.geotexmem.2008.11.004

Wagoner, M. P., Buttlar, W. G., & Paulino, G. H. (2005). Disk-shaped compact tension test for asphalt concrete fracture. *Experimental Mechanics, 45(3), 270-277.* https://doi.org/10.1007/BF02427951

Wang, D., Wang, S.-L., Tighe, S., Bhat, S., & Yin, S. (2023). Construction of geosynthetic-reinforced pavements and evaluation of their impacts. *Applied Sciences, 13(18), 10327.* https://doi.org/10.3390/app131810327

Zamora-Barraza, D., Calzada-Pérez, M. A., Castro-Fresno, D., & Vega-Zamanillo, A. (2011). Evaluation of anti-reflective cracking systems using geosynthetics in the interlayer zone. *Geotextiles and Geomembranes, 29(2), 130-136.* https://doi.org/10.1016/j.geotexmem.2010.10.005

Zhou, F., & Scullion, T. (2005). *Overlay tester: A rapid performance related crack resistance test.* Report No. FHWA/TX-05/0-4467-2, Texas Transportation Institute, College Station, TX.

Zhou, F., Im, S., Sun, L., & Scullion, T. (2017). Development of an IDEAL cracking test for asphalt mix design and QC/QA. *Road Materials and Pavement Design, 18(sup4), 405-427.* https://doi.org/10.1080/14680629.2017.1389082

Zornberg, J. G., & Thompson, N. G. (2012). Application guide and specifications for geotextiles in roadway applications. Report No. FHWA/TX-10/0-5812-1, Center for Transportation Research, University of Texas at Austin.